



HAL
open science

Engineered Biomimetic platforms to analyse molecular and cellular role of Heparan Sulfate on BMP2 bioactivity

Julius Sefkow-Werner

► To cite this version:

Julius Sefkow-Werner. Engineered Biomimetic platforms to analyse molecular and cellular role of Heparan Sulfate on BMP2 bioactivity. Biotechnology. Université Grenoble Alpes [2020-..], 2021. English. NNT : 2021GRALS036 . tel-04348099

HAL Id: tel-04348099

<https://theses.hal.science/tel-04348099v1>

Submitted on 16 Dec 2023

HAL is a multi-disciplinary open access archive for the deposit and dissemination of scientific research documents, whether they are published or not. The documents may come from teaching and research institutions in France or abroad, or from public or private research centers.

L'archive ouverte pluridisciplinaire **HAL**, est destinée au dépôt et à la diffusion de documents scientifiques de niveau recherche, publiés ou non, émanant des établissements d'enseignement et de recherche français ou étrangers, des laboratoires publics ou privés.



THÈSE

Pour obtenir le grade de

DOCTEUR DE L'UNIVERSITÉ GRENOBLE ALPES

Spécialité : BIS - Biotechnologie, instrumentation, signal et imagerie pour la biologie, la médecine et l'environnement

Arrêté ministériel : 25 mai 2016

Présentée par

Julius SEFKOW-WERNER

Thèse dirigée par **Catherine PICART**, Ingénieur Chercheur, Université Grenoble Alpes
et co-encadrée par **Elisa MIGLIORINI**, CNRS

préparée au sein du **Laboratoire Laboratoire des matériaux et du génie physique**
dans l'**École Doctorale Ingénierie pour la Santé la Cognition et l'Environnement**

Plateformes biomimétiques pour déchiffrer les rôles moléculaires et cellulaires du sulfate d'héparane sur la bioactivité de BMP2

Engineered Biomimetic platforms to analyse molecular and cellular role of Heparan Sulfate on BMP2 bioactivity

Thèse soutenue publiquement le **15 décembre 2021**,
devant le jury composé de :

Madame CATHERINE PICART

Ingénieur HDR, CEA CENTRE DE GRENOBLE, Directrice de thèse

Madame SYLVIE RICARD-BLUM

Professeur des Universités, UNIVERSITE LYON 1 - CLAUDE BERNARD,
Rapporteuse

Madame STEPHANIE DESCROIX

Directeur de recherche, CNRS DELEGATION PARIS CENTRE,
Rapporteuse

Monsieur JULIEN GAUTROT

Professeur associé, Queen Mary University of London, Examineur

Madame KARINE ANSELME

Directeur de recherche, CNRS DELEGATION ALSACE, Examinatrice

Monsieur EMMANUEL BELAMIE

Directeur d'études, EC PRATIQUE DES HAUTES ETUDES,
Examineur

Monsieur ANTOINE DELON

Professeur des Universités, UNIVERSITE GRENOBLE ALPES, Président

**Engineered biomimetic platforms to analyze the
molecular and cellular role of heparan sulfate on BMP2
bioactivity**

Acknowledgements

An uncountable number of people accompanied me over the time of my PhD project and contributed to the outcome summarized in this manuscript. I am very thankful for their support and their confidence in me, which helped me to persevere over the last years.

First, I want to express my deepest gratitude to Elisa Migliorini for her excellent supervision throughout the project with high dedication, competence and joy. She encouraged me to start the PhD despite my background being far away from this scientific field and taught me with great enthusiasm and patience the skills and tools needed to reach independence. Her tremendous support during the writing of this manuscript was very helpful in a scientific and moral way. It was very precious to be given the opportunity to learn something entirely new and this led to me finding an occupation in which I see bigger purpose. We became a great team, starting with our four arms together under the cell culture hood and I sincerely hope that our friendship will last longer than the duration of this project.

Catherine Picart was directing this thesis and I thank her very much for her guidance throughout the project with great ideas, precious comments on the articles and the manuscript, broad knowledge and stimulating discussions. Her vision to heal large bone fractures using synthetic implants was giving a global context to my studies, which inspired me and gave me the feeling to work on something useful. Besides her radiating passion for science, her human and kind leadership approach applied to our group will very positively remain in my memories.

I am extremely grateful to my family and especially to my mother and father for their great moral support but also for the education I received from them over the last three decades. They always prioritized learning, personal growth and experiences, which set me up with a strong and universal set of skills to encounter the divers challenges brought up throughout the thesis. Equally important was the help from my friends who supported me despite the long distance and from those who became close to me over the course of the last years here in Grenoble. We shared countless hours accompanied by good food, drinks, music and laughter but we also went together on adventures in the surrounding mountains. I want to thank in particular Dorina for her joy, dedication, inspiration and help here in Grenoble as well as Sarah, Christoph, Oliver, Lukas and Jonathan for our long lasting and meaningful friendship. Many thanks also to Lorenzo, Chiara, Marion, Nico, Marena, Adam, Julia, Alvaro, Nao, Inès, Carmen, Carolin, Guillaume and many more.

I consider myself very lucky that I was part of a research unit with very strong cohesion, which came along with an attitude of mutual support and a joyful work environment. I am deeply grateful to Paul Machillot who stood out by mastering many of the techniques available in the laboratory. He was involved throughout the whole project by giving introductions, technical support, scientific feedback and sharing his detailed knowledge on various subjects. Without him, many things would have not been possible or would have advanced in a much slower pace and he was a great climbing and running partner. I further acknowledge following members of the group for their contribution to the results: Jean Le Pennec was strongly contributing to the development of the automated liquid handling routine notably by developing the graphical user interface and the underlying algorithm. He further gave precious feedback in numerous discussions and was a great sports friend. Adria Sales helped a lot by improving protocols, sharing analysis techniques, discussing science and talking German with me. Elaine Castro-Ramirez significantly advanced the project by her work with glass surfaces and Bertin Ndayishimiye successfully conducted the high-content studies on bone morphogenetic proteins and heparan sulfate. In addition, Joao Lopes and Lea Aubert participated by characterization with surface sensitive techniques. Finally, I am very grateful for the positive environment, all the different cakes, lunch breaks, team events, common sport activities, discussions and help provided by the team members mentioned above as well as by Valia Khodr, Laura Clauzier, Lauriane Bosc, Charlotte Garot, Arun Kumar, Frédéric Rooms and others.

While the PhD project started at the laboratory LMGP at Grenoble INP, our group moved to the BCI laboratory at CEA after 2 years. At LMGP, I would like to point out the incredible working atmosphere created by every single member of the lab and strongly supported by the direction. That for, I would like to give special thanks to Carmen Jimenez and Franz Bruckert for their tight involvement in the everyday life at the laboratory, the great organization and their sincere interest in the members of the laboratory. I also wish to thank Michele San Martin, Annie Ducher, Josiane Viboud and Nadjib Medjaldi for all the administrative and technical help, very smooth procedures and especially their great mood and kindness. Further, I very much appreciated the scientific discussions with and critical questions of Marianne Weidenhaupt, which always brought a different view on the subject. Lastly, it was a great pleasure to share the office, drink coffee, go out for drinks, eat cake, participate the running dinners and create ever-lasting memories with all the other PhD students, post docs and interns, commonly called and not exaggerated the “LMGP family”. Arriving at CEA, I gratefully

acknowledge the assistance and frankness of the BCI group and the new administration, which facilitated a lot our integration into the new locality.

Over the course of the project, we developed several fruitful collaborations with other laboratories, which I will remember as a particular joyful part of this time.

I am deeply indebted to Antoine Delon at LiPhy and IAB who generously accepted the challenge to introduce me to the exciting field of fluorescence fluctuation spectroscopy, far from my competences. I will not forget the endless but rewarding and fun hours together in front of the confocal microscope, many times conducting the very “very” last measurement. The common article would have never been possible without his profound theory, the discussions and his writing. I also wish to thank Irène Wang for the discussions and her contribution to the article.

Further, I would like to extend my sincere thanks to the group in Essen (GER) around Andrea Vortkamp for their expertise with heparan sulfate, which was instrumental for all experiments related to cell surface heparan sulfate. I was kindly welcomed for a two-week stay at their laboratory where Velina Bachvarova and Ann-Christine Severmann dedicated a lot of their time to facilitate joint experiments. Throughout our project, I acknowledge our fruitful discussions, their methodological help and eventually their comments on the corresponding chapter of the manuscript. Many thanks go further to Fatima Asar for her contributions to data analysis.

At CEA Leti, the help of Christophe Licitra cannot be overestimated. He agreed to dive together into the field of spectroscopic ellipsometry in wet environments, which resulted in transforming his precious apparatus into a swimming pool. We had a great time puzzling together over the new challenges coming along with merging our two fields and I thank him a lot for all his explanations and his feedback on the article and the manuscript.

For the synthesis of several molecules, Didier Boturyn and Remy Lartia at DCM extended a great amount of assistance by explaining to me the corresponding protocols, characterization methods and hands-on advice during the synthesis. Without them, many experiments would not have been possible. Moreover, I thank Melissa Degardin for her comments on the common article.

I also acknowledge the PTA cleanroom facility represented by Thierry Chevolleau and Corinne Perret as well as the microscopy platform μ Life governed by Laëtitia Kurzawa, which played a significant role in sample preparation and analysis respectively.

We further maintained a continuous scientific exchange with different members from IAB, which positively influenced the directions chosen for further experiments. Special thanks go to Corinne Albiges-Rizo, Olivier Destaing and Amaris Guevara.

Throughout the first two years I was provided with precious feedback, promising ideas, discussions and encouragement by my “Comité de suivi individuel de thèse”. Many thanks thus go to Liliane Guerente, Elisabetta Cavalcanti-Adam and Ralf Richter. I also very much appreciated the comments and propositions by the jury, which increased the quality of the manuscript and gave many new ideas for future research. I would like to recognize the assistance of the doctoral schools IMEP2 and ISCE of the University Grenoble Alps for their guidance and information, which helped a lot during the different stages of my project. Lastly, special thanks go to the financial support from University Grenoble Alps who funded my thesis with the grant IDEX-IRS 2018–2021 and further to Fondation Recherche Médicale (No. DEQ20170336746), ANR CODECIDE (No. ANR-17-CE13–022), ANR GlyCON (No. ANR-19-CE13-0031-01 PRCI), the Initiative de Recherche Stratégique, CNRS GDR 2088 "BIOMIM", ANR-17-EURE-0003, GRAL, ERC POC BIOACTIVECOATINGS 2015 and ERC POC REGENERBONE 2017.

List of abbreviations

aBMP: Bone morphogenetic protein adsorbed to immobilized heparan sulfate
ACF: Autocorrelation function
ALP: Alkaline phosphatase
aSurfen: Surfen adsorbed to heparan sulfate
bAtto: Biotinylated Atto565
BMP: Bone morphogenetic protein
BMPRI and BMPRII: Bone morphogenetic protein receptor type 1 and type 2
bPEGthiol: biotinylated Polyethylene glycol-thiol
cRAD: Biotinylated polyethylene glycol with cyclic arginine-beta alanine-aspartic acid peptide
cRGD: Biotinylated polyethylene glycol with cyclic arginine-glycine-aspartic acid peptide
CS: Chondroitin sulfate
csCS: Cell surface chondroitin sulfate
CW: Cardin Weintraub motif
CHO WT: Chinese hamster ovarian endothelial cells wild type
CHO KO: Chinese hamster ovarian endothelial cells knock out for the Ext1 gene
csHS: Cell surface heparan sulfate
EC: Effective concentration
ECM: Extracellular matrix
FCS: Fluorescence correlation spectroscopy
FFS: Fluorescence fluctuation spectroscopy
FGF: Fibroblast growth factor
Fn: Fibronectin
GAG: Glycosaminoglycan
GF: Growth factor
HA: Hyaluronic acid
HepII domain: Heparin binding domain
Hp: Heparin
hPDSCs: Human periosteum-derived stem cells
HSPG: Heparan sulfate proteoglycan
HS: Heparan sulfate
iBMP2: Immobilized bone morphogenetic protein 2
ICS: Image correlation spectroscopy
iHS: Immobilized heparan sulfate
LTBP: Latent TGF- β binding protein
LAP: Latency-associated propeptide
LbL: Layer-by-layer
MP: Mesenchymal progenitor
OWLS: Optical waveguide lightmode spectroscopy
PDMS: Polydimethylsiloxane
pbFCS: Photobleaching fluorescence fluctuation spectroscopy
pbICS: Photobleaching image correlation spectroscopy
PG: Proteoglycan
PEG: Polyethylene glycol
PEGthiol: Polyethylene glycol-thiol
PLL: Poly-L-Lysine
PLL-g-PEGbiotin50%: PLL(20)-g[3.5]-PEG(2)/PEGbiotin(3.4)50%
PSF: Point spread function
QCM-D: Quartz crystal microbalance with dissipation monitoring

SAv: Streptavidin
SAvAlexa or SAv-Alex: Streptavidin Alexa555
sBMP2: Soluble BMP2
SD: Standard deviation
SE: Spectroscopic Ellipsometry
SEM: Standard error of the mean
SERS: Surface-enhanced Raman spectroscopy
SiO₂: Silicon oxide
SMC: Smooth muscle cell
SPR: Surface plasmon resonance
sSurfen: Surfen in solution
VEGF: Vascular endothelial growth factor

Abstract (English)

The extra cellular matrix (ECM) provides mechanical structure to embedded cells and gives biochemical cues to regulate homeostasis and differentiation. The structural molecule fibronectin contains adhesion motifs such as the RGD sequence with high specificity for β_1 - and β_3 -integrins but also binding domains for the glycosaminoglycan (GAG) heparan sulfate (HS). GAGs have a high swelling capacity due to their negative charge but also interact with growth factors to protect them from degradation and thus serve as a reservoir. HS binds bone morphogenetic protein 2 (BMP2), which is known for its osteoinductive potential and is clinically applied to heal large bone defects in combination with 3D scaffolds. In the human body, HS are bound to core proteins forming HS proteoglycans who are either part of the ECM or appear at the cell surface. The role of extra cellular and cell surface HS together with integrins on BMP2 signaling and cellular adhesion is currently under scientific debate. Few studies suggest that exogenous HS up-regulates BMP2 signaling whereas cell surface HS negatively influences BMP2 bioactivity. Further, BMP2 induces integrin-mediated cellular adhesion and cell surface HS mediates cell adhesion to fibronectin. However, it is not known how integrins influence BMP2 signaling or how they interact together with immobilized HS and adsorbed BMP2 with respect to osteogenic differentiation. Further, the relation between exogenous and cell surface HS is rarely addressed. We respond to these questions by engineering 2D biomimetic model surfaces based on a streptavidin monolayer, which allows co-immobilizing biotinylated molecules of interest and presenting them to cells. The adhesion ligand cRGD is co-functionalized with oriented HS to which BMP2 adsorbs and the areal mass densities and binding kinetics are precisely characterized *ex situ* using surface sensitive techniques such as spectroscopic ellipsometry (SE) and quartz crystal microbalance. For the first time, we apply fluorescence based image correlation spectroscopy to characterize biomimetic surfaces *in situ* for molecular density and measure values comparable to *ex situ* SE. We further develop this technique by combining it with photo bleaching to reveal information about the average number and distribution of fluorophores per molecule to increase the accuracy. To improve the reproducibility and the high content potential of our biomimetic approach, we created an automated protocol to fabricate homogenous biomimetic platforms with a liquid handling robot. Upon user demand, multiple independent conditions of the biomimetic platform can be build-up in parallel inside 96-well plates and allow studying the effect of members of the BMP family in different concentrations adsorbed to immobilized HS. First, we find that β_1 - and β_3 -integrins

are both fundamental for the BMP2-SMAD signaling and ALP expression in C2C12 cells, markers for early BMP2 activity and osteogenic differentiation, respectively. Also, BMP2 bound to exogenous HS enhances osteogenic differentiation compared to BMP2 directly immobilized on the platform and HS sustains BMP2 activity. We have further evidence that BMP2 adsorbed on HS is more bioactive than BMP4, BMP6 and BMP7 regarding early BMP2 signaling. By plating CHO wild type cells and those with a cell surface HS (csHS) deficiency, we reveal a positive effect of csHS on BMP2 signaling at low adsorbed BMP2 doses, which is in contradiction to results with higher doses in literature. Finally, we show that csHS has a negative effect on cell spreading on cRGD surfaces and even more on surfaces presenting cRGD and exogenous HS. We conclude that automatically fabricated, precisely characterized and highly flexible biomimetic streptavidin platforms are a great tool to study the combinatorial influence of growth factors, GAGs and peptides on cell fate.

Abstract (French)

La matrice extracellulaire (MEC) fournit une structure mécanique aux cellules et régule l'homéostasie et la différenciation. La molécule structurelle fibronectine contient des motifs d'adhésion tels que la séquence RGD avec une haute spécificité pour les β_1 - et β_3 -intégrines mais aussi des domaines de liaison pour le glycosaminoglycane (GAG) héparan sulfate (HS). De plus, Le HS se lie à la protéine morphogénétique osseuse 2 (BMP2), connue pour son potentiel ostéoinductif est qui est ainsi appliquée cliniquement pour guérir de grands défauts osseux. Dans le corps humain, les HS sont liés à des protéines centrales formant des protéoglycanes HS qui font partie de la MEC ou apparaissent à la surface des cellules. Le rôle des HS extracellulaires et de surface des cellules, ainsi que des intégrines, dans la signalisation de la BMP2 et l'adhésion cellulaire font actuellement l'objet d'un débat scientifique. Quelques études suggèrent que les HS exogènes régulent à la hausse la signalisation de la BMP2, tandis que les HS de surface des cellules influencent négativement la bioactivité de la BMP2. De plus, la BMP2 induit une adhésion cellulaire médiée par l'intégrine et le HS de surface cellulaire médiatise l'adhésion cellulaire à la fibronectine. Cependant, l'influence des intégrines sur la signalisation de la BMP2 est méconnue. Il en va de même pour les interactions entre les intégrines et HS immobilisé et la BMP2 adsorbée dans le cadre de la différenciation ostéogénique. En outre, la relation entre les HS exogènes et ceux de la surface cellulaire est rarement abordée. Nous répondons à ces questions en concevant des surfaces modèles biomimétiques 2D basées sur une monocouche de streptavidine. Dessus, le ligand d'adhésion cRGD est co-fonctionnalisé avec des HS orientés sur lesquels la BMP2 s'adsorbe. La fonctionnalisation est précisément caractérisée *ex situ* à l'aide de techniques sensibles aux surfaces. Nous appliquons de plus la spectroscopie de corrélation d'image basée sur la fluorescence pour caractériser *in situ* les surfaces biomimétiques en termes de densité moléculaire. Nous développons cette technique en la combinant avec le photoblanchiment pour révéler des informations sur le nombre moyen et la distribution des fluorochromes par molécule afin d'augmenter la précision. Pour améliorer la reproductibilité et le potentiel de contenu élevé de notre approche biomimétique, nous avons créé un protocole automatisé pour fabriquer des plateformes biomimétiques homogènes à l'aide d'un robot de manipulation de liquides. De multiples conditions peuvent être construites en parallèle dans des plaques à 96 puits et permettent d'étudier l'effet des membres de la famille des BMP à différentes concentrations adsorbées sur l'HS immobilisée. Nous constatons que les intégrines β_1 - et β_3 sont fondamentales

pour la signalisation BMP2-SMAD et l'expression de l'ALP dans les cellules C2C12, marqueurs de l'activité précoce de la BMP2 et de la différenciation ostéogénique, respectivement. La BMP2 liée à un HS exogène améliore la différenciation ostéogénique par rapport à la BMP2 directement immobilisée et le HS soutient l'activité de la BMP2. De plus, la BMP2 adsorbée sur le HS est plus bioactive que la BMP4, la BMP6 et la BMP7 en ce qui concerne la signalisation précoce de la BMP2. En plaçant des cellules CHO de type sauvage et celles présentant une déficience en HS à la surface cellulaire (csHS), nous révélons un effet positif du csHS sur la signalisation BMP2 à de faibles doses de BMP2 adsorbées. Enfin, nous montrons que le csHS a un effet négatif sur la propagation des cellules sur les surfaces de cRGD et encore plus sur les surfaces présentant du cRGD et du HS exogène. Nous concluons que les plateformes biomimétiques fabriquées automatiquement, caractérisées avec précision et hautement flexibles sont un excellent outil pour étudier l'influence combinatoire des facteurs de croissance, des GAGs et des peptides sur le destin cellulaire.

Table of contents

Acknowledgements	5
List of abbreviations	9
Abstract (English)	11
Abstract (French)	13
Chapter I: Introduction	17
I.A Foreword (English)	19
I.B Foreword (French).....	21
I.C The interface between cells and the extracellular matrix	25
I.C.1 Integrins	26
I.C.2 Bone morphogenetic proteins and osteogenic differentiation	28
I.C.3 Heparan sulfate proteoglycans.....	34
I.C.4 Cellular models.....	40
I.D Biomimetic surfaces to study cell-ECM interaction	43
I.D.1 2D systems to mimic growth factor presentation in the ECM	44
I.D.2 The biomimetic streptavidin platform	50
I.D.3 Streptavidin monolayers on glass surfaces.....	53
I.E Surface characterization of biomimetic films.....	57
I.E.1 Label-free surface characterization tools	58
I.E.2 Fluorescence-based surface characterization tools	63
I.F Automated fabrication, parallelization and miniaturization of 2D biomaterials	67
I.F.1 Lithography, micro-contact printing and additive manufacturing	68
I.F.2 Automated liquid handling for 2D biomaterial fabrication.....	72
I.G Objective and positioning of the thesis	77
Chapter II: Automated fabrication of biomimetic streptavidin platforms for high quantity analysis of cellular response to growth factors	79
II.A Article summary (English).....	81
II.B Article summary (French)	83
II.C Article 1 (ready for submission to ACS Applied Materials and Interfaces).....	87
II.D Supplementary information	117
II.E Transition.....	121
Chapter III: Combining fluorescence fluctuations and photobleaching to quantify surface density	123
III.A Article summary (English)	125
III.B Article summary (French).....	129
III.C Article 2 (Submitted to arXiv: 2110.14319 in October 2021).....	133
III.D Supplementary information	157
III.E Transition	173
Chapter IV: Heparan sulfate co-immobilized with cRGD ligands and BMP2 on biomimetic platforms promotes BMP2-mediated osteogenic differentiation	175
IV.A Article summary (English)	177
IV.B Article summary (French)	179
IV.C Article 3 (Published in Acta Biomaterialia)	183

IV.D Supplementary information	217
IV.E Additional online resources	225
IV.F Transition	231
Chapter V: The role of cell surface heparan sulfate and exogenous heparan sulfate on BMP2 signaling and cellular adhesion	233
V.A Article summary (English)	235
V.B Article summary (French)	237
V.C Article 4 (in preparation)	239
V.D Supplementary information	261
Chapter VI: Conclusion and outlook	263
VI.A Automated fabrication of biomimetic streptavidin platforms	265
VI.B <i>In situ</i> characterization of the number of molecules volumes	266
VI.C The role of iHS and csHS on BMP2 signaling and adhesion	268
VI.D Conclusion (French summary)	271
Bibliographic references	275
Annex.....	289
Estimation of contribution	291
Curriculum Vitae	293

Chapter I: Introduction

I.A Foreword (English)

In the clinical field of bone repair, bone defects are categorized into small fractures with self-healing capacity and large so-called critical size defects, which need surgical intervention (Roddy *et al.*, 2018). Biodegradable synthetic bone grafts replace traditional inert implants or autologous grafts and aim to give osteoinductive and osteoconductive cues to stimulate bone tissue regeneration (Stevens, 2008). A promising strategy for bone graft design and engineering is to mimic the natural environment of bone, which consists of the extracellular matrix (ECM) and embedded cells (Bouyer *et al.*, 2020). This way, stem cells respond to growth factors (GF) in a natural way and undergo the process of osteogenic differentiation, which eventually leads to the formation of new bone tissue.

Bone morphogenetic proteins (BMP) and notably BMP2, are known for their potential to induce osteogenic differentiation (Obradovic Wagner *et al.*, 2010). They naturally bind to the glycosaminoglycan (GAG) heparan sulfate (HS) in the ECM (Ruppert, Hoffmann and Sebald, 1996), which was shown to upregulate the osteogenic potential of BMP2 (Migliorini *et al.*, 2017). HS is further present at the cell surface where it negatively influences BMP2 activity. Indeed, absence of cell surface HS leads to enhanced BMP2 signaling and causes ectopic bone formation described as hereditary multiple exostosis (Pacifci, 2017). Other molecules influencing BMP2 activity are integrins, which are transmembrane proteins at the cell surface (Fourel *et al.*, 2016). They bind to ligands in the ECM to mediate cell adhesion. In this work, we aim at understanding the role of HS and integrins in cellular adhesion, BMP2 signaling and osteogenic differentiation and further distinguish between exogenous HS and cell surface HS.

Researcher thus develop well-characterized *in vitro* and *in vivo* model systems to study the interaction between cells and the ECM, for example between adhesion ligands, GAGs and GFs. While 3D models are a most realistic representation of this system and often applied in bone repair studies, 2D models are easier to engineer and to characterize and thus are more relevant in molecular studies. A 2D approach previously developed by our group is based on a streptavidin monolayer, which serves as a base to immobilize biotinylated molecules of interest *via* the strong biotin-streptavidin interaction (Migliorini *et al.*, 2014). In this work, we use these platforms to co-present adhesion ligands, HS and BMPs in a biomimetic way and plate cells on top to study their adhesion and BMP-mediated signaling.

For the precise control of these platforms as well as for conclusions on the distinct role of the different molecules, different surface sensitive characterization tools are necessary. Quartz-crystal microbalances and spectroscopic ellipsometry allow time-resolved measurements of the surface density of adsorbed molecules but require specific substrates compatible with the techniques (Migliorini, Weidenhaupt and Picart, 2018). However, characterization techniques for measuring the surface density directly on the substrates used for cellular studies are scarce. We respond in this PhD project to this challenge by further developing image correlation spectroscopy and applying it for the first time to characterize streptavidin platforms *in situ* (Mets *et al.*, 2014).

The fabrication of systems to study cellular interaction with ECM compounds is done manually, in an automated way or a combination of both (Ranga *et al.*, 2014; Machillot *et al.*, 2018; Grubb and Caliarì, 2021). While manual fabrication brings the advantage of high flexibility regarding experimental conditions and tools, it is time consuming, prone to errors and comes along with a limited number of parallel conditions. Automated fabrication on the other hand delivers highly reproducible results and opens doors for high content studies but changes in the experimental conditions often demand for elaborate adaptations of the fabrication routine (Ranga *et al.*, 2014; Machillot *et al.*, 2018). Part of this PhD project is the automation of the fabrication of biomimetic streptavidin platform while maintaining a degree of flexibility with respect to changing experimental conditions.

This manuscript begins with a description of the state of the art with respect to the above-introduced subjects and positions the thesis in this context. Then, four result chapters written in the style of articles follow and thus contain the methodological details. The last chapter concludes on the overall results and gives perspectives for further research. In the annex, an estimation of the author's contribution regarding the four result chapters is provided as well as the author's CV. French summaries of the chapters appear throughout the manuscript to respect the requirements of the doctoral school for a thesis written in English.

I.B Foreword (French)

Dans le domaine clinique de la réparation osseuse, les défauts osseux sont catégorisés en petites fractures à capacité d'auto-guérison et en grands défauts dits de taille critique, qui nécessitent une intervention chirurgicale (Roddy et al., 2018). Les greffons osseux synthétiques biodégradables remplacent les implants inertes traditionnels ou les greffons autologues et visent à donner des signaux ostéoinductifs et ostéoconductifs pour stimuler la régénération du tissu osseux (Stevens, 2008). Une stratégie prometteuse pour la conception et l'ingénierie des greffons osseux consiste à imiter l'environnement naturel de l'os, qui se compose de la matrice extracellulaire (ECM) et des cellules intégrées (Bouyer et al., 2020). De cette façon, les cellules souches répondent aux facteurs de croissance (GF) de manière naturelle et subissent le processus de différenciation ostéogénique, qui conduit finalement à la formation d'un nouveau tissu osseux.

Les protéines morphogénétiques osseuses (BMP) et notamment la BMP2, sont connues pour leur potentiel à induire une différenciation ostéogénique (Obradovic Wagner et al., 2010). Elles se lient naturellement au glycosaminoglycane (GAG) héparane sulfate (HS) dans la ECM (Ruppert, Hoffmann et Sebal, 1996), ce qui a permis de réguler à la hausse le potentiel ostéogénique de BMP2 (Migliorini et al., 2017). Le HS est également présent à la surface des cellules où il influence négativement l'activité de BMP2. En effet, l'absence de HS à la surface des cellules entraîne une augmentation de la signalisation de BMP2 et provoque une formation osseuse ectopique décrite comme une exostose multiple héréditaire (Pacifici, 2017). D'autres molécules influençant l'activité de la BMP2 sont les intégrines, qui sont des protéines transmembranaires à la surface des cellules (Fourel et al., 2016). Elles se lient à des ligands dans l'ECM pour médier l'adhésion cellulaire. Dans ce travail, nous visons à comprendre le rôle des HS et des intégrines dans l'adhésion cellulaire, la signalisation du BMP2 et la différenciation ostéogénique et à mieux distinguer les HS exogènes des HS de surface cellulaire.

Les chercheurs développent donc des systèmes de modèles *in vitro* et *in vivo* bien caractérisés pour étudier l'interaction entre les cellules et la ECM, par exemple entre les ligands d'adhésion, les GAGs et les GFs. Alors que les modèles 3D sont la représentation la plus réaliste de ce système et sont souvent appliqués dans les études de réparation osseuse, les modèles 2D sont plus faciles à concevoir et à caractériser et donc plus pertinents dans les études moléculaires. Une approche 2D précédemment développée par notre groupe est basée sur une

monocouche de streptavidine, qui sert de base pour immobiliser des molécules biotinylées d'intérêt *via* la forte interaction biotine-streptavidine (Migliorini et al., 2014). Dans ce travail, nous utilisons ces plateformes pour coprésenter des ligands d'adhésion, des HS et des BMP de manière biomimétique et plaquer des cellules dessus pour étudier leur adhésion et la signalisation médiée par les BMP.

Pour le contrôle précis de ces plateformes ainsi que pour les conclusions sur le rôle distinct des différentes molécules, différents outils de caractérisation sensibles à la surface sont nécessaires. Les microbalances à cristal de quartz et l'ellipsométrie spectroscopique permettent des mesures résolues dans le temps de la densité de surface des molécules adsorbées mais nécessitent des substrats spécifiques compatibles avec ces techniques (Migliorini, Weidenhaupt et Picart, 2018). Cependant, les techniques de caractérisation permettant de mesurer la densité de surface directement sur les substrats utilisés pour les études cellulaires sont rares. Nous répondons dans ce projet de thèse à ce défi en développant davantage la spectroscopie de corrélation d'image et en l'appliquant pour la première fois pour caractériser les plateformes de streptavidine *in situ* (Mets et al., 2014).

La fabrication de systèmes pour étudier l'interaction cellulaire avec les composés de l'ECM est faite manuellement, de manière automatisée ou une combinaison des deux (Ranga et al., 2014 ; Machillot et al., 2018 ; Grubb et Caliari, 2021). Si la fabrication manuelle présente l'avantage d'une grande flexibilité en ce qui concerne les conditions expérimentales et les outils, elle prend du temps, est sujette à des erreurs et s'accompagne d'un nombre limité de conditions parallèles. La fabrication automatisée, quant à elle, fournit des résultats hautement reproductibles et ouvre la voie à des études à haut contenu, mais les changements dans les conditions expérimentales exigent souvent des adaptations élaborées de la routine de fabrication (Ranga et al., 2014 ; Machillot et al., 2018). Une partie de ce projet de doctorat est l'automatisation de la fabrication de la plateforme de streptavidine biomimétique tout en maintenant un degré de flexibilité par rapport aux changements de conditions expérimentales.

Ce manuscrit commence par une description de l'état de l'art par rapport aux sujets introduits ci-dessus et positionne la thèse dans ce contexte. Ensuite, quatre chapitres de résultats rédigés dans le style d'articles suivent et contiennent les détails méthodologiques. Le dernier chapitre conclut sur les résultats globaux et donne des perspectives pour des recherches ultérieures. En annexe, une estimation de la contribution de l'auteur concernant les quatre chapitres de résultats est fournie ainsi que le CV de l'auteur. Les résumés français des chapitres

apparaissent tout au long du manuscrit afin de respecter les exigences de l'école doctorale pour une thèse écrite en anglais.

I.C The interface between cells and the extracellular matrix

The ECM is a three-dimensional molecular structure present in all organisms and regulates cell morphogenesis, homeostasis and differentiation (**Figure 1**) (Frantz, Stewart and Weaver, 2010; Yue, 2014). Its molecular composition and role varies depending on the type of organism and the specific apparatus. The bone ECM consists to 60% of inorganic compounds with mainly hydroxyapatite (Ramesh, Moratti and Dias, 2018). The other 40% are organic compounds with collagen type I as the most abundant protein complemented with a variety of non-collagenous proteins continuously synthesized by cells (Lin *et al.*, 2020). Collagen gives structure and strength to the ECM and thus to the bone. The other proteins are further divided into the sub-groups proteoglycans (PGs), γ -carboxyglutamic acid-containing proteins, glycoproteins and small integrin-binding ligand n-linked glycoproteins (SIBLINGs).

PGs are negatively charged, large molecules with a core protein to which GAGs are attached *via* their reducing end (Kjellén and Lindahl, 1991) and can be categorized along the localization parameters as intracellular, cell surface, pericellular and extracellular (**Figure 1**) (Iozzo and Schaefer, 2015). Extracellular PGs, as structural components, participate together with collagen in regulating ECM tissue mechanics due to their ability to swell or to stiffen (Chen *et al.*, 2020) but also lubricate and protect, for example, cartilage tissue (Lohmander, 1988). They further regulate the capacity of the ECM to act as a reservoir for cytokines and GFs, which is primarily due to the different types of GAGs bound to the core protein (Macri, Silverstein and Clark, 2007). GAGs categorize into heparin, HS, chondroitin sulfate (CS), keratin sulfate, dermatan sulfate and hyaluronic acid (Zhang, Zhang and Linhardt, 2010). They are highly sulfated linear polysaccharides with strong negative charges (except hyaluronic acid, that is not sulfated), which render them highly hydrophilic. This is among others a mechanism for their interaction with proteins (Vallet, Clerc and Ricard-Blum, 2021).

Extracellular glycoproteins are proteins with binding motifs for cellular adhesion, which consist of oligosaccharides (glycans) bound to amino acid side chains (Kobata, 2004; Xu and Mosher, 2011). Common examples in the ECM are fibronectin, vitronectin and laminin, which carry the well-known integrin binding sequence arginine-glycine-aspartic acid (RGD) (Plow *et al.*, 2000; Van der Flier and Sonnenberg, 2001) (**Figure 1**). Cells thus adhere to the ECM mainly *via* integrins.

In the following three chapters, integrins, the GF BMPs and heparan sulfate PGs (HSPGs) are presented in detail and how they participate in cell-matrix interaction.

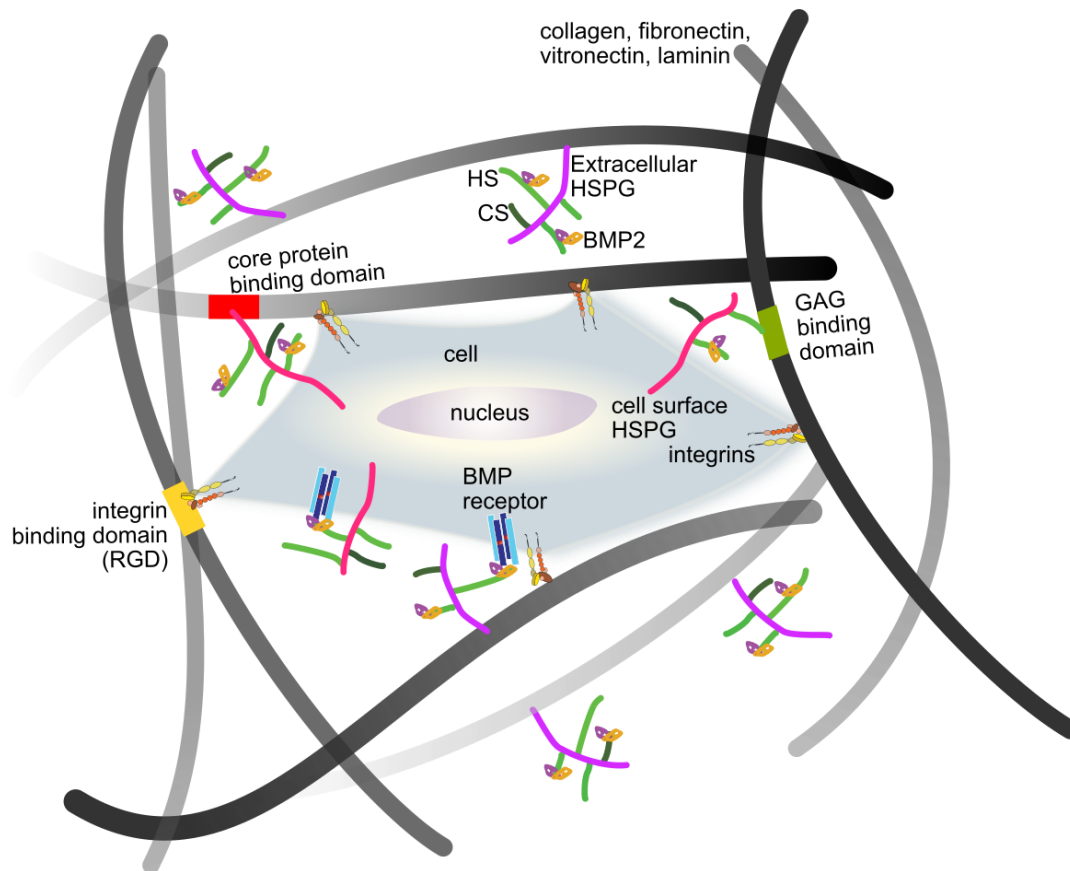


Figure 1: Schematic of the ECM with relevant elements. Cells are imbedded in the ECM, which consists of the structure giving proteins collagen, fibronectin, vitronectin and laminin. Extracellular heparan sulfate proteoglycans (extracellular HSPG) bind to the structural proteins. The GAG side chains HS and chondroitin sulfate (CS) bind bone morphogenetic protein 2 (BMP2). Cells adhere to the ECM *via* integrins, which have a high affinity for the integrin binding domain of the structural proteins, notably the arginine-glycine-aspartic acid (RGD) motif. Intercellular HSPGs (cell surface HSPGs) are present at the cell membrane and can bind *via* the core protein to the PG binding domains of the structural proteins as well. GAGs further bind to fibronectin *via* the heparin binding domain (HepII domain). Upon BMP2 presentation *via* HS the BMP receptor complex forms to initiate a signaling cascade.

I.C.1 Integrins

Integrins are transmembrane receptors and link the cell skeleton to the surrounding extracellular matrix (Barczyk, Carracedo and Gullberg, 2010; Kechagia, Ivaska and Roca-Cusachs, 2019). They form heterodimers from a family of 18 α - and 8 β -subunits and thus can appear in 24 different heterodimers. Each of these pairings has a binding specificity to a certain component in the ECM defined by the α -subunit (**Figure 2**). All 24 heterodimers are categorized in four families regarding their ligands in the ECM to which they bind *via* ionic interaction. Fibronectin, vitronectin and fibrinogen share the common binding motif RGD,

which has a high affinity for β_1 and β_3 integrins (Humphries, Byron and Humphries, 2006). Integrins bind to the triple-helical GFOGER sequence of collagen specific for the α -subunit. β_1 - and β_4 -integrins adhere to laminin, which recognize either so called coiled-coil regions, short tails and laminin globular domains (Yamada and Sekiguchi, 2015).

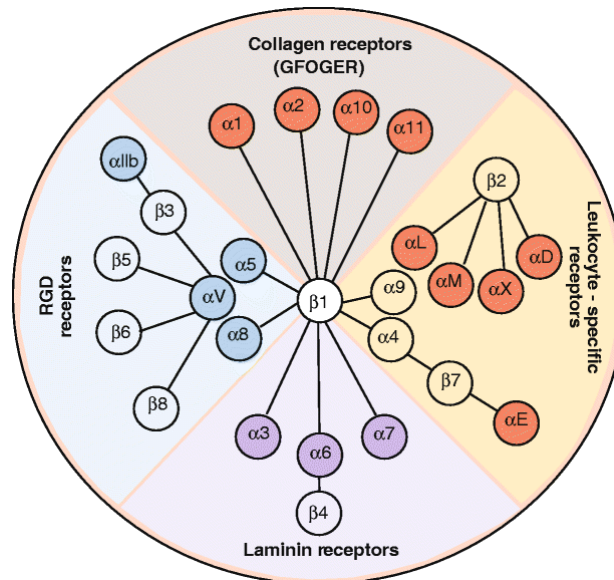


Figure 2: Integrins form heterodimers between 18 α - and 8 β -subunits. They adhere specifically to ECM components such as RGD, collagen or laminin that is defined by the α -subunit. Figure adapted from (Barczyk, Carracedo and Gullberg, 2010).

Integrin expression is regulated in the nucleus, and they dimerize in the endoplasmic reticulum and Golgi apparatus (Kechagia, Ivaska and Roca-Cusachs, 2019). Expressed into the cytoplasm, they remain inactive due to their covered calcium-ion molecules and they migrate into the plasma membrane where they can freely diffuse. Only upon mechanical forces and extracellular magnesium-ions, integrins bend and expose their binding sites for ligands in the ECM. Receptors are continuously endocytosed where they are mostly recycled but also degraded (**Figure 3**).

Integrins are key-regulators of cellular adhesion to the ECM and this interaction is orchestrated by either bio-chemical signals or mechanical force (Kechagia, Ivaska and Roca-Cusachs, 2019). When talin binds to the cytoplasmic domain of the β -integrin subunit, integrins change their conformational state from inactive “bent closed” to either “extended closed” or “extended open” with increasing affinity for ligands (**Figure 3**). It is not yet fully understood how talin is recruited from the cytoplasm. This leads to early adhesion of cells to the ECM and is called nascent adhesion. Nascent adhesions can mature by clustering of integrins and binding to F-actin *via* talin, proto-oncogene tyrosine-protein kinase (SRC), focal adhesion

kinase (FAK) and vinculin to form focal adhesions. These focal adhesions transmit forces between the ECM and the cell *via* actin-stress fibers and act as major signaling hubs for biochemical signaling and mechanotransduction (Seetharaman and Etienne-Manneville, 2018; Humphries *et al.*, 2019).

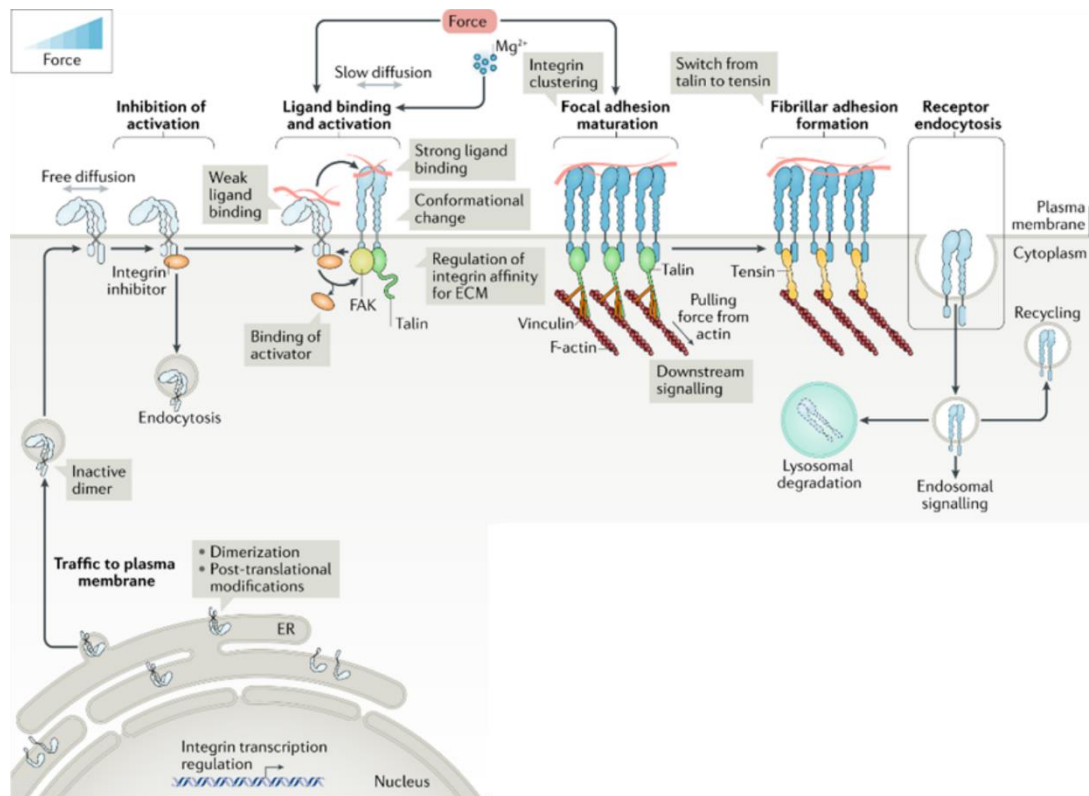


Figure 3: Integrins expression and integrin-mediated adhesion. Integrins are expressed from the endoplasmic reticulum and migrate to the cell membrane to serve as transmembrane receptors for ECM adhesion ligands. When activated, they can bind to ECM proteins as fibronectin and form focal adhesions to transmit forces between the ECM and the cell. Figure adapted from (Kechagia, Ivaska and Roca-Cusachs, 2019).

1.C.2 Bone morphogenetic proteins and osteogenic differentiation

Bone morphogenetic proteins (BMP) are members of the transforming GF (TGF β) superfamily, cytokines, which control development, differentiation and proliferation. BMPs thus influence various processes and structures in the whole human body (Obradovic Wagner *et al.*, 2010). In the 1960s, the activity of BMPs on bone formation was identified (Urist, 1965) but only 20 years later the responsible proteins were discovered and cloned, notably BMP2 and BMP4 (Wozney *et al.*, 1988). BMP2 was clinically approved by the federal drug agency and is used to repair large bone defects *via* collagen sponge scaffolds (Geiger, Li and Friess, 2003). However, 2011 it was shown that this clinical approach led to severe side effects, notably ectopic bone formation (Carragee, Hurwitz and Weiner, 2011).

In skeletal tissues, BMP2, BMP4, BMP6 and BMP7 induced bone and cartilage formation. BMP2, BMP6 and BMP9 had the highest osteogenic potential in murine pluripotential C3H10T1/2 cells (Katagiri and Watabe, 2016). BMP2 is a homodimer initially synthesized from a 453 residue-long pro-protein which gets glycosylated, cleaved and dimerized (**Figure 4**) (Scheufler, Sebald and Hülsmeier, 1999). Its final form consists of the 114 C-terminal pro-protein residues and has binding sites for BMP receptor type 1 (BMPRI) and BMP receptor type 2 (BMPRII), both receptors expressed at the cell membrane. Further, it possesses the Cardin-Weintraub motif, which allows it to bind to heparin (Hp) and HS with an affinity of 20×10^{-9} M (Ruppert, Hoffmann and Sebald, 1996). The Cardin-Weintraub motif is defined as [-X-B-B-X-B-X-] and [-X-B-B-B-X-X-B-X-] which represents two sequences of basic (B) and hydrophobic (X) amino acid residues (Cardin and Weintraub, 1989). Ruppert et al. identified triplets of basic residues at the N-terminal of human BMP2, which corresponds to the second of the above sequences (Ruppert, Hoffmann and Sebald, 1996). BMP2 is expressed into the ECM and can also be internalized by cells (Gilde *et al.*, 2016). In the ECM, BMP2 is bound to exogenous HSPGs, protecting it from proteolysis or is present at the cell surface bound to cell surface HSPGs (Jiao *et al.*, 2007). Among the antagonists against BMP activity, noggin is the most relevant for BMP2 regulated differentiation (Zhu *et al.*, 2006). It binds to BMP2 preventing it to interact with BMPRs at the cell membrane.

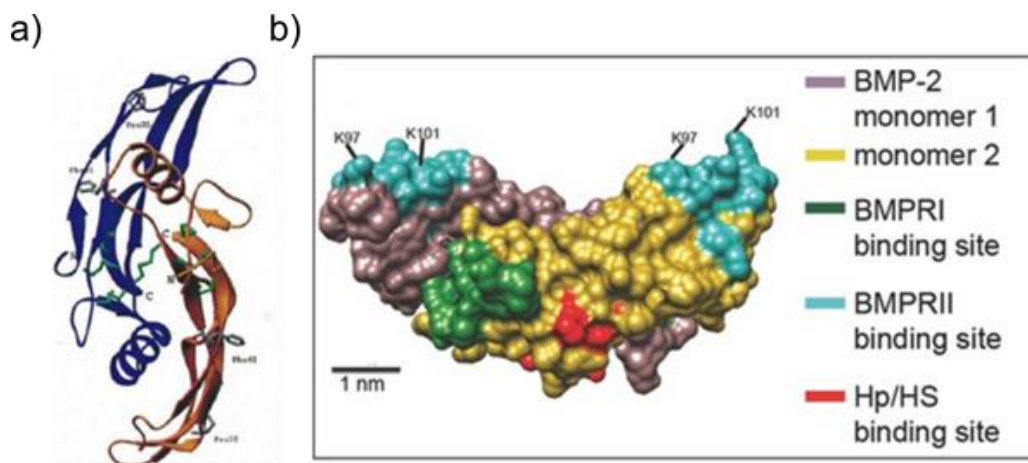


Figure 4: Schematic of BMP2 structure and binding sites. a) Structure of the BMP2 homodimer. b) It has binding sites for BMPRI, BMPRII and heparin (Hp)/HS. The Hp/HS binding site is the Cardin-Weintraub motif. Figure adapted from (Scheufler, Sebald and Hülsmeier, 1999; Migliorini et al., 2017).

Bone is a complex tissue constantly being remodeled by osteoclasts, which resorb bone and osteoblasts, which form new bone (**Figure 5**) (Long, 2012). Osteoblasts are part of the osteoblastic lineage and origin from mesenchymal progenitors (MP) *via* pre-osteoblasts. For intramembranous ossification mainly present in the skull and clavicle, MPs differentiate

directly into osteoblasts. The so-called endochondral ossification in all other parts of the skeleton begins with differentiation of MP into chondrocytes and perichondral cells, which then become osteoblasts. Osteoblasts have a high capacity to produce ECM molecules like collagen type I, osteocalcin or alkaline phosphatase (ALP). This organic matrix is called osteoid and mineralizes over time by deposition of inorganic hydroxyapatite. Some of the osteoblasts differentiate into osteocytes, which remain embedded in the mineralized bone while other osteoblasts disintegrate or remain as bone lineage cells. Osteoclasts are present at the bone surface and participate in bone remodeling by resorbing bone tissue. After their cell death, osteoblast progenitors are recruited to replace the missing bone tissue.

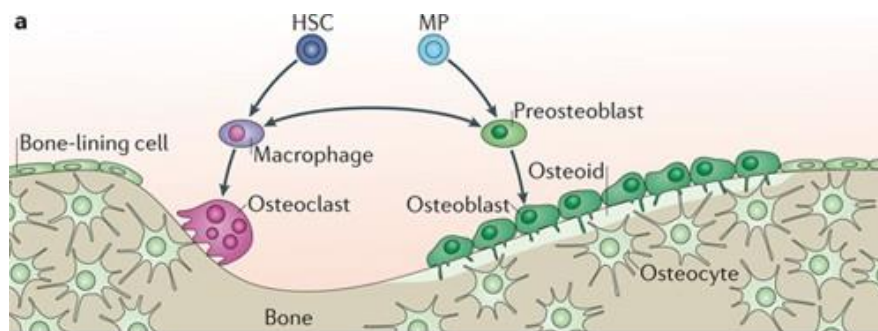


Figure 5: Schematic of bone remodeling. Osteoclasts resorb bone and osteoblasts form new bone. Osteoblasts express matrix molecules, which form the osteoid. Later, hydroxyapatite deposits to mineralize the tissue. Osteocytes are differentiated osteoblasts incorporated in mineralized bone tissue. Figure adapted from (Long, 2012).

To induce differentiation of cells at different stages of the osteoblastic lineage, a variety of signaling molecules are involved with hedgehog, notch, WNT, fibroblast growth factor (FGF) and BMP being the most prominent (Long, 2012). These bioactive molecules induce a signaling cascade from the cell membrane into the nucleus, which leads to the expression of specific transcription factors, and thus determine cell fate. BMP signaling is divided into the canonical SMAD pathway and the non-canonical non-SMAD pathway (**Figure 6**) (Wu, Chen and Li, 2016). BMP binds to BMPRII, which then forms a hetero-tetrameric complex with BMPRI and leads to the phosphorylation of the latter (Long, 2012). The tetrameric structure is needed so that the BMP2 dimer can bind to the complex. This activates SMAD1, SMAD5 and SMAD8 through phosphorylation followed by the formation of a complex with SMAD4. This complex translocates into the nucleus where it recruits co-factors and transcription factors to regulate the expression of osteogenic genes. In the less understood non-SMAD pathway, the activated BMPR complex leads to phosphorylation of TAK1, which initiates the MAPK, MKK-p38 or MKK-ERK1/2 pathway. They also upregulate osteogenic gene expression in the nucleus (Wu, Chen and Li, 2016).

At different stages of differentiation, cells express different levels of transcription factors for corresponding gene expression. Sox9 is a marker for chondrogenesis and undifferentiated osteogenic MPs. Runx2 is obligatory for osteogenic differentiation in both endochondral and intramembranous ossification. Further downstream, Osterix regulates osteoblast differentiation and is more specific for bone in comparison to Runx2 (Long, 2012). Typical read-outs for late osteogenic differentiation is the quantification of the osteocalcin gene (Zoch, Clemens and Riddle, 2016) and ALP (Katagiri, 1994), which are expressed by mature osteoblasts.

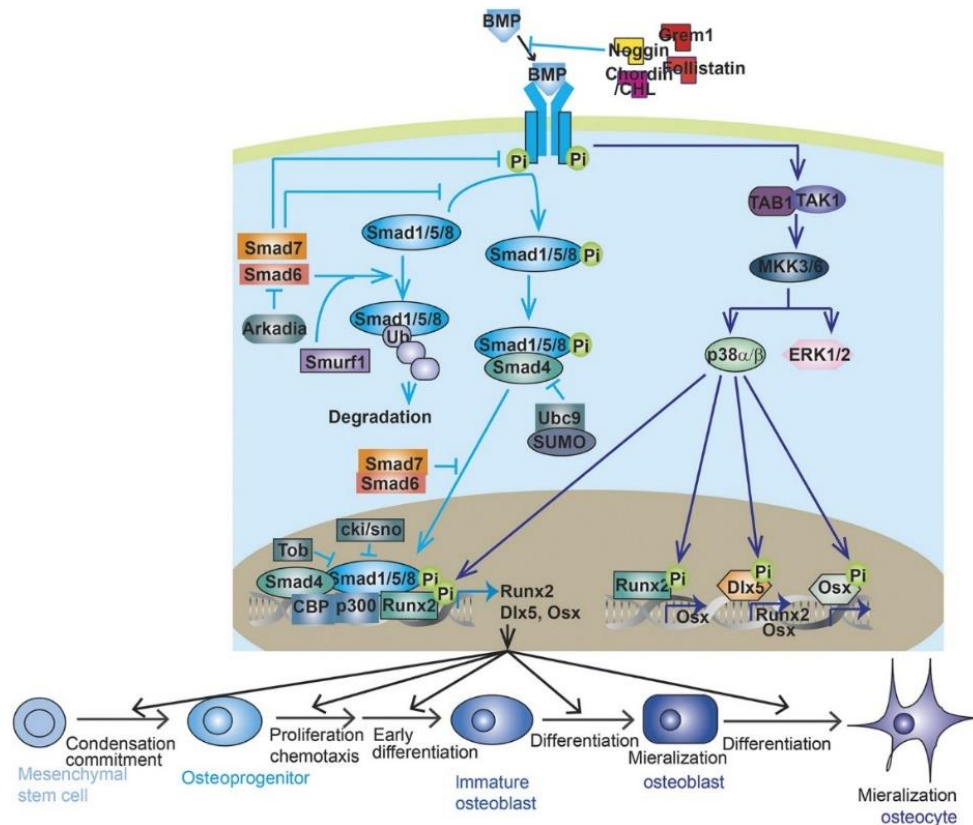


Figure 6: Schematic of BMP2 signaling. BMP2 binding to the BMPR induces the SMAD and the non-SMAD signaling pathway, which lead to the expression of osteogenic genes in the nucleus. Figure adapted from (Wu, Chen and Li, 2016).

BMP-mediated signaling is known to interfere with signaling of other bioactive GFs as for example $TGF\beta$ or WNT, either in an inhibiting or enhancing way (Long, 2012). In a broader sense, some GF and integrins-mediated signaling mutually activate each other (Ivaska and Heino, 2011). Indeed, the signaling cross-talk between integrins and GF signaling is currently under investigation by many research groups, also motivated by a potential dose reduction of bioactive molecules in medicine application if co-presented with adhesion ligands (Monteiro A., Kollmetz and Malmström, 2018). Monteiro et al. categorized the different types of interaction into collaborative, concomitant, inhibitory, force-dependent and direct activation of

signaling (**Figure 7**). Collaborative signaling is a mutual positive dependency of both GF and integrin receptors. If a GF binds to its receptor, integrin mediated adhesion is enhanced, and activation of integrins up-regulates GF-signaling. For concomitant signaling, the receptors act independently from each other but they eventually activate the same signaling molecules further downstream. In the case of direct activation of signaling, activated integrins can activate the GF receptor without GFs being involved. In addition, a negative influence is possible where integrin activation blocks or down-regulates GF regulated signaling. Force-dependent signaling requires not only integrin activation but also applied mechanical stress in order to activate the GF receptors.

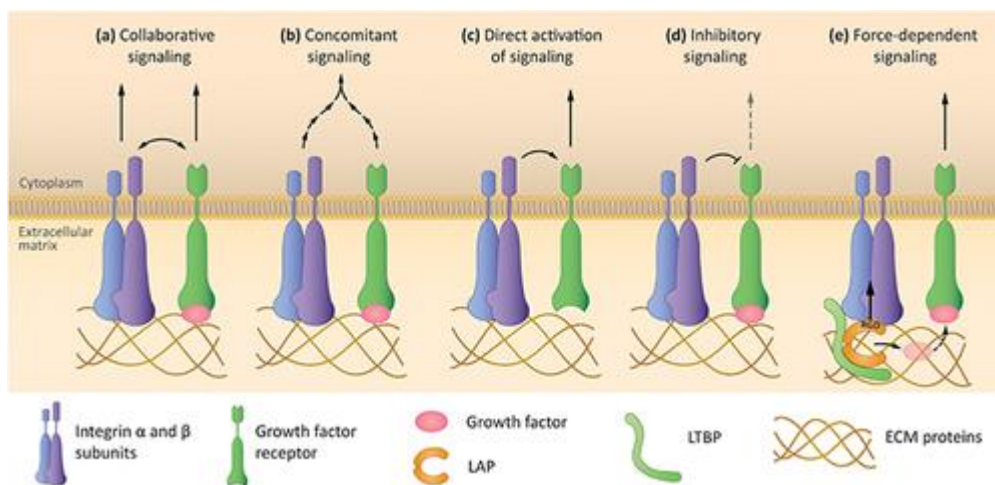


Figure 7: Schematic of various types of interaction between integrins and GF. a) Collaborative signaling. b) Concomitant signaling. c) Direct activation of signaling. d) Inhibitory signaling. e) Force-dependent signaling depends on the latency-associated propeptide (LAP), which binds to TGF β and contains the RGD motif. This complex further binds to latent TGF β binding protein (LTBP). Only upon integrin binding to RGD the conformational state changes so that TGF β can be released and bind to its receptor. Adapted from (Monteiro A., Kollmetz and Malmström, 2018).

In the specific case of BMP and integrins, interesting discoveries were made in the past years. It was shown that matrix bound BMP binding to the BMPRs induced β_3 -integrin mediated spreading of cells (**Figure 8**) (Fourel *et al.*, 2016). While on stiff biomimetic layer-by-layer (LbL) films (high cross-linking degree) C2C12 cells were able to spread independently of BMP2, cells could not spread on soft films (low cross-linking degree). Soluble BMP2 (sBMP2) in the media binding to the dorsal side of cells did not have any impact but matrix-bound BMP2 (iBMP2) binding to the BMPRs at the ventral side of the cell induced cell spreading. In 2D cell culture, the ventral side of a cell is the side facing the surface whereas the dorsal side is exposed to the cell media (Ballester-Beltrán *et al.*, 2012). They explain this effect by the direct activation of β_3 -integrins due to BMP2-mediated activation of the BMPRs,

independently of the SAMD pathway. Finally, they showed that activated β_3 -integrins were necessary for BMP2 mediated SMAD1/5/9 phosphorylation.

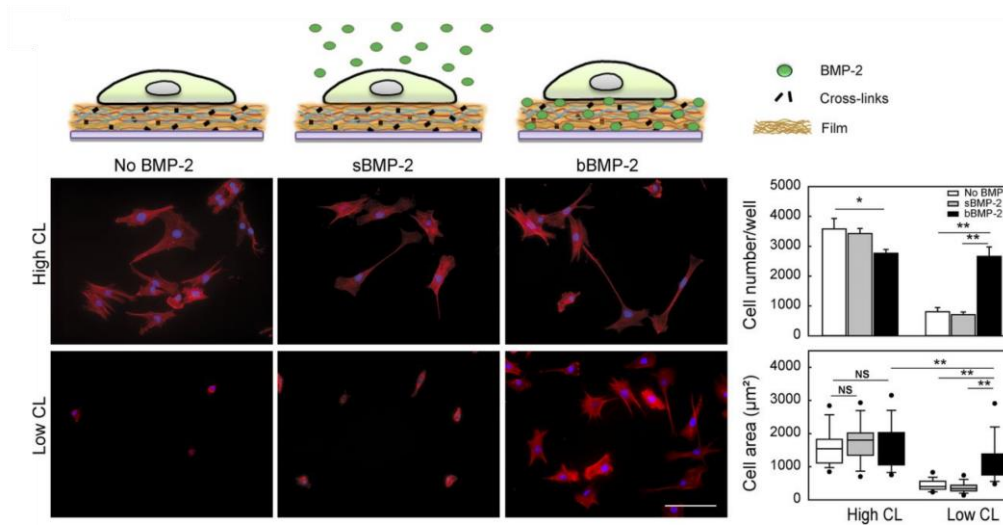


Figure 8: Matrix bound BMP2 induced β_3 -integrin mediated cell spreading. C2C12 cells did not adhere on soft films with low crosslinking (CL) degree and only matrix-bound BMP2 (bBMP-2), but not soluble BMP2 (sBMP-2), induced integrin activation and thus cell adhesion. Scale-bar = 100 μm . Figure adapted from (Fourel et al., 2016).

Martino et al. found further that using fibronectin with binding sites for BMP2 and integrins led to lower doses of BMP2 needed for bone regeneration (Martino and Hubbell, 2010). *In vivo* studies with hydrogels presenting integrin-binding fibronectin fragments and BMP2 revealed the same results (Kisiel, Martino, et al., 2013). Louis-Hernandez et al. applied this strategy to heal critical bone defects (Llopis-Hernández et al., 2016). The type of integrins involved is context dependent as shown in hydrogels where β_1 -integrins upregulated vascular endothelial growth factor (VEGF) mediated vascularization in contrary to β_3 -integrins (García, Clark and García, 2016). Further, the reduced spatial availability of integrin ligands such as RGD has been demonstrated to negatively influence Runx2 and ALP expression (Frith, Mills and Cooper-White, 2012). In addition to that, *in vivo* studies with drosophila revealed that collagen IV-mediated integrin activation was required for a peak pSMAD/1/5/9 signal (Sawala et al., 2015). Further studies on the integrin-BMP2 crosstalk are reviewed by Monteiro et al. (Monteiro A., Kollmetz and Malmström, 2018).

The role of BMP2 on integrin-mediated adhesion and spreading is subject to current studies and first results indicate an influence on integrins on early BMP2 signaling. However, few is known about the effect of the spatial distribution and absolute quantity of integrin ligands on BMP2 signaling or the influence of specific integrins on late osteogenic differentiation.

I.C.3 Heparan sulfate proteoglycans

Sarrazin et al. (Sarrazin, Lamanna and Esko, 2011) and AnnaVal et al. (AnnaVal *et al.*, 2020) review structure, biosynthesis and function of HSPGs, which consist of a core protein and HS chains covalently bound to the core-protein *via* their reducing end (**Figure 9**). In some cases, other GAGs as CS or highly sulfated heparin can also bind next to HS. These HSPGs are either membrane-bound (syndecan 1-4, glypican 1-6, other) or ECM-bound (perlecan, agrin, collagen XVIII, Testican/SPOCK) with core protein mass ranging from 31 to 400 kDa. Serglycin stands aside as the only intracellular HSPG. Between one and four HS, CS or heparin chains can bind to one core protein.

HS is a highly disperse and linear polysaccharide chain with 10-200 disaccharide units made of D-glucuronic acid (GlcA) bound to N-acetyl-D-glucosamine (GlcNAc) (Sasisekharan and Venkataraman, 2000). Each of these disaccharides has an individual structure, which comes from 3-O-, 6-O- or N-sulfation of glucosamine and 2-O sulfation of glucuronic acid. Further, β -D-glucuronic acid can epimerize to become α -L-iduronic acid. Considering also varying chain lengths, abundant different combinations rise and it is currently studied, which impact these different structures have on HS functions (Ashikari-Hada *et al.*, 2004; Kreuger and Kjellén, 2012; Chopra *et al.*, 2021).

HSPG and their GAG side chains are synthesized and expressed by cells. It starts with gagsylation inside the Golgi apparatus or at the interface with the endoplasmic reticulum (AnnaVal *et al.*, 2020). First, a tetrachsacharide primer is synthesized *via* five different enzymes: two O-xylosyltransferases (XylT-1 or XylT-2), two galactosyltransferases (GalT-2 and GlcAT-1) and glucuronosyltransferase I (GlcAT-1). It attaches to a serine residue of the PG core-protein by sequential binding of the monomers xylose, two galactoses and a glucuronic acid. From that point, the HS chain is further elongated by alternately adding GlcA and GlcNAc with the help of the glycosyltransferases EXT1 and EXT2. EXT1 is the most active while EXT2 can enhance the effect of EXT1 and the activity of both enzymes is regulated by gene expression, protein-protein interaction or phosphorylation. As a next step, HS chains follow different stages of maturation, namely GlcNAc de-N-acetylation/re-N-sulfation, GlcA C5 epimerization and GlcA/IdoA and GlcN O-sulfation. Sulfated and epimerized disaccharides are then called S-domains while acetylated ones are named NA-domains. After succeeded biosynthesis, mature HSPG structure can be further modified. Heparanase cleaves HS chains whereas the family of

sheddase is aiming to cut the core-protein, which releases HSPG into the ECM. Finally, the extracellular enzymes Sulfs could alter the 6-O sulfation of HS.

CS as the second GAG occasionally present in HSPG differs also in size and degree of sulfation (Mikami and Kitagawa, 2013). Its structure is made of repetitive disaccharide monomers glucuronic acid and N-acetylgalactosamine and it binds to the core-protein *via* a tetrasaccharide of xylose, two galactose, and one glucuronic acid residue, same as HS. This is followed by chain elongation and sequential sulfation. In addition, heparin sometimes binds to HSPG core-proteins and is the most sulfated GAG (Lima, Rudd and Yates, 2017). It shares its disaccharide structure with HS but is more sulfated.

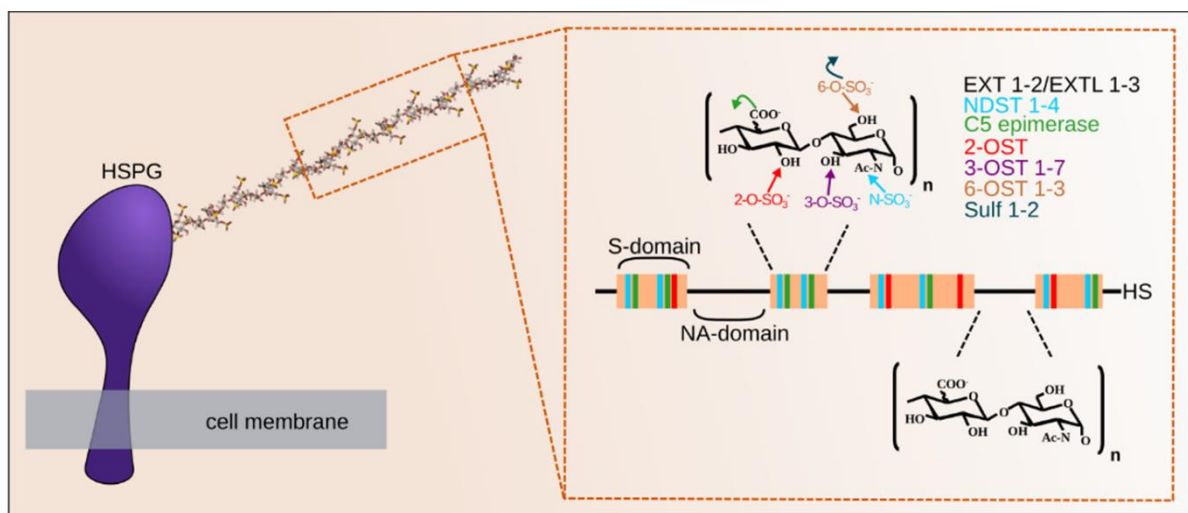


Figure 9: Schematic of the structure of HSPGs. HS chains attach to the core-protein and are elongated chains of disaccharide repetitions polymerized with the help of exostosins (EXTs) enzymes. Some of the disaccharides are sulfated (S-domains) *via* the enzymes N-deacetylase/N-sulfotransferase (NDSTs), C5 epimerase and 2-, 3- and 6-O-sulfotransferases (OSTs). Sulf enzymes can further modify the HS chain and NA-domains are non-sulfated domains. Adapted from AnnaVal et al. (AnnaVal et al., 2020).

The HSPG biological function is mainly mediated by the GAG chains whereas the core-protein rather serves as a scaffold for GAG presentation as well as defining the position of the PG either in the ECM or at the cell surface (Dreyfuss *et al.*, 2009; Sarrazin, Lamanna and Esko, 2011; AnnaVal *et al.*, 2020). Nevertheless, it has been shown that the core-proteins have binding domains to for example fibronectin, which allows them to bind to ECM structural molecules (Heremans *et al.*, 1990). HS on the other hand has a vast library of binding sites for different categories of proteins due to the high structural variety (Dreyfuss *et al.*, 2009; Nugent, Zaia and Spencer, 2013). It can bind to molecules on the cell surface, for example fibroblast GF receptors, to the ECM *via* collagens, fibronectin, vitronectin or laminin, to GFs, notably to FGF or to members of the TGF β family but also to cytokines and chemokines as BMPs (Chen, Zhao

and Mundy, 2004; Salazar, Gamer and Rosen, 2016; Sedlmeier and Sleeman, 2017). Billings *et al.* compared different BMPs regarding their specific binding domains for HS (Billings *et al.*, 2018). BMP2 and BMP4 are known to bind to HS *via* the Cardin-Weintraub (CW) motif, which has been initially identified as an amino acid sequence in proteins responsible for heparin binding and is localized close to the N-terminus of BMP2 and BMP4 (Cardin and Weintraub, 1989; Ruppert, Hoffmann and Sebald, 1996; Choi *et al.*, 2010). BMP5/6 and 7 however present a CW-like motif at the C-terminus of the protein (Billings *et al.*, 2018). It is not yet fully understood which specific sulfation pattern of HS is responsible for the binding of BMP2 besides recent evidence for a preference of N-sulfation over 6-O sulfation (Smith *et al.*, 2018). The small molecule Surfen (bis-2-methyl-4-amino-quinolyl-6- carbamide) has been identified as a HS antagonist, principally binding to charged sulfated disaccharides of HS, heparin and CS *via* electrostatic interaction (Schuksz *et al.*, 2008). Surfen binding to cell surface HS (csHS) of cultured cells blocked the binding of FGF2 that prevented csHS modulated signaling.

Due to their structural properties and their broad interaction with proteins, HSPGs participate in many biophysical processes across different organ systems (Bishop, Schuksz and Esko, 2007; Sarrazin, Lamanna and Esko, 2011). Various mechanisms define the interaction between HS and proteins (Xu and Esko, 2014; Meneghetti *et al.*, 2015; Vallet, Clerc and Ricard-Blum, 2021). HS binding proteins are defined as proteins, which bind to HS with a physiological relevant strength and at a physiological pH. Further criteria are sufficient binding to heparin despite washing with buffer with isotonic saline, binding to HS in isotonic saline and presence of the protein in a relevant biological context (Xu and Esko, 2014). The basic principle for the binding between HS and proteins is ionic interaction. The negatively charged carboxyl and sulfate groups in the HS chain interact with the positively charged arginine and lysine residues in the protein. Further, polar asparagine, histidine and glutamine form hydrogen bonds with HS. The CW motif presented earlier is one specific example of an amino acid sequence in HS binding proteins (Cardin and Weintraub, 1989). But also the 3D arrangement at the protein surface of spaced and short basic amino acid sequences plays a significant role (Rudd *et al.*, 2017). Further, neutral sequences between the basic residues can define specificity of the binding to a GAG (Sarkar and Desai, 2015).

Among others, HSPG release bound GFs, cytokines and chemokines to induce signaling cascades, act as co-receptors at the cell membrane to alter signaling kinetics or interact with integrins to induce cell adhesion to the ECM and between cells. They further regulate

development, cell proliferation, immune response, tissue repair and ECM assembly (Bishop, Schuksz and Esko, 2007). Following the objective of the thesis, I elaborate further the role of HS on BMP signaling, notably BMP2, and its influence on cellular adhesion while differentiating between exogenous HS and csHS (Nugent, Zaia and Spencer, 2013; Migliorini *et al.*, 2020).

Several groups have shown that HS has a role on BMP2 signaling. It was proven that mice mutant for the EXT1 glycosyltransferase, usually responsible for elongating the HS chain, led to increased BMP signaling (Huegel *et al.*, 2015). This defect caused abnormal bone growth at long bones, which is a rare pediatric disease called hereditary multiple exostoses (Pacifici, 2017, 2018). BMP2 mutated for the HS binding domain was strongly increasing BMP2 activity (Ruppert, Hoffmann and Sebald, 1996), which supports this finding but on the other hand, increased binding properties of BMP2 *via* addition of amino acid sequences at the N-terminal also increased osteoinduction (Würzler *et al.*, 2004). Gerstner *et al.* showed that EXT1-deficient chondrocytes from mice were more sensitive to BMP4- and BMP6-induced SMAD1/5/8 phosphorylation and less sensitive to mechanical-load regulated ERK1/2 phosphorylation compared to wild type cells (Gerstner *et al.*, 2021). *In vivo* studies in EXT1 knock-out mice revealed an increase in BMP signaling in cartilage, which is in line with the studies presented above (Kawashima *et al.*, 2020). Different results were observed in chondrocytes where CS compensated the lack of HS in EXT1-deficient cells. CS was further shaved with chondroitinase, which then reduced BMP2 signaling and thus indicated a positive influence of csCS (Bachvarova *et al.*, 2020). The effect of csHS might thus be cell-type dependent. The Surfen treatment of chondrocytes in micro mass cultures increased BMP2-induced chondrogenic response similar to heparinase treatment (Huegel *et al.*, 2013).

Other studies looked at the effect of exogenous HS on BMP2 signaling. Presenting BMP2 in solution bound to exogenous HS derived from a bone marrow stromal cell line up-regulated ALP activity and osteocalcin expression in C2C12 cells, which was less pronounced in commercially available HS (Bramono *et al.*, 2012). They explain this effect with a prolonged BMP2 half-life, modulated BMP2 distribution on the cell surface and reduced noggin-BMP2 interaction. The same group created a collagen scaffold co-presented with a BMP2-affinity selected HS variant, which then enhanced the bioactivity of endogenous BMP2 and healed a critical size bone defect in rabbits (Murali *et al.*, 2013; Smith *et al.*, 2017). Fisher *et al.* studied the effect of HSPG on chondrogenesis and differentiated between exogenous HS and syndecan-

3 (Fisher *et al.*, 2006). While BMP2 bound to exogenous HS up-regulated chondrogenic differentiation and SMAD1/5/9 phosphorylation, removing syndecan-3 from the cell surface had the same effect. As a control, overexpressed syndecan-3 reduced BMP2 mediated signaling. Migliorini *et al.* go one step further to study the role of exogenous HS by immobilizing it side-specific on streptavidin (SAv) platforms to mimic its natural presentation in the ECM instead of presenting it in solution (Migliorini *et al.*, 2017). They find that HS prolonged SMAD1/5/9 phosphorylation compared to sBMP2 and enhanced signaling with respect to immobilized BMP2.

Another role of HS in BMP2 signaling is its function as co-receptor for BMP2 and BMP4 induced signaling (Kuo, Digman and Lander, 2010). Up-on BMP binding to BMPRI, HS helped to recruit BMPRII to form the receptor complex, which then triggers SMAD1/5/9 phosphorylation. Very recent data shows that HSPGs were the main mediators for BMP2 internalization in CHO cells and lack of csHS thus reduced internalization and induced endogenous BMP2 expression (Kim *et al.*, 2021).

Apart from BMP signaling, HSPGs mediate cellular adhesion, spreading and the formation of focal adhesions (Longley *et al.*, 1999; Bishop, Schuksz and Esko, 2007; Velleman and Song, 2017). LeBaron *et al.* compared CHO wild type (WT) cells and HS-deficient cells on fibronectin substrates with integrin binding sites and substrates only containing the fragments of fibronectin with the heparin binding site (LeBaron *et al.*, 1988). While both cell types adhered and spread equally on fibronectin, probably due to integrin binding, the HS deficient cells were not able to adhere to the fragments with only heparin binding sites. HS deficient cells in addition did not form focal adhesions on fibronectin whereas WT could do so. This demonstrates that HS is not crucial for cellular adhesion but its interaction with the ECM is necessary to form focal adhesions. Mahalingam *et al.* studied then the influence of HS as part of the HSPG on cell adhesion and found that a heparin oligosaccharide chain with a length of at least 14 disaccharides was needed to compete with fibroblasts for binding to the HepII domain of fibronectin as well as N-sulfations (Mahalingam, Gallagher and Couchman, 2007). It was observed that N-sulfations but also 6-O sulfations of syndecan-4, were required to form focal adhesions. Indeed, CHO cells with reduced N-sulfations were not able to form focal adhesions. And when syndecan-4 was knocked-down in endothelial cells, focal-adhesions complexes disappeared and vinculin decoupled from F-actin filaments (Cavalheiro *et al.*, 2017). Also on applied materials as nano-zirconia surfaces, silencing of different syndecans led to abnormal

cellular morphology in osteoblasts (Sun *et al.*, 2020). It was early reported that syndecan-4 was present in focal adhesion together with β_1 and β_3 integrins when cells adhered to fibronectin, laminin, vitronectin and collagen I (Woods and Couchman, 1994). Approaching this topic from the opposite direction revealed, that treatment of cells with heparinase to disrupt HSPG, decreased cellular adhesion to the ECM in the same cell type (Moon *et al.*, 2005).

Independently on cell-matrix interaction, HSPG were further able to sense the shear forces of blood passing by at the luminal surface and thus influencing the direction of cell migration. Recent studies confirm, that the proximity between integrin ligands and syndecan ligands increased the adhesion of endothelial cells (Karimi *et al.*, 2018). They advanced this approach by engineering a biomaterial to combine these so-called nano clusters with an interface to shear flow and demonstrated that cells needed both ligands to be able to align themselves along the flow. Moreover, the efficiency in recruitment of cells from the flow medium was increased (Karimi *et al.*, 2021). Levy-Adam *et al.* also studied the effect of heparinase on cell adhesion but deactivated its enzymatic activity. This led to clustering of syndecans and thus improved adhesion and spreading (Levy-Adam *et al.*, 2008). Finally, experiments with the HS antagonist Surfen caused an inhibition of cellular adhesion of CHO cells to the to the HepII domain of fibronectin (Schuksz *et al.*, 2008).

While the role of cell surface HS on cell adhesion and morphology is already well studied, exogenous HSPG remain less explored. Extracellular perlecan co-presented with fibronectin reduced cellular adhesion of smooth muscle cells (SMCs) (Lundmark *et al.*, 2001). Treating perlecan with heparinase to cleave the HS chains re-established cellular adhesion, which means that the inhibitory effect is due to HS chains and not the core protein. While heparin led to similar results, CS or hyaluronan were not able to inhibit adhesion. The same experiment on laminin did not show any inhibitory effect and they further found that the heparin binding sites of fibronectin were not regulating the inhibitory effect of heparin. The authors hypothesize that fibronectin binding to heparin leads to a conformational change of fibronectin altering cell-binding capacity before molecular adsorption to the substrate. However, another group reasons the inhibitory effect of perlecan with the core protein (Villar, Hassell and Brandan, 1999). Whitelock *et al.* observed adhesion of SMCs and endothelial cells to perlecan-coated substrates from venous and arterial sources and also measured increased adhesion up-on HS removal from the core protein (Whitelock *et al.*, 1999). Lord *et al.* further added, that also the differential glycosylation of perlecan derived from either SMCs or endothelial cells influenced the effect

of perlecan on cellular adhesion (Lord *et al.*, 2014). Analogous studies with aggrecan and endothelial cells revealed an inhibitory effect of aggrecan on cell adhesion and the cleavage of CS side chains improved adhesion (Johnson *et al.*, 2005).

In summary, HSPG play a major role in BMP signaling and regulate cellular adhesion and spreading. Deciphering the underlying mechanism is subject to many studies and tools are needed to well distinguish between csHS and exogenous HS as well as between PG and GAG chains. Systems that are more complex further allow to study synergistic signaling between different active components of the ECM, notably between integrins, HSPG and BMPs.

I.C.4 Cellular models

To understand the interaction between cells and their surrounding ECM a variety of experimental set-ups exists and each demands for a well-suited model. Affinity studies between for example GFs and their receptors can be performed independently of cells. *In vitro* studies however demand for a cell model, which is always a trade-off between being most realistic while remaining accessible and easy to handle (Czekanska *et al.*, 2014). Also for ethical reasons, *in vitro* models should be privileged as long as possible. Complex *in vivo* studies with animals can reveal information about the influence of an experiment on the entire organism and are needed in pre-clinical studies for translation into human medicine applications (Pearce *et al.*, 2007). One objective of this thesis is to study the effect of different ECM components and their influence on cell adhesion and BMP2 signaling. Cellular models thus should be sensitive to the ECM stimuli by expressing the corresponding receptors, that can activate signaling pathways as for example integrin-mediated adhesion and BMP2-mediated signaling. Working with well-characterized cell models common in the field permits comparability of acquired data between research groups (Kartsogiannis and Ng, 2004; Czekanska *et al.*, 2014). Immortalized cell lines, proliferating continuously, offer the advantage to be easy to culture, available in high numbers and affordable (Kartsogiannis and Ng, 2004). Cells can also be isolated from different species, which adds time-consuming and expensive animal care and dissection. Human derived cell lines avoid species differences if conclusions on the human organisms are desired and are advantageous over primary human osteoblast cells with limited availability due to donation scarcity (Czekanska *et al.*, 2012).

Cells used in the osteogenic context origin from pluripotential mesenchymal stem cells, which can differentiate into myoblasts, chondroblasts, fibroblasts, adipocytes and osteoblasts (Kartsogiannis and Ng, 2004). Differentiating into a line-specific progenitor cell commits them to their fate and differentiation advances *via* different stages to terminate for example as osteocytes as explained earlier (**Figure 5**). We chose C2C12 murine myoblast precursors with their capability to differentiate into osteoblasts up-on BMP2 stimulation (Katagiri *et al.*, 1994). Human periosteum-derived stem cells (hPDSCs) complemented these studies to confirm results with a human cellular model (Bolander *et al.*, 2017; Groeneveldt *et al.*, 2020). Chinese hamster ovarian cells were further used due to their BMP2 responsiveness and the availability of mutated clones with HS-regulating EXT1 gene deletion (Tjio and Puck, 1958; Lidholt *et al.*, 1992).

C2C12 cells are mononucleated murine myoblast precursors sub-cloned from C2 myoblasts (YAFFE and SAXEL, 1977) and differentiate into multinucleated myotubes up-on confluence monolayer formation after 6 days (Katagiri *et al.*, 1994). These myotubes are the base for contractile skeletal muscle cells. C2C12 treated with 300 ng/ml sBMP2 differentiated into osteoblasts from day 2 quantified *via* increasing levels of ALP expression and osteocalcin expression. 100 ng/ml BMP2 was identified as the threshold concentration to induce osteogenic differentiation. C2C12 cells have been further characterized to not express endogenous BMP2 (Crouzier *et al.*, 2009), an important information when studying BMP2 signaling.

hPDSCs appear at the periosteum from where they are recruited for bone repair (Colnot, 2009). They have recently shown their clinical relevance in competition with bone marrow derived stem cells. While the latter privileged intramembranous ossification by direct bone formation, hPDSCs undergo endochondral ossification, which is more relevant in fracture repair (Bolander *et al.*, 2017). hPDSCs differentiate up-on BMP2 stimulation into osteoblasts and into chondrocytes. SMAD1/5/9 phosphorylation was up-regulated after 60 min, osterix and sox9 expression from day 3 and ALP expression from day 6. In contrary to C2C12 cells, hPDSCs produce endogenous BMP2.

CHO cells are an immortalized epithelial cell line derived from chinees hamster ovarian cells (Tjio and Puck, 1958) and are widely used for the expression and industrial production of recombinant proteins (Jérôme *et al.*, 2017). Various mutations of this cell line exist, which aim to suppress the expression of targeted proteins (Lewis *et al.*, 2013). As explained earlier, it is common practice to alter the expression of HS *via* genetic mutations *in vivo* or in cell lines for

example by deleting genes responsible for the expression of enzymes involved in the biosynthesis of HS. CHO cells mutant for the enzyme EXT1 (Annaval *et al.*, 2020), have strongly downregulated csHS, which makes this cell type a suitable candidate to study the difference between csHS and exogenous HS on cell adhesion and BMP2 signaling (Lidholt *et al.*, 1992). Indeed, in preliminary results CHO cells have been shown to be BMP2 responsive.

I.D Biomimetic surfaces to study cell-ECM interaction

Historically, cells were cultured in Petri-dishes with a rigid plastic bottom allowing the cells to adhere. To study their response to biochemical cues and thus to reveal signaling mechanisms, it was, and still is, common practice to add soluble bioactive compounds into the culturing media. Cells adhere to the plastic substrates non-specifically *via* their ventral side and receptors on the cell surface of the dorsal side respond to ligands in solution. Over time, it became clear that this model does not correspond to the situation of cells in mammals, which are surrounded by the ECM, giving them mechanical and biochemical cues from all sides in a three-dimensional space. For example, matrix rigidity was shown to influence BMP2 signaling (Crouzier *et al.*, 2011) and also topography such as curvotaxis mediated cell adhesion and gene expression (Pieuchot *et al.*, 2018). It was further revealed that different biochemical cues influence each other as explained above along the example of integrin and GF signaling (Monteiro A., Kollmetz and Malmström, 2018). A need arose for new model systems representing this complex environment and researchers began to adopt the ancient concept of biomimicry. The idea is to learn from evolutionary well-established solutions in nature to engineer models and tools mimicking those as precise as possible (Choi *et al.*, 2015). This opened the interdisciplinary field between material science, surface chemistry and biology, and materials used in this context are referred to as biomaterials. With continuous advancement of micro- and nanotechnologies, these models became more sophisticated and gained in precision up to the molecular scale. Still, each engineered system is designed to give answers to a specific question and might come along with disadvantages when applied in another context. The field of cell-ECM interaction can be divided into three-dimensional (3D) and two-dimensional (2D) model systems (Duval *et al.*, 2017). While 3D models and products can be more realistic in representing the ECM, they are much more complicated to develop and more difficult to characterize with common 2D surface characterization tools. However, for bone repair applications, 3D implants are compulsory and a representation of the ECM as realistic and complex as possible is desired. Hydrogels either used in tissue engineering application (Mantha *et al.*, 2019) or in the context of micro-organs on chips (Verhulsel *et al.*, 2014) can be considered as 2D or 3D material. 2D model surfaces are easier to engineer, to characterize and generally more easy-to-use. They have the advantage to be more flexible, which is crucial to respond quickly to new scientific questions. The representation of the natural environment lacks its 3D characteristics but the precise control by characterization opens doors for sophisticated surface

designs. 2D concepts could in return become candidates for a combination with 3D materials by serving as surface coatings.

Often, research aims at understanding the mechanism between selected molecules related to cell response without the influence of other factors. Since cells already represent a complex system, 2D *in vitro* model surfaces are a great choice to mimic selected features from the ECM without further uncontrolled influences from the material side (Migliorini *et al.*, 2016; Dhavalikar *et al.*, 2020). This approach is especially interesting for GF, which *in vivo* are matrix-bound and released the moment the matrix degrades. This chapter aims to present the current state of the art of 2D model surfaces mimicking parts of the ECM to study the interaction between ECM molecules and cells. The biomimetic SAV model surface is introduced as a versatile tool to study synergies between integrin-regulated cellular adhesion, HS and BMP2 mediated signaling.

1.D.1 2D systems to mimic growth factor presentation in the ECM

Different 2D systems are currently applied to study the interaction between ECM molecules and cells in the field of GFs signaling, cellular adhesion and mechanotransduction (Migliorini *et al.*, 2016; Huang, Yuan and Liu, 2020). A 2D biomaterial is usually build-up *via* a bottom-up approach starting from a substrate, which is ideally transparent to enable microscopic analysis (Dubiel, Martin and Vermette, 2011). This substrate might undergo further treatment. Then, biomolecules build a layer on top, which present for example cellular adhesion motifs, GFs and other molecules of interests. As a next step, cells are plated to responds to the biomaterial and are usually covered by cell culture medium possibly presenting further bioactive compounds. Following parameters and characteristics influence the choice of a suitable system (Migliorini *et al.*, 2016):

- Control of distance between molecules and their surface density
- Control of surface topography
- Control of rigidity
- Temporal release of bioactive molecules
- Degree of complexity e.g. co-presentation

Schwab et al. developed a surface coated with gold nanoparticles using block copolymer micellar nanolithography with particle sizes corresponding to the size of BMP2 (**Figure 10**) (Schwab *et al.*, 2015). Controlled distance between nanoparticles allowed different surface concentrations of immobilized BMP2 and revealed a minimal BMP2 concentration needed for BMP2 mediated SMAD1/5/9 phosphorylation as well as sustained signaling compared to sBMP2. In a very recent study, instead of only passivating the area between the nanodots, they immobilized $\alpha_v\beta_1$ integrin selective ligand or cRGD using click-chemistry (Posa *et al.*, 2021). It was found, that the co-presentation of $\alpha_v\beta_1$ integrins and iBMP2 induced the recruitment of $\alpha_v\beta_3$ integrins in focal adhesions. Colak et al. also combined patterns with RGD by functionalizing surfaces with polymer brushes (Colak, Di Cio and Gautrot, 2018). Peptides like RGD could bind specifically to the brushes based on UV or visible light activated thiol-ene coupling. Human umbilical vein endothelial cells adhered well to RGD comparable to collagen controls and did not adhere to plain brushes. To create for example circular patterns with a diameter of 50 μm , photomasks were used to guide the light only to the desired spots. Cellular adhesion followed the topography imposed by the patterning. They propose to use these substrates to systematically study peptides with specific affinity for selected integrins as well as ECM geometry.

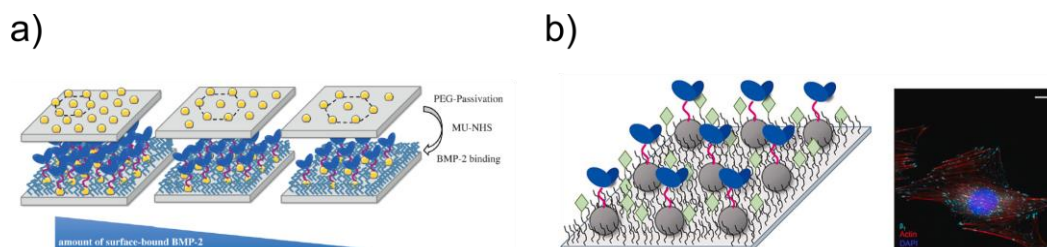


Figure 10: BMP2 presentation via gold-nanoparticles with tunable distances. a) Gold-nanoparticles were functionalized with immobilized BMP2 (dark blue) and the distance was controlled *via* the density of the nanoparticles. b) Integrin ligands (green) were further added in between the nanoparticles. Cells adhered to the surface and responded to BMP2. Adapted from (Schwab et al., 2015; Posa et al., 2021).

To better control the stoichiometry between osteoinductive ligand and adhesion ligand, Oliver-Cervelló et al. developed a system to co-immobilize cRGD and a BMP2-derived peptide covalently bound to an anchor in a 1:1 ratio (**Figure 11**) (Hoyos-Nogués *et al.*, 2017; Oliver-Cervelló *et al.*, 2021a). Since BMP2 also leads to side effects when applied in medicine applications (James *et al.*, 2016) they were interested in peptides derived from BMP2 known to be responsible for osteoinductive activity. The DIWIWA peptide was taken from the BMP2 wrist epitope, covering the residues 30-34 and was shown to interact with the BMPRI and had osteogenic potential. C2C12 cells plated on co-immobilized RGD and DIWIWA peptide

adhered and spread better than on peptide-only or RGD-only surfaces. In addition, p38 signaling was up-regulated on co-functionalized surfaces and even higher than BMP2 induced signaling. However, only BMP2 was able to activate the pSAM1/5/9 pathway and not the peptide.

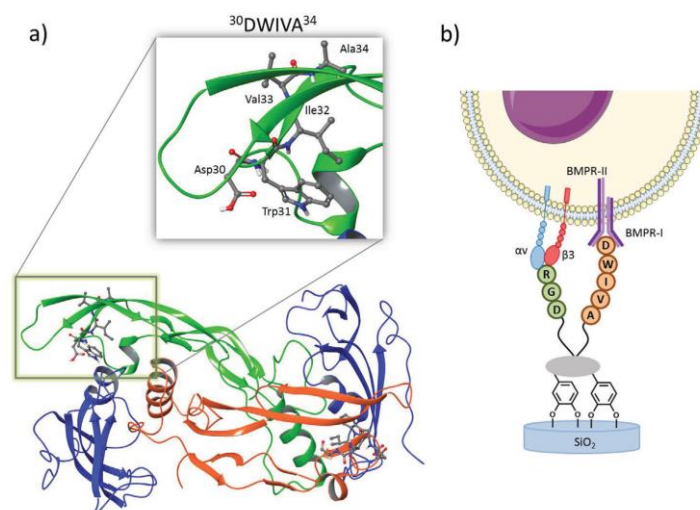


Figure 11: BMP2-derived peptides are co-presented with RGD. a) The structure of BMP2 includes the DWIWA peptide. b) Covalent co-presentation of stoichiometric RGD and BMP2-derived osteogenic peptide DWIWA on SiO₂ via the anchor 1-3,4-dihydroxyphenylalanine (DOPA), a lysine branching point and a spacer. Adapted from (Oliver-Cervelló et al., 2021b).

At a larger length scale, Hauff et al. used micro-contact printing to create thin 20 μm stripes of cell-adhesive biotinylated fibronectin to guide single cell migration into a specific direction (Hauff *et al.*, 2015). Biotinylated BMP2 was then immobilized to the fibronectin layer using NeutrAvidin as a linker. They were able to show, that immobilized BMP2 and sBMP2 increased cell migration velocity at later time points compared to the negative control. Oberhansel et al. also used micro-contact printing and dip-pen nanolithography to create spots with 4 or 5 μm diameter with spacing from 5 to 22 μm. They functionalized a gold surface with biotinylated PEG-thiol (bPEGthiol) to immobilize SAV. Onto SAV, biotinylated BMP2 could bind and thus presented larger areas of BMP2 to C2C12 cells, who positively responded to BMP2 via upregulated osterix. This approach is suitable to easily study variable patterns in combination with immobilized BMP2 instead of sBMP2. A similar approach was done by Fitzpatrick et al. who micro-patterned fibronectin and iBMP2 on LbL films and showed that increasing area of the pattern ranging between 500 μm² and 1500 μm² enhanced SMAD1/5/9 phosphorylation (Fitzpatrick *et al.*, 2017).

Other approaches work with BMP2 gradients, for example using inkjet printing of BMP2 *via* bioink on fibrin (Miller *et al.*, 2009), inspired by gradients influencing embryonal development in zebrafish (Ramel and Hill, 2013). Another gradient was achieved using microfluidics to create a concentration-dependent adsorption of BMP2 into a LbL film (Almodóvar *et al.*, 2014). Azria *et al.* created chitosan-collagen microspheres deposited on surfaces and created a gradient by mixing bare- and functionalized microspheres deposited on a flat mold (Azria *et al.*, 2018). Since PC12 cells adhered best on chitosan microspheres combined with collagen compared to simple chitosan microspheres. This system is intended to guide for example neural cell migration and differentiation by fabricating gradients bearing GF.

LbL thin films present another family of biomaterials, which are designed to release GFs previously entrapped into an ECM-mimicking multi-layer film (Crouzier *et al.*, 2009, 2011; Boudou *et al.*, 2010; Gribova, Auzely-Velty and Picart, 2012; Monge *et al.*, 2015). In general, they are fabricated by alternating incubation of differently charged molecules, which principally interact *via* electrostatic interaction. In the case of a biomimetic film for GF studies, Crouzier *et al.* used sodium hyaluronate anions and PLL cations as alternating compounds and controlled the thickness of the film as well as the stiffness *via* the number of layers and the degree of cross-linking with 1-ethyl-3-(3-dimethylaminopropyl)carbodiimide respectively (**Figure 12**). This way, they designed a tunable material able to adapt to different mechanical conditions. They further controlled the amount of BMP2 adsorbed into the film by initial incubation concentrations and thus created a reservoir of BMP2, which was only partly released after 7 h of rinsing and remained into the film for at least 9 days. Recent studies showed increased C2C12 cellular area and number to different degrees of crosslinking and a dose response to BMP2, 4, 7 and 9 adsorbed into the film at different concentrations quantified *via* ALP expression (Machillot *et al.*, 2018). These films also have demonstrated their potential in *in vivo* studies to regenerate critical-size bone defects in mini pigs (Bouyer *et al.*, 2020). 3D printed clinical-grade polylactide scaffolds were coated with the LbL film, which was loaded with BMP2. They achieved to regenerate the defect using BMP2 doses 20 to 75-fold lower than used in collagen sponges currently used in clinical applications.

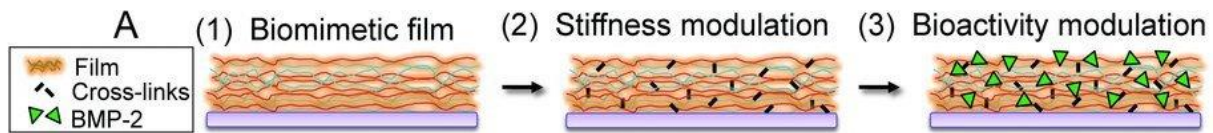


Figure 12: Schematic of LbL films. Differently charged sodium hyaluronate and PLL were alternately incubated and bound to each other *via* electrostatic interaction. The thickness and stiffness is regulated by the number of layers and the degree of additional crosslinking respectively. Soluble GFs as for example BMP2 are incubated and adsorbed into the film. Adapted from (Crouzier *et al.*, 2011).

While the above approaches aimed at mimicking either distance, mechanical and adhesive properties or the immobile characteristic of GFs, the influence of other relevant ECM molecules, notably GAGs, was not addressed. As elaborated before, they play an important role in GFs signaling and adhesion, which demands for model systems to mimic this type of GFs presentation (Migliorini *et al.*, 2016).

Kim *et al.* coated titanium with highly sulfated heparin to then immobilize BMP2 on this modified surface (Kim *et al.*, 2014). Cells proliferated better on surfaces containing heparin and BMP2 compared to samples without heparin, and ALP activity after 14 days was up-regulated compared to the controls. Another group managed to immobilize heparin covalently bound to poly-l-lactide and polycaprolactone *via* acrylamide (Edlund, Dånmark and Albertsson, 2008). BMP2 bound to heparin and C3H10T1 cells were growing most on co-functionalized substrates presenting heparin and BMP2. In addition, Chen *et al.* used a self-assembled monolayer to immobilize heparin and adsorbed BMP2 and also found increased cell area and ALP expression compared to conditions without heparin (Chen *et al.*, 2018). Using an LbL-technique, Anouz *et al.* alternated the polycation chitosan and the native or oxidized polyanions heparin or CS. Films were loaded with BMP2 and collagen was added on oxidized GAGs to improve cellular adhesion (Anouz *et al.*, 2018). BMP2 and oxidized heparin with additional collagen layer induced the best C2C12 spreading and ALP activity was up-regulated only on oxidized GAGs in the presence of adsorbed BMP2.

Instead of covering whole surfaces, groups are also working with microparticles covered with heparin to immobilize BMP2 for effective therapeutic GF delivery (Hettiaratchi *et al.*, 2014; Tellier *et al.*, 2015). Further, the broad field of ECM-mimicking hydrogels (Yue *et al.*, 2020) can be combined with GAGs as for example CS (Anjum *et al.*, 2016). The amount of CS as part of the hydrogel together with poly(ethylene glycol) (PEG) was tunable and cellular adhesion could further be improved by incorporation of RGD peptides. Finally, different amounts of BMP2 were incorporated and bone marrow-derived MSC inside the gel expressed more ALP in the CS-containing gel compared to the pure PEG gel. Also working with

hydrogels, Kisiel et al. used hyaluronan gels combined with either dermatan sulfate or heparin precomplexed with BMP2 (Kisiel, Klar, *et al.*, 2013). This prolonged the delivery rate of BMP2 compared to BMP2 not bound to GAGs.

A further challenge is to present GAGs in an oriented way as they appear in the ECM, side-specifically bound to their core protein. Migliorini et al. further developed a SA_v self-assembled monolayer, which allowed to immobilize biotinylated molecules in a controlled manner (Migliorini *et al.*, 2017). They compared BMP2 directly immobilized on the surface with BMP2 adsorbed on immobilized HS (iHS) and controlled the surface density of BMP2 with surface sensitive techniques (**Figure 13**). This permitted conclusions on stoichiometric relations between BMP2 and iHS as well as to control equal amounts of BMP2 in both conditions. aBMP2 induced higher phosphorylation of SAMD1/5/9 compared to BMP2 directly immobilized *via* biotin to SA_v and sustained signaling for 3 h compared to sBMP2. Other groups worked with comparable systems but either in a less sophisticated way (Oberhansl *et al.*, 2014) or focused on molecular and chemical studies not involving cells (Dubacheva *et al.*, 2017).

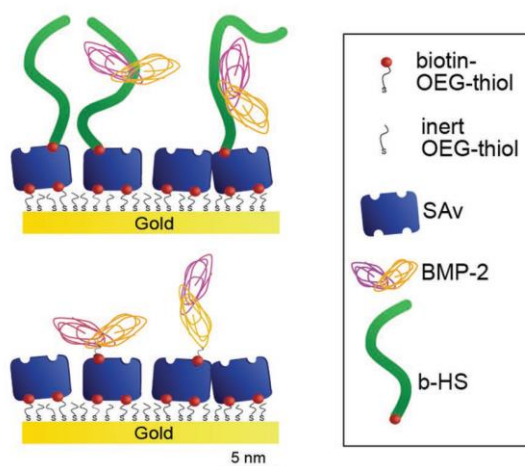


Figure 13: The biomimetic SA_v platform. A SA_v monolayer bound to gold *via* a mix of biotin-oligo(ethylene glycol)-thiol (biotin-OEG-thiol) and inert oligo(ethylene glycol)-thiol (inert OEG-thiol). This allowed to immobilize biotinylated molecules in a controlled manner. BMP2 was presented *via* oriented iHS and compared to immobilized BMP2. Adapted from (Migliorini et al., 2017).

The above approaches all present sophisticated ways to study the interaction between the ECM and each corresponds to specific needs related to the addressed scientific question. In the scope of this work, the SA_v platform was adopted as an approach to respond to the objective of the thesis for the following reasons:

- The technique is already well developed and expertise available in the group
- The biotin-SAv binding allows a flexible adaptation of the platform design
- The platform can be precisely characterized using surface sensitive technique
- Cells respond to BMP2 adsorbed on HS

1.D.2 The biomimetic streptavidin platform

The biomimetic SAv platform as introduced above (**Figure 13**) comes along with many advantages but also carries opportunities for further development and thus to exploit its full potential. In this chapter, the concept of the SAv platform is explained in detail and the opportunities for further development are illustrated.

The idea behind the design of the platform is to immobilize molecules of interest from the ECM in a controlled way and to present them to cells. The binding of other molecules however, as for example those present in the media or expressed by cells, is undesired. A second requirement is flexibility, in other words, easy changes of the design of the platform *via* different immobilized molecules. Finally, the platform needs to be compatible with microscopy systems, which requires transparency of the base substrate. The tetramer SAv with a high affinity and specificity for one biotin molecule at each of the four monomers is an ideal candidate to serve as an intermediate compound. Forming a self-assembled monolayer on the transparent substrate *via* a biotinylated linker, it presents free biotin binding sites for the specific binding of biotinylated molecules of interest (**Figure 14**).

The protein SAv has a molecular weight of about 53 kDa, has its isoelectric point at 6.03 and does not possess carbohydrate receptors (Chaiet and Wolf, 1964; Michael Green, 1990; Laitinen *et al.*, 2006). This reduces biochemical interactions at neutral pH but the four biotin binding sites keep their high affinity towards biotin with a K_d of 10^{-14} - 10^{-16} M⁻¹. In SAv, the biotin binding sites are organized pair-wise at opposing faces of the molecule. The binding between biotin and SAv thus is one of the strongest known in nature and comparable to covalent binding. Biotin, also known as vitamin B₇, is a small molecule with 244 Da. The concept of biotinylation describes the chemical coupling between other molecules and biotin to enable further binding to SAv and biotinylated molecules will be named bX or iX (Fairhead and Howarth, 2015). The SAv-biotin pairing is widely applied in very different context (Dundas,

Demonte and Park, 2013). SAV-based biosensors are designed to detect biotinylated molecules and in immunohistology studies, fluorescent SAV binds to selectively biotinylated molecules at the cell surface.

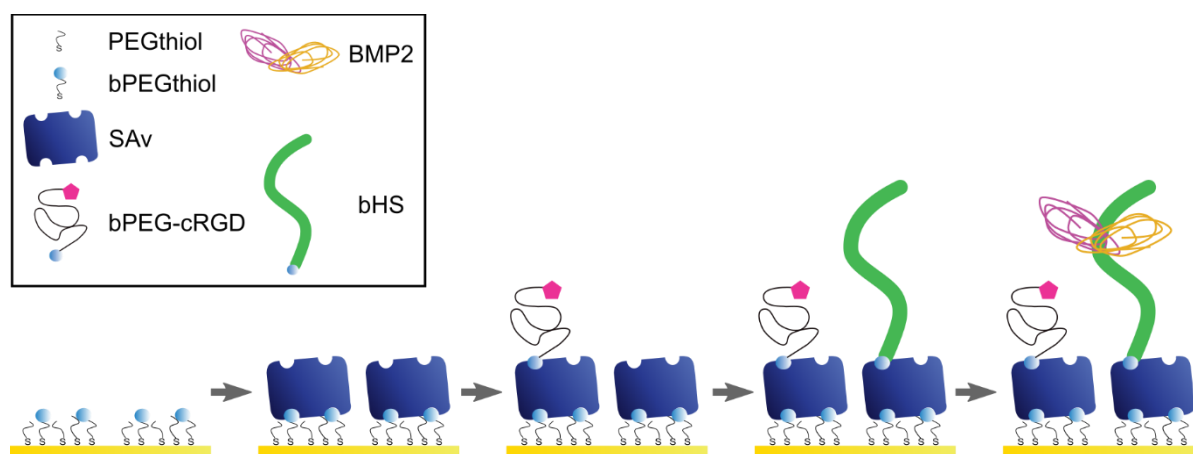


Figure 14: Sequential buildup of the SAV biomimetic platform on gold substrates. Molecules are dissolved in solution and are incubated on the substrate to either form self-assembled monolayers (PEGthiol/biotinPEGthiol (bPEGthiol), SAV), to bind to SAV (bPEG-cRGD, iHS) or to adsorb on immobilized molecules (adsorbed BMP2 (aBMP2)). In the case of cRGD, incubation is stopped before saturation of the biotin binding sites of SAV to remain sites available for subsequent biotinylated molecules.

To create a SAV self-assembled monolayer on the base substrate, a biotinylated linker is applied. The system from Migliorini *et al.* is based on gold-sputtered 2.4 cm x 2.4 cm microscopy glass coverslips, which remain transparent due to the thin layer of 1.5 nm Cr and 8 nm Au (Migliorini *et al.*, 2017). Gold interacts very well with Sulphur and self-assembled monolayers using this material property are widely studied and known as thiols (Bain *et al.*, 1989; Bürgi, 2015). Migliorini *et al.* used a mixture of bPEGthiol and PEGthiol dissolved in ethanol, which binds to the oxygen plasma-activated gold surface and forms a self-assembled monolayer with the PEG or bPEG chain ends facing up-wards (Migliorini *et al.*, 2014). PEG is further known to effectively reduce molecular adsorption (Zalipsky and Harris, 1997). The specific ratio of 95:5 PEGthiol/bPEGthiol passivates the gold surface against non-specific adsorption and offers just the optimal amount of biotin to bind SAV without saturating available biotin binding sites localized at the top of the protein (Migliorini *et al.*, 2014). The passivated gold surfaces were either placed into small plastic dishes for further functionalization and cellular studies or glued onto custom-made carriers, splitting the surface into four separated areas to increase the number of conditions.

Subsequently, SAV binds to form a monolayer (Richter *et al.*, 2007), which is the common base for all further biomimetic platform designs. SAV is dissolved in neutral HEPES buffer and

incubated on the gold surfaces to bind to the available biotin molecules on the surface. Surface sensitive techniques show that binding slows down over time until saturation and areal mass density calculations suggest a tightly packed monolayer (Migliorini *et al.*, 2014).

Biotinylated molecules also dissolved in neutral hepes buffer bind *via* biotin to SAV and it was found that about 1.7 biotinylated molecules were immobilized per SAV molecule (Dubacheva *et al.*, 2017). A further development of this platform is the co-presentation of biotinylated molecules on the same platform as for example a cellular adhesion peptide and HS (Migliorini *et al.*, 2014). Due to measurements of the binding kinetics of biotinylated molecules to SAV using quartz crystal microbalance with dissipation monitoring (QCM-D), the incubation time of a molecule to saturate is deduced and can be tuned by changing the concentration of the molecule in the buffer. Interruption of binding to SAV thus results in a partly saturated sub-monolayer and allows sequential binding of the second molecule of interest to the remaining binding sites.

Aside biotinylated molecules, also non-biotinylated molecules can interact with and bind to the platform. As described earlier, HS has binding sites for BMP2 (Ruppert, Hoffmann and Sebald, 1996), which defines the natural presentation of BMP2 in the ECM. BMP2 can thus adsorb on SAV platforms pre-functionalized with iHS (Migliorini *et al.*, 2017). In comparison with the SAV-biotin binding, this link is partly reversible. Finally, it was shown that cells adhere to co-functionalized surfaces and respond to biochemical cues over a period of three days.

The biomimetic SAV platform has demonstrated its flexibility and simplicity while presenting complex but well controlled experimental conditions to cells, mimicking selected aspects of the ECM. In this project, we used this system to specifically activate selected integrins and to co-present integrin ligands in different surface concentrations, iHS and BMPs.

Nevertheless, this system carries potential to be further developed since the current design comes along with limitations regarding the categories cost, fabrication time and characterization:

Cost

- Gold-sputtering demands for expensive clean-room access

Fabrication time

- Functionalization is done by manual pipetting

- Gold-sputtering is time-consuming and adds an additional layer to control
- Gluing of surfaces onto carrier is a delicate work-step

Characterization

- Microscopy is complicated due to non-standardized sample carrier. This leads to non-planar surfaces and incompatibility with automated image acquisition
- High-adsorptive gold layer demands for high laser powers in fluorescence-based microscopy and might cause diffraction artifacts
- Surface characterization requires auxiliary substrates compatible with surface sensitive techniques. A direct quantitative measurement *in situ* is not yet adopted

1.D.3 Streptavidin monolayers on glass surfaces

SAv monolayers can be build up on glass surfaces, which are popular in cellular studies due to their optical properties in microscopy. Glass-bottom multi-well plates for example are laboratory equipment with standardized dimensions, which makes them compatible with multichannel pipettes, characterization tools as plate readers and microscopes and its design is recognized by software-applications *via* corresponding templates.

Amorphous silicon oxide (SiO₂) is the most common glass and this material is known to be chemically inert and highly transparent. Previous efforts to build up biomimetic SAv platforms on glass were based on the concept of lipid bilayers binding electrostatically to the surface and presenting biotin for SAv to form a monolayer (Migliorini *et al.*, 2014). However, this approach turned out to be not sufficiently stable and it was doubtful that the lipid bilayer would withstand mechanical forces transduced *via* adhering cells. Another solution is the silanization of the glass surface, which is based on the chemical coupling between APTES (amino-propyl-triethoxy-silane) and SiO₂ (Lapin and Chabal, 2009). Coupling this technique with biotinylated PEG allows further immobilizing SAv. However, studies in our group revealed problems with non-specific adsorption to silane-PEG-biotin-based SAv platforms.

A well characterized concept for SAv monolayer formation is based on biotin-derivatized Poly(L-lysine)-g-poly(ethylene glycol) (**Figure 15**) (Huang *et al.*, 2002). The PLL backbone of PLL(20)-[3.5]g-PEG(2)/PEGbiotin(3.4)50% (PLL-g-PEGbiotin50%) is positively charged and

thus binds electrostatically to negatively charged glass surfaces after oxygen plasma activation. A defined ratio of the L-lysine monomers is intended to carry a PEG chain with a 2 kDa chain length, in this case one out of 3.5 (grafting ratio). Further, 50% of the PEG chains are biotinylated and 3.4 kDa long to expose biotin for SA_v binding. It was shown that this technique is well controlled and biotinylated molecules bound to the SA_v layer (**Figure 15**).

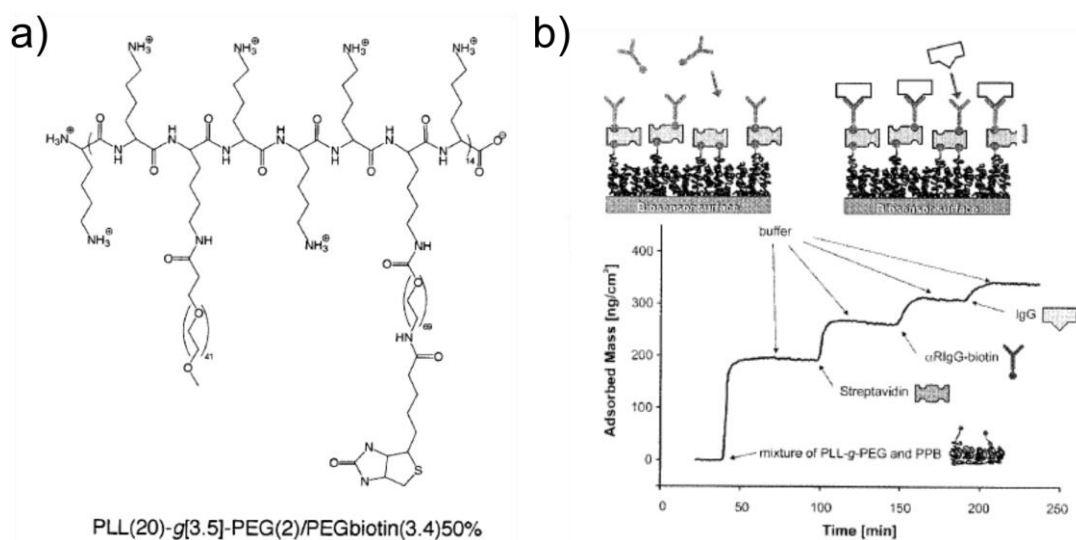


Figure 15: Schematic of PLL(20)-[3.5]g-PEG(2)/PEGbiotin(3.4)50% and its binding to Nb₂O₅ chips. a) Chemical structure of PLL(20)-[3.5]g-PEG(2)/PEGbiotin(3.4)50% (PLL-g-PEGbiotin50%) with a PLL backbone to which PEG and biotinPEG chains are attached on one side. The other side of the PLL backbone has positively charged groups to enable electrostatic interaction with glass. b) OWLS measurement of PLL-g-PEG/PEGbiotin mixture binding to Nb₂O₅ chips and SA_v binding to the biotin molecules. Afterwards, biotinylated goat anti rabbit immunoglobulin (α RIgG-biotin) occupied available biotin binding sites of the SA_v layer. Adapted from (Huang et al., 2002).

It was further found that pre-assembling NeutrAvidin with biotinylated molecules in a stoichiometric 3:4 ratio improved the molecular organization of NeutrAvidin molecules and led to a higher amount of biotinylated molecules binding to SA_v (**Figure 16**) (Zhen *et al.*, 2004).

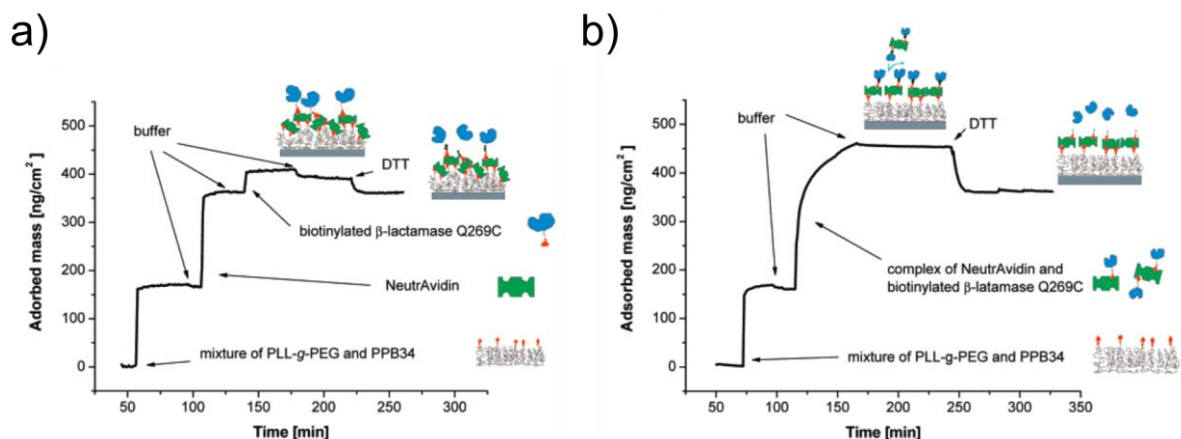


Figure 16: Subsequent binding of NeutrAvidin and biotinylated β -lactamase against pre-mixing NeutrAvidin and β -lactamase before binding to PLL-g-PEG/PEGbiotin. a) OWLS measurement of NeutrAvidin binding to a PLL-g-PEG/PEGbiotin34% layer and biotinylated β -lactamase occupying afterwards the remaining binding sites. b) An alternative strategy was to pre-couple biotinylated β -lactamase with NeutrAvidin in a molar ratio of 3:4 before binding to PLL-g-PEG/PEGbiotin on the surface. This resulted in a higher overall adsorption and an improved layer organization. The removal of the β -lactamase with Dithiothreitol (DTT) revealed that the amount of NeutrAvidin was comparable in both approaches but the adsorbed biotinylated compound was higher in the pre-mix case. Adapted from (Zhen et al., 2004).

PLL-g-PEGbiotin50% is thus an interesting candidate to buildup SA_v monolayers on glass surfaces and to immobilize biotinylated molecules. However, this approach was not yet applied to fabricate biomimetic platforms in the context of cellular studies. Using PLL-g-PEGbiotin50% as a linker for biomimetic SA_v platforms inside 96-well plates carries the potential to improve the experimental workflow due to the compatibility of the plates with other systems and to enhance the imaging properties (**Figure 17**).

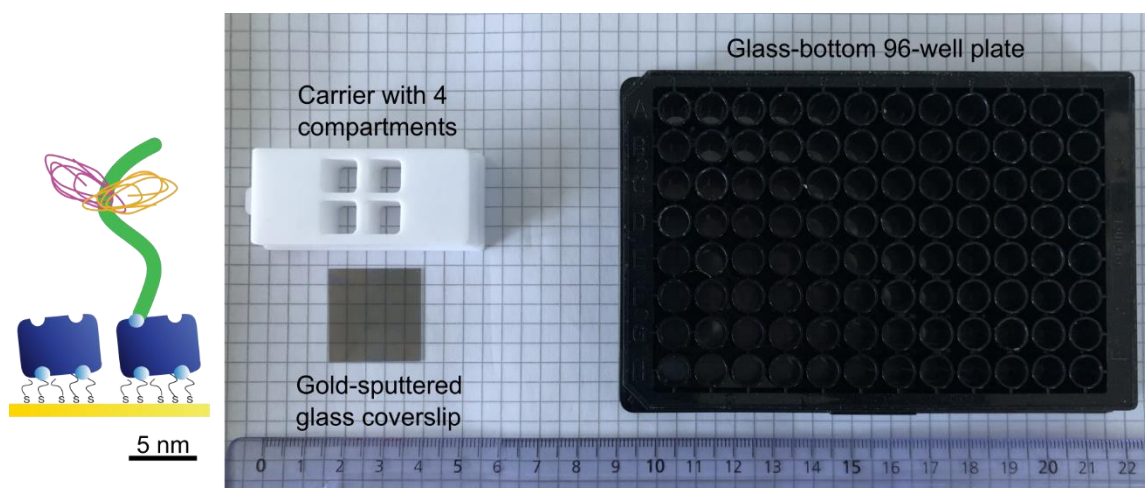


Figure 17: Picture of the state-of-the-art custom-made gold-based system and a glass-bottom 96-well plate offering potential for high-content studies. Gold-sputtered coverslips were glued onto a custom-made carrier to separate the surface into four compartments to then buildup a SA_v monolayer *via* bPEGthiol as done by Migliorini et al. (Migliorini et al., 2017) (left). Glass bottom 96-well plates are a common substrate for cellular studies and carry potential to improve the experimental workflow for biomimetic SA_v platform fabrication (right).

I.E Surface characterization of biomimetic films

Biomaterials mimicking the ECM need to be well characterized to permit conclusions on the isolated effect of selected components of the ECM. It is important to assure that the biomaterial fabrication routine leads to a homogenous surface without defects to present the same condition to cells independently of their location on the substrate. Secondly, the molecular surface density of all compounds of the biomaterial is a meaningful measure since it allows to conclude on stoichiometric relations between the interacting molecules as well as to compare results between different conditions and other studies. Knowing for example the molecular surface density of integrin ligands or BMP2 and thus their average distance can help to define critical thresholds for cell adhesion (Arnold *et al.*, 2004; Schwab *et al.*, 2015). During 2D biomaterial development, technical parameters such a binding kinetics of interacting molecules are of relevance to tune the fabrication process as well as to control sub-monolayers. Stiffness of a 2D biomaterial can further be of interest as well as information about the degree of hydration in the case of hydrated layers or the orientation of GAGs or proteins to assure binding site availability.

The characterization of hydrated layers exposes the researcher to a particular experimental environment because the characterization is often required to take place at a solid-liquid interface (Migliorini, Weidenhaupt and Picart, 2018). Challenges could include control of temperature, pH, buffer, optical parameters, micro fluidics, biomaterial degradation or stability to name a few. This comes along with a high demand for precision since the required resolution is often in the micron- and nanoscale.

Characterization techniques are divided into *in situ* and *ex situ* measurements while the correct attribution depends on the perspective of the experiment. *In situ* measurements are conducted in the local setting of the experiment. *Ex situ* measurements on the other hand are performed outside of the initial experimental environment. In case of the biomimetic SAV platform, the typical experiment cascade consists of two main steps. First, the specific platform is designed to respond to the desired experimental conditions. Then, cells are plated onto the platform and cellular response is analyzed. The design and the characterization of the platform is performed on auxiliary substrates compatible with the characterization techniques while cell experiments are conducted inside compartments or 96-well plates (**Figure 17**) (Migliorini *et al.*, 2017; Machillot *et al.*, 2018). Hence, characterization on auxiliary substrates is *in situ* from

the perspective of the platform design but can be considered *ex situ* when taking the point of view from the cell experiment. In this project, the words *in situ* and *ex situ* are used from the perspective of the cell experiments.

The biomimetic SAV platform was characterized *ex situ* for molecular surface density using surface sensitive techniques but it remained an open question to quantify molecular surface density *in situ* on substrates used for cell experiments. In this chapter, I give a brief overview on commonly applied 2D characterization techniques separated into label-free techniques and fluorescence-based techniques. In higher detail, I explain QCM-D and spectroscopic ellipsometry (SE) used in our studies. Then, I introduce the principles of fluorescent-based image correlation spectroscopy (ICS) which we applied and further developed to characterize the molecular surface density *in situ* on substrates used for cell experiments.

I.E.1 Label-free surface characterization tools

Migliorini et al. (Migliorini, Weidenhaupt and Picart, 2018) and Saftics et al. (Saftics *et al.*, 2021) review common label-free techniques applicable for the characterization at solid-liquid interfaces.

The surface plasmon resonance (SPR) characterization technique is sensitive to molecular binding events on a surface due to resulting changes of the properties of an evanescent electrical field (Mauriz, García-Fernández and Lechuga, 2016). An SPR set-up following the Kretschmann configuration consists of a glass prism attached to a thin gold surface. A single wavelength light beam passes through the prism and in consequence falls with multiple angles onto the gold surface. The light beam is reflected and captured by a detector to measure its intensity. In the conducting gold layer, free electrons diffuse and adsorb the energy of the incoming light beam only at a specific angle called the surface plasmon resonance angle. This causes them to resonate, and leads to an evanescent field propagating at the gold-liquid interface. Since the energy of the incoming light is adsorbed, the intensity captured at this angle by the detector is strongly decreased and forms a characteristic peak. Further, the evanescent field is sensitive to its environment such as changes of the refractive index. Upon molecular binding to the gold surface, the surface plasmon resonance angle thus changes and leads to a shift of this characteristic peak. This allows to deduce molecular surface density down to 0.1

ng/cm². However, the specific sensors are costly and the technique is limited to 20 nm layer thickness.

Optical waveguide lightmode spectroscopy (OWLS) as SPR is sensitive to changes of the refractive index at the surface of a sensor (Vörös *et al.*, 2002). A HeNe-laser beam enters into a waveguide with a specific incident angle aimed for total reflection. The material of the waveguide has a high refractive index, which is the case for SiO₂ or TiO₂, to be distinguishable from the liquid media with lower refractive indices. The surface of the sensor is grated to allow the light to enter the waveguide, which leads to internal reflections. A result is an evanescent field propagating along the interface between sensor and bound molecules and depends on the refractive index and the thickness of the layer. This field is described by transverse and electric polarization mode, which occur at two different angles. The angles are measured and both, the refractive index and the thickness, can be deduced and molecular surface density down to 0.5 ng/cm² measured. Also here, waveguides are special substrates to be bought.

Surface-enhanced Raman spectroscopy (SERS) is another common technique to quantify proteins on a surface (Fleischmann, Hendra and McQuillan, 1974; Mosier-Boss, 2017) but different proteins can not be distinguished from each other. A combination with an immunoassay can solve this issue (Shin *et al.*, 2020). Two additional techniques based on evanescent waves are dual polarization interferometry (DPI) (Kozma *et al.*, 2014) and ATR-FTIR (Barth and Zscherp, 2002), which however only give relative parameters or reveal information about the secondary structure of proteins respectively (Migliorini, Weidenhaupt and Picart, 2018) and thus are not further explained.

QCM-D measures the change of frequency of an oscillating sensor crystal up-on mass adsorption and further the change in dissipation caused by the visco-elastic properties of the layer (Reviakine, Johannsmann and Richter, 2011). The sensor quartz crystal is oscillating due to the piezoelectric effect in a shear-thickness mode, induced by alternating applied voltages (**Figure 18 a**). Matching the frequency of the alternating voltages with the resonance frequency of the crystal results in a standing wave with its odd overtones (1):

$$f_n = nc/2d \quad (1)$$

n is the order of the overtone, c the speed of sound in the crystal and d the thickness of the crystal. The crystal is operated in the so-called ring-down mode, turning-off the voltage for each data point and measuring frequency as well as dissipation. Since the piezoelectric effect

is bi-directional, the oscillation induces a measurable voltage with a corresponding frequency and amplitude, the latter decaying in function of time due to attenuation. From this information the dissipation or bandwidth can be derived. **Figure 18 b** shows the oscillating signal with low dissipation in air (blue) and the highly and exaggerated attenuated signal in water (red). Typical dissipation of a crystal in water is around 3.5×10^{-4} .

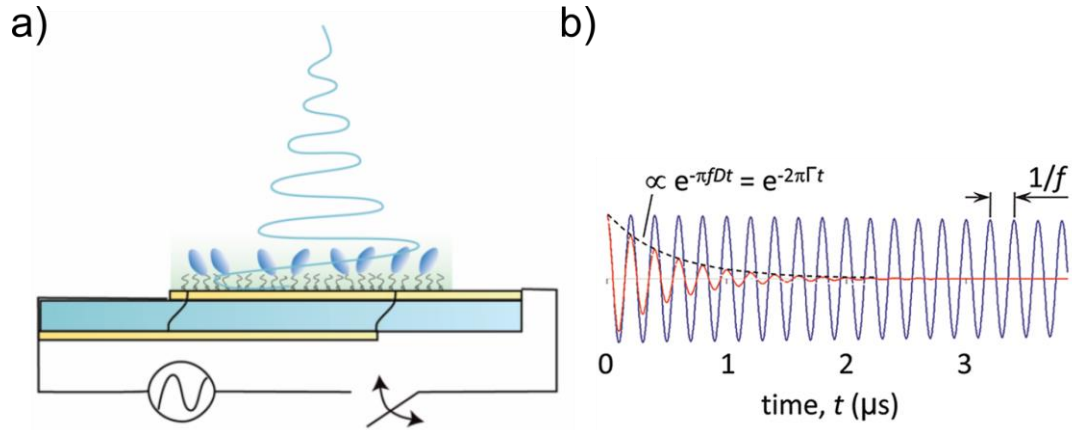


Figure 18: QCM-D measurement principle. a) An oscillating quartz crystal changes its resonance frequency upon molecular adoption. This frequency and the dissipation caused by visco-elastic properties of the film are measured. b) The graph presents the low dissipation in air (blue) and the high dissipation in water (red) where f is the frequency. Adapted from (Reviakine, Johannsmann and Richter, 2011; Migliorini, Weidenhaupt and Picart, 2018).

The system operates in liquid environment and molecules dissolved in buffer enter the chamber to bind to the crystal. Time-resolved *in situ* measurements detect a change in frequency up-on molecular binding and in case of changing viscoelastic properties a change in dissipation, too. Sauerbrey (Sauerbrey, 1959) discovered a linear relationship between the change in resonance frequency and the mass, described by (2):

$$\Delta f_n = - \frac{n}{c} m_f \quad (2)$$

C is the is a material constant based on material properties and the fundamental resonance frequency of the crystal and m_f the areal mass density. However, this formula has to be used with caution since it depends strongly on the properties of the layer. In case of homogenous lateral films, a condition expected in the case of biomimetic SA_v platforms, the change in dissipation needs to be much smaller than the inverse change in frequency. This defines a rigid layer and permits the use of the Sauerbrey equation. Worth to note is that the shifts in frequency and dissipation depend on the adsorbed layer and thus include the molecule and coupled solvent. Therefore, the areal mass density has to be interpreted as the so-called wet mass and additional information about the degree of hydration are necessary to deduce the dry mass. In

case of non-rigid films, viscoelastic models need to be applied for correct data analysis. Also in case of monolayers of discrete particles, data treatment becomes more sophisticated.

In summary, QCM-D is a powerful tool to follow *in situ* the functionalization of surfaces in four parallel chambers and is thus applied to design and characterize the sequential buildup of biomimetic SAV platforms on gold- or SiO₂-coated crystals. To receive further information about the mass of the adsorbed molecules without the coupled solvent, measurements with for example SE are required.

SE is an optical characterization tool sensitive to optical interfaces and thickness of the in-between layers by measuring changes of polarization (Hinrichs and Eichhorn, 2014). Linear polarized light is a planar transversal electromagnetic wave and SE works with two polarized waves standing perpendicular to each other (p-polarized and s-polarized). The projection of both waves onto a planar surface is described as an ellipse with the ellipsometric angles Δ and Ψ , depending on the phase shift between the waves and their resulting amplitude, respectively. If these waves fall on a surface with an incident angle, both waves are reflected differently, which results in a relative change of Δ and Ψ (**Figure 19**). The relationship between the different reflection coefficients of the p-polarized and s-polarized waves r_p and r_s and the ellipsometric angles Δ and Ψ is described as (3):

$$\frac{r_p}{r_s} = \tan \Psi e^{i\Delta} \quad (3)$$

The reflected light is captured in a detector, the ellipsometric angles Δ and Ψ are measured and then compared to those from the incident light. Different parameters influence these angles, which can be categorized into two groups: experimental conditions as for example the angle of incidence and the wavelength of the light but also sample-specific material conditions like the refractive index, thickness and dielectric functions. Further, light is reflected, transmitted, scattered and diffracted at every optical interface and thus demands for a layer-resolved view on the acquired data. The effects of all these parameters on the elliptical polarization state are well described with theoretical concepts. On the other hand, the measured ellipsometric angles Δ and Ψ don't provide enough information to directly deduce values for all the parameters. Therefore, models describing each layer of the surface are created and unknown parameters empirically fitted based on the measured angles and based on additional theoretical values describing well studied material properties.

SE can be used to characterize surfaces in liquid environment, as it is the case for biomimetic SAV platforms. Gold- or SiO₂-coated surfaces are placed into a liquid flow module to incubate molecules and measure the change of the ellipsometric angles *in situ*. Hydrated layers can be modelled with the Cauchy model which describes the refractive index of the adsorbed layer as a function of the wavelength (Cauchy, 1836). The layer-thickness d_A and its refractive index n_A are then fitted and if the refractive index of the ambient buffer n_C is known as well as the refractive index increment of the hydrated layer dn/dc , the de-Feijter equation (4) can be applied to calculate the areal mass density (De Feijter, Benjamins and Veer, 1978):

$$M = d_A \frac{n_A - n_C}{dn/dc} \quad (4)$$

Even though the results require modelling and thus are not a direct read-out, the technique is precise down to 1 nm thick films and can also distinguish different layers from each other (Migliorini, Weidenhaupt and Picart, 2018). Comparing it with QCM-D further allows to calculate the degree of hydration of the layer (Reviakine, Johannsmann and Richter, 2011). Nevertheless, SE measurements demand for reflective substrates as well as no geometrical constraints to allow the light to fall on the surface at an angle. It is thus not applicable on glass substrates inside 96-well plates used for cellular studies and is considered an *ex situ* measurement from that point of view.

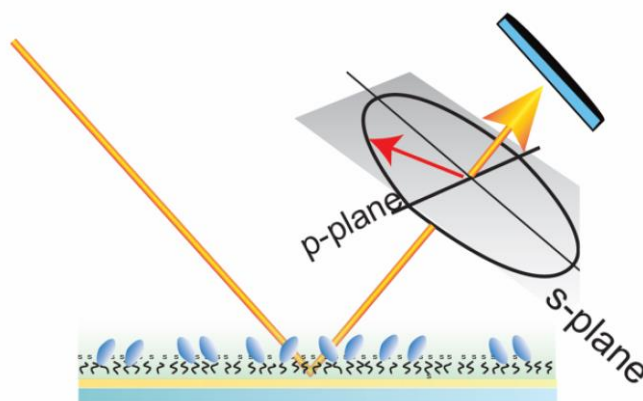


Figure 19: SE measurement principle. Polarized light is reflected at the functionalized surface and changes its elliptical polarization state depending on optical properties of the layer. The elliptical polarization state of two perpendicular polarized light waves, one along the p-plane, the other one along the s-plane, is represented by the ellipsometric angles Δ and Ψ in form of a resulting amplitude vector (red arrow). Adapted from (Migliorini, Weidenhaupt and Picart, 2018).

In conclusion, a variety of surface sensitive techniques exists to characterize surfaces with hydrated layers from which we chose QCM-D and SE as the most suiting methods to characterize multi-layered biomimetic SAV platforms *ex situ*. For *in situ* characterization inside

glass bottom 96-well plates, fluorescence based methods are considered, compatible with the geometrical and optical properties of the sample.

I.E.2 Fluorescence-based surface characterization tools

Fluorescence-based characterization relies on the principle to detect emitted light from fluorescent molecules, which are bound to the molecules of interest (Sanderson *et al.*, 2014). It is typically used to quantify labelled proteins in cells using fluorescent microscopes, to visualize adsorption of molecules to surfaces or to measure concentrations in solutions as with the well-known ELISA assay. The detected signal depends on many different factors as for example on the intensity of the excitation laser defining the number of photons emitted by the fluorescent molecules as well as on different fluorophore specific quantum yields. In addition, the lateral resolution defined by about half of the wavelength of emitted light hinders image resolution down to the molecular scale. Thus, conditions are often compared relative to each other in a semi-quantitative matter based on total intensity since absolute quantification demands for calibration, more complex acquisition protocols or advanced data treatment (Verdaasdonk, Lawrimore and Bloom, 2014). Recent advances in super resolution microscopy permit to identify single molecules with a distance from 10 nm to each other but those techniques are scarce compared to classic confocal microscopes and not applicable for dense samples (Balzarotti *et al.*, 2017). But also with classical confocal microscopes available in most laboratory facilities, single molecular quantification protocols are developed, notably ratiometric comparison of fluorescence microscopy, stepwise photobleaching or image correlation spectroscopy (Coffman and Wu, 2012; Verdaasdonk, Lawrimore and Bloom, 2014).

Stepwise photobleaching is a common technique to quantify single molecules and is based on the principle that fluorophores can irreversibly bleach when exposed to high excitation laser intensities (Verdaasdonk, Lawrimore and Bloom, 2014). Counting the number of bleaching steps to reduce the image intensity down to the background signal directly indicates the number of initial molecules (**Figure 20**). The bleaching intensities need to be chosen sufficiently low to avoid simultaneous bleaching of two fluorophores, which would bias the data. Since bleaching of a fluorophore is a statistical process, the probability to bleach multiple fluorophores increases with the number of molecule in the sample. This method thus works best with no more than 30 molecules per region of interest. While this method is precise to quantify

the number of fluorophores, it is not possible to conclude on the number of labelled molecules if the number of fluorophores per molecule is not known. In conclusion, this technique is powerful for samples with low molecular density and with known number of fluorophores per molecule, which is not always the case for densely packed molecules in monolayers.

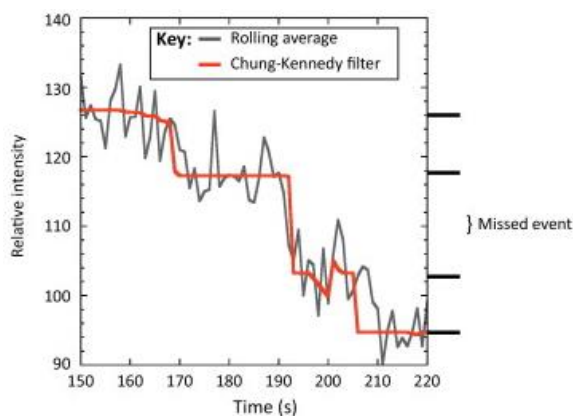


Figure 20: Stepwise photobleaching principle. A sample is photobleached over time, which results in decreasing intensity. In case a step represents the bleaching of a single fluorophore, the number of molecules can be deduced based on the number of bleaching steps. If many molecules are on the surface it is more likely that multiple fluorophores are bleached in one cycle and bias the measurement (missed event). Adapted from (Coffman and Wu, 2012).

A second option is to compare measured fluorescent intensities to a known standard (Coffman and Wu, 2012). If the expression of a protein in a cell is well characterized in an absolute way, it can be labelled with a fluorophore and serve as a reference. The molecule of interest is also labelled with a fluorophore and the ratio of the intensities between control and molecule of interest permits direct conclusion on the number of molecules. To distinguish the signal from the reference molecule and the molecule of interest, either different fluorophores with similar properties have to be chosen or cells with the control molecule and those with the molecule of interest have to be on different samples. Further, it needs to be verified if labelling the molecules alters their expression in the cell, and if the labelling is efficient, the latter can be measured with immuno blots. Compared to the stepwise photobleaching, this method is not limited to a maximum number of molecules but again demands for a precise control of the degree of labelling of standard and molecule of interest. This technique could be applied on surfaces if the surface density of a labeled molecule is known as well as the degree of labelling for both molecules.

Another indirect measurement is the micro bicinchoninic acid assay (μ BCA), which measures protein concentration in solution and can be used to compare concentrations before and after molecular adsorption on the surface. However, no information about the spatial

distribution can be deduced and the sensitivity down to 500 ng/ml is not always sufficient (Smith *et al.*, 1985).

Fluorescence fluctuation spectroscopy (FFS) is the family of optical techniques, which detects single molecules based on statistical intensity fluctuations (Rigler and Elson, 2001). For applied measurements in solution in fluorescence correlation spectroscopy (FCS), labelled molecules diffuse in an observation volume defined by the point spread function (PSF) of a confocal microscope. The total measured intensity thus fluctuates over time due to molecules leaving and entering the observation volume. The temporal autocorrelation function (ACF) of the time-resolved signal thus reveals information about the total number of molecules inside the PSF. Image correlation spectroscopy (ICS) relies on the same principle but is based on intensity fluctuations in function of the position using confocal images (Petersen *et al.*, 1993). Here, the confocal laser scans the sample and each pixel represent the signal of all molecules inside the PSF. In this case, the spatial ACF G of the image is calculated in the x- and y-direction of the image (**Figure 21**). Images are acquired in a way that the area of the PSF exceeds the size of a pixel, which leads to the situation that a fraction of the signal emitted by the same molecules is captured in different pixels. Adjacent pixels thus are correlated to each other since they share to some extent the same molecular information. The ACF (5) describes the intensity fluctuations between adjacent pixels and is defined by

$$G(\xi, \eta) = \frac{\langle \delta F(x,y) \delta F(x+\xi, y+\eta) \rangle}{\langle F(x,y)^2 \rangle} \quad (5)$$

where $F(x,y)$ is the intensity at the pixel (x,y) and ξ and η the spatial increment in the x- and y-direction. The ACF has its highest value if ξ and η are vanishing against 0, the image being almost fully superimposed with itself. The value of the ACF (6) at this point can be described as

$$G(0,0) = \frac{1}{N} \quad (6)$$

with N being the total number of molecules per PSF. In other words, the lower the number of particles or molecules in the image, the higher are the fluctuations between pixels and vice versa. The amplitude of the ACF is thus inversely proportional to the number of molecules.

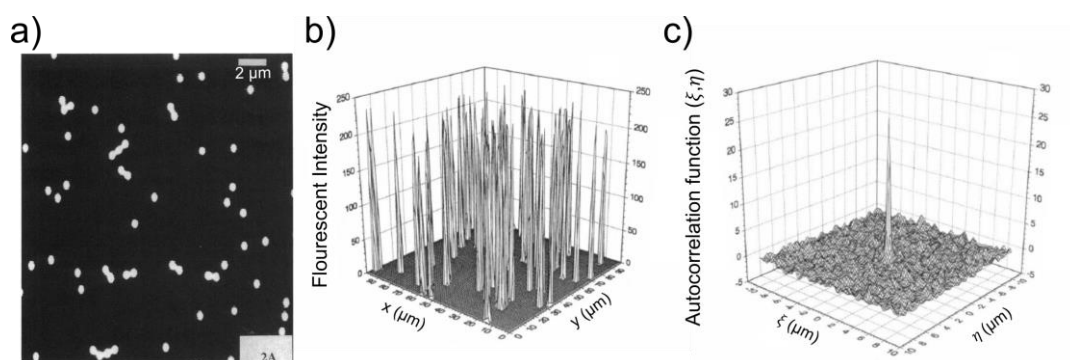


Figure 21: Principle of ICS. a) Image with a known number of fluorescent beads with a diameter of 0,44 μm in the range of the size of the Point spread function (PSF). b) A graph shows the fluorescent intensity of each bead in the image. c) The spatial ACF of the image is calculated where ξ and η represent the shift of the image against itself in the x and y direction. The width of the ACF is related to the size of the PSF and its amplitude is inversely proportional to the number of particles. Adapted from (Petersen et al., 1993).

However, this method is only reliable if the precise number of fluorophores per molecule and their distribution is known. If molecules are heterogeneously labelled with fluorophores, fluctuations are not just related to the number of molecules but also to the intensity variations between molecules. The formula thus underestimates the total number of molecules (Kolin and Wiseman, 2007; Delon *et al.*, 2010). ICS is very powerful because it is not dependent on the intensity of the image and can theoretically cover a large range of molecular densities. Interestingly, ICS is applied to study single proteins at cells (Rossow *et al.*, 2010; Macháň and Wohland, 2014) but is not known in the field of biomaterial characterization.

In summary, ICS is the most suitable candidate to be adopted for *in situ* characterization of SA_v platforms but precision is still limited.

I.F Automated fabrication, parallelization and miniaturization of 2D biomaterials

Automation of fabrication processes has been an ever-important subject in industry to save labor time, increase reproducibility and in consequence to be more efficient than the competitor is. The development of automated processes initially demands resources such as research and financial efforts but the investment pays off over time with reduced costs per output. The choice to automate or to privilege manual labor thus depends on the features of the product of interest. Products with low lot size or highly complex design are less adapted for automation since a new product might replace them before the automation effort could pay off. Products with high lot sizes and simple architectures thus are more eligible to automation. However, if an automated fabrication system offers a certain degree of flexibility, it can become attractive even in the case of more complex products with lower throughput.

Biomedical research facilities are usually much smaller compared to typical industrial companies, they don't produce large quantities of the same product and due to the nature of science they change frequently the design of the experiments. Hence, it is common practice to fabricate samples with manual efforts to profit from the advantage of high flexibility. Nevertheless, research facilities profit from the advancements in industry in various ways. Companies provide common chemical reagents, standardized substrates and standard fabrication steps to allow the researcher to outsource fractions of the manual labor for a gain in time or due to lack of expertise. In addition, automation hardware and software is sold to laboratories to automate fabrication steps or sample analysis. An example are liquid handling robots to automate the repetitive and standardized protocol of sample treatment for polymerase chain reaction (Stangegaard *et al.*, 2009). Still, the core of an experiment, which defines the uniqueness and thus holds the potential for novel discoveries, is often not automated. In the case of 2D biomaterials for cellular studies, experiments are defined by different conditions of the material. It is hence of great interest to address this subject by developing highly flexible automation protocols for the fabrication of biomaterials, which allow to quickly respond to new experimental conditions (Vasilevich and de Boer, 2018; Grubb and Caliarì, 2021). Automation needs to be distinguished from high throughput even though automation becomes more attractive and later indispensable with rising throughput. However, up to a certain point, high throughput strategies can also be based on a high degree of miniaturization and parallelization combined with manual labor.

This chapter introduces the state of the art of miniaturization, parallelization and automation procedures in the context of 2D biomaterial fabrication and elucidates in higher detail automated liquid handling.

1.F.1 Lithography, micro-contact printing and additive manufacturing

Grubb et al. recently reviewed fabrication methods used in biomimetic disease modelling and ordered the approaches along the categories parallelization and automation (Grubb and Caliarì, 2021).

Parallelization and miniaturization are often combined and are fundamental for high throughput studies. It can mean to create many replicates of the same substrate or different but similar versions of it while keeping sample volume low. Two popular approaches are soft lithography (Qin, Xia and Whitesides, 2010) and micro-contact printing (Alom Ruiz and Chen, 2007). Soft lithography is a common method to fabricate patterns in the nanoscale inside soft materials as for example poly(dimethyl siloxane) (PDMS). A solid master is created using a photomask, which guides light onto a silicon wafer coated with a solid photoresist (**Figure 22**). Either by degradation or cross-linking, a pattern remains and serves as a re-usable mold to cast PDMS or other elastomers. The high resolution allows to design very different and detailed topographies and the mask guarantees high reproducibility between replicates. On the other hand, the design and fabrication of the master are time-consuming and demand access to a clean room, which makes the change of experimental conditions difficult. Due to advances in accuracy of 3D printing, masks can also be processed with that technology and thus renders them more available and flexible. In summary, fabricated masks allow tuning dimensions, patterns and advanced structures corresponding to the specific need of an experiment with a high degree of parallelization and miniaturization.

Micro-contact printing in the contrary is a technique to deposit small volumes onto a surface and is thus useful to present for example proteins or adhesion ligands to cells in a defined 2D spatial pattern (**Figure 23**) (Alom Ruiz and Chen, 2007). A mask presenting these features can be created using lithography and subsequently converted into a stamp. Then, the molecule dissolved in solution, so-called ink, is printed onto a surface following the features of the stamp. Theoretically, the same stamp could be used with a different molecule of interest but changing the pattern demands for a greater effort as stated above. It is also possible to deposit

micro volumes onto surface *via* contact printing using small metal pins (Zhang, Lee and Kilian, 2017). The flexibility of the pattern is though very limited due to the rather fixed geometry of the metal pins but can be an easy alternative since no mask is needed.

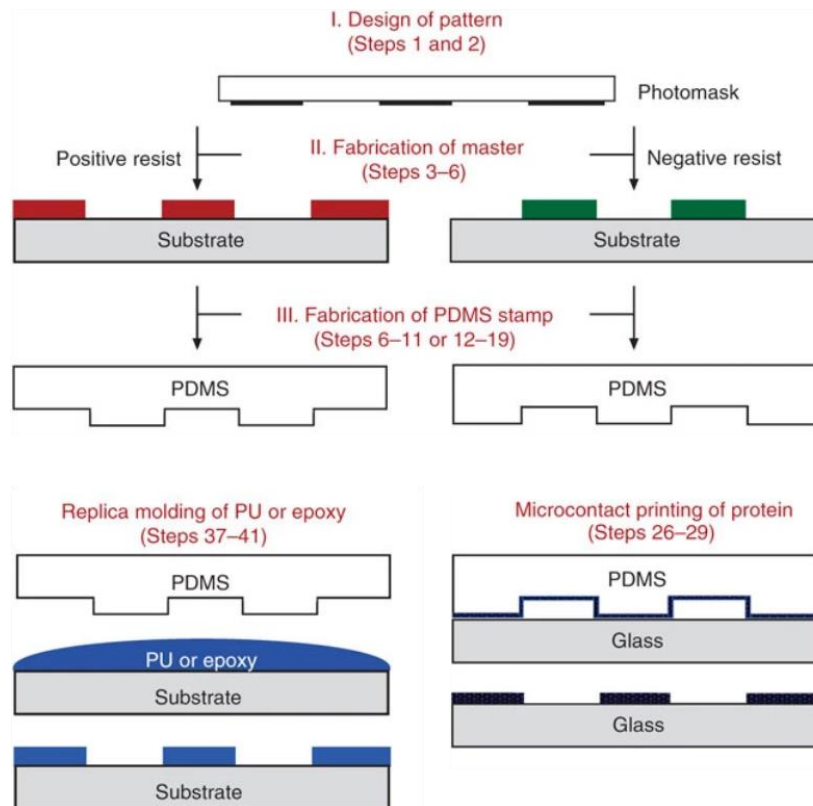


Figure 22: Fabrication procedure of masks using lithography. Positive resist degrades upon light and negative resist crosslinks if exposed. Afterwards, poly(dimethyl siloxane) (PDMS) stamps are created from those masks and can be used to mold replicas in materials of interest such as polyurethane (PU), epoxy or other (left) or as stamps for micro-contact printing (right). Adapted from (Qin, Xia and Whitesides, 2010).

The large category of additive manufacturing including 3D printing and 3D bio-printing is becoming widely adopted due to its flexibility and precision and is primarily used to fabricate 3D models out of the scope of this thesis (Ma *et al.*, 2018). For 2D surfaces, inkjet or non-contact printing is applied (Saunders and Derby, 2014; Zhang, Lee and Kilian, 2017). Here, the drops of dissolved molecules are printed onto a surface without touching it in contrary to micro-contact printing (**Figure 23**). This allows to deposit multiple different solutions one after the other onto the same position and thus carries high freedom for experimental design. A typical radius of a functionalized surface is as small as 10-50 μm (Saunders and Derby, 2014).

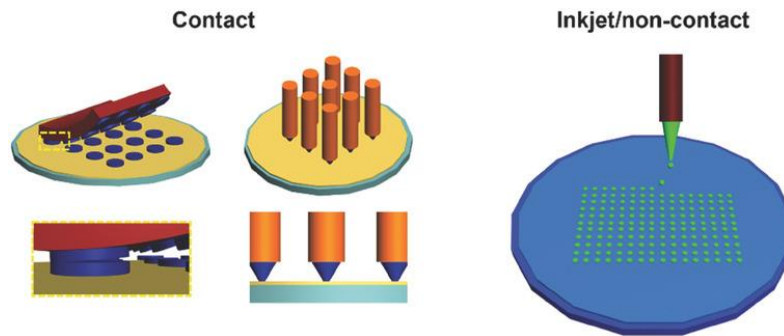


Figure 23: Contact and non-contact printing principle. Contact printers deposit molecules *via* a stamp or pins and by direct contact to the surface (left). Inkjets or other forms of non-contact printers do not touch the surface (right). Adapted from (Zhang, Lee and Kilian, 2017).

Wang et al. created a stamp using lithography presenting a pattern of lines with different width, density and alignment (**Figure 24**) (Wang *et al.*, 2018). This stamp was used to print fibronectin following these patterns onto a PDMS-coated coverslip to then study the effect of these 2D parameters on cell morphology.

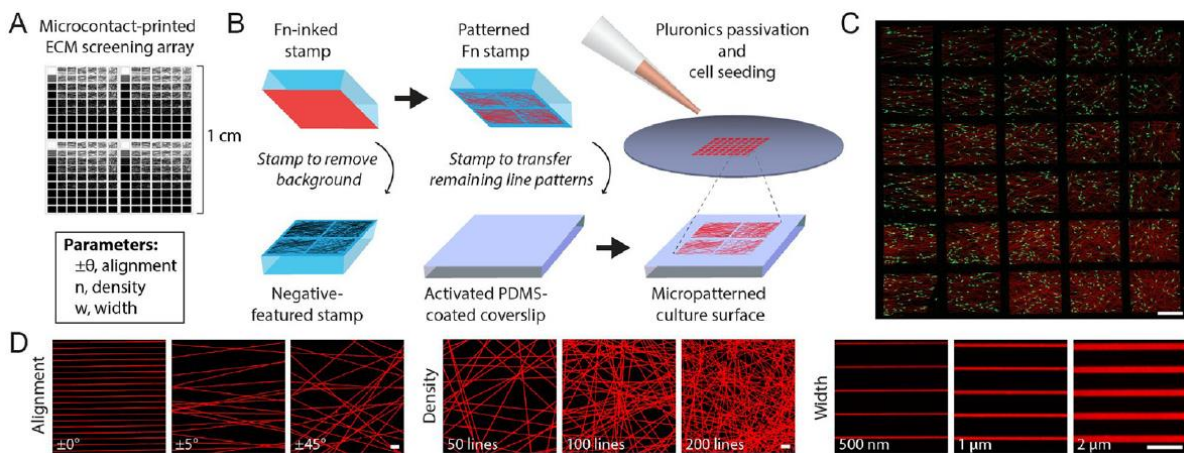


Figure 24: Preparation of fibronectin patterns. a) A photomask contains 252 different ECM conditions (alignment, density and width). b) A flat stamp was coated with Alexa555-labelled fibronectin (Fn). A UV-activated negative-featured stamp removed Fn from the background and the remaining pattern was then transferred onto an activated PDMS-coated coverslip. Cells were seeded to respond to fibronectin depending on the pattern. c) Fluorescence image of 3T3 cells (green) adhering to the Fn patterns (Scale bar is 1 mm). d) Visualization of the three different control parameters alignment, density and width (Scale bar is 10 μ m). Adapted from (Wang et al., 2018).

Kourouklis et al. applied contact printing to immobilize different ECM molecules on hydrogels (Kourouklis, Kaylan and Underhill, 2016). Hydrogels were prepared with different elastic moduli by varying precursor ratios. Then, different combinations of collagen I, III, IV, fibronectin and laminin were contact-printed from a multi-well plate onto the hydrogels to study the combined effect of stiffness, ECM composition and TGF β 1. A very similar study was conducted with mouse embryonic stem cells but without varying the stiffness (**Figure 25**)

(Flaim, Chien and Bhatia, 2005). In addition, inkjet printing was applied to pattern collagen for cellular studies (Roth *et al.*, 2004).

Extracellular matrix microarray

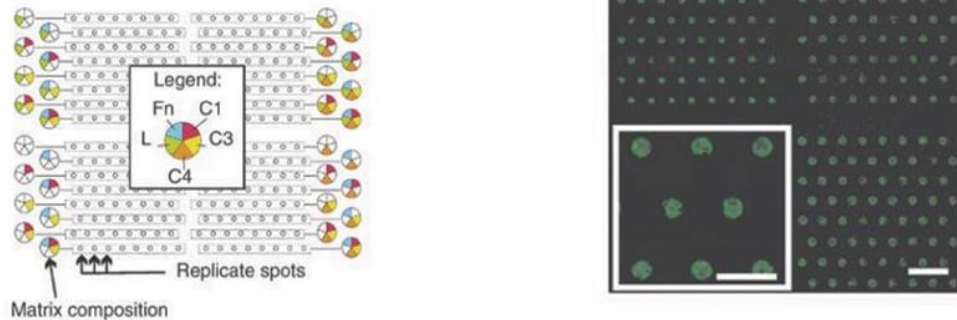


Figure 25: Microarray of different combinations of ECM molecules. The molecules collagen I (C1), III (C3), IV (C4), fibronectin (Fn) and laminin (L) were pre-mixed inside multi-well plates (left) and then immobilized on a substrate, using a robotic DNA spotter (Scale bar = 50 μm) (right). Adapted from (Flaim, Chien and Bhatia, 2005).

Lithography-based micromolding can also be used to create concave microwells inside PDMS with 500 μm diameter (**Figure 26**) (Lee *et al.*, 2018). To study the interaction with the ECM, wells were further functionalized with APTES, laminin and PLL and it was found that cells adhered best on PLL and laminin. Spheroid formation, however, was fastest on PDMS, delayed on APTES and not occurring on laminin and PLL and could thus be controlled *via* ECM molecules.

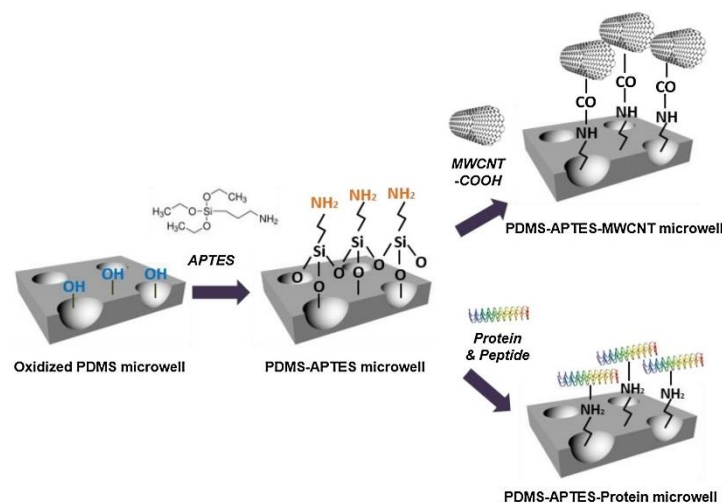


Figure 26: Concave microwells molded into PDMS using lithography-based masks. Wells were further functionalized with (3-aminopropyl)triethoxysilane (APTES) to then add multi-walled carbon nanotubes (MWCNTs) or ECM molecules such as laminin or PLL to study neuronal adhesion and spheroid formation. Adapted from (Lee *et al.*, 2018).

The above examples demonstrate how lithography, contact and non-contact printing can be used and combined to achieve a high degree in miniaturization and parallelization *via* microarrays and microwells. They are relatively easy to implement and offer advantages for high-content screening of different conditions and come along with low material consumption. While especially lithography-based methods offer a high complexity for 2D and 3D patterns, the complexity and control of the presentation of ECM molecules is limited or time consuming with low throughput.

I.F.2 Automated liquid handling for 2D biomaterial fabrication

Liquid handling robots take over repetitive manual pipetting by controlled aspiration and dispense of liquids over a large range of volumes by moving liquid handling arms in a 3-dimensional space (workstation) (Kong *et al.*, 2012). The concept of automated liquid handling is similar to the principle of typical manually operated pipettes or syringes. Liquid handling robots are sold in all sizes with a different number of dependent or independent arms. The workstation can further be equipped with additional hardware such as grippers, heating units and other mechanical or static elements. A user operates the robot *via* software, which allows to design the workstation and to create liquid handling protocols. Once validated, these protocols are very powerful to repeat the same routine without major human involvement in future experiments. However, since a protocol is highly specific for the demand of each experiment with each single liquid handling operation precisely defined, their flexibility is limited. Changes in the experimental design, which might involve adaptations of the workstation or modified order of liquid handling operation usually involve time-consuming modifications of the liquid handling protocol in the operating software.

Liquid handling robots are vastly applied in industrial biotechnology replacing human labor force, increasing productivity and reproducibility and become more and more relevant in life science for high content screening (Kong *et al.*, 2012; Zeng *et al.*, 2020). In the field of genomics and proteomics the amount of parallel conditions, which involve liquid handling, are enormous but also groups working with biomaterials began to adopt liquid handling robots.

Machillot *et al.* automated the fabrication of LbL films inside multi-well plates (**Figure 27**) (Machillot *et al.*, 2018). The incubation times and the number of multilayers would cause long manual fabrication and a high degree of repetition of pipetting steps is prone to errors. 96-well

plates with a flat bottom were chosen because they were suitable for imaging, provided sufficient surface area for cellular studies and were compatible with common liquid handling robots while offering a sufficient degree of parallelization. One of the two polyelectrolytes was aspirated from the stock and dispensed into the wells. After incubation, the solution was aspirated from the wells and dispensed into the waste. A similar routine followed for rinsing before the second polyelectrolyte was incubated. This routine then was repeated depending on the number of desired multilayers. Homogeneity of the LbL film was optimized by implementing automated plate tilting during aspiration and dispense as well as adapting pipetting parameters. The result was a reproducible homogeneous film in all wells and in different plates making this system a great candidate for cellular studies. But even though experimental parameters as for example the number of multilayers or the choice of wells could be easily changed, all wells were always presenting the same condition and single well parameters as for example the type of loaded protein were conditioned manually afterwards.

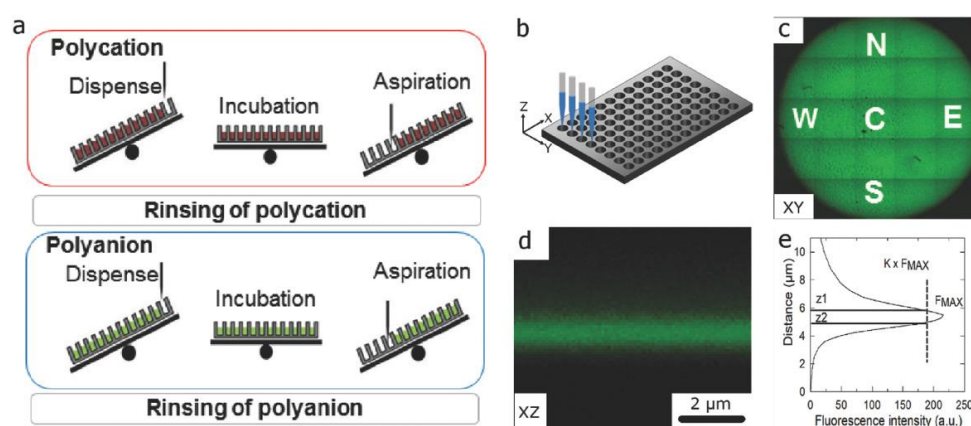


Figure 27: Automated fabrication of polyelectrolyte LbL films inside 96-well plates using a liquid handling robot. a) Process of LbL film fabrication. polycations were dispensed, incubated and aspirated flowed by a rinsing cycle. The same routine was subsequently performed with polyanions and repeated multiple times to achieve multiple layers. b) Schematic of a liquid-handling robot treating multiwell plates with a well diameter of less than 10 mm. c) Tile-scan of fluorescent-labeled LbL films inside a well. d) Z-stack of the LbL film to measure film thickness. e) Quantification of the thickness of LbL films based on the z-stack. Adapted from (Machillot et al., 2018).

Aiming at a high degree in parallelization and a variety of conditions, Ranga et al. developed an automated liquid handling routine to fabricate 1024 unique conditions mimicking the ECM inside micro wells by combining factors from a material library using automated liquid handling (**Figure 28**) (Ranga *et al.*, 2014). The cell-laden hydrogels were thus tuned for elasticity by polymer concentration, degradation *via* peptide sequence, with different ECM components as fibronectin or laminin as well as with cell-cell interaction molecules and soluble factors. A nanoliter liquid handling robot took over mixing steps of the precursors related to the

formation of the hydrogels, dispense into the micro wells of the precursor and subsequently dispense and mixing of cells, soluble factors and cross-linking agent. This liquid handling protocol was programmed in matlab defining all moves. Cellular response to these conditions was analyzed *via* cellular area and green fluorescence protein response with automated image acquisition and analysis. This approach enabled to identify the combinational effects of various parameters at once with a high degree in miniaturization and complexity. In future studies, the same liquid handling protocol can be applied with a different materials library following the presented material categories. On the other hand, removing one of those categories or replacing for example the soluble factors by a higher variety of ECM compounds would come along with major changes in the protocol.

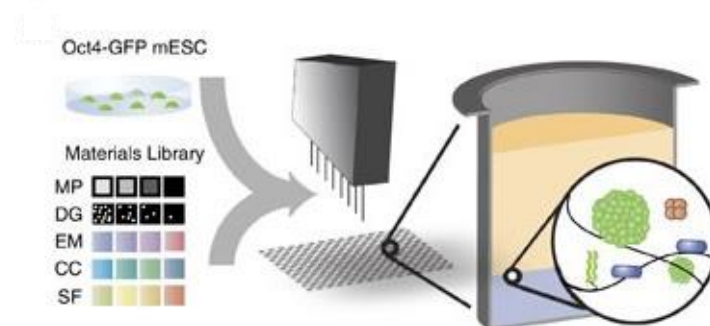


Figure 28: Automated fabrication of different hydrogel conditions. A nanoliter liquid handling robot built 1024 unique cell-laden hydrogels inside microwells to study simultaneously the combinational effect of different parameters of the ECM such as mechanical properties (MP), degradability (DG), ECM components (EM), Cell-cell interaction components (CC) and soluble factors (SF). Adapted from (Ranga et al., 2014).

Eggert et al. responded to the problem of protocol flexibility in hydrogel fabrication as well as to adaptability by other laboratories with the development of a liquid handling workstation together with a flexible protocol generator (**Figure 29**) (Eggert *et al.*, 2021). The liquid handling robot was assembled with commercially available parts and was able to mix and dispense gelatin methacryloyl hydrogel precursors as well as to heat and UV-crosslink gels. Focus of the system was to easily control the stiffness of hydrogels, which depended primarily on the concentration of the polymer as well as on the exposure time and UV-light intensity when crosslinking. A graphical user interface to easily define these parameters individually for each single well and automated execution of this protocol enabled high throughput production of reproducible hydrogels or stiffness gradients. Further combination with the design-of-experiment approach helped to identify the ideal mix of concentration, exposure time and intensity for a desired stiffness in a highly efficient manner. A higher complexity was reached by the combination of gelatin-based hydrogels with an alginate-based hydrogel. This approach

was indeed very promising since it automated key fabrication steps possibly applicable for other types of hydrogels and especially due to its easy-to-use graphical experimental set-up. It was further shown that the set-up could be used to change cell culture media. However, this workstation was not yet applied to fabricate biomaterials outside the hydrogel context.

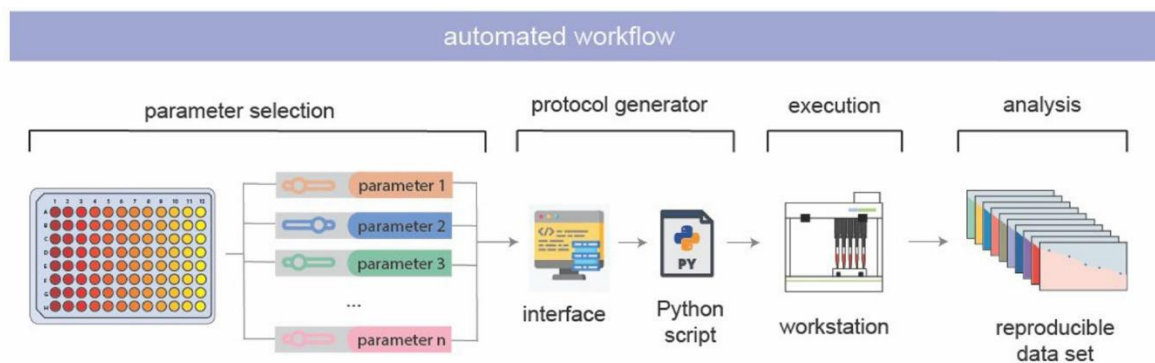


Figure 29: Workflow with graphical user interface to enter experimental conditions. The custom-developed workstation and the graphical user interface allowed the user to select parameters to generate a protocol, which was executed by the workstation. The result were automatically fabricated different hydrogels inside 96-well plates. Adapted from (Eggert et al., 2021).

In summary, liquid handling robots get more and more adopted in life science laboratories and have demonstrated their potential to automate repetitive tasks in a reproducible and easy way in biomaterial fabrication. While automation starts with the investment into a suitable workstation, the development of a protocol responding to the specific need of a project is demanding further efforts. In case of the biomimetic SA_v platform, we identified a potential for automation due to the high amount of repetitive pipetting steps as well as the long fabrication time. Compared to hydrogels or LbL film, the build-up of the platform does not involve steps as for example cross-linking, mixing or heating. On the other hand, a protocol needs to be able to process a high amount of different compounds entirely independent from each other and to adapt flexibly to changing incubation times and experimental designs. In addition, a certain degree of parallelization and compatibility with 96-well plates is desired to increase throughput and to be compatible with other laboratory equipment.

The liquid handling robot Tecan Evo100 is chosen due to its availability in the laboratory as well as pre-existing routines from the LbL automation (Machillot *et al.*, 2018). It has four arms, which are operated with air displacement technology for aspiration and dispense of liquids. They can be addressed individually and their spacing is variable so that containers such as 96-well plates and tube carriers with different dimensions can be accessed. The workstation further contains a tilting unit for the plate carrier previously shown to improve aspiration and dispense. Protocols can be created with the manufacturer's software Evoware and additional

custom-made software allows the user to graphically define a set of variables and to select wells for the LbL film fabrication.

To address the above listed requirements for automated SA_v platform fabrication, the following functionalities were identified to be implemented:

1. Liquid handling protocol compatible with a variable number of compounds with individual incubation times and other features
2. Development and calibration of a compound rack to hold a high number of Eppendorf tubes
3. Further development of the custom-made software to graphically assign independent conditions to single wells, define variables such as incubation time and to define places in the compound rack for the solutions

I.G Objective and positioning of the thesis

As introduced above, exogenous HS positively influences BMP2 signaling but its role on osteogenic differentiation when site-specifically immobilized is not known. Integrins regulate BMP2 signaling and BMP2 induces β_3 -integrin mediated cellular adhesion and spreading on soft substrates. Nevertheless, the specific role of β_1 - and β_3 -integrins and their spatial distribution on BMP2-signaling and osteogenic differentiation still needs to be investigated as well as the effect of BMP2 on cellular adhesion to surfaces presenting integrin ligands. On the other hand, csHS was found to have a negative influence on BMP2 activity and it mediates cell adhesion *via* the HepII domain of fibronectin. However, the interaction between csHS and exogenous HS regarding BMP2 signaling, cellular adhesion and spreading remains under scientific debate. With biomimetic SAv platforms, we aim at co-presenting the β_3 -integrin ligand cRGD together with oriented, exogenous HS and aBMP2 to study the crosstalk between integrins and BMP2 signaling and the role of HS in this crosstalk. By the combination of a biomimetic approach with cellular biology tools such as silencing of β_1 - and β_3 -integrins and knocking down enzymes for HS synthesis, we intend to reveal the specific influence of each cellular component.

To realize these experiments, many different conditions need to be investigated simultaneously, which demands for a high degree in parallelization and in consequence favors automation. So far, biomimetic platforms were built-up by manual pipetting on gold sputtered surfaces inside custom-made supports and no available automation method was offering sufficient flexibility to be adopted for this purpose. We aim at automating the fabrication of different biomimetic SAv platforms inside commercialized glass-bottom 96-well plates upon user demand with PLL-g-PEGbiotin50% as a linker between glass and SAv. Since precise characterization of biomimetic surfaces regarding homogeneity and areal mass density is crucial to understand cellular mechanisms, surface sensitive techniques such as SE and QCM-D are intended to deliver this data *via* auxiliary model substrates *ex situ*. So far, *in situ* characterization methods of biomimetic surfaces are not quantitative or demand for calibration with reference samples. We address this topic by applying for the first ICS inside 96-well plates to quantify molecular density and homogeneity *in situ* on surfaces fabricated by the liquid handling robot. In a different context, it was shown that fluorescence-based ICS returns biased data if the precise distribution of fluorophores per molecule of interest is not known. To respond

to this problem we intend to deduce these two parameters by combining classic ICS with a photobleaching routine *in situ* without additional calibration and validate the results with SE.

We address these questions in four chapters starting with the automated fabrication of biomimetic SAV platforms followed by their *in situ* characterization and finishing with cellular studies on the role of HS, BMP2 and integrins (**Figure 30**).

Chapter II: Biomimetic SAV platforms are engineered on glass using PLL-g-PEGbiotin50% as a linker. We develop a fully automated fabrication protocol to functionalize up to 96 different biomimetic SAV platforms inside commercially available glass-bottom 96-well plates. Then, surfaces are characterized *in situ* for homogeneity and molecular surface density using ICS and *ex situ* with QCM-D and SE.

Chapter III: With highly homogenous Alexa55-labelled SAV (SAVAlexa) platforms we intend to further develop ICS by combining it with photobleaching. This reveals information about the average number and distribution of Alexa555 fluorophores per SAV to reduce uncertainty of standard ICS. The self-calibrated *in situ* method is compared to SE measurements on thermal SiO₂ surfaces *ex situ* to demonstrate its value for surface characterization.

Chapter IV: cRGD, HS and aBMP2 are co-presented on SAV platforms to study the interaction between integrins, HS and BMP2 on cellular adhesion and osteogenic differentiation in C2C12 cells and hPDSCs. We use silencing RNA to decipher the role of β_1 - and β_3 -integrins.

Chapter V: We aim at distinguishing the role of exogenous HS and csHS. CHO WT cells and those without csHS are plated on SAV platforms with cRGD, exogenous HS and BMP2. Cellular response is analyzed *via* cellular adhesion, spreading and early BMP2 signaling.

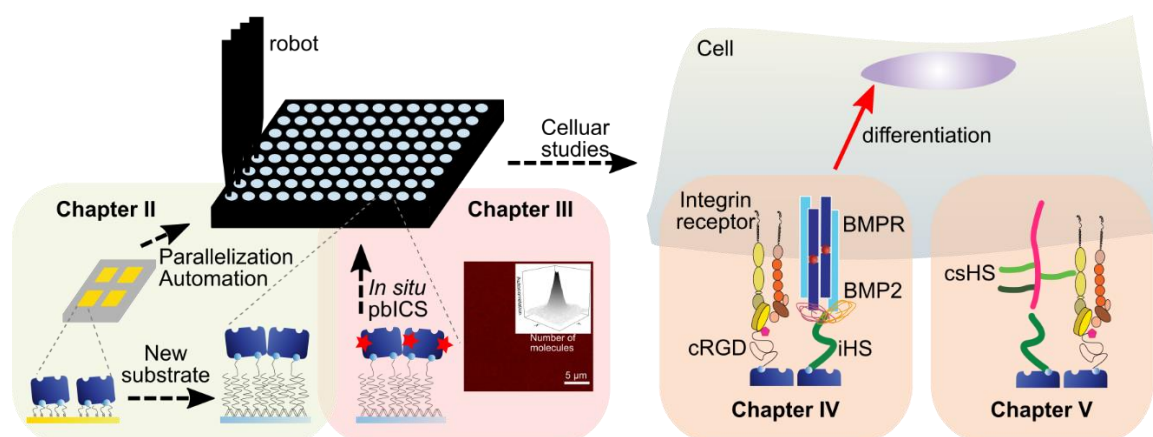


Figure 30: Schematic of the four objectives addressed in this PhD project.

Chapter II: Automated fabrication of biomimetic streptavidin platforms for high quantity analysis of cellular response to growth factors

II.A Article summary (English)

The ECM provides structure to embedded cells, regulates adhesion and mechanotransduction and serves as a reservoir for GFs. HS is abundantly present in the ECM and binds BMPs, which are known to participate in bone regeneration, cancer, iron metabolism and cell differentiation in general (Ruppert, Hoffmann and Sebald, 1996; Obradovic Wagner *et al.*, 2010; Sarrazin, Lamanna and Esko, 2011). Further, GF signaling and integrin-mediated signaling interact with each other (Ivaska and Heino, 2011). To study this environment, sophisticated model systems are needed, which can represent this complexity while providing a high degree in flexibility and parallelization (Monteiro A., Kollmetz and Malmström, 2018). Usually, miniaturized approaches come along with high-content potential but lack complexity and flexibility whereas complex models bring time-consuming fabrication and low parallelization. The SA_v platform was developed to co-present different biotinylated molecules of interest such as adhesion ligands, GAGs and GFs to mimic the natural environment of cells (Migliorini *et al.*, 2014, 2017; Thakar *et al.*, 2017). So far, these precisely characterized and versatile platforms are build-up on gold-sputtered glass coverslips and attached to custom-made supports, which rendered them unsuitable for high-content studies. In this article, we aim at developing a protocol to build-up SA_v platforms on glass surfaces on the bottom of standardized 96-well plates, which then allows to automate its fabrication with a liquid handling robot (Machillot *et al.*, 2018).

To allow conclusions on the role of molecules on cell fate, biomaterials need to be well characterized for homogeneity and molecular surface density. Surface sensitive techniques as QCM-D or SE provide precise measures for surface density but don't reveal information about the lateral distribution (Migliorini, Weidenhaupt and Picart, 2018). As many other techniques, they rely on specific substrates compatible with the technique, which does not allow *in situ* characterization inside 96-well plates. Fluorescence-based methods, as for example typical epifluorescence or confocal microscopy, can be applied on 96-well plates, but these techniques are only semi-quantitative (Coffman and Wu, 2012; Verdaasdonk, Lawrimore and Bloom, 2014). Image correlation spectroscopy (ICS) quantifies the number of fluorescent-labelled molecules by calculating the ACF of confocal images (Petersen *et al.*, 1993). This technique is occasionally applied to measure the number of proteins involved in processes at the cell membrane but not known for biomaterial characterization. We intend to characterize SA_v platforms fabricated by a liquid handling robot using ICS *in situ* and compare results to *ex situ*

characterization with QCM-D and SE. As a proof of concept for high content studies, we aim at functionalizing a whole 96-well plate with iHS and aBMP2, aBMP4, aBMP6 and aBMP7 at different concentration to study early BMP response *via* SMAD1/5/9 phosphorylation.

We identified PLL-g-PEGbiotin50% as a suitable linker between activated glass surfaces and SAV. SAV pre-mixed with the cell adhesion ligand cRGD in the stoichiometric ratio 3:4 bound to PLL-g-PEGbiotin50%, measured with QCM-D and SE (Huang *et al.*, 2002; Zhen *et al.*, 2004). iHS occupied to the remaining binding sites and aBMPs adsorbed to iHS to present a complex and biomimetic condition to cells. Imaging whole wells functionalized with SAVAlexa555 or SAV and biotin Atto565 (bAtto565) with automated microscopy revealed a homogeneous fabrication of the platforms by the developed automated liquid handling protocol. With pbICS, we measured $336 \pm 34 \text{ ng/cm}^2$ SAVAlexa and $0.79 \pm 0.19 \text{ ng/cm}^2$ of the small molecule bAtto565, which was chosen as a model for biotinylated molecules. Based on acquisitions at five different positions over the well we concluded homogeneous molecular distribution throughout the well. The areal mass density of SAVAlexa acquired with SE was $252 \pm 32 \text{ ng/cm}^2$ but bAtto565 was not detectable. The difference between pbICS and SE was explained by different substrates altering PLL-g-PEGbiotin50% adsorption.

C2C12 cells adhered homogeneously over the whole surface and responded equally to BMP2 presented *via* iHS at different positions. We then adapted the concentration of BMP2, BMP4, BMP6 and BMP7 in a way that they equally adsorbed to iHS and prepared serial dilutions to identify EC₅₀ values for aBMP adsorbed to iHS based on their bioactivity. We observed, that BMP2 was 10 times more active than BMP4, BMP6 and BMP7 regarding SMAD1/5/9 phosphorylation.

In summary, we developed an automated and flexible liquid handling protocol to fabricate different biomimetic SAV platforms upon user demand inside standardized 96-well plates. For the first time, we characterized biomaterials for molecular surface density *in situ* with pbICS and provided a proof of concept for high-content studies. In the future, this approach can serve to systematically reveal the role of GFs and/or other bioactive proteins in cellular mechanisms.

II.B Article summary (French)

La ECM fournit une structure aux cellules incorporées, régule l'adhésion et la mécanotransduction et sert de réservoir pour les GFs. Le HS est abondamment présent dans l'ECM et se lie aux BMP, qui sont connus pour participer à la régénération osseuse, au cancer, au métabolisme du fer et à la différenciation cellulaire en général (Ruppert, Hoffmann et Sebald, 1996 ; Obradovic Wagner et al., 2010 ; Sarrazin, Lamanna et Esko, 2011). De plus, la signalisation GF et la signalisation médiée par les intégrines interagissent entre elles (Ivaska et Heino, 2011). Pour étudier cet environnement, des systèmes modèles sophistiqués sont nécessaires, qui peuvent représenter cette complexité tout en offrant un haut degré de flexibilité et de parallélisation (Monteiro A., Kollmetz et Malmström, 2018). Habituellement, les approches miniaturisées sont accompagnées d'un potentiel de contenu élevé mais manquent de complexité et de flexibilité, tandis que les modèles complexes nécessitent une fabrication longue et une faible parallélisation. La plateforme SAV a été développée pour coprésenter différentes molécules biotinylées d'intérêt telles que des ligands d'adhésion, des GAG et des GF pour imiter l'environnement naturel des cellules (Migliorini et al., 2014, 2017 ; Thakar et al., 2017). Jusqu'à présent, ces plateformes polyvalentes et caractérisées avec précision sont construites sur des lamelles de verre frittées à l'or et fixées à des supports sur mesure, ce qui les rendait inadaptées aux études à haut contenu. Dans cet article, nous visons à développer un protocole pour construire des plateformes SAV sur des surfaces en verre au fond de plaques 96 puits standardisées, ce qui permet ensuite d'automatiser leur fabrication avec un robot de manipulation de liquides (Machillot et al., 2018).

Pour permettre des conclusions sur le rôle des molécules sur le destin cellulaire, les biomatériaux doivent être bien caractérisés pour leur homogénéité et la densité de surface moléculaire. Les techniques sensibles à la surface telles que QCM-D ou SE fournissent des mesures précises de la densité de surface mais ne révèlent pas d'informations sur la distribution latérale (Migliorini, Weidenhaupt et Picart, 2018). Comme beaucoup d'autres techniques, elles reposent sur des substrats spécifiques compatibles avec la technique, ce qui ne permet pas une caractérisation *in situ* à l'intérieur de plaques à 96 puits. Les méthodes basées sur la fluorescence, comme par exemple l'épifluorescence typique ou la microscopie confocale, peuvent être appliquées sur des plaques à 96 puits, mais ces techniques ne sont que semi-quantitatives (Coffman et Wu, 2012 ; Verdaasdonk, Lawrimore et Bloom, 2014). La spectroscopie de corrélation d'images (ICS) quantifie le nombre de molécules marquées par

fluorescence en calculant l'ACF des images confocales (Petersen et al., 1993). Cette technique est occasionnellement appliquée pour mesurer le nombre de protéines impliquées dans des processus au niveau de la membrane cellulaire mais n'est pas connue pour la caractérisation de biomatériaux. Nous avons l'intention de caractériser les plateformes SAV fabriquées par un robot de manipulation de liquide en utilisant ICS *in situ* et de comparer les résultats à la caractérisation *ex situ* avec QCM-D et SE. Comme preuve de concept pour des études à haut contenu, nous voulons fonctionnaliser une plaque entière de 96 puits avec de l'iHS et de l'aBMP2, aBMP4, aBMP6 et aBMP7 à différentes concentrations pour étudier la réponse précoce de BMP *via* la phosphorylation SMAD1/5/9.

Nous avons identifié PLL-g-PEGbiotin50% comme un lieu approprié entre les surfaces de verre activées et SAV. SAV pré-mélangé avec le ligand d'adhésion cellulaire cRGD dans le rapport stoechiométrique 3:4 s'est lié à PLL-g-PEGbiotin50%, mesuré avec QCM-D et SE (Huang et al., 2002 ; Zhen et al., 2004). iHS a occupé les sites de liaison restants et aBMPs adsorbé à iHS pour présenter une condition complexe et biomimétique aux cellules. L'imagerie de puits entiers fonctionnalisés avec SAVAlexa555 ou SAV et biotine Atto565 (bAtto565) avec la microscopie automatisée a révélé une fabrication homogène des plateformes par le protocole automatisé de manipulation des liquides développé. Avec pbICS, nous avons mesuré 336 ± 34 ng/cm² de SAVAlexa et $0,79 \pm 0,19$ ng/cm² de la petite molécule bAtto565 - qui a été choisie comme modèle pour les molécules biotinylées. Sur la base d'acquisitions à cinq positions différentes sur le puits, nous avons conclu à une distribution moléculaire homogène dans tout le puits. La densité de masse surfacique de SAVAlexa acquise avec SE était de 252 ± 32 ng/cm² mais bAtto565 n'était pas détectable. La différence entre pbICS et SE s'explique par le fait que les différents substrats modifient l'adsorption de PLL-g-PEGbiotin50%.

Les cellules C2C12 ont adhéré de manière homogène sur toute la surface et ont répondu de la même manière à la BMP2 présentée *via* l'iHS à différentes positions. Nous avons ensuite adapté la concentration de BMP2, BMP4, BMP6 et BMP7 de façon à ce qu'ils s'adsorbent de manière égale sur l'iHS et avons préparé des dilutions en série afin d'identifier les valeurs EC₅₀ pour les BMP adsorbées sur l'iHS en fonction de leur bioactivité. Nous avons observé que BMP2 était 10 fois plus active que BMP4, BMP6 et BMP7 en ce qui concerne la phosphorylation de SMAD1/5/9.

En résumé, nous avons développé un protocole de manipulation liquide automatisé et flexible pour fabriquer différentes plateformes SAV biomimétiques à la demande de l'utilisateur

dans des plaques 96 puits standardisées. Pour la première fois, nous avons caractérisé les biomatériaux pour la densité de surface moléculaire *in situ* avec pbICS et fourni une preuve de concept pour les études à haut contenu. À l'avenir, cette approche pourra servir à révéler systématiquement le rôle des GF et/ou d'autres protéines bioactives dans les mécanismes cellulaires.

II.C Article 1 (ready for submission to ACS Applied Materials and Interfaces)

Automated fabrication of biomimetic streptavidin platforms for high-content analysis of cellular response to growth factors

Julius Sefkow-Werner^{1,2}, Jean Le Pennec², Paul Machillot², Bertin Ndayishimiye², Elaine Castro-Ramirez², Joao Lopes², Christophe Licitra³, Irene Wang⁴, Antoine Delon⁴, Catherine Picart^{2*}, Elisa Migliorini^{2*}

¹Univ. Grenoble Alpes, CNRS, Grenoble INP**, LMGP, 38000 Grenoble, France

²Univ. Grenoble Alpes, CEA, INSERM, CNRS, ERL 5000, Grenoble, France

³Univ. Grenoble Alpes, CEA, Leti, F-38000 Grenoble, France

⁴Univ. Grenoble Alpes, CNRS, LiPhy, Grenoble, France

*Co-Corresponding authors

Migliorini Elisa, 17 rue des Martyrs 38016 GRENOBLE

Tel : (33)-04 56 52 93 24

Email :

elisa.migliorini@cea.fr

catherine.picart@cea.fr

** Institute of Engineering Univ. Grenoble Alpes

Abstract

The automation of biomaterials fabrication offers great potential for fast, reproducible and labor reducing biomaterials fabrication but also requires special protocol development. Competitive systems demand for a high degree in miniaturization and parallelization while maintaining flexibility regarding the experimental design. Few groups succeeded to apply automated protocols inside standardized multi-well plates to present a biomaterial to cells but experimental conditions were subsequently prepared manually or linked with elaborate processes and low flexibility. We have previously demonstrated that streptavidin-based biomimetic platforms can be employed to study the interface between the extracellular matrix and mammalian cells by immobilization of biotinylated molecules. So far, this versatile and flexible approach imposed limits for high-content studies due to the need of manual pipetting and frequent change of experimental conditions. We introduce for the first time a fully automated and adaptable workflow to functionalize glass-bottom multi-well plates with customized streptavidin-based biomimetic platforms using a liquid handling robot and combine

it with automated image acquisition and analysis. Platforms were characterized *in situ* for molecular surface density using fluorescence-based image correlation spectroscopy. We measured a densely packed and homogeneous streptavidin monolayer with $336 \pm 34 \text{ ng/cm}^2$, in agreement with standard *ex situ* spectroscopic ellipsometry measurements. C2C12 cells adhered and responded homogeneously to bone morphogenetic protein 2 (BMP2) presented *via* its natural ligand heparan sulfate (HS). With the automated protocol we functionalized a full 96-well plate presenting BMP2,4,6 and 7 in five different concentrations soluble and adsorbed to immobilized HS to study the effect of HS on different BMPs bioactivity. The high flexibility makes our approach a powerful candidate to investigate the role of ECM components on cell signaling by developing a large variety of biomimetic surfaces.

Introduction

Biomimetic approaches gain influence in the design and fabrication of biomaterials for biomedical applications such as tissue repair and drug screening or in fundamental research when studying the interface between cells and their surrounding extracellular matrix (ECM) [1], [2].

Biomimetics in cellular studies means to model the natural environment of cells as precisely as possible, notably mimicking their surrounding ECM regarding its molecular composition [3] and physical properties [4]. These models help for example to reveal synergies between the ECM components and growth factors (GFs) which influence cellular fate [5], [6]. Also spatial proximity between cellular adhesion ligands and GFs [7] as well as matrix elasticity [4] or topography [8] play a role in cell signaling. Various biomaterials to study these parameters in 2D and 3D were extensively reviewed and each of them helps to respond to a specific need [7], [9]–[11].

Due to high complexity of the ECM models and the need for flexibility in biomaterial design for fundamental research, most of the workflow from fabrication to data analysis is manual and thus time-consuming [12]. This makes these approaches less suitable for high-content studies, which on the other hand gain popularity and influence for biomaterial and drug screening. Vasilevich et al. predicted a rising involvement of robotics and automation covering almost the integral workflow of an experiment [13]. The researcher would formulate a precise question, later recover the desired biomaterial and present data to the scientific community,

while the central robot takes over the experimental design, biomaterial fabrication, cell culture and data analysis. Those ideas are still in the far future but a present review summarizes to what extent automation is already implemented in research laboratories related to biomimetic disease modelling and thus enabling high-content studies [14]. Soft lithography or micro contact printing is suitable to achieve a high degree of parallelization and miniaturization by creating PDMS microwells [15], which can further include bioactive compounds [16]. The degree of flexibility however is limited due to the time-consuming design and fabrication of new masks. Other techniques suitable to build high complexity platforms are bio-printers and liquid handling robots, which produce spatially controlled 3D structures or take over repetitive liquid handling typically performed by manual pipetting respectively. Additionally to the advantage of saving manual labor time, a study shows that manual pipetting accuracy depends on the individual operator and thus decreases data reproducibility [17], [18].

Standardized multi-well plate systems with for example 96 wells offer a degree of miniaturization, which reduces the amount of precious cells and expensive molecule consumption per condition while still providing sufficient sample volume and thus are adopted for automated biomaterial fabrication [14]. They are commercially available in different versions and compatible with common laboratory equipment, such as liquid handling robots, multichannel pipettes, plate readers and microscopes. This makes them candidates for automation over the whole experimental workflow from fabrication, data acquisition and treatment [18]–[21]. Examples of liquid handling robots in industry [22] or of automated cell culture [23] demonstrate the broad application potential and interest of this technology. Regarding biomaterial fabrication, Brooks et al. describes the fabrication of 2D and 3D hydrogels on glass using a liquid handling robot inside 96-well plates and further immobilized ECM proteins [20]. Machillot et al. built-up a polyelectrolyte multilayer film inside 96-well plates for cellular studies by executing iterative cycles of incubation and rinsing of the three involved electrolytes using a liquid handling robot [18]. This assured high reproducibility between the equally functionalized wells and plates but the loading of bone morphogenetic proteins (BMPs) in different concentrations was still done by hand. Sales et al. further automated the workflow of this system by applying automated microscopy and automated image analysis to perform a high-content screening of cell adhesion and response to BMPs [19]. While the previous approaches succeed to combine complex biomaterials and high-content studies using 96-well plates, an automated, simple and flexible workflow for the discrete

treatment of single wells with typical liquid handling operations is not yet developed despite a solution specifically adapted for automated fabrication of hydrogels [21].

The precise characterization of the functionalization of biomaterials inside the 96-well plates (*in situ*) presented to cells is crucial. For 2D platforms, surface sensitive techniques as quartz crystal micro balance with dissipation monitoring (QCM-D) or spectroscopic ellipsometry (SE) among others track and measure binding events and the surface density of molecules build-up on model-substrates *ex situ* [24]–[27]. This suits well to design and optimize new experimental conditions but a quantitative characterization *in situ* is, so far, not possible. Fluorescence microscopy reveals only relative intensity changes between different conditions based on labeled molecules of interest [28], [29]. Image correlation spectroscopy (ICS), part of the fluorescence fluctuation spectroscopy (FFS) family [30], is applied for cellular studies [31] but not used for biomaterial characterization. It works with highly resolved fluorescent images of labeled molecules of which the spatial autocorrelation function is calculated. The spatial autocorrelation reveals intensity fluctuations and its amplitude indicates the number of molecules per point spread function (PSF). This approach was so far limited in precision if the number of fluorescence labels per molecule is not precisely known [32], which is the case for large commercially available labeled proteins. Our group further developed this method by combining it with a photo bleaching routine to estimate the average number and distribution of labels per molecule and to increase the precision of the measurement by up to 20% [33].

We previously developed a biomimetic platform based on a streptavidin (SAv) monolayer, build-up on gold-sputtered glass surfaces [27]. SAv is commonly used for analytical assays or as antibody conjugate and for biochemical studies of molecular interactions [34]. The high affinity and specificity between SAv and biotin permits to immobilize biotinylated molecules of interest in a highly controlled manner to reveal their specific role on cell fate. Recently, we co-presented biotinylated cRGD peptide for the specific activation of β_3 integrins together with the biotinylated glycosaminoglycan (GAG) HS (iHS), the natural ligand of the osteoinductive bone morphogenetic protein 2 (BMP2) [35]–[37]. BMPs play a role in various biological processes throughout the body [38]. BMP2 is mainly involved in the development of the musculoskeletal system, BMP4 regulates cancer, BMP6 is taking part in the ion metabolism and BMP7 participates fat cell differentiation [6]. Nevertheless, the effect of the HS is only partially explored [35],[39]–[41] and the distinction between endogenous cell surface HS and exogenous HS as part of the ECM rarely considered. Regarding exogenous HS, we examined

the synergy between integrins, iHS and BMP2 adsorbed on iHS (aBMP2) *via* cell adhesion and BMP2 signaling. cRGD upregulated BMP2 mediated signaling and osteogenic differentiation of C2C12 myoblasts and iHS sustained the BMP-SMAD signal for longer time than conditions where BMP2 was presented immobilized on the surface without HS [35]. Nevertheless, comparable data for the role of HS on BMP4, 6 and 7-mediated SMAD signaling is not yet published.

In this work, we present for the first time the automated fabrication of customized biomimetic SA_v platforms on glass bottom 96-well plates to study cellular responses to GF-presentation *via* HS. The discrete functionalization of each single well of the 96-well plates and the analysis of cellular readouts is fully automated using a liquid handling robot, automated image acquisition and analysis (**Figure 1**). The custom made graphical user-interface permits the operator to individually assign different biomimetic SA_v platforms to discrete wells of choice and to enter experimental parameters in minutes. A SA_v monolayer binds *via* an intermediate PLL(20)-g[3.5]-PEG(2)/PEGbiotin(3.4)50% layer (PLL-g-PEGbiotin50%) [42]–[44] to the glass surface of a 96-well plate and offers free biotin binding sites for biotinylated molecules. We co-present the adhesion peptide cRGD together with the glycosaminoglycan HS to promote cellular adhesion and to present GFs as *in vivo*, respectively. The automated approach allows us to simultaneously study different concentrations of BMP2, BMP4, BMP6 and BMP7 adsorbed on HS and in soluble condition to study SMAD1/5/9 phosphorylation of BMP responsive C2C12 mouse myoblasts [19], [45], [46]. With QCM-D and SE, we characterize these biomimetic platforms *ex situ* and we apply ICS *via* confocal fluorescence microscopy images *in situ* for molecular surface density quantification and homogeneity analysis.

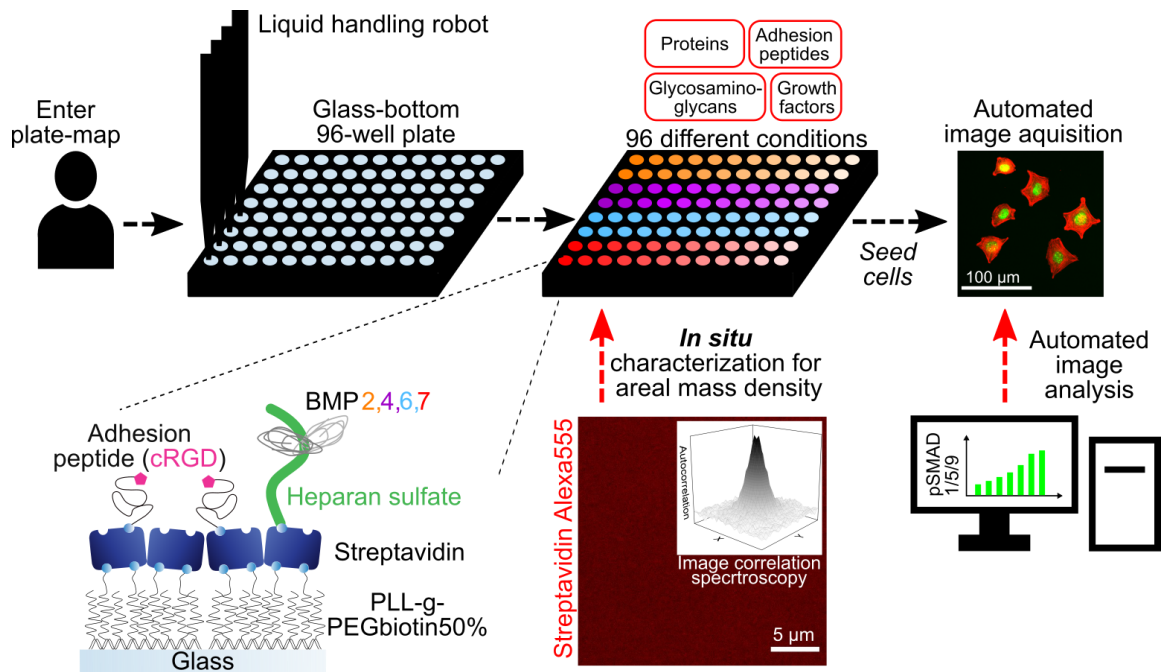


Figure 1: Schematic of automated platform fabrication, surface characterization and cellular studies. A user communicates the plate-map corresponding to the experimental plan to the liquid handling robot. Glass bottom 96-well plates are then automatically functionalized with different biomimetic platforms co-presenting cellular adhesion ligands, glycosaminoglycans and growth factors. In this work, streptavidin binds to the linker PLL-g-PEGbiotin50%. Then, biotinylated cRGD and biotinylated heparan sulfate bind to streptavidin and BMP2,4,6 or 7 adsorb to heparan sulfate. The areal mass density of fluorescence labelled molecules such as StreptavidinAlexa555 is characterized *in situ* using image correlation spectroscopy. Cells are seeded on the platforms for biophysical assays using automated images acquisition and automated image analysis to quantify for example BMP-mediated SMAD1/5/9 phosphorylation inside the nucleus.

Methods

Buffers and molecules

10 mM Hepes working buffer (Sigma Aldrich, France) at pH 7.2 with 150 mM NaCl (Sigma Aldrich, Saint-Quentin Fallavier, France) was used for dilution and rinsing of all molecules if not further specified. PLL(20)-g[3.5]-PEG(2)/PEGbiotin(3.4)50% (PLL-g-PEGbiotin50%, ~107 kDa, SuSoS AG) consists of a Poly-L-Lysine backbone (~ 20 kDa, ~ 100 monomers) with one PEG chain (2 kDa) or one PEG biotin chain (3.4 kDa) grafted to one of 3.5 PLL monomers in a 50% ratio. Stock solution (10 μM) was stored at 4 °C for up to 2 months and diluted to 100 nM upon use. Details for SA_v (SA_v, 55 kDa, Sigma Aldrich), biotinylated cyclic RGD pentapeptide (cRGD, 3.9 kDa) and biotinylated HS (iHS, 12 kDa) can be found in previous works [35], [47]. BiotinAtto565 (bAtto, 922 Da, Sigma Aldrich). Streptavidin Alexa Fluor® 555 conjugate (SA_vAlexa, ~55kDa, Molecular probes) was used for ICS studies and

homogeneity analysis. For some conditions, SAV or SAVAlexa were pre-bound to cRGD at a molar ratio of 3:4 and incubated for 30 min before binding to PLL-g-PEBbiotin50% on the surface. BMP2 (26 kDa, R&D Systems Inc., USA), BMP4 (24 kDa, Peprotech, France), BMP6 (30 kDa, R&D Systems Inc., USA) and BMP7 (26 kDa, Olympus Biotech, France) were serial-diluted to reach the concentrations to bind to iHS or to be added to the cell media.

Surface functionalization

For *ex situ* characterization, biomimetic platforms were built up either on silicon dioxide (SiO₂) crystals (QSX 303, Biolin scientific, Sweden) for QCM-D measurements and on thermally oxidized silicon wafers with 60 nm SiO₂ for SE analysis. For *in situ* characterization and cellular studies glass bottom 96-well plates (Grainer bio-one, Germany) were used. Substrates were UV/ozone activated (UV/Ozone ProCleaner Plus, Bioforce) for 10 min to clean and charge the surface. To interact with the substrates, molecules subsequently flowed inside a liquid chamber for crystals (QCM-D) and wafers (SE) or were pipetted by the liquid-handling robot (Evo 100, Tecan) in case of 96-well plates with the concentrations mentioned in **Table 1**.

Ex situ characterization with quartz crystal micro balance with dissipation monitoring (QCM-D)

With QCM-D (QSense Analyzer, Biolin scientific, Sweden) binding events of the sequential buildup of the biomimetic platform were measured on auxiliary SiO₂ coated QCM-D crystals *ex situ*. In case the film was sufficiently rigid, the adsorbed mass was calculated with the Sauerbrey equation, a linear relationship between the change in resonance frequency Δf_n and the mass for different overtones n (1),

$$\Delta f_n = -\frac{n}{c} m_f \quad (1)$$

C is a material constant based on material properties and the fundamental resonance frequency of the crystal and m_f is the areal mass density. This mass represents the sum of adsorbed compound and coupled solvent. Dissolved molecules in the concentrations stated in **Table 1** passed through the liquid chamber *via* a peristaltic pump with 15 μ l/min (IPC4, Ismatec, Germany) followed by rinsing with HEPES as described in more detail elsewhere [5].

The measured time for a molecule to saturate on the surfaces indicated the incubation time used for each molecule when building-up the biomimetic platforms inside 96-well plates.

Ex situ characterization with spectroscopic ellipsometry (SE)

We used SE (RC2, J.A. Woollam, USA) complementary to QCM-D to measure the mass of molecules of the biomimetic platform *ex situ* on auxiliary silicon wafers covered with 60 nm thermal SiO₂. Due to optical constraints, it was not possible to use amorphous glass surfaces as in 96-well plates. A peristaltic pump (IPC4, Ismatec, Germany) pumped the molecules or the rinsing buffer with 100 μl/min into the liquid chamber (500 μl liquid cell, J.A. Woollam), which was tightly screwed on the wafer.

SE measures the change of the ellipsometric angles Ψ and Δ of polarized light upon changes of the refractive index and thicknesses of optical layers [48]. We measured the SiO₂ layer in buffer and fitted its thickness and the angle of incidence offset based on the known optical properties of thermal SiO₂ with the WOOLLAM model SIO₂_JAW3 on a fixed 1 nm Intr_JAW3 layer to account for the SiO₂/Si interfacial layer [49]. The refractive index for the Hepes buffer was modeled with a Cauchy dispersion law with parameters A set to 1.324, B set to 0.00322 and C set to 0 [50]. Molecular adsorption to this base substrate was then modelled using a Cauchy layer where thickness and parameter A were fitted. B was set to 0.00322 and C to 0 [51]. The areal mass density was calculated using the De Feijter equation (2)

$$M = d_A \frac{A_A - A_C}{dn/dc} \quad (2)$$

with d_A as the fitted thickness of the adsorbed layer, A_A its fitted Cauchy parameter A and A_C the Cauchy parameter of the ambient buffer [52]. The corresponding refractive index increments dn/dc relative to water for each molecule were 0.18 (SA_v, SA_vAlexa, SA_v/cRGDmix) and 0.158 (PLL-g-PEGbiotin50%, bHS) [42].

Automated liquid handling

The liquid handling robot was used to fabricate different biomimetic platforms at the bottom of the wells of a 96-well plate. First, the user entered the experimental design of the 96-well plate into a custom-made graphical user interface, defining the corresponding wells and

incubation time for each molecule and their position in the compound rack. Each well can thus represent a different biomimetic platform or replicates of those. Then, molecule solutions in their adjusted concentrations (**Table 1**) based on QCM-D measurements and rinsing buffer were placed into racks and up to three UV/ozone-activated 96-well plates were put on the plate carrier.

The operating software of the liquid handling robot executed a custom-made script with the user-entered parameters well selection_n and incubation time_n for each molecule *n* as input. For each of the defined molecules an iterative cycle was run:

1. Aspiration of storage buffer from wells_n to empty the wells
2. Aspiration of solution_n from compound rack position_n and dispense of 60 µl inside well selection_n
3. Waiting for incubation time_n
4. Rinsing wells_n *via* five loops of dispense and aspiration of rinsing buffer

Horizontal tilting of the plate by 30° during all aspiration steps assured precise aspiration and was previously shown to improve homogeneity of layer-by-layer films [18]. To incubate molecules that have identical incubation times the user could force the script to skip rinsing loops of those molecules, incubate them all at once in parallel and rinse them together after the common incubation timer has finished. PLL-g-PEGbiotin50% and biotinylated molecules were incubated much longer than measured since incubation inside wells is static and not under flow as in QCM-D. BMP incubated as long as measured in QCM-D. Plates were then ready for cellular studies and were always used the same day.

In situ characterization inside 96-well plates with image correlation spectroscopy (ICS)

A fluorescence-based approach was used to quantify the homogeneity of glass bottom 96-well plates functionalized by the robot as well as to measure the areal mass density of different components of the biomimetic platform. SAvAlexa replaced SAV and bAtto served as a representative molecule for the binding of functional biotinylated molecules to SAV.

Wells were functionalized by the robot with PLL-g-PEGbiotin50% followed by either SAvAlexa, SAvAlexa/cRGDmix or SAV and subsequently bAtto in the latter case. The plate was imaged *in situ* with an automated image acquisition system (InCell Analyzer 2500, 20x,

Molecular Devices) for qualitative defect-characterization in the macroscale. These immunofluorescence images of the whole well were further treated to remove artefacts due to uneven illumination or optical constraints. An average image based of at least 20 images not touching the well's border was calculated to represent the acquisition bias. All images of this well were then divided by this average image and in a next step stitched together for a 96-well montage. Intensities were analyzed along a vertical and horizontal line.

To quantify the areal mass density of SAvAlexa and bAtto, a series of ten acquisitions at five different positions throughout the well was taken with the Leica SP8 confocal microscope with a HC PL APO 63x/1.2 water-immersed objective. The focal plane was identified at maximum intensity, stabilized with automated focus control and a field of 25 μm x 25 μm with 512x512 pixel was imaged with 1% laser intensity at 561nm and 1.2 μs pixel dwell time. Images were then analyzed using the principle of ICS as described elsewhere ([32], [33]). In summary, the confocal images were split-up into 64 sub-images and the spatial autocorrelation function was calculated for each sub-image. This autocorrelation function reveals intensity fluctuations and its amplitude is inversely proportional to the number of molecules in the observation area [30]. The observation area is defined by the waist of the point spread function specific for each microscope and the used objective and ranges around 230 nm. An additional photo bleaching routine revealed the average number and distribution of fluorophores per molecule and was used to correct the number of molecules by the factor 1.2 for SAvAlexa and 1.09 for bAtto. Representative 63x images were equally contrast treated to retain relative intensity differences.

Cell culture

To study cellular compatibility of PLL-g-PEGbiotin50%-based biomimetic platforms, C2C12 mouse myoblasts (CRL-1772, ATCC, USA) were chosen as BMP-responsive reference cells [46]. They were cultured on tissue-treated polystyrene cell culture flasks in Dulbecco's modified Eagle's growth medium (DMEM, Gibco) supplemented with 10% heat-deactivated fetal bovine serum (FBS, PAA Laboratories, Toronto, Canada) and antibiotic-antimycotic (1%, Gibco) at 37 °C and 5% CO₂ [18]. Cells were passed at sub-confluence with Trypsin EDTA (Gibco) and discarded after 12 passages. Four hours prior to manual seeding onto biomimetic platforms inside 96-well plates, cells were serum starved with FBS-free growth media and then detached from the flask with Accutase (Sigma) and re-suspended in FBS-free growth media.

C2C12 cell adhesion and differentiation for microscopy analysis

To study cellular adhesion on biomimetic platforms *via* cell number, 31 000 serum starved C2C12 cells per cm² were plated on functionalized 96-well plates, incubated (37 °C, 5 % CO₂) and after 45 min nucleus-stained with 10 ng/ml Hoechst. Cells were imaged after 1 h with the Zeiss Axio Observer 7 epifluorescence microscope (Carl Zeiss Sas) and then rinsed with PBS to remove non-adherent cells before again imaging remaining cells at the same position. Nuclei were counted using an ImageJ plugin to calculate the percentage of adherent cells.

For the quantification of cellular area and the phosphorylation of SMAD1/5/9 translocated into the nucleus upon BMP2 stimulation, 31 000 serum starved cells per cm² were plated on functionalized surfaces and sBMP2,4,6,7 was added into the cell media in different concentrations. Cells were incubated (37 °C, 5 % CO₂), rinsed after 1 h 30 min with PBS and fixed with 4% paraformaldehyde. Nuclei membranes were permeabilized with 0.2% (w/v) Triton X-100 (Sigma-Aldrich) for 3 min and blocked with 3% BSA for 1 h. Primary rabbit anti-pSMAD1/5/9 (Cell Signaling Technology, Danvers, Ma, USA) diluted 1:400 in PBS and 3% BSA were incubated overnight at 4 °C. After rinsing, secondary goat anti-rat/rabbit Alexa Fluor 488 (Thermo Fischer Scientific), 1:500, F-actin Phalloidin-Rhodamine (Sigma-Aldrich), 1:1000 and DAPI, 1:1000, were incubated for 60 min in PBS and 3% BSA at RT. 2.5% (w/v) Dapco (Sigma-Aldrich) in PBS at pH=7.8 was used as anti-fade [35]. Cells were imaged with InCell Analyzer 2500 using the 20x objective on three channels and images were analyzed with automated image analysis software InCarta (General Electric) as previously described [19]: pSMAD1/5/9 intensity was measured only inside the nucleus under a mask defined by the DAPI signal and background subtracted for at least 50 cells per well.

Statistical Analysis and data treatment

For cell experiments, each condition was prepared as technical duplicate in two different wells and experiments were repeated in three biological replicates. Means were tested for statistical significance between different conditions with the non-parametric Mann-Whitney test with $p \leq 0.05$ and based on at least three biological replicates. To calculate the half-maximal effective concentration (EC₅₀), data was fitted with Origin using the dose response curve (4-parameter logistic model [53]). For the negative control, we assigned an auxiliary BMP concentration 10⁻⁴ times lower than the lowest BMP concentration instead of zero. The

coefficient of variation (CV) was used as a measure for the overall homogeneity of stitched full well immuno fluorescence images by dividing the standard deviation of its intensity by its mean intensity. Then, the homogeneity is expressed by the mean and standard deviation of the CV over three wells. To assess the reproducibility of the functionalization, the CV of the mean intensity of five confocal images per well of three wells and two independent plates was calculated.

Results

Ex situ characterization of biomimetic platforms on QCM-D crystals and SiO₂ wafers

To identify the concentration and the incubation times of each molecule needed to build-up a reproducible biomimetic platform, we followed the functionalization of the biomimetic platforms step-by-step on SiO₂ crystals with QCM-D. We call this characterization *ex situ* since it is performed on auxiliary substrates with respect to the characterization inside 96-well plates – even though the measurements were taken in real time during the course of incubation.

PLL-g-PEGbiotin50% saturated the surface after 30 min with an average frequency shift of -23.4 ± 2.9 Hz (**Figure 2 a**). A positive shift in dissipation of $2.8 \pm 0.3 \times 10^{-6}$ indicated a softening of the layer. SAV pre-coupled in solution with the cellular adhesion peptide cRGD at the molar ratio 3:4 saturated after 30 min, decreasing the frequency further by -31.1 ± 2.6 Hz. Zhen et al. [44] showed that the binding of SAV to PLL-g-PEGbiotin50% was increased when SAV was pre-linked with a biotinylated molecule, probably due to improved layer organization. iHS bound to the remaining biotin binding sites with -4.6 ± 1.3 Hz and BMP2 (192 nM) adsorbed specifically to iHS with -11.7 ± 2.8 Hz. About 50% of BMP2 was partly removed from iHS when rinsed until equilibrium was reached and we further measured that BMP2 bound only marginally and reversibly to the SAV/cRGDmix (**SI Fig 1 d**). BSA bound non-specifically to SiO₂ with 2.5 Hz but the passivation with PLL-g-PEGbiotin50% led to non-measurable BSA binding after all incubation steps (**SI Fig 1 c, e**). Biotinylated molecules bound as well to a plain SAV layer as seen *via* the example of iHS (**Figure 2 b**) and also a sequential functionalization of cRGD, iHS and aBMP2 was feasible but more difficult to control (**SI Fig 1 a**). It was

demonstrated that we could fabricate complex biomimetic surfaces presenting three different functional molecules.

We further observed that SiO₂ crystals aged from their third regeneration cycle, which lead to up to 25% higher molecule adsorption starting with PLL-g-PEGbiotin50% and propagating through the consecutive compounds (**SI Fig 1 a, b**). Data in **Figure 2** was acquired on new crystals while experiments in **SI Fig 1** were conducted on crystals regenerated at least 3 times.

We conclude that SAV/cRGD mix has the highest potential to bind further functional molecules and is the most practical and straightforward approach for automated platform fabrication since it more simple than incubating SAV and cRGD sequentially. **Table 1** lists the concentrations and incubation times based on the measurements with QCM-D and later used for functionalization with the liquid handling robot.

Table 1: Molecule concentrations and incubation times based on QCM-D measurements.

<i>Compound</i>	<i>Concentration (μg/ml)</i>	<i>Incubation time for sturation (min)</i>
PLL-g-PEGbiotin50%	10	45
Streptavidin (SAv)	10	30
Streptavidin Alexa555 (SAvAlexa)	10	30
SAv/cRGDmix 3:4 (SAv/cRGDmix) or SAvAlexa/cRGDmix 3:4 (SAvAlexa/cRGDmix)	10 (SAv or SAvAlexa) + 1 (cRGD)	30 min pre-coupling, then 45 for saturation
Biotinylated cyclic arginylglycylaspartic acid (cRGD)	0.25	4 min (partly saturated)
biotin Atto565 (bAtto)	10	30
Biotinylated heparan sulfate (iHS)	10	30
adsorbed BMP2,4,6,7 (aBMP2,4,6,7)	0.01 - 10	90-130
soluble BMP2,4,6,7 (sBMP2,4,6,7)	0.005 - 5	until cell fixation

We then characterized these platforms with SE on SiO₂-coated wafers to measure adsorbed mass of the immobilized compounds. PLL-g-PEGbiotin50% bound to glass with 119 ± 9 ng/cm², SAV then with 264 ± 6 ng/cm² and SAV/cRGDmix with 343 ± 25 ng/cm² (**Figure 2 c**). For further fluorescence-based *in situ* measurements we also quantified SAVAlexa binding with 253 ± 31 ng/cm² and SAVAlexa/cRGDmix with 315 ± 6 ng/cm² (**SI Fig 1 f**).

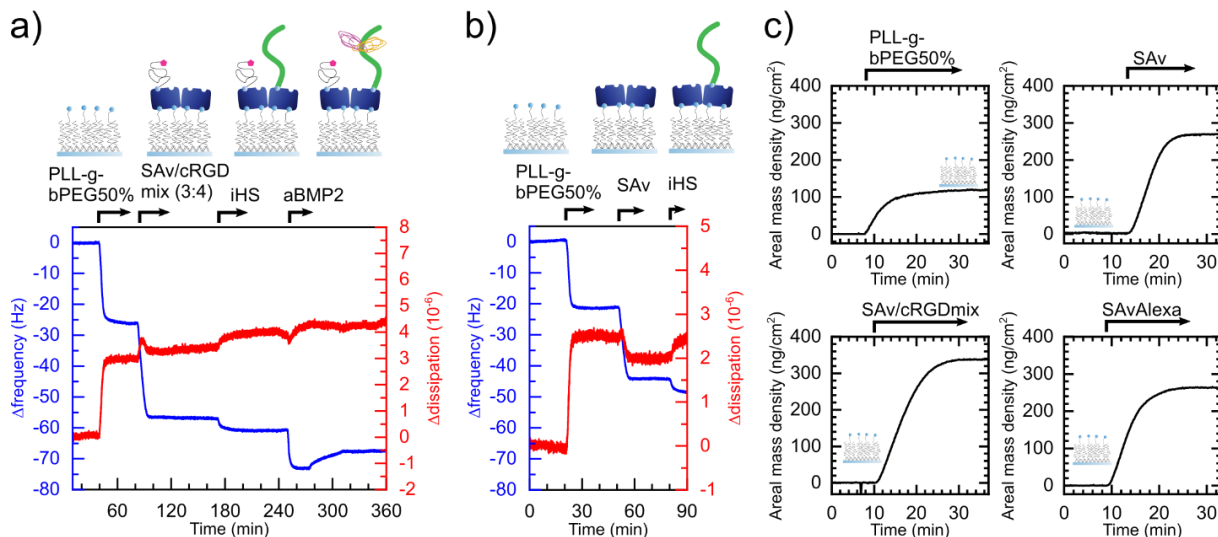


Figure 2: Ex situ QCM-D and SE characterization of sequential biomimetic platform functionalization
 a) QCM-D graph showing the frequency change and dissipation change upon the sequential buildup of a biomimetic platform on plasma activated SiO₂ crystals. SAV and cRGD were pre-coupled in solution with a molar ratio of 3:4 before binding to the PLL-g-PEGbiotin50% layer. Black arrows indicate periods of incubation followed by rinsing with buffer. b) Graph showing the change in frequency by SAV binding to PLL-g-PEGbiotin50% and iHS occupying the remaining biotin binding sites measured with QCM-D. c) Graph showing the change of the areal mass density of PLL-g-PEGbiotin50% binding to plasma activated SiO₂ wafers measured with SE (c, top left). Black arrows indicate time of incubation followed by rinsing with buffer. Areal mass density was calculated using the de Feijter equation (2) based on measured Δthickness and Δrefractive index. The other three panels show SAV, SAV/cRGDmix and SAVAlexa binding to PLL-g-PEGbiotin50%.

In situ characterization of biomimetic platforms fabricated by a liquid handling robot

Biomimetic platforms were fabricated inside glass bottom 96-well plates using a liquid handling robot (**Figure 1**). To characterize surface homogeneity and areal mass density *in situ* with fluorescent-based approaches, SAVAlexa was immobilized on PLL-g-PEGbiotin50%. The homogeneity of biotinylated molecules binding to SAV was tested by immobilizing bAtto on unlabeled SAV in a second incubation step. bAtto would bind to the free biotin pockets on SAV and therefore was chosen as a model for biotinylated functional molecules. As a third condition, we tested SAVAlexa bound to cRGD with the molar ratio of 3:4 before binding to PLL-g-PEGbiotin50%.

With QCM-D, we measured that SAVAlexa bound with a frequency shift of $-18.6 \text{ Hz} \pm 0.7 \text{ Hz}$ to the PLL-g-PEGbiotin50% layer, that is about 25% less than that of unlabeled SAV ($-24.7 \pm 2.2 \text{ Hz}$) (**SI Fig 2 a**); on the other hand, we observed a higher decrease in dissipation. Plotting both binding curves normalized to the time we observed that molecules saturated after an equivalent time. We thus chose SAVAlexa as a suitable molecule to study the SAV-base-layer

homogeneity. bAtto binding could not be measured by QCM-D and neither SE probably due to its low molecular weight and hence low adsorbed mass.

Stitched and shading-corrected 20x fluorescent images of wells acquired with the automated microscope show the global appearance of wells functionalized with the liquid handling robot (**Figure 3 a**). The body of all wells only presented few minor defects; however, in some cases artefacts, such as sickle-shaped black spots (white arrows) at the same place where the tips of the liquid handling robot touched the surface, were present close to the border of the well. Intensity measurements along a line from left to right and from top to bottom, both passing through the center (grey lines), visualize that SAvAlexa, SAvAlexa/cRGDmix and SAv+bAtto surfaces were uniform and reproducible over three different wells (**Figure 3 b**). Tight histograms of the montage of the stitched and shading corrected images further show that wells were reproducible and uniform (**SI Fig 2 b**). The CV based on intensity distribution of the full well images is in average 0.035 ± 0.007 for SAvAlexa, 0.062 ± 0.017 for SAvAlexa/cRGDmix and 0.073 ± 0.011 SAv+bAtto.

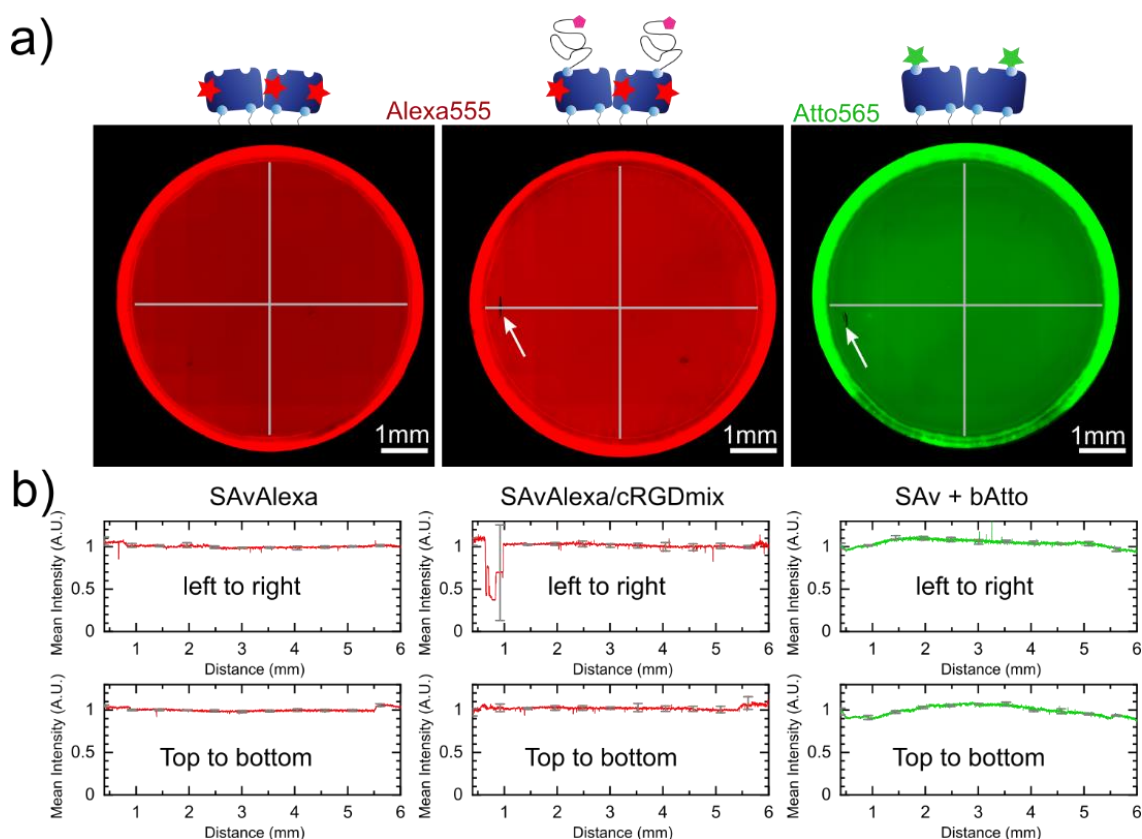


Figure 3: Homogeneity analysis of wells of a 96-well plate functionalized by the robot with PLL-g-PEGbiotin50%, SAvAlexa and bAtto a) Representative stitched and shading-corrected 20x IF images of whole wells presenting different surface functionalization, white arrow indicating the presence of artifacts due to pipetting tips touching the surface. b) Graphs showing the intensity quantification of stitched 96-well images along a line from left to right and top to bottom (n=3 wells, error bars=SD).

Representative 63x confocal images showed no systematic defects at the microscale (the size of a typical spread cell) (**Figure 4 a**). The grain-like structure was then compared to a simulated image based on the random placement of SAvAlexa-like fluorescence emitting entities, which showed a similar morphology (**SI Fig 3 a**).

Mean intensity comparison (count rate) over three wells per condition revealed a 15% higher signal of SAvAlexa/cRGDmix compared to SAvAlexa (**Figure 4 b**). The bAtto signal could not be compared due to the different fluorophore. The CV based on average intensities of five confocal images inside each of three different wells and two independent replicates was 0.04 for SAvAlexa, 0.07 for SAvAlexa/cRGDmix and 0.25 for bAtto.

To quantify the areal mass density of SAvAlexa and bAtto molecules at five different positions *in situ*, we applied ICS directly inside 96-well plates based on 63x confocal images. An exemplary autocorrelation function over the entire SAvAlexa image is represented in **Figure 4 c**. The 25x25- μm greyscale map exemplarily represents the areal mass densities of 64 sub-images for the SAvAlexa sample deduced from the corresponding autocorrelation functions (**Figure 4 d**). We applied ICS on the above-mentioned simulated image, which presents a similar theoretical molecular density and equal image size (**SI Fig 3 b-e**). We showed that fluctuations between the sub-images were similar for the simulated image by comparing their CV (**SI Fig 3 e**).

Through the absolute quantification of the adsorbed mass with ICS *in situ* at five different positions of the well we observed a homogeneous functionalization of SAvAlexa, SAvAlexa/cRGDmix and SAv + bAtto (**Figure 4 e**). SAvAlexa saturated the surface in average with $336 \pm 34 \text{ ng/cm}^2$ and the SAvAlexa/cRGDmix condition presented an average of $334 \pm 45 \text{ ng/cm}^2$. Then, $0.79 \pm 0.19 \text{ ng/cm}^2$ bAtto bound to SAv.

Compared to simple intensity measurements, ICS further revealed information about the fluorescence intensity per molecule, which revealed that SAvAlexa molecules bound to cRGD were brighter than plain SAvAlexa molecules. This might be explained by different spatial organization of these molecules on the surface with an impact on fluorophore efficiency, which didn't influence ICS analysis but biased relative intensity comparison between both conditions.

We conclude that surfaces fabricated by the liquid handling robot are homogeneous and that biotinylated functional molecules modelled *via* bAtto bind homogeneously on top. With ICS studies, we succeeded to measure the areal mass density of labeled molecules *in situ*.

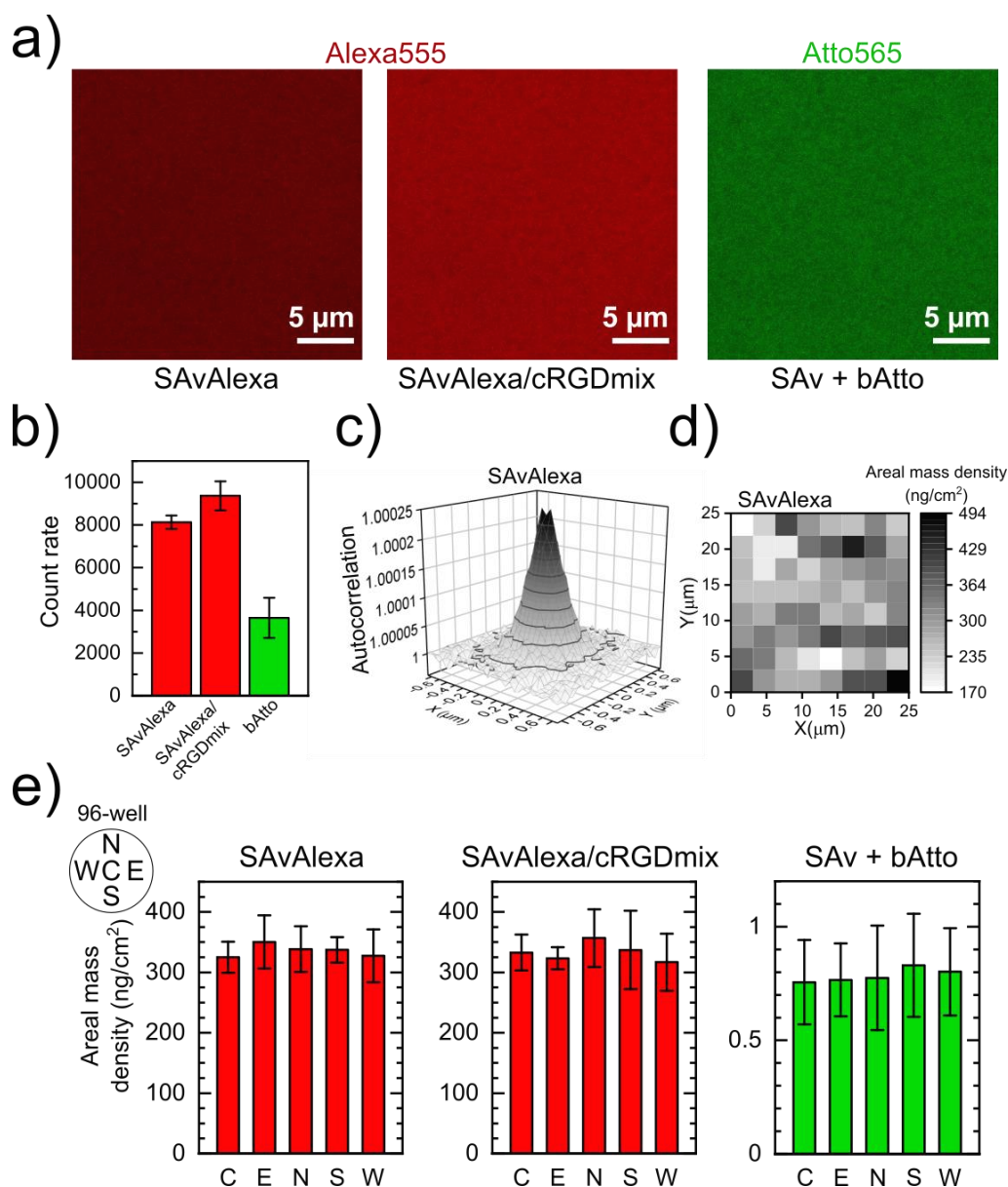


Figure 4: *In situ* characterization for areal mass density of SAvAlexa, SAvAlexa/cRGDmix and SAvAlexa + bAtto a) Representative 63x confocal images taken inside the wells. b) Graph showing the count rate quantification of 63x confocal images acquired at five positions inside each well (n=3 wells, error bars = SD). c) Exemplary spatial autocorrelation function calculated from the whole image to deduce the number of molecules *via* its amplitude. d) Representative greyscale map visualizing the areal mass density per sub-image (3.1x3.1 μm) measured *via* ICS. e) Graphs showing the areal mass density *via* ICS at five different positions per well (n=3 wells, 2 replicates, error bars = SD).

ICS derived areal mass densities were compared to complementary SE and QCM-D measurements summarized in **Table 2**. Because QCM-D derived masses include the mass of the solvent, masses were higher than the masses deduced from ICS and SE, which are based on the number of molecules or the thickness respectively. The mass of SAvAlexa is the only one directly comparable between both ICS and SE. ICS is the only technique to measure molecular

densities *in situ* inside 96-well plates without passing *via* auxiliary substrates as needed for SE or QCM-D. It is further sufficiently sensitive to measure very small densities as seen with bAtto.

Table 2: Comparison of QCM-D, SE and ICS to measure the areal mass density *ex situ* and *in situ*. The measured mass of SAvAlexa/cRGDmix for ICS presents only the SAvAlexa part whereas for QCM-D and SE the mass of the whole complex is measured. Values are given as mean and SD. ICS measurements were not possible on un-labelled molecules and QCM-D and SE were not sufficient sensitive to measure bAtto binding. QCM-D derived mass represents the sum of adsorbed molecule and solvent. Values are given as mean \pm SD over at least 3 replicates.

<i>Compound</i>	<i>Molecular weight(kDa)</i>	<i>Mass QCM-D (ng/cm²)</i>	<i>Mass SE (ng/cm²)</i>	<i>Mass ICS (ng/cm²)</i>
PLL-g-PEGbiotin50%	107	420 \pm 52	120 \pm 8.7	N.A.
SAv	55	444 \pm 41	263 \pm 6	N.A.
SAvAlexa	55	335 \pm 13	253 \pm 33	336 \pm 34
SAv/cRGDmix 3:4	N.A.	559 \pm 46	343 \pm 25	N.A.
SAvAlexa/cRGDmix	N.A.	N.A.	315 \pm 6	334 \pm 45
bAtto	0.922	N.A.	N.A.	0.79 \pm 0.19

Cellular adhesion and BMP2 signaling on biomimetic platforms in 96-well plates

To study the compatibility of biomimetic platforms fabricated by the liquid handling robot with cellular studies we measured C2C12 cell response inside 96-well plates. We quantified specific and homogeneous adhesion to cRGD as well as homogeneous BMP2-signaling.

While 86.6 ± 4.2 % of cells adhered to saturated cRGD and spread well, only 10.0 ± 0.1 % remained on bPEG-functionalized surfaces and remained round (**Figure 5 a**). A comparison of cellular adhesion between different positions throughout the well revealed no significant difference (**Figure 5 b**). We showed that C2C12 cells adhered specifically to cRGD and homogeneously over the whole surface (**Figure 5 b**).

Platforms functionalized with a sub-monolayer of cRGD and co-functionalized with iHS and aBMP2 (2.5 μ g/mL for 90 min) were fabricated and sBMP2 at 100 ng/ml was used as a control. Seeded cells were fixed after 1.5 h and F-actin, nucleus and pSMAD1/5/9 were stained to quantify BMP2 signaling. Cells still spread on platforms with the sub-saturated layer of cRGD with an area of 951 ± 9 μ m² and slightly more on the co-functionalized platform with 1009 ± 17 μ m² (Mean \pm SEM over three biological replicates).

We quantified homogeneous BMP2 response by analyzing pSMAD1/5/9 intensity at five positions throughout the surface (**Figure 5 c**). sBMP2 and aBMP2 equally induced SMAD1/5/9 phosphorylation with significant difference to the negative controls and the signal was evenly intense at the five different positions.

We conclude that C2C12 adhesion on PLL-g-PEGbiotin50% based platforms is specific to cRGD and that platforms sequentially buildup by the robot present the functional molecules cRGD, bHS and aBMP2 throughout the whole well.

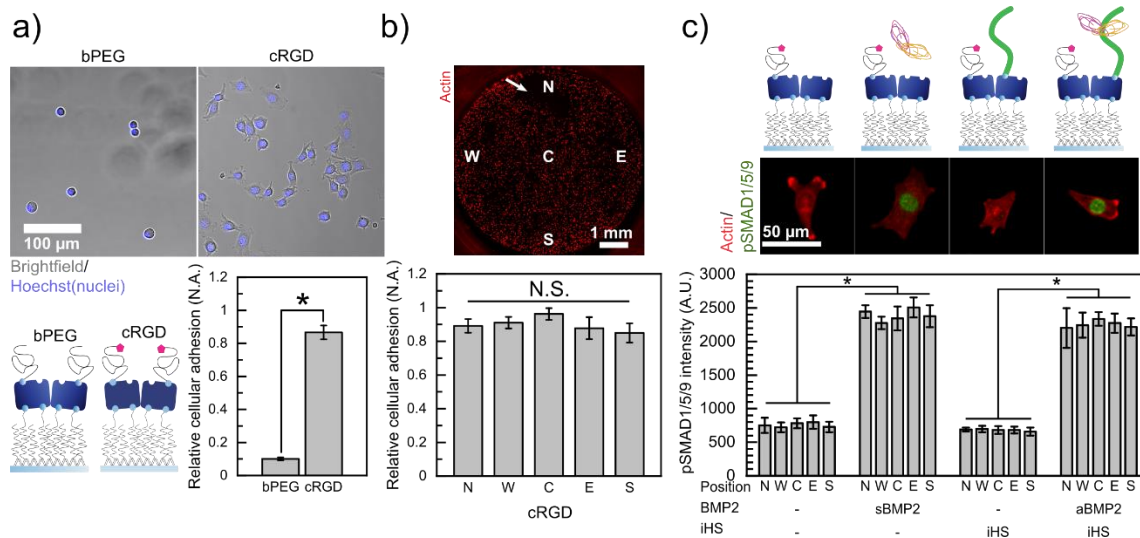


Figure 5: C2C12 cell adhesion to cRGD and BMP2-induced pSMAD1/5/9 signaling a) Representative bright-field images of C2C12 cells adhering to bPEG and cRGD with graph showing the corresponding quantification of relative cellular adhesion after rinsing. b) Representative stitched 10x Immunofluorescence image of fixed and actin labelled C2C12 cells adhering throughout the whole well. The white arrow indicates rinsing artifacts during staining. Below, a graph shows the quantification of relative cellular adhesion of C2C12 cells on saturated cRGD platforms at five positions throughout the well. c) Automatically acquired representative immunofluorescence images of C2C12 cells on cRGD and/or BMP2-presenting platforms stained for actin and pSMAD1/5/9. Below is a graph showing the pSMAD1/5/9 intensity quantification at five positions throughout the well processed using automated image analysis software. All experiments were at least repeated 3 times, error bars = SEM and significance was tested with Mann-Whitney for $p \leq 0.05$.

C2C12 dose response to sBMP2,4,6,7 or aBMP2,4,6,7

We took advantage of the high-content fabrication protocol to look at the dose response of C2C12 cells to four different BMPs in parallel by comparing the EC_{50} values and to study the effect of HS on BMP signaling. With the liquid handling robot we functionalized a 96-well plate presenting 42 different conditions in technical duplicates presenting the BMPs either in solution (sBMP2,4,6,7) or adsorbed on iHS (aBMP2,4,6,7) for 130 min and quantified SMAD1/5/9 phosphorylation with automated microscopy and image analysis (**Figure 6 a**).

We identified initial aBMP2,4,6,7 concentrations in a way that all BMPs bound with comparable frequency shifts to iHS before rinsing using QCM-D (**SI Fig 4 a**). Those concentrations in the range of 3-10 $\mu\text{g/mL}$ were high and were expected to induce maximal SMAD1/5/9 phosphorylation. From this BMP2,4,6,7 specific base concentration, we chose a step-wise 100 fold dilution and also added a 10 $\mu\text{g/ml}$ common upper concentration.

The liquid handling robot functionalized the 96-well plate with the biomimetic platforms presenting BMP2,4,6 and 7 in 5 different concentrations adsorbed to iHS in technical duplicates. Soluble BMPs were added by hand to the cell media the moment cells were plated and covered a concentration range of factor 1000. The plate was automatically imaged and analyzed for pSMAD1/5/9 signal inside the nucleus.

A trained user took 15 min to enter the experimental parameters *via* the custom-made graphical user interface. The robot functionalized this specific whole plate in 6 h of which roughly 4 h were waiting time for molecule incubation and 2 h liquid handling operations. Automated image acquisition and analysis took one hour each with additional 15 min user interaction for both steps to set up the microscope and to calibrate the image analysis software.

Representative single cell images of the negative control, an intermediate BMP concentration and a plateau condition show pSMAD1/5/9 translocated into the nucleus (**Figure 6 b**). For all sBMP2,4,6,7 and aBMP2,4,6,7 conditions, we observed a BMP dose-dependent positive response in C2C12 cells *via* the phosphorylation of SMAD1/5/9 (**Figure 6 c**). The sBMP2,4,6,7 concentration of 1 $\mu\text{g/ml}$, which in all cases represented an upper plateau pSMAD1/5/9 signal, was significantly higher than the negative control. Also, when comparing the aBMP2,4,6,7 conditions, the comparable concentration of 3, 5, 10 and 5 $\mu\text{g/ml}$ respectively induced a plateau pSMAD1/5/9 signal, which was significantly higher than the negative control and comparable to the plateau induced by corresponding sBMP2, 4, 6 and 7. Statistical significance between intermediate concentrations to the negative control and to either sBMP2,4,6,7 at 1 $\mu\text{g/ml}$ or aBMP2,4,6,7 at 3, 5, 10 or 5 $\mu\text{g/ml}$ was tested.

To quantify differences between different BMPs we calculated the EC_{50} , which defines the BMP concentration where 50% of the pSMAD1/5/9 signal between the negative control and the plateau was measured (**SI Fig 4 b**) and summarized results in **Table 3**. sBMP2 thus was more potent to induce SMAD1/5/9 phosphorylation than sBMP4,6 and 7 which were comparable to each other. In addition, aBMP2 was more bioactive than aBMP4 and aBMP7 but

for aBMP6 the fit for the dose response curve failed because at high aBMP6 concentrations the plateau of the pSMAD1/5/9 response was not reached. Hammers et al. measured in a similar experiment with soluble BMPs EC₅₀ values for sBMP2,4,6 and 7 **Table 3** [54].

We conclude that the automated fabrication protocol is a powerful tool to study many different conditions in parallel upon user demand. Together with automated image acquisition and analysis, we presented a fast and reproducible workflow for high-content studies with a complex biomaterial. Here, we were able to identify sBMP2,4,6,7 and aBMP2,4,6,7 concentrations in the dynamic range of induced SMAD1/5/9 phosphorylation, which allows direct comparison of the BMPs bioactivity. Those so-called critical concentrations can further serve to measure the influence of other factors on SMAD1/5/9 phosphorylation such as gene mutations, drugs, receptors or molecules from the extra cellular space.

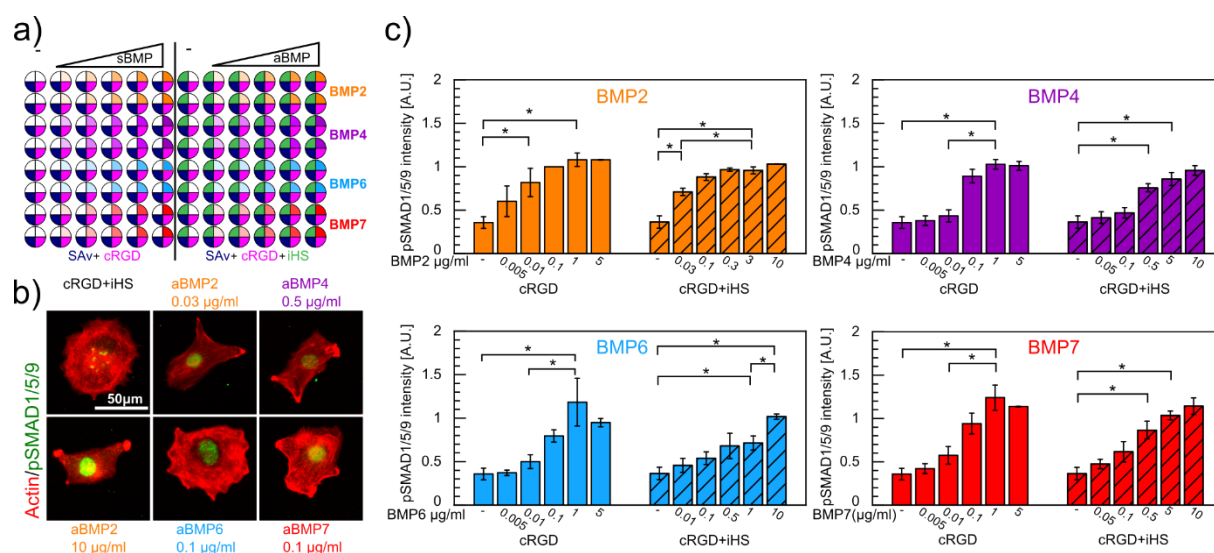


Figure 6: Automated high-content study of C2C12 cell response to sBMP2,4,6,7 and aBMP2,4,6,7. a) Schematic of a 96-well plate with 42 different conditions in duplicates fully functionalized by the robot. sBMP2,4,6 and 7 in different concentrations were added by hand into the cell media when cells were plated. b) Representative and equally treated images of C2C12 cells plated inside the 96-well plate functionalized by the robot, fixed after 90 min and labelled for actin and pSAMd1/5/9 translocated into the nucleus. BMP concentrations were chosen to represent a condition close to the EC₅₀ concentration c) Graphs show the quantification of pSMAD1/5/9 translocated into the nucleus. Values were normalized to the sBMP2 condition at 0.1 µg/ml. Each experiment was the average of two wells and the error bars represent the SEM. Significance was tested with Mann-Whitney and p < 0.05 for n = 3. The aBMP2,4,6 and 7 concentrations represent the concentrations used for the incubation on iHS and don't permit a quantitative conclusion on the amount of aBMP2/4/6/7 eventually adsorbed on iHS.

Table 3: EC₅₀ values for sBMP2,4,6 and 7 and aBMP2,4,6 and 7 on cRGD platforms compared to values of a similar study with C2C12 cells on tissue culture plates [54]. Values are given as mean ± SD over three replicates.

	EC ₅₀ (μg/ml)		EC ₅₀ (nM)		EC ₅₀ (nM)
	sBMP	aBMP	sBMP	aBMP	sBMP [54]
BMP2 (26 kDa)	0.007 ± 0.001	0.028 ± 0.007	0.269 ± 0.038	1.08 ± 0.27	0.033 ± 0.002
BMP4 (24 kDa)	0.027 ± 0.003	0.227 ± 0.033	1.13 ± 0.13	9.46 ± 1.38	0.010 ± 0.0004
BMP6 (30 kDa)	0.035 ± 0.022	fit failed	1.12 ± 0.73	fit failed	1.3 ± 0.032
BMP7 (26 kDa)	0.042 ± 0.011	0.294 ± 0.150	1.62 ± 0.42	11.3 ± 5.77	5.9 ± 0.22

Discussion

In this manuscript, we presented for the first time the automated functionalization of SAV biomimetic platforms built-up on glass bottom 96-well plates for cellular studies. For that we developed an automated experimental workflow to fabricate on-demand biomimetic platforms using custom-made software, a liquid handling robot and automated image acquisition and analysis. Functionalized surfaces were characterized *in situ* using ICS and compared to results from *ex situ* measurements on model substrates *via* QCM-D and SE. C2C12 cells responded to co-presented cRGD and on iHS adsorbed aBMP2,4,6,7 *via* specific adhesion and SMAD1/5/9 phosphorylation.

Automated liquid handling protocols for biomaterials have been rarely developed before and none of the previous studies addressed single wells with a large choice of different solutions. The originality of our system relies in the possibility to assign complex and independent experimental conditions to each individual well. Moreover, it is possible to choose between using few wells only or the plate as a whole, resulting in optimized material consumption and allowing low-content preliminary studies. In addition, the number of replicates is flexible, which is important if different cell types are studied in parallel on identical conditions or different read-outs on the same condition are desired. Lastly, the advantage of using SAV as a base opens this system to a vast field of applications due to its specific affinity to biotin.

By transferring all liquid handling operations to the liquid handling robot, the user's participation in the experiment was reduced by hours depending on the complexity of the experimental plan and a source for human errors was eliminated [17]. Adaptation to other glass bottom multi-well supports is possible due to the large range of compatible pipetting hardware

offered by TECAN but would also come along with further development of the graphical user interface. In addition, cell seeding and adding soluble factors to the media would be feasible with this set-up under the condition that the system is placed under sterile environment.

We applied ICS for the first time to quantify molecular densities in fluorescence confocal images acquired *in situ* in the context of surface characterization of biofilms where this technique is not common [26]. Calculated number of molecules per observation area translated into mass per area allow direct comparison to measurements acquired with QCM-D and SE (**Table 2**). Wet mass densities for SAV, SAVAlexa and SAV/cRGDmix, calculated with the Sauerbrey equation based on the shift in frequency measured with QCM-D, include the coupled solvent and can be interpreted as an upper limit compared to dry mass densities acquired with SE and ICS [55]. The rather high differences between the wet mass density of SAV, SAVAlexa and SAV/cRGD mix could indicate different degrees of hydration also hinted by different viscoelastic properties measured *via* the shift in dissipation (**Figure 3 a, SI Fig 2 a**) [24]. With neither QCM-D nor SE we were able to detect the small molecule bAtto binding to SAV whereas with ICS we reproducibly measured $0.79 \pm 0.19 \text{ ng/cm}^2$. The SE measurements for SAV and SAVAlexa were comparable to each other while the SAVcRGDmix bound with an increase of 80 ng/cm^2 . Since ICS measurements suggest that the amount of SAVAlexa on the surface in its pure version or coupled to cRGD is similar, the additional mass describes mostly the amount of cRGD on the surface. Interestingly the amount of bAtto bound on SAV layer is more than an order of magnitude lower than the cRGD pre-coupled with SAVAlexa. This may indicate that when we premixed SAV and cRGD we avoided the long PLL-g-PEGbiotin chains from occupying the biotin pockets available on streptavidin, in line with Zhen et al. [44].

ICS derived areal mass densities were comparable to the ones measured with SE with a difference of 32% for SAVAlexa while the standard deviation between replicates ranges around 10-20% for both approaches. We thus validated ICS as a suitable technique to characterize biomimetic SAV platforms *in situ*. One source for this difference can origin from the two different substrates used, glass for ICS and thermal SiO₂ for SE. With SE, we measured $120.2 \pm 8.7 \text{ ng/cm}^2$ PLL-g-PEGbiotin50% and $253.2 \pm 32.8 \text{ SAVAlexa}$. Indeed, other studies show that the binding of PLL-g-PEGbiotin depends on the substrate [56]. Huang et al. show that PLL-g-PEGbiotin with different percentages of grafted biotin bind all similar with 2.5 pmol/cm^2 (268 ng/cm^2 for PLL-g-PEGbiotin50%) to NbO₂ to which SAV adsorbed with 369 ng/cm^2 [42]. Städler et al. however measured on the same substrate $218 \pm 16 \text{ ng/cm}^2$ of PLL-g-PEGbiotin

with 350 ng/cm² Neutravidin adsorption [57]. But experiments on SiO₂ show 145 ng/cm² for a PLL-g-PEGbiotin layer and subsequent SAV binding of only 120 ng/cm² [58].

While ICS avoids passing *via* tools with auxiliary substrates such as QCM-D, SE, OWLS or *via* indirect measurements (μ BCA), it has other constraints: Compounds need to be labelled with a fluorophore, which might alter molecular binding properties and also leads to negligence of un-labelled molecules [59]. While confocal microscopes are abundant in research facility, specific analysis software to calculate the autocorrelation function and to deduce the number of molecules per observation area is scarcely available and analysis relies on custom-made tools, extensions and experienced users. Nevertheless, we proved that this method is more accurate to characterize biomaterials *in situ* than simple relative intensity comparison done with any fluorescent microscopy due to artefacts from varying fluorophore efficiency between samples probably related to quenching (**Figure 4 e, f**) [60].

As proof-of-concept of our functionalization workflow, we studied the dose-response of C2C12 cells to different concentrations of BMP2,4,6,7 in parallel adsorbed to iHS or in soluble condition. The calculated the EC₅₀ values proved that BMP2 is the most potent among the four studied GFs in soluble form and adsorbed on HS because it already induces SMAD1/5/9 phosphorylation at lower concentrations. Hammers et al. measured one and two orders of magnitude lower EC₅₀ values for sBMP2 and sBMP4 respectively whereas sBMP6 and sBMP7 were comparable [54]. Their use of typical tissue culture plates compared to our cRGD platforms could explain these differences. Sales et al. also compared concentrations of matrix-bound BMP2,4 and 7 to each other and found higher SMAD1/5/9 phosphorylation induced by BMP2 compared to BMP4 and BMP7 at low concentrations [19]. However, at higher concentrations, BMP7 was inducing the highest signal among all. Brigaud et al. compared BMP2,6,7 combined with fibronectin by quantifying the expression of osteogenic markers from three to nine days [61]. They found that fibronectin enhanced and maintained the osteogenic activity of the BMPs. Thanks to the novel workflow here reported it will be possible to perform a systematic study of the effect of different GFs and of different GAGs on cellular signaling.

Conclusion

We presented an automated workflow for the functionalization of a biomimetic model platform inside glass bottom 96-well plates followed by automated image acquisition and

analysis. With a graphical user interface, we empowered the user to enter a complex experimental set-up in minutes, presenting a maximum of 96 different conditions on the same plate for up to three identical plates in parallel. A custom-made software translated this plan into liquid handling commands, which were executed by a liquid handling robot in a reproducible and homogeneous way. By characterizing the wells with image correlation spectroscopy, we applied a rarely used tool to measure for the first time molecular density of biomimetic surfaces *in situ* without evasion *via* model surfaces, possibly useful to characterize other biomimetic surfaces. With a high-content approach, we found that aBMP2,4,6 and 7 adsorbed in very low doses on iHS could induce SMAD1/5/9 phosphorylation and that BMP2 is the most effective among them at comparable doses. The proof of concept experiment proves that it is possible to design complex plate maps and aims to inspire other research facilities to adopt this approach to study the synergies between peptides, GFs and glycosaminoglycans.

Declaration of competing interest

The authors declare that they have no competing financial interests or personal relationships that could have appeared to influence the work reported in this paper.

Acknowledgements

We acknowledge Dr. Didier Boturyn and Remy Lartia from DCM in Grenoble for the synthesis of the cRGD peptide. For fruitful discussions, we thank Prof. Ralf Richter (University of Leeds), Dr. Liliane Guerente (DCM Grenoble) and Dr. Elisabetta Ada Cavalcanti-Adam (MPI Heidelberg) as well as the members of our group BRM at CEA. Hajar Ajiyel, Marie Dutoit, Samy Idelcadi and Julia Levy from Grenoble INP further contributed to software development. This project received funding from: Fondation Recherche Médicale (No. DEQ20170336746), ANR CODECIDE (No. ANR-17-CE13-022), ANR GlyCON (No. ANR-19-CE13-0031-01 PRCI) and the Initiative de Recherche Stratégique, University Grenoble Alps (IDEX- IRS 2018–2021). This work has been supported by CNRS GDR 2088 "BIOMIM", ANR-17-EURE-0003, GRAL, ERC POC BIOACTIVECOATINGS 2015 and ERC POC REGENERBONE 2017.

Bibliographic references

- [1] J. F. Mano, I. S. Choi, and A. Khademhosseini, “Biomimetic Interfaces in Biomedical Devices,” *Adv. Healthc. Mater.*, vol. 6, no. 15, pp. 2–3, 2017, doi: 10.1002/adhm.201700761.
- [2] A. S. Curry, N. W. Pensa, A. M. Barlow, and S. L. Bellis, “Taking cues from the extracellular matrix to design bone-mimetic regenerative scaffolds,” *Matrix Biol.*, vol. 52–54, pp. 397–412, 2016, doi: 10.1016/j.matbio.2016.02.011.
- [3] R. O. Hynes, “The extracellular matrix: Not just pretty fibrils,” *Science (80-.)*, vol. 326, no. 5957, pp. 1216–1219, 2009, doi: 10.1126/science.1176009.
- [4] A. J. Engler, S. Sen, H. L. Sweeney, and D. E. Discher, “Matrix Elasticity Directs Stem Cell Lineage Specification,” *Cell*, vol. 126, no. 4, pp. 677–689, 2006, doi: 10.1016/j.cell.2006.06.044.
- [5] E. Migliorini et al., “Enhanced biological activity of BMP-2 bound to surface-grafted heparan sulfate,” *Adv. Biosyst.*, vol. 1, no. 4, p. 1600041, 2017, doi: 10.1002/adbi.201600041.
- [6] E. Migliorini, A. Guevara-Garcia, C. Albiges-Rizo, and C. Picart, “Learning from BMPs and their biophysical extracellular matrix microenvironment for biomaterial design,” *Bone*, vol. 141, no. July, p. 115540, 2020, doi: 10.1016/j.bone.2020.115540.
- [7] I. Monteiro A., T. Kollmetz, and J. Malmström, “Engineered systems to study the synergistic signaling between integrin-mediated mechanotransduction and growth factors (Review),” *Biointerphases*, vol. 13, no. 6, p. 06D302, 2018, doi: 10.1116/1.5045231.
- [8] M. J. Vassef et al., “Immune Modulation by Design: Using Topography to Control Human Monocyte Attachment and Macrophage Differentiation,” *Adv. Sci.*, vol. 7, no. 11, pp. 1–9, 2020, doi: 10.1002/advs.201903392.
- [9] J. Nicolas, S. Magli, L. Rabbachin, S. Sampaolesi, F. Nicotra, and L. Russo, “3D extracellular matrix mimics: fundamental concepts and role of materials chemistry to influence stem cell fate,” *Biomacromolecules*, vol. 21, no. 6, pp. 1968–1994, 2020, doi: 10.1021/acs.biomac.0c00045.
- [10] M. Pagel and A. G. Beck-Sickinger, “Multifunctional biomaterial coatings: Synthetic challenges and biological activity,” *Biol. Chem.*, vol. 398, no. 1, pp. 3–22, 2017, doi: 10.1515/hsz-2016-0204.
- [11] W. He, M. Reaume, M. Hennenfent, B. P. Lee, and R. Rajachar, “Biomimetic hydrogels with spatial- and temporal-controlled chemical cues for tissue engineering,” *Biomater. Sci.*, vol. 8, no. 12, pp. 3248–3269, 2020, doi: 10.1039/d0bm00263a.
- [12] S. Eggert and D. W. Huttmacher, “In vitro disease models 4.0 via automation and high-throughput processing,” *Biofabrication*, vol. 11, no. 4, 2019, doi: 10.1088/1758-5090/ab296f.
- [13] A. Vasilevich and J. de Boer, “Robot-scientists will lead tomorrow’s biomaterials discovery,” *Curr. Opin. Biomed. Eng.*, vol. 6, pp. 74–80, 2018, doi: 10.1016/j.cobme.2018.03.005.
- [14] M. L. Grubb and S. R. Caliari, “Fabrication approaches for high-throughput and biomimetic disease modeling,” *Acta Biomater.*, vol. 132, no. xxxx, pp. 52–82, Sep. 2021, doi: 10.1016/j.actbio.2021.03.006.
- [15] M. E. Afshar et al., “A 96-well culture platform enables longitudinal analyses of engineered human skeletal muscle microtissue strength,” *Sci. Rep.*, vol. 10, no. 1, pp. 1–16, 2020, doi: 10.1038/s41598-020-62837-8.
- [16] T. Kaufmann and B. J. Ravoo, “Stamps, inks and substrates: Polymers in microcontact printing,” *Polym. Chem.*, vol. 1, no. 4, pp. 371–387, 2010, doi: 10.1039/b9py00281b.

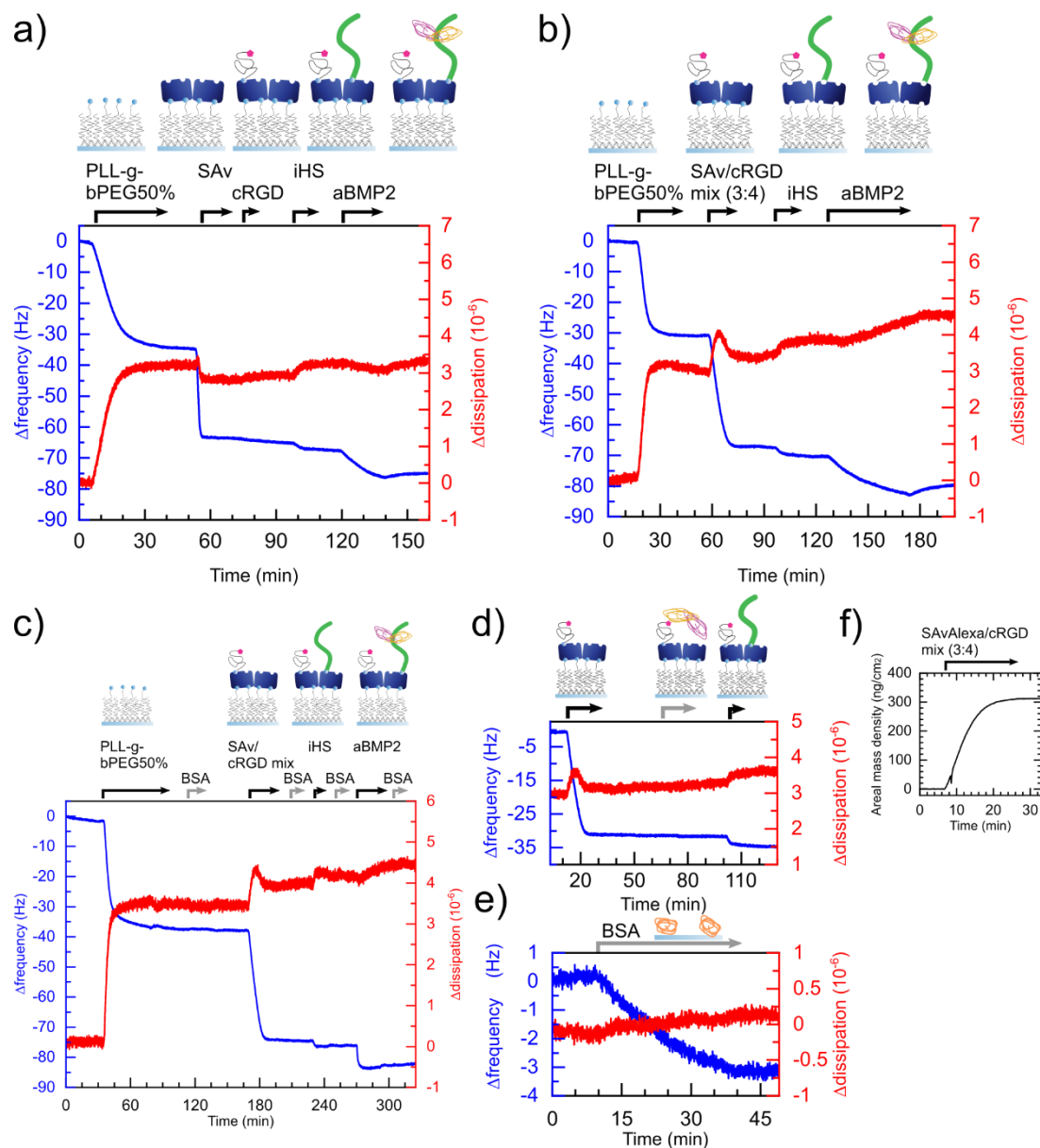
- [17] G. Lippi, G. Lima-Oliveira, G. Brocco, A. Bassi, and G. L. Salvagno, “Estimating the intra- and inter-individual imprecision of manual pipetting,” *Clin. Chem. Lab. Med.*, vol. 55, no. 7, pp. 962–966, 2017, doi: doi:10.1515/cclm-2016-0810.
- [18] P. Machillot et al., “Automated Buildup of Biomimetic Films in Cell Culture Microplates for High-Throughput Screening of Cellular Behaviors,” *Adv. Mater.*, vol. 30, no. 27, pp. 1–8, 2018, doi: 10.1002/adma.201801097.
- [19] A. Sales et al., “Differential bioactivity of four BMP-family members as function of biomaterial stiffness,” *bioRxiv*, 2021, doi: 10.1101/2021.02.10.430282.
- [20] E. A. Brooks et al., “Complementary, semiautomated methods for creating multidimensional PEG-based biomaterials,” *ACS Biomater. Sci. Eng.*, vol. 4, no. 2, pp. 707–718, 2018, doi: 10.1021/acsbiomaterials.7b00737.
- [21] S. Eggert, M. Kahl, N. Bock, C. Meinert, O. Friedrich, and D. W. Hutmacher, “An open-source technology platform to increase reproducibility and enable high-throughput production of tailorable gelatin methacryloyl (GelMA) - based hydrogels,” *Mater. Des.*, vol. 204, p. 109619, 2021, doi: 10.1016/j.matdes.2021.109619.
- [22] W. Zeng, L. Guo, S. Xu, J. Chen, and J. Zhou, “High-throughput screening technology in industrial biotechnology,” *Trends Biotechnol.*, vol. 38, no. 8, pp. 1–19, 2020, doi: 10.1016/j.tibtech.2020.01.001.
- [23] A. Kletzmayer, F. Clement Frey, M. Zimmermann, D. Eberli, and C. Millan, “An automatable hydrogel culture platform for evaluating efficacy of antibody-based therapeutics in overcoming chemoresistance,” *Biotechnol. J.*, vol. 15, no. 5, pp. 1–11, 2020, doi: 10.1002/biot.201900439.
- [24] I. Reviakine, D. Johannsmann, and R. P. Richter, “Hearing what you cannot see and visualizing what you hear,” *Anal. Chem.*, vol. 83, pp. 8838–8848, 2011.
- [25] G. V. Dubacheva et al., “Controlling multivalent binding through surface chemistry: Model study on streptavidin,” *J. Am. Chem. Soc.*, vol. 139, no. 11, pp. 4157–4167, 2017, doi: 10.1021/jacs.7b00540.
- [26] E. Migliorini, M. Weidenhaupt, and C. Picart, “Practical guide to characterize biomolecule adsorption on solid surfaces (Review),” *Biointerphases*, vol. 13, no. 6, p. 06D303, 2018, doi: 10.1116/1.5045122.
- [27] E. Migliorini et al., “Well-defined biomimetic surfaces to characterize glycosaminoglycan-mediated interactions on the molecular, supramolecular and cellular levels,” *Biomaterials*, vol. 35, no. 32, pp. 8903–8915, 2014, doi: 10.1016/j.biomaterials.2014.07.017.
- [28] J. C. Waters and T. Wittmann, “Chapter 1 - Concepts in quantitative fluorescence microscopy,” in *Quantitative Imaging in Cell Biology*, vol. 123, J. C. Waters and T. Wittman, Eds. Academic Press, 2014, pp. 1–18.
- [29] W. J. Galush, J. A. Nye, and J. T. Groves, “Quantitative fluorescence microscopy using supported lipid bilayer standards,” *Biophys. J.*, vol. 95, no. 5, pp. 2512–2519, 2008, doi: 10.1529/biophysj.108.131540.
- [30] N. O. Petersen, P. L. Höddelius, P. W. Wiseman, O. Seger, and K. E. Magnusson, “Quantitation of membrane receptor distributions by image correlation spectroscopy: concept and application,” *Biophys. J.*, vol. 65, no. 3, pp. 1135–1146, 1993, doi: 10.1016/S0006-3495(93)81173-1.
- [31] R. Macháň and T. Wohland, “Recent applications of fluorescence correlation spectroscopy in live systems,” *FEBS Lett.*, vol. 588, no. 19, pp. 3571–3584, 2014, doi: 10.1016/j.febslet.2014.03.056.
- [32] R. De Mets, I. Wang, J. Gallagher, O. Destaing, M. Balland, and A. Delon, “Determination of protein concentration on substrates using fluorescence fluctuation microscopy,” in *Proc.SPIE*, Mar. 2014, vol. 8950, doi: 10.1117/12.2040355.

- [33] J. Sefkow-Werner, E. Migliorini, C. Picart, D. Wahyuni, I. Wang, and A. Delon, “Combining fluorescence fluctuations and photobleaching to quantify surface density,” Oct. 2021, doi: arXiv:2110.14319.
- [34] B. Nguyen, F. A. Tanious, and W. D. Wilson, “Biosensor-surface plasmon resonance: Quantitative analysis of small molecule-nucleic acid interactions,” *Methods*, vol. 42, no. 2, pp. 150–161, 2007, doi: 10.1016/j.ymeth.2006.09.009.
- [35] J. Sefkow-Werner et al., “Heparan sulfate co-immobilized with cRGD ligands and BMP2 on biomimetic platforms promotes BMP2-mediated osteogenic differentiation.,” *Acta Biomater.*, vol. 114, pp. 90–103, Sep. 2020, doi: 10.1016/j.actbio.2020.07.015.
- [36] R. Ruppert, E. Hoffmann, and W. Sebald, “Human bone morphogenetic protein 2 contains a heparin-binding site which modifies its biological activity,” *Eur. J. Biochem.*, vol. 237, no. 1, pp. 295–302, 1996, doi: 10.1111/j.1432-1033.1996.0295n.x.
- [37] S. Sarrazin, W. C. Lamanna, and J. D. Esko, “Heparan Sulfate Proteoglycans,” *Cold Spring Harb. Perspect. Biol.*, vol. 3, no. 7, pp. a004952–a004952, Jul. 2011, doi: 10.1101/cshperspect.a004952.
- [38] V. S. Salazar, L. W. Gamer, and V. Rosen, “BMP signalling in skeletal development, disease and repair,” *Nat. Rev. Endocrinol.*, vol. 12, no. 4, pp. 203–221, 2016, doi: 10.1038/nrendo.2016.12.
- [39] W.-J. Kuo, M. A. Digman, and A. D. Lander, “Heparan Sulfate Acts as a Bone Morphogenetic Protein Coreceptor by Facilitating Ligand-induced Receptor Hetero-oligomerization,” *Mol. Biol. Cell*, vol. 21, no. 22, pp. 4028–4041, Sep. 2010, doi: 10.1091/mbc.e10-04-0348.
- [40] J. Brkljacic et al., “Exogenous heparin binds and inhibits bone morphogenetic protein 6 biological activity,” *Int. Orthop.*, vol. 37, no. 3, pp. 529–541, 2013, doi: 10.1007/s00264-012-1714-3.
- [41] A. Irie, H. Habuchi, K. Kimata, and Y. Sanai, “Heparan sulfate is required for bone morphogenetic protein-7 signaling,” *Biochem. Biophys. Res. Commun.*, vol. 308, no. 4, pp. 858–865, 2003, doi: 10.1016/S0006-291X(03)01500-6.
- [42] N.-P. Huang, J. Vörös, S. M. De Paul, M. Textor, and N. D. Spencer, “Biotin-Derivatized Poly(α -lysine)- g -poly(ethylene glycol): A Novel Polymeric Interface for Bioaffinity Sensing,” *Langmuir*, vol. 18, no. 1, pp. 220–230, Jan. 2002, doi: 10.1021/la010913m.
- [43] L. A. Ruiz-Taylor et al., “Monolayers of derivatized poly(L-lysine)-grafted poly(ethylene glycol) on metal oxides as a class of biomolecular interfaces,” *Proc. Natl. Acad. Sci. U. S. A.*, vol. 98, no. 3, pp. 852–857, 2001, doi: 10.1073/pnas.98.3.852.
- [44] G. Zhen et al., “Immobilization of the Enzyme β -Lactamase on Biotin-Derivatized Poly(α -lysine)- g -poly(ethylene glycol)-Coated Sensor Chips: A Study on Oriented Attachment and Surface Activity by Enzyme Kinetics and *in situ* Optical Sensing,” *Langmuir*, vol. 20, no. 24, pp. 10464–10473, Nov. 2004, doi: 10.1021/la0482812.
- [45] C. Sieber, J. Kopf, C. Hiepen, and P. Knaus, “Recent advances in BMP receptor signaling,” *Cytokine Growth Factor Rev.*, vol. 20, no. 5–6, pp. 343–355, 2009, doi: 10.1016/j.cytogfr.2009.10.007.
- [46] T. Katagiri et al., “Bone morphogenetic protein-2 converts the differentiation pathway of C2C12 myoblasts into the osteoblast lineage,” *J. Cell Biol.*, vol. 127, no. 6 I, pp. 1755–1766, 1994, doi: 10.1083/jcb.127.6.1755.
- [47] D. Thakar et al., “Binding of the chemokine CXCL12 α to its natural extracellular matrix ligand heparan sulfate enables myoblast adhesion and facilitates cell motility,” *Biomaterials*, vol. 123, pp. 24–38, 2017, doi: 10.1016/j.biomaterials.2017.01.022.
- [48] R. P. Richter, K. B. Rodenhausen, N. B. Eisele, and M. Schubert, “Coupling Spectroscopic

- Ellipsometry and Quartz Crystal Microbalance to Study Organic Films at the Solid-Liquid Interface,” in *Ellipsometry of Functional Organic Surfaces and Films*, K. Hinrichs and K.-J. Eichhorn, Eds. Cham: Springer International Publishing, 2018, pp. 391–417.
- [49] C. M. Herzinger, B. Johs, W. A. McGahan, J. A. Woollam, and W. Paulson, “Ellipsometric determination of optical constants for silicon and thermally grown silicon dioxide via a multi-sample, multi-wavelength, multi-angle investigation,” *J. Appl. Phys.*, vol. 83, no. 6, pp. 3323–3336, 1998, doi: 10.1063/1.367101.
- [50] I. Carton, A. R. Brisson, and R. P. Richter, “Label-free detection of clustering of membrane-bound proteins,” *Anal. Chem.*, vol. 82, no. 22, pp. 9275–9281, Nov. 2010, doi: 10.1021/ac102495q.
- [51] A. L. Cauchy, *Mémoire sur la dispersion de la lumière*. Prague: chez J. G. Calve, 1836.
- [52] J. A. De Feijter, J. Benjamins, and F. A. Veer, “Ellipsometry as a tool to study the adsorption behavior of synthetic and biopolymers at the air-water interface,” *Biopolymers*, vol. 17, no. 7, pp. 1759–1772, 1978, doi: 10.1002/bip.1978.360170711.
- [53] J. L. Sebaugh, “Guidelines for accurate EC50/IC50 estimation,” *Pharm. Stat.*, vol. 10, no. 2, pp. 128–134, 2011, doi: 10.1002/pst.426.
- [54] D. W. Hammers, M. Merscham-Banda, J. Y. Hsiao, S. Engst, J. J. Hartman, and H. L. Sweeney, “Supraphysiological levels of <sc>GDF</sc> 11 induce striated muscle atrophy,” *EMBO Mol. Med.*, vol. 9, no. 4, pp. 531–544, Apr. 2017, doi: 10.15252/emmm.201607231.
- [55] F. F. Hook et al., “A comparative study of protein adsorption on titanium oxide surfaces using *in situ* ellipsometry, optical waveguide lightmode spectroscopy, and quartz crystal microbalance/dissipation,” *Colloids Surfaces B Biointerfaces*, vol. 24, no. 2, pp. 155–170, 2002, doi: 10.1016/S0927-7765(01)00236-3.
- [56] G. L. Kenausis et al., “Poly(L-lysine)-g-poly(ethylene glycol) layers on metal oxide surfaces: Attachment mechanism and effects of polymer architecture on resistance to protein adsorption,” *J. Phys. Chem. B*, vol. 104, no. 14, pp. 3298–3309, 2000, doi: 10.1021/jp993359m.
- [57] B. Städler, D. Falconnet, I. Pfeiffer, F. Höök, and J. Vörös, “Micropatterning of DNA-tagged vesicles,” *Eur. Cells Mater.*, vol. 7, no. SUPPL.1, p. 86, 2004.
- [58] R. Marie, A. B. Dahlin, J. O. Tegenfeldt, and F. Höök, “Generic surface modification strategy for sensing applications based on Au/SiO₂ nanostructures,” *Biointerphases*, vol. 2, no. 1, pp. 49–55, 2007, doi: 10.1116/1.2717926.
- [59] M. (Ed.). Cooper, *Label-free biosensors: Techniques and applications*. Cambridge: Cambridge University Press, 2009.
- [60] W. Bae, T. Y. Yoon, and C. Jeong, “Direct evaluation of self-quenching behavior of fluorophores at high concentrations using an evanescent field,” *PLoS One*, vol. 16, no. 2 February 2021, pp. 1–8, 2021, doi: 10.1371/journal.pone.0247326.
- [61] I. Brigaud et al., “Synergistic effects of BMP-2, BMP-6 or BMP-7 with human plasma fibronectin onto hydroxyapatite coatings: A comparative study,” *Acta Biomater.*, vol. 55, pp. 481–492, Jun. 2017, doi: 10.1016/j.actbio.2017.04.013.

II.D Supplementary information

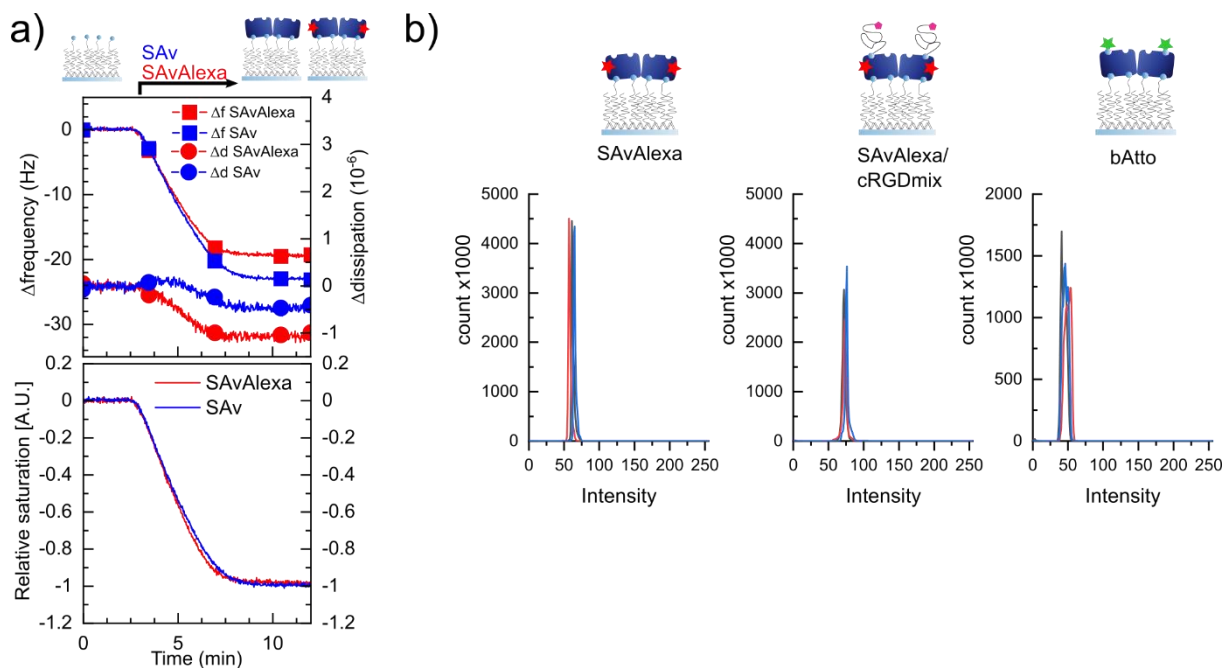
Supplementary figure 1



SI Fig 1: QCM-D and SE measurements of the sequential co-functionalization and non-specific binding. Graphs showing the change in frequency and dissipation upon molecular binding events measured with QCM-D. Black arrows indicate time of incubation followed by rinsing with buffer a) Sequential functionalization on at least 3 times regenerated SiO₂ crystals resulting in increased PLL-g-PEGbiotin50% adsorption compared to new crystals. SAV bound to the previous layer, also more compared to new crystals. Then cRGD was incubated at a concentration of 0.25 μ g/ml but incubation was intentionally interrupted before saturation to keep biotin-binding sites available for subsequent compounds. We previously found that cRGD at 0.25 μ g/ml needed 20 min to saturate. Thus, interrupting after four minutes led to a sub-monolayer with a barely visible frequency shift of -0.8 ± 0.1 Hz. iHS then saturated the remaining binding sites with -1.8 ± 0.3 Hz after 10 min and increased further the dissipation. Finally, BMP2 with a concentration of 5 μ g/ml adsorbed to iHS and saturated after 20 min with 6.1 ± 1.3 Hz of which some is partly removed by rinsing. b) Pre-coupled SAV and cRGD in molar ratio 3:4 were incubated on PLL-g-PEGbiotin50% on regenerated crystals. The mix adsorbed more than the sum of single SAV

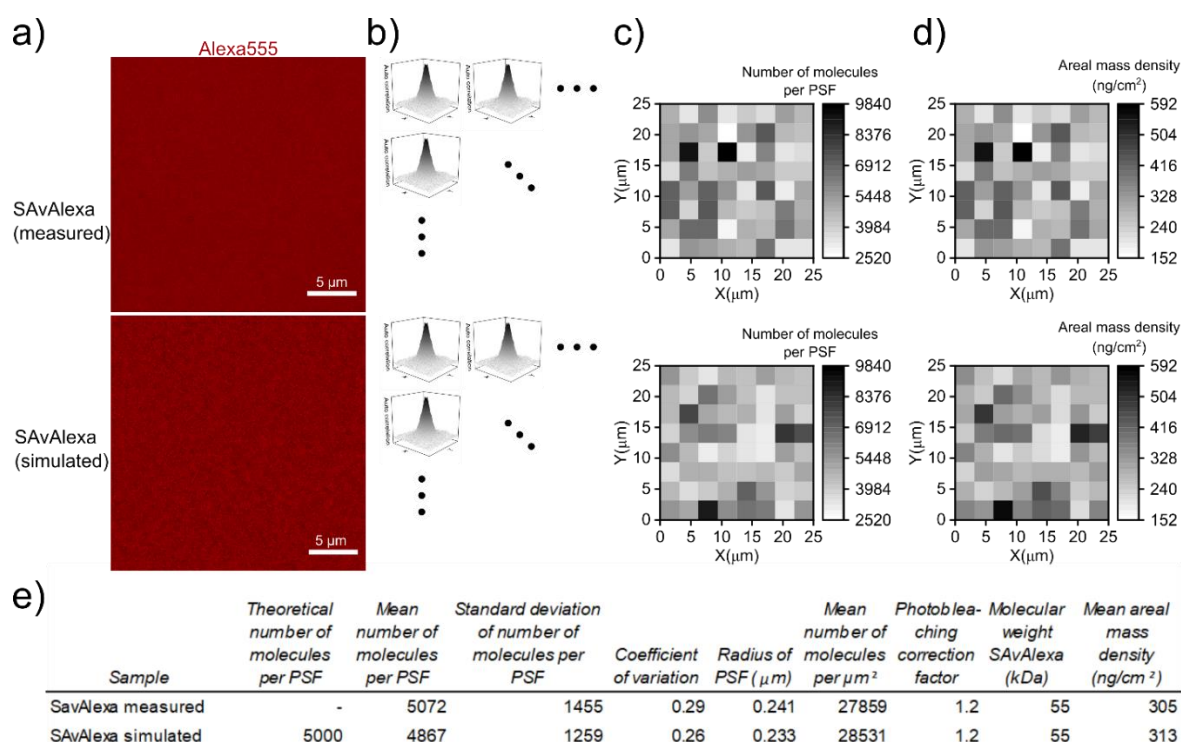
and cRGD incubated one after each other. This also resulted in more free biotin-binding sites as seen by higher iHS adsorption and higher aBMP2 adsorption. c) BSA (grey arrows) at 50 $\mu\text{g/ml}$ didn't bind measurable to different elements of the biomimetic platform d) BMP2 at 5 $\mu\text{g/ml}$ didn't bind measurable to SAV/cRGDmix. e) BSA irreversibly adsorbed to activated glass with a frequency shift of -3 Hz. f) Graph showing the binding of SAVAlexa/cRGDmix measured with SE.

Supplementary figure 2



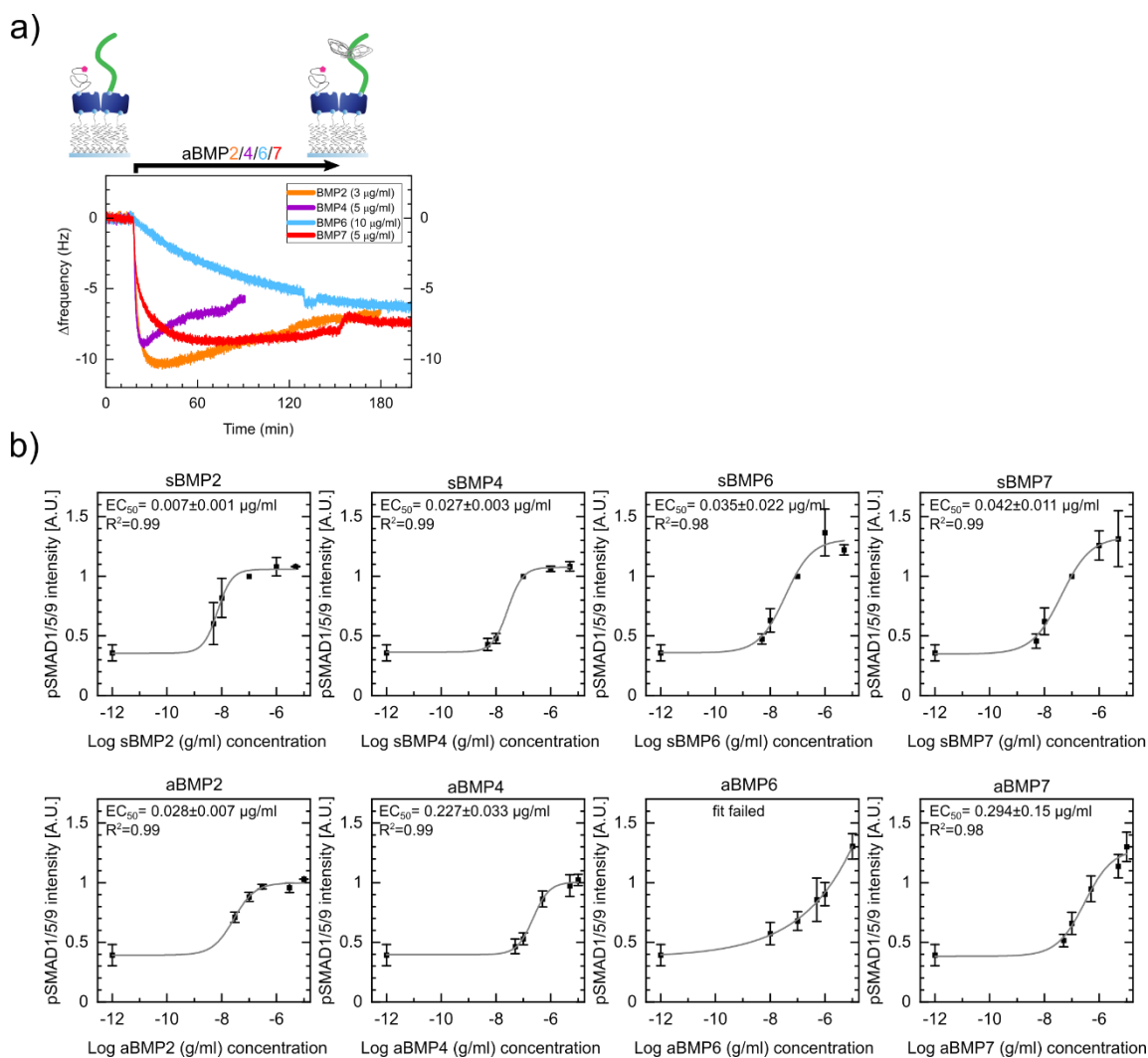
SI Fig 2: Comparison between SAV and SAVAlexa binding kinetics and reproducibility of surface functionalization a) Graphs comparing the change in frequency and dissipation upon the binding of SAV or SAVAlexa to PLL-g-PEGbiotin50% measured with QCM-D in an absolute (top) and relative (bottom) way. The black arrow indicates time of incubation followed by rinsing with buffer b) Graph showing the histograms of three different wells (red, black and blue curve) for three different surfaces each to represent the inter-well homogeneity. The scale (from 0 to 255) represent the entire dynamic range of the microscope.

Supplementary figure 3



SI Fig 3: Comparison between an image acquired on SAVAlexa surfaces and a corresponding simulated image a) Representative 63x IF image of SAVAlexa with approximately 5000 molecules per PSF (top) and simulated IF image based on a theoretical molecular density of 5000 molecules per PSF randomly placed (bottom). Both images presented the same grain-like structure b) IF images were divided into 8 x 8 sub-images for statistical reasons and to assess homogeneity in the micron scale. For each of the sub-images the ACF was calculated. c) *Via* the amplitude of ACF, the number of molecules per PSF was deduced. The grayscale maps show the number of molecules per PSF for each sub-image for the measured SAVAlexa sample and a similar simulated image. d) To calculate the areal mass density, the number of molecules was divided by the corresponding area of the PSF. The number of molecules per area was multiplied by a correction factor depending on the average number and distribution of Alexa fluorophores per SAV. This correction factor was measured by combining ICS with photobleaching as described elsewhere [1]. The areal mass density was then deduced *via* the molecular weight of SAVAlexa and is represented as a grayscale map. e) Calculating the mean number of molecules over the 64 sub-images covered the influence of photon noise, local statistical fluctuations of molecular distribution as well as difficult ACF fits of sub-images with only few pixels. The comparable CV between the simulated and the measured image suggested that SAVAlexa molecules immobilized on PLL-g-PEGbiotin50% follow a random placement and could be precisely quantified using ICS.

Supplementary figure 4



SI Fig 4: Binding kinetics of different BMPs to iHS and fitted curves for the calculation of EC_{50} values
a) QCM-D graph showing the change in frequency upon binding of BMP2,4,6,7 to iHS. Individual concentrations were chosen in a way that the shift in frequency between the BMP2,4,6,7 was in the range of factor 2. b) Graphs showing fitted dose response curves for sBMP2,4,6,7 and aBMP2,4,6,7 induced SMAD1/5/9 phosphorylation in C2C12 cells based on the data from **Figure 6**. The negative control is presented as -12 log BMP (g/ml) concentration. Curves were fitted with Origin using the dose response function with variable Hill slope (4-parameter logistic model) and R^2 and relative EC_{50} values were deduced. The data for aBMP6 was not possible to fit because an upper plateau was not reached.

Bibliographic references

- [1] J. Sefkow-Werner, E. Migliorini, C. Picart, D. Wahyuni, I. Wang, and A. Delon, “Combining fluorescence fluctuations and photobleaching to quantify surface density,” Oct. 2021, doi: arXiv:2110.14319.

II.E Transition

Biomimetic surfaces were automatically fabricated inside 96-well plates and characterized *in situ* with pbICS for molecular surface density. In some studies, ICS was used to quantify molecules at the cell perimeter but the technique was not yet adopted for surface characterization and was limited in accuracy for molecules heterogeneously labelled with different numbers of fluorophores. To be applicable for the quantification of biomimetic surfaces inside 96-well plates, we developed this technique in parallel to the development of the automation protocol. The next chapter presents the principle of pbICS to deduce information about the distribution of fluorophores on molecules with heterogeneous labelling and to characterize biomimetic surfaces *in situ* for molecular surface density.

Chapter III: Combining fluorescence fluctuations and photobleaching to quantify surface density

III.A Article summary (English)

2D biomimetic model surfaces are becoming a popular tool for cellular studies because they permit to represent selected aspects of the ECM to reveal signaling mechanisms in cells (Monteiro A., Kollmetz and Malmström, 2018). This demands for precise surface characterization regarding molecular surface density to permit conclusion on the quantitative role of the molecules of interest. Common techniques such as SE or QCM-D conduct measurements *ex situ* on specially adapted auxiliary surfaces and not on the surfaces used for cellular studies (Migliorini, Weidenhaupt and Picart, 2018). *In situ* techniques are often fluorescence-based, which includes labelling the molecules of interest with a dye but these techniques are only semi-quantitative or not adapted for dense monolayers. Either measured intensities are compared to a known standard, which in return demands for calibration, or, in the case of step-wise photobleaching, only samples with very low molecular density can be processed (Coffman and Wu, 2012). The field of fluorescence fluctuation spectroscopy (FFS) intends to quantify absolute molecular numbers in an observation volume and can be applied either in solutions *via* fluorescence correlation spectroscopy (FCS) or in the case of image correlation spectroscopy (ICS) on surfaces with immobilized molecules (Petersen *et al.*, 1993; Slaughter and Li, 2010). The principle behind these techniques is based on intensity fluctuations caused by a statistically varying number of molecules in the observation volume, which is defined by the known dimension of the microscope-specific PSF.

FCS measures the time-resolved fluorescence signal of molecules diffusing in solutions and thus continuously passing in and out of the PSF volume, which results in a fluctuating intensity signal. The amplitude of these fluctuations depends on the number of diffusing molecules in solution, which share the same characteristic diffusion constants. In case of high concentrations, the relative intensity fluctuations compared to the overall mean intensity are very low. For low concentrations in contrary, the effect is very pronounced. The relative amplitude of these fluctuations thus is directly related to the number of molecules in the PSF. To identify this amplitude based on the acquired time-resolved measurements, the ACF of the signal is calculated.

ICS is comparable to FCS but based on confocal images of immobilized molecules and aims at measuring the fluctuations between pixels (Petersen *et al.*, 1993). Here, molecules do not diffuse but the confocal laser scans the sample and each pixel thus represents the combined

signal of all molecules in the area of the PSF. The pixel size is chosen much smaller than the area of the PSF, which means that the intensity signal of adjacent pixels is based on a common fraction of molecules and is thus correlated to a certain extent. The amplitude of the intensity fluctuations between the pixels thus depends, as previously explained in FCS, on the number of molecules. The spatial ACF of the image is calculated and its amplitude reveals the number of molecules.

FCS methods work well if the number of fluorophores per molecule is homogenous, means, that all molecules carry exactly the same number. This, however, is not the case for commercially available large proteins, which are heterogeneously labeled with multiple fluorophores following a distribution with a mean (m) and a standard deviation (σ). Often, these two parameters are not known. Observed fluctuations in FCS and ICS thus do not just depend on the number of molecules but also on m and σ with an underestimation of the number of molecules in consequence (Müller, 2004; Kolin and Wiseman, 2007).

In this article, we aim at applying ICS for the first time to characterize molecular surface densities of biomimetic surfaces *in situ* and further address the bias caused by heterogeneous labelling with a photobleaching approach. By combining ICS or FCS with photobleaching (pbICS and pbFCS), we developed a self-calibrated method to deduce m and σ as well as the non-biased number of immobilized molecules on surfaces or molecules in solution.

First, we provided a theoretical description to take into account the heterogeneous labelling of molecules and the total number of molecules. Briefly, the total fluorescence signal is the average brightness of a molecule multiplied by the number of molecules. Due to the heterogeneous labelling, the brightness of a single molecule depends on the brightness of a single fluorophore, m and σ . The aim of the experimental set-up was to measure these three parameters and then to calculate the non-biased total number of molecules. Applying multiple bleaching steps, we destroyed fluorophores until the remaining signal is only based on one single fluorophore per molecule, which directly revealed one of the three parameters. The average brightness per molecule thus decreased over the course of the bleaching routine and the slope of this decrease was the second parameter deduced from the experiment. However, this single output parameter depends on the two parameters m and σ of the labelling distribution and thus had two degrees of freedom. Additional assumptions based on the measured average brightness and reasonable possible combinations of m and σ allowed to define a range for the parameters m and σ .

With pbICS we quantified a SA_vAlexa monolayer at different surface concentrations ranging over two orders of magnitude and validated the results with comparable SE measurements (Sefkow-Werner *et al.*, 2021). In addition, with this highly sensitive method we detected the adsorption of the small biotinylated molecule bAtto to SA_v, which was not measurable with SE. pbFCS control experiments of those molecules dissolved in solution and confined in small micro-wells generated comparable results for the values m and σ .

The proposed set of self-calibrated and sensitive methods served to characterize densely or thinly functionalized biomimetic surfaces *in situ*. Additional information about m and σ was deduced and once characterized with photobleaching, simple ICS or FCS data without photobleaching could be corrected posterior.

III.B Article summary (French)

Les surfaces modèles biomimétiques 2D deviennent un outil populaire pour les études cellulaires car elles permettent de représenter certains aspects de l'ECM afin de révéler les mécanismes de signalisation dans les cellules (Monteiro A., Kollmetz et Malmström, 2018). Cela exige une caractérisation précise de la surface concernant la densité de la surface moléculaire pour permettre de conclure sur le rôle quantitatif des molécules d'intérêt. Les techniques courantes telles que la SE ou la QCM-D effectuent des mesures *ex situ* sur des surfaces auxiliaires spécialement adaptées et non sur les surfaces utilisées pour les études cellulaires (Migliorini, Weidenhaupt et Picart, 2018). Les techniques *in situ* sont souvent basées sur la fluorescence, ce qui inclut le marquage des molécules d'intérêt avec un colorant mais ces techniques ne sont que semi-quantitatives ou non adaptées aux monocouches denses. Soit les intensités mesurées sont comparées à un standard connu, ce qui demande en retour une calibration, soit, dans le cas du photoblanchiment par paliers, seuls les échantillons à très faible densité moléculaire peuvent être traités (Coffman et Wu, 2012). Le domaine de la spectroscopie de fluctuation de fluorescence (FFS) vise à quantifier le nombre absolu de molécules dans un volume d'observation et peut être appliqué soit dans des solutions *via* la spectroscopie de corrélation de fluorescence (FCS), soit dans le cas de la spectroscopie de corrélation d'image (ICS) sur des surfaces avec des molécules immobilisées (Petersen et al., 1993 ; Slaughter et Li, 2010). Le principe de ces techniques est basé sur les fluctuations d'intensité causées par un nombre statistiquement variable de molécules dans le volume d'observation, qui est défini par la dimension connue du PSF spécifique au microscope.

La FCS mesure le signal de fluorescence résolu dans le temps des molécules qui diffusent dans les solutions et qui entrent et sortent donc continuellement du volume PSF, ce qui entraîne une fluctuation du signal d'intensité. L'amplitude de ces fluctuations dépend du nombre de molécules diffusant dans la solution, qui partagent les mêmes constantes de diffusion caractéristiques. Dans le cas de concentrations élevées, les fluctuations d'intensité relatives par rapport à l'intensité moyenne globale sont très faibles. Pour de faibles concentrations au contraire, l'effet est très prononcé. L'amplitude relative de ces fluctuations est donc directement liée au nombre de molécules dans le PSF. Pour identifier cette amplitude à partir des mesures acquises en temps résolu, on calcule l'ACF du signal.

L'ICS est comparable à la FCS mais se base sur des images confocales de molécules immobilisées et vise à mesurer les fluctuations entre les pixels (Petersen et al., 1993). Ici, les molécules ne diffusent pas mais le laser confocal balaie l'échantillon et chaque pixel représente donc le signal combiné de toutes les molécules dans la zone du PSF. La taille du pixel est choisie beaucoup plus petite que la zone du PSF, ce qui signifie que le signal d'intensité des pixels adjacents est basé sur une fraction commune de molécules et est donc corrélé dans une certaine mesure. L'amplitude des fluctuations d'intensité entre les pixels dépend donc, comme expliqué précédemment dans FCS, du nombre de molécules. L'ACF spatial de l'image est calculé et son amplitude révèle le nombre de molécules.

La méthode FFS fonctionne bien si le nombre de fluorophores par molécule est homogène, c'est-à-dire que toutes les molécules en portent exactement le même nombre. Ce n'est toutefois pas le cas des grandes protéines disponibles dans le commerce, qui sont marquées de manière hétérogène avec de multiples fluorophores suivant une distribution avec une moyenne (m) et un écart-type (σ). Souvent, ces deux paramètres ne sont pas connus. Les fluctuations observées dans les FCS et ICS ne dépendent donc pas seulement du nombre de molécules mais aussi de m et σ avec une sous-estimation du nombre de molécules en conséquence (Müller, 2004 ; Kolin et Wiseman, 2007).

Dans cet article, nous visons à appliquer l'ICS pour la première fois afin de caractériser les densités de surface moléculaire de surfaces biomimétiques *in situ* et de traiter le biais causé par le marquage hétérogène avec une approche de photoblanchiment. En combinant ICS ou FCS avec le photo-blanchiment (pbICS et pbFCS), nous avons développé une méthode auto-calibrée pour déduire m et σ ainsi que le nombre non biaisé de molécules immobilisées sur des surfaces ou de molécules en solution.

Tout d'abord, nous avons fourni une description théorique pour prendre en compte le marquage hétérogène des molécules et le nombre total de molécules. En bref, le signal de fluorescence total est la luminosité moyenne d'une molécule multipliée par le nombre de molécules. En raison de l'étiquetage hétérogène, la luminosité d'une seule molécule dépend de la luminosité d'un seul fluorophore, de m et de σ . L'objectif du dispositif expérimental était de mesurer ces trois paramètres, puis de calculer le nombre total de molécules sans biais. En appliquant plusieurs étapes de blanchiment, nous avons détruit les fluorophores jusqu'à ce que le signal restant ne soit basé que sur un seul fluorophore par molécule, ce qui a révélé directement l'un des trois paramètres. La luminosité moyenne par molécule a donc diminué au

cours de la routine de blanchiment et la pente de cette diminution a été le deuxième paramètre déduit de l'expérience. Cependant, ce paramètre de sortie unique dépend des deux paramètres m et σ de la distribution de l'étiquetage et avait donc deux degrés de liberté. Des hypothèses supplémentaires basées sur la luminosité moyenne mesurée et des combinaisons raisonnables possibles de m et σ ont permis de définir une plage pour les paramètres m et σ .

Avec pbICS, nous avons quantifié une monocouche de SAVAlexa à différentes concentrations de surface allant sur deux ordres de grandeur et validé les résultats avec des mesures comparables de SE (Sefkow-Werner et al., 2021). En outre, avec cette méthode très sensible, nous avons détecté l'adsorption de la petite molécule biotinylée bAtto sur SAV, qui n'était pas mesurable avec SE. Les expériences de contrôle pbFCS de ces molécules dissoutes en solution et confinées dans de petits micropuits ont généré des résultats comparables pour les valeurs m et σ .

L'ensemble proposé de méthodes sensibles et auto-calibrées a permis de caractériser *in situ* des surfaces biomimétiques densément ou finement fonctionnalisées. Des informations supplémentaires sur m et σ ont été déduites et une fois caractérisées avec le photoblanchiment, les simples données ICS ou FCS sans photoblanchiment ont pu être corrigées a posteriori.

Combining fluorescence fluctuations and photobleaching to quantify surface density

Julius Sefkow-Werner,^{†,¶} Elisa Migliorini,^{*,†} Catherine Picart,[†] Dwiria Wahyuni,^{‡,§}

Irène Wang,[‡] and Antoine Delon^{*,‡}

[†] *BRM ERL 5000 CEA/CNRS/UGA, France*

[‡] *LIPHY, Université Grenoble Alpes and CNRS, F-38000 Grenoble, France*

[¶] *Univ. Grenoble Alpes, CNRS, Grenoble INP, LMGP, 38000 Grenoble, France*

[§] *Current address: Tanjungpura University, Pontianak, Indonesia*

E-mail: elisa.migliorini@cea.fr; antoine.delon@univ-grenoble-alpes.fr

Abstract

We establish a self-calibrated method, called *pbFFS* for *photobleaching Fluctuation Fluorescence Spectroscopy*, which aims at characterizing molecules or particles labelled with an unknown distribution of fluorophores. Using photobleaching as a control parameter, pbFFS provides information on the distribution of fluorescent labels and a more reliable estimation of the absolute density or concentration of these molecules. We present a complete theoretical derivation of the pbFFS approach and experimentally apply it to measure the surface density of a monolayer of fluorescently tagged streptavidin molecules that can be used as a base platform for biomimetic systems. The surface density measured by pbFFS is consistent with the results of spectroscopic ellipsometry, a standard surface technique. However, pbFFS has two main advantages: it enables *in situ* characterization (no dedicated substrates are required) and is applicable to low masses of adsorbed molecules, as demonstrated here by quantifying the

density of biotin-Atto molecules that bind to the streptavidin layer. Besides molecules immobilized on surfaces, we also applied pbFFS to molecules diffusing in solution, to confirm the distribution of fluorescent labels found on surfaces. Hence, pbFFS provides a set of tools to investigate molecules labelled with a variable number of fluorophores, with the aim to quantify either the number of molecules or the distribution of fluorescent labels, the latter case being especially relevant for oligomerization studies.

Introduction

Biomimetic approaches are popular in medical applications and cellular studies. As the extracellular matrix (ECM) plays a complex role on cell response to drugs, growth factors and morphological cues,¹ it is advantageous to design biomaterials mimicking the natural environment of cells in the body for enhancing the efficiency of biomedical products. Moreover these biomaterials can bring a deeper understanding of the influence of selected components of the ECM on cellular processes such as proliferation, migration and differentiation.² Developing these platforms requires a precise control of the immobilized compounds. Standard surface techniques include spectroscopic ellipsometry and quartz crystal microbalance with dissipation monitoring (QCM-D).^{3,4} However, these techniques are *ex situ* since the platforms have to be built on auxiliary substrates, which may affect the functionalization process. Moreover, low masses of adsorbed molecules cannot be detected by the above techniques. Fluorescence-based methods would, in principle, allow *in situ* characterization (i.e. with the substrates used for cellular studies), as well as detection of small surface densities of adsorbed molecules.

Using fluorescently-labelled molecules, a simple image provides relative information on molecular density through its intensity, but estimating the absolute value of the number of molecules requires additional and fragile calibrations.⁵ There are alternative approaches based on single molecule strategies, but they are adapted only for very low surface densities.⁶ On the other hand, Fluorescence Fluctuation Spectroscopy (FFS) techniques,⁷ and

more specifically Image Correlation Spectroscopy (ICS) which is suited to the characterization of immobile molecules, are intended for absolute quantification. These methods derive historically from Fluorescence Correlation Spectroscopy (FCS) and are based on the notion that signal originating from a submicrometric region within the sample, corresponding to the Point Spread Function (PSF) of the microscope, exhibits statistical fluctuations, since this PSF region does not always include the same number of molecules. The relative amplitude of these fluctuations provides an estimation of the average number of molecules in the PSF region and hence the concentration or density. Molecules cross the PSF either by spontaneous motion, as in the case of FCS, or by scanning the excitation laser (as in confocal microscopy), as in the case of ICS. ICS has been used to assess oligomerization,⁸ or qualitatively detect the presence of aggregates through an increase of brightness or a corresponding decrease of number density.^{9,10}

In fact, standard FFS techniques can only provide reliable quantitative information if all molecules have the same brightness (or if the distribution of brightness is known). Yet commercially available large proteins are rarely all labelled with the same number of fluorophores, so that they present a distribution of brightness. In this case, the number density of fluorescent entities (molecules or particles) estimated by conventional FFS is underestimated: indeed, part of the measured fluctuations would be due to variations in brightness and not only in number of entities, as usually assumed in FFS. More precisely, if the brightness distribution is characterized by a mean value, $\bar{\epsilon}$ and a standard deviation, σ_{ϵ} , it can be shown (following^{9,11}) that the mean number of entities in the PSF volume or area, as measured by FFS, is related to the true number of entities, N , by:

$$N_{FFS} = \frac{N}{1 + (\sigma_{\epsilon}/\bar{\epsilon})^2} \quad (1)$$

Consequently, the wider the brightness distribution, the more pronounced the underestimation of the number density. The same bias affects the estimation of average brightness (which

tends to be overestimated). Using only standard FFS methods, there is no way to evaluate this bias.

The present work aims at using photobleaching as a control parameter to measure accurately the density of surfaces coated with multiply-labelled entities. The combination of FFS and photobleaching has been proposed previously and used to estimate the degree of fluorescent labelling,¹² the size of oligomers^{13,14} or the surface density of molecules.¹⁵ However the practical implementations were either limited to the specific case of a Poisson distribution of brightness,^{12,15} or failed to decipher the real parameters that could be deduced from the photobleaching decay.^{13,14} We present here a complete theoretical description of a method combining ICS to photobleaching, which is not specific to ICS and can be extended to other FFS techniques (for instance FCS, as in¹²): we name it *pbFFS* for *photobleaching FFS*. Compared to previous work, we present a more in-depth theoretical derivation. We show that the measured brightness always decays linearly with photobleaching, whatever the distribution of fluorescent labels, and hence exactly two outputs can be extracted from this decay: (i) the brightness of a single fluorescent label, (ii) a factor depending on the mean and variance of the number of fluorescent labels per entity. We stress the fact that the presented method has the advantage to be *calibration free*.

The pbFFS method is experimentally validated on substrates covered with monolayers of streptavidin molecules via a linker, used as a platform to build biomimetic surfaces step by step by adsorbing biotinylated molecules on top of it.^{3,16} We applied pbFFS to streptavidin (SAv), fluorescently tagged with Alexa (SAv-Alex). Thanks to an additional assumption about the fluorescent labelling, we could bracket the mean number of fluorescent labels per SAv and, hence, estimate the absolute number density of SAv molecules covering the substrate. The resulting densities have been validated by independent spectroscopic ellipsometry measurements. We show that pbFFS is capable of measuring SAv surface densities that span over two orders of magnitude. Then, pbFFS was used to quantify the number of biotinylated fluorescent molecules (Atto labelled biotin, bAtto) that attach to a streptavidin base layer.

In this case, the mass of adsorbed molecules was too low to be measured with accuracy by QCM-D or ellipsometry (since the mass of bAtto is only 1 kDa as compared to SA_v which is 55 kDa). Interestingly, we also found by performing control photobleaching-FCS experiments that bAtto molecules are prone to aggregation in solutions, which potentially impacts the way they bind to the SA_v base layer.

Principles of photobleaching Fluctuation Fluorescence Spectroscopy

As illustrated in Fig. 1A and D, a pbFFS experiment consists in alternating photobleaching phases, where a high laser power is sent into the sample to bleach a fraction of the fluorescent labels (e.g. Alexa) borne by the entities (e.g. streptavidin) and measurement phases at a reduced laser power. During the latter, the fluorescence signal, F , the mean number of entities, N_{FFS} and the brightness, defined as $B_{FFS} = F/N_{FFS}$, are measured. As more fluorescent labels are photobleached, the image intensity (in ICS, Fig. 1B) or the photon count rate (in FCS, Fig. 1C) decreases, while the autocorrelation amplitude increases, denoting a reduction of the number of entities N_{FFS} in the PSF submicrometric region.

We consider a sample consisting of entities labelled with multiple fluorophores of identical brightness, ϵ . The distribution of the number of these labels per entity before photobleaching is characterized by its mean and its standard deviation, named respectively m and σ . It can be shown (see Section S1 of the Supporting Information (SI)) that the measured brightness B_{FFS} is an affine function of the photobleaching stage p , defined as the fluorescence signal normalized to its initial value, i.e. $p = F/F(1)$:

$$B_{FFS}(p) = \epsilon(1 + S_{\sigma m}p) \quad (2)$$

where $S_{\sigma m}$ is the slope normalized by the single label brightness. It is related to the standard

deviation and mean value of the distribution according to:

$$S_{\sigma m} = \sigma^2/m + m - 1 \quad (3)$$

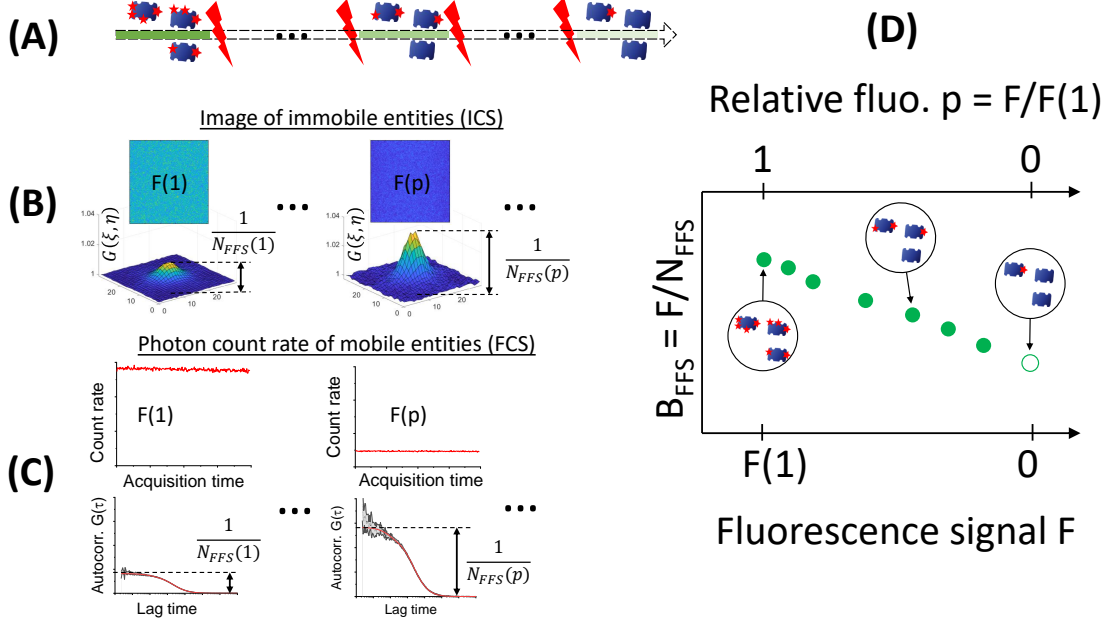


Figure 1: Principle of a pbFFS experiment. Part (A) shows, along the dashed arrow, the photobleaching phases (red flashes) that alternate with the measurement phases (green sections of decreasing intensities). During the latter, the number of unbleached fluorescent labels borne by the entities decreases. The fluorescence signal, F , corresponds to the mean image intensity of immobilized fluorescent entities measured by ICS (B), or to the mean photon count rate of mobile fluorescent entities measured by FCS (C). The number of entities measured by FFS, N_{FFS} , also decreases as can be seen by the increased amplitude of the spatial autocorrelation in ICS, $G(\xi, \eta)$, or temporal autocorrelation in FCS, $G(\tau)$. Part (D) shows that the brightness measured during the successive phases, defined as $B_{FFS} = F/N_{FFS}$, plotted *vs* the fluorescence signal, monotonously decreases upon photobleaching and tends towards that of a single fluorescent label.

The true total number of entities is then given by:

$$N = F(1)/m\epsilon \quad (4)$$

The linear decay of the measured brightness *versus* the fluorescence signal is valid for any

distribution of fluorescent labels, assuming that all fluorescent labels have the same brightness, ϵ and a constant probability to bleach, whatever their number in the entities. A straightforward result of any pbFFS experiment is the single label brightness, ϵ . This is an interesting output since, using Eq. 4, one can derive the total number of fluorescent labels, $Nm = F(1)/\epsilon$. The exploitation of the slope, $S_{\sigma m}$, is more complex, because we see from Eq. 3 that, in the general case, it is impossible to independently determine the mean value, m and the standard deviation, σ , of the number of fluorescent labels per entity. However, specific fluorescent label distribution add constraints such that, in practice, the m values are reduced to some range (For details see Section S2 in SI). This is the case for the SAV monolayer, as discussed in the next section.

Implementation of the analysis method

Effect of background

When performing pbFFS experiment we sometimes observe, both on surface and in solution, photobleaching decays that do not exhibit a linear behavior (as the red line in the schematic Fig. 2A), but drop down to lower values of the brightness when the fluorescence signal gets small (green curve). This is due to an uncorrelated background, BG , that contributes to the detected signal, thus making the relative fluctuations smaller and consequently the apparent number of entities larger, hence a lower brightness, as described in.¹⁷ It is nevertheless possible to incorporate the background as a free parameter in the photobleaching decay analysis by rewriting Eq. 2 as:

$$B_{FFS}(p) = \epsilon \left(1 - \frac{r_{BG}}{p} \right) \left(1 + S_{\sigma m} \frac{p - r_{BG}}{1 - r_{BG}} \right) \quad (5)$$

where $r_{BG} = BG/F(1)$ stands for the background normalized to the total initial signal (i.e. including the background itself). Correspondingly, p becomes the relative total signal,

including the background. The latter originates, either from light scattering (due to the glass substrate or to the walls of the PDMS microwells), or from some bulk fluorescence that would be not properly filtered out by the confocal detection. This effect appeared to be especially pronounced and difficult to mitigate in solutions. The fit of the photobleaching decay shown in Fig. 2A thus gives the parameters ϵ , $S_{\sigma m}$ (and BG , if relevant).

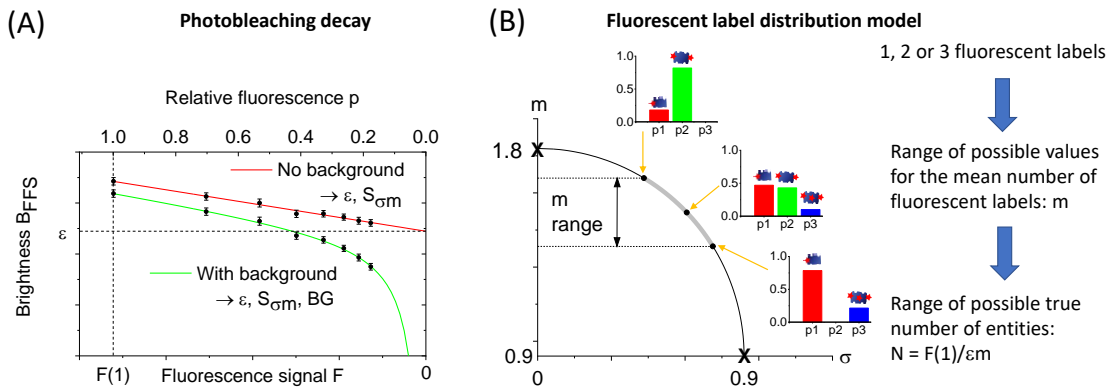


Figure 2: Schematics of the implementation of the brightness decay analysis: (A) Upon photobleaching, the brightness, B_{FFS} , decreases linearly *versus* the fluorescence signal, F or p (red solid line), thus providing the output parameters ϵ and $S_{\sigma m}$; in case of background (green solid line) an additional parameter, BG , can be estimated by fitting the decay (see text for details). (B) By combining the relation between m and σ corresponding to the measured value of $S_{\sigma m}$ and the constraints deriving from three non-nil probabilities (p_1 , p_2 and p_3 for 1, 2 or 3 fluorescent labels), the possible m values are restricted to a limited range; three examples of distributions of probabilities corresponding to the minimum, maximum and central values of m are depicted for $S_{\sigma m} = 0.8$. Finally, this analysis provides a value of the mean number of fluorescent labels, m , which combined with the initial fluorescence signal, $F(1)$ and the parameter ϵ , leads to an estimation of the true number of entities, N .

Taking into account the fluorescent label distribution

The degree of fluorescent labelling of SAv-Alex given by the manufacturer being 2, we take this number as an approximate value and consider that each SAv protein can bear 1, 2 or 3 Alexa labels, with probabilities p_1 , p_2 and p_3 . The key point is that this discrete distribution of probabilities has only 2 independent degrees of freedom (since, once the probabilities p_1 and p_2 are known, the last one, p_3 , automatically follows). Additionally, we show in SI, Section S1, that, due to Eq. 3, the σ , m values are constrained along a circle. Combined

with the properties of the distribution, this leads to a limited range of possible mean number of fluorescent labels. In our current situation, it can be shown (see SI, Section S2, Eq. S11 to S15 and Fig. S1) that if $S_{\sigma m} \leq 1$, then $\frac{3}{3-S_{\sigma m}} \leq m \leq \frac{2}{2-S_{\sigma m}}$, while if $1 < S_{\sigma m} \leq 2$, then $\frac{3}{3-S_{\sigma m}} \leq m \leq \frac{6}{4-S_{\sigma m}}$ (we never measured $S_{\sigma m} > 2$). Fig. 2B schematically shows a few examples of distributions of probabilities (p_1, p_2, p_3) , which correspond to the value $S_{\sigma m} = 0.8$ that is often found for SA_v-Alex, spanning from the narrowest distribution (minimum value of σ), with the largest mean value, m , to the widest one, with the smallest m . Clearly, the latter distribution is unrealistic, as it would correspond to SA_v proteins that never bear 2 fluorescent labels, while most of them bear 1 fluorescent label and some 3! It can be shown (SI, Section S2) that the condition to have a probability to bear 3 fluorescent labels smaller than that for 2 implies $m > \frac{1}{1-\frac{3}{8}S_{\sigma m}}$.

Interestingly, if we had hypothesised that SA_v proteins could bear 2, 3 or 4 Alexa labels, this would lead to, either no solution when $S_{\sigma m} < 1$ or, for the few cases where we measured $1 \leq S_{\sigma m} \leq 1.5$, to a vast majority of SA_v molecules bearing 2 Alexa labels and almost none bearing 3 or 4, which is consistent with the model retained throughout this work (see Section S2 of SI, Eq. S16).

Concerning the biotinylated fluorescent molecules, it is clear from the bAtto formula (given in the product specification) that they correspond to one single Atto dye. However, as already noted above, as a SA_v protein of the base layer exposes from 1 to 3 free biotin binding sites, several bAtto molecules can colocalize on a single SA_v protein. Therefore, we also assume that biotinylated entities can bear 1, 2 and 3 fluorescent labels.

To conclude, from the analysis of the brightness decay, we obtain a range of values for m , and hence a range of values for the true number of fluorescent entities, $N = F(1)/m\epsilon$, which in turn leads to the final surface density given by $N/\pi w_r^2$.

Experimental results

Streptavidin layers are densely packed

Photobleaching ICS experiments have been performed on SAV layers with different percentages of fluorescently labelled SAV (SAV-Alex) of 1%, 10%, 50% and 100%. Since ICS usually performs better for relatively low surface densities, these dilutions aimed at testing the robustness of our method in a range of densities relevant for biomimetic surfaces. See Section S4 of SI about sample preparation, acquisition protocol and data analysis.

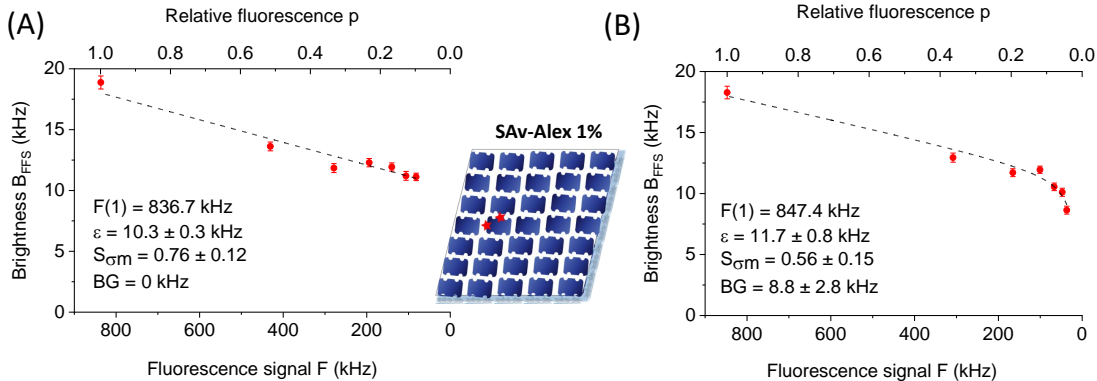


Figure 3: Characteristic brightness decay *versus* the fluorescence signal for a SAV layer prepared with 1% dilution of SAV-Alex. (A) Example without background (i.e. fixed to 0), showing the linear decay and the fit (dashed black line) with the ϵ and $S_{\sigma m}$ outputs corresponding to the measured (red) points; the errors bars are the standard errors of the mean calculated from 8×8 sub-images; (B) In presence of background, the corresponding parameter, BG , can be fitted (it represents about 1% the initial fluorescence signal, $F(1)$), while the other outputs, ϵ and $S_{\sigma m}$, are consistent with the results of the background-free case.

We see in Fig. 3A a plot of a characteristic brightness decay *versus* the fluorescence signal obtained for 1% dilution of SAV-Alex. The parameters estimated from the fit, $\epsilon = 10.3$ kHz and $S_{\sigma m} = 0.76$, correspond to an initial brightness, given by $B_{FFS}(1) = \epsilon(1 + S_{\sigma m})$, that is about 1.8 times larger than the single fluorescent label brightness. Consequently, if the distribution of the number of fluorescent labels per molecule was single-valued, one would be close to the situation of 2 Alexa dyes per SAV, which corresponds to the manufacturer specifications. However, using the theory presented in Section S2 of SI, we can estimate

the range of m values compatible with both the possible numbers of fluorescent labels and the estimated value of $S_{\sigma m}$ at [1.40, 1.61] (see SI, Section S2, Fig. S1 and Eq. S14). This corresponds to a surface density of fluorescently labelled SAV, at 1% dilution, in the range of 316-363 molecules per μm^2 (using $w_r = 0.22 \mu m$ for this data set). We also show, in Fig. 3B, another result obtained with the same dilution of SAV-Alex, but exemplifying the consequence of a background on the brightness decay. Although the background accounts only for about 1% of the total initial signal, the deformation from linearity of the brightness decay is very pronounced at the end of the process. However, the decay can still be well fitted using one additional parameter, BG , while the other parameters remain consistent with their values estimated without background.

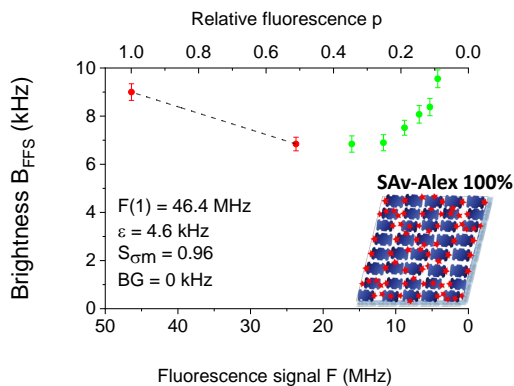


Figure 4: Example of the dramatic consequence, for the brightness decay, of the fluorescence quenching between Alexa555 fluorophores of a streptavidin layer prepared with 100% of SAV-Alex. Note that the single fluorescent label brightness, ϵ , is more than twice smaller than its value at high dilution (see Fig. 3), while the $S_{\sigma m}$ parameter, estimated from the 2 first points, stays consistent.

A physically different situation occurs at high surface densities of fluorescently labelled SAV, as shown in Fig. 4 for a layer containing 100% of SAV-Alex. This curve exhibits a dramatic brightness recovery after an initial decay. By fitting the first part of the brightness variation, assumed to be linear, we estimated the $S_{\sigma m}$ parameter at a value, 0.96, reasonably close to the one measured at 1% dilution. Conversely, the single fluorescent label brightness, $\epsilon = 4.6 \text{ kHz}$, is found to be more than 2 times lower than the value measured at high

dilutions of SAV-Alex (see Fig. 3). We suggest that fluorescence quenching between identical fluorophores can explain this behavior: at 100% concentration, the mean distance between the Alexa555 dyes is of the order of the size of the streptavidin molecules, that is ≈ 5 nm. At such short distances, the reduction of the fluorescence quantum yield can be very pronounced.¹⁸ When photobleaching occurs, the mean distance between intact fluorescent labels increases, thereby reducing self-quenching so that the brightness tends towards its normal value. Because this is not within the scope of the present work, we did not study further the exact shape of the brightness curve, but we tentatively made use of the 100% concentration results to estimate the surface density of SAV. Using the waist size found for this 100% SAV-Alex case, $w_r = 0.25\mu m$ and $m = 1.7$ (middle of the range corresponding to $S_{\sigma m} = 0.96$), we estimate 30330 streptavidin molecules per μm^2 . First, this number is close to 100 times the surface density measured at 1% dilution. Second, it corresponds to a mean distance of 5.7 nm between streptavidins, which is consistent with the assumption of a densely packed layer, given the size of a streptavidin molecule.¹⁹ Therefore, although based solely on the first 2 points, the results obtained for 100% of fluorescently labelled SAV are compatible with the lower-density case. Experiments have also been performed with 10% and 50% dilutions, the results of which are reported and synthesized in Table 1. Overall, our SAV-Alex results are consistent with each other, with a clear trend towards more fluorescent quenching as the surface density of SAV-Alex increases.

Streptavidin in solution has the same fluorescent label distribution

In order to get an independent estimation of the fluorescent label distribution, we also applied our method to SAV-Alex molecules freely diffusing in solution. We found a value of $S_{\sigma m}$ very consistent with the estimations on surfaces (around 0.8), as illustrated in Fig. 5A. As a control case, Fig. 5B shows that Sulforhodamine B sodium salt (SRB) solutions lead to a constant brightness when photobleaching, as expected for a single dye molecule.

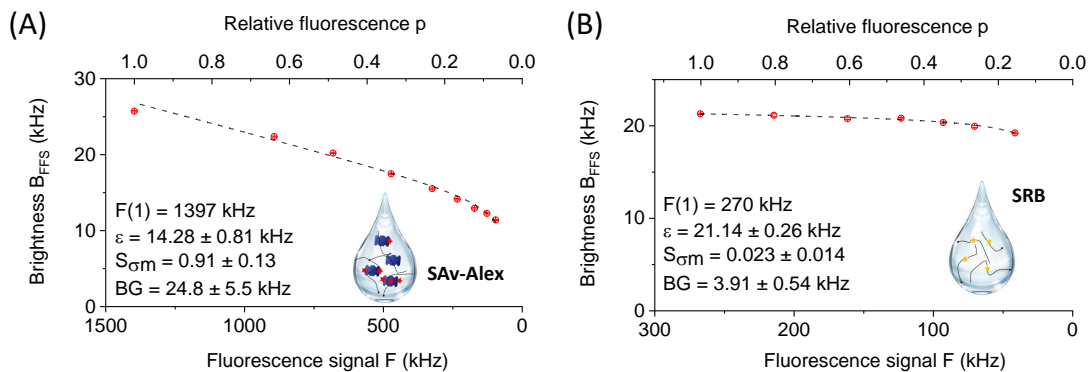


Figure 5: Examples of brightness decays measured by FCS, for solutions confined in PDMS microwells. (A) SAV-Alex molecules, where the normalised slope, $S_{\sigma m}$, is close to its value found on surfaces (see Fig. 3); (B) SRB in HEPES, clearly showing an almost constant brightness, in agreement with the expected behavior of a single dye molecule. For both cases a background of up to 2% is estimated. Note that the error bars are smaller than the point size.

Biotinylated molecules bind to about 10% of the streptavidin base layer

Next we investigated the surface density of biotinylated molecules deposited on top of SAV layers, in order to show the potential of pbFFS as a characterization tool for developing biomimetic surfaces. Fluorescent bAtto molecules bound on a streptavidin base layer were observed. The brightness decay, as shown in Fig. 6A, exhibits a normalized slope, $S_{\sigma m} = 0.21$, which is significantly smaller than the one observed for a SAV-Alex layer. This means that this case is close to the one of a single fluorescent label per labelled SAV. Assuming the same type of distribution (i.e. over 1, 2 or 3 fluorescent labels), the range of m values that corresponds to $S_{\sigma m} = 0.21$ is estimated to $[1.08, 1.12]$ (see SI, Fig. S1 and Eq. S14). Two quantities can be estimated from these measurements: the surface density of bAtto molecules given by $F(1)/\varepsilon\pi w_r^2$, which is 3708 molecules per μm^2 and the density of *fluorescently labelled* SAV given by $F(1)/(m\varepsilon\pi w_r^2)$ with $m = 1.1$, center of the range estimated above, which is approximately $3370/\mu\text{m}^2$. Since we found previously ~ 30330 SAV per μm^2 in the base layer, this implies that about 1 in 10 SAV molecules can carry a bAtto molecule. Note that the areal

mass density reported, from different experiments, in Table 1 is that of bAtto molecules.

Each SAV has 4 biotin binding sites: at least one of these is used to bind to the PLL-g-PEGbiotin base layer, so that the *a priori* number of available sites for bAtto is between 0 and 3. Our data indicate that many SAV molecules could not bind any bAtto, presumably due to steric hindrance. More precisely, using $m \sim 1.1$, we can deduce that among the *fluorescently labelled* SAV, about 90% of SAV bound only one bAtto (see Eq. S12 in SI), leaving 10% that carry more than one bAtto. Two mechanisms can lead to this distribution: either bAtto bind to SAV as single molecules, in which case a few SAV have more than one occupied biotin-binding pocket, or bAtto preexist as dimers, trimers, etc. in the solution used for incubation, in which case, SAV may present only one pocket occupied by a bAtto complex. Indeed, the fact that Atto dyes are moderately hydrophilic²⁰ could favor aggregation.

To assess bAtto aggregation in solution, we performed pbFFS experiments with bAtto solutions (FCS), as reported in the next paragraph.

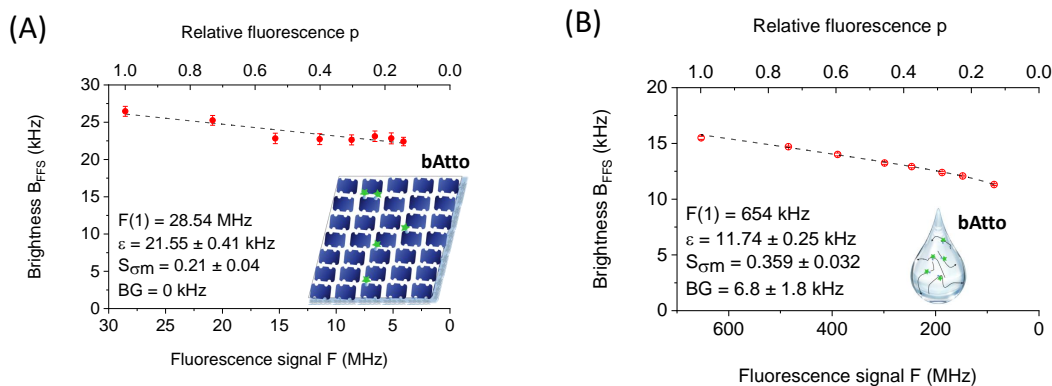


Figure 6: Brightness decay of biotinylated fluorescent molecules (bAtto), measured on surface and in solution. (A) ICS measurements for bAtto bound to a streptavidin base layer, exemplifying the lower normalised slope value, $S_{\sigma m} = 0.21$, compared to SAV-Alex (the fact that bAtto exhibits a single fluorescent label brightness different from that of Alexa555 labelled SAV is only due to the photophysical properties of these dyes); (B) FCS measurements for bAtto freely diffusing in solution. Note that the error bars are smaller than the point size.

Biotinylated molecules slightly aggregate in solution

We show in Fig. 6B an example of a photobleaching experiments with bAtto in solution. Globally, we recovered values of the normalised slope close to those found on surface (i.e. $S_{\sigma m} \approx 0.2 - 0.3$), which is clearly distinct from the single molecule case of SRB in solution shown in Fig. 5B. This range of values for $S_{\sigma m}$ corresponds (see SI, Fig. S1) to a mean number of fluorescent labels per diffusing entity, m , between 1 and 1.2, as summarized in Table 1. Since one bAtto molecule definitively corresponds to a single Atto dye, we conclude that unspecific aggregation occurs between bAtto molecules in solution, despite the moderate concentration ($< \mu\text{M}$). As a consequence, although the concentrations used to incubate the SAV base layer with bAtto are much lower than those used for FCS experiments (which should mitigate the aggregation trend), we cannot exclude that each SAV has only one bAtto binding site occupied by an aggregate. In this case, the number of available biotin binding sites on the SAV layer is not that of the number of bound bAtto molecules (i.e. $3708 / \mu\text{m}^2$) but rather that of the number of SAV molecules labelled with bAtto (i.e. $3370 / \mu\text{m}^2$).

Note that the difference in brightness between bAtto in solution and on a SAV layer, shown in Fig. 6, is not relevant, as the ICS and FCS experiments are performed on surface and in bulk, respectively (with different microscopy setups). The same remark stands for SAV results shown in Fig. 5A and Fig. 3.

Table 1: Degree of fluorescent labelling (m values) and areal mass density (when applicable) measured with pbFFS for different molecules, on surface and in solution. For SAV-Alex molecules diluted at 50, 10 and 1%, the estimated areal mass density is linearly extrapolated to 100% SAV. Values are given as mean \pm SD

Molecule	Sample	Fluo. Label.	Density (ng/cm^2)
SAV-Alex	Surface 100%	1.79 ± 0.39	239 ± 34
SAV-Alex	Surface 50%	1.22 ± 0.05	303 ± 50
SAV-Alex	Surface 10%	1.94 ± 0.22	293 ± 69
SAV-Alex	Surface 1%	1.74 ± 0.36	284 ± 70
SAV-Alex	Solution	1.58 ± 0.18	n/a
bAtto	Surface	1.13 ± 0.09	0.82 ± 0.23
bAtto	Solution	1.125 ± 0.057	n/a
SRB	Solution	1.013 ± 0.011	n/a

pbFFS results agree with spectroscopic ellipsometry

We present in Table 1 the degree of fluorescent labelling (m) corresponding to different molecules, SAv-Alex, bAtto and SRB, in solution and on surfaces. For each case, the lower and upper values of the m ranges estimated for the different experiments were pooled altogether to give a mean and a standard deviation (SD) of m . When applicable, these values were then used to derive the areal mass density of SAv molecules. Although the photobleaching decay curves of 100% SAv-Alex have a limited number of exploitable points (due to the above mentioned quenching effect), the corresponding pbFFS estimation of the density is in fairly good agreement with the spectroscopic ellipsometry result that gives $246 \pm 36 \text{ ng/cm}^2$.²¹ The linear extrapolation to 100% SAv of the SAv-Alex molecules diluted at 1, 10 and 50% tends to show a higher areal mass density, but this effect may be related to the uncertainty of dilutions. We also stress the fact that, although the degree of labelling found for 50% dilution differs from the other cases, the corresponding areal mass density stays consistent with the other results.

Concerning bAtto, the reported areal mass density of $0.82 \pm 0.23 \text{ ng/cm}^2$ is that of the total number of bAtto molecules bound to the SAv base layer. This value holds whatever the distribution of bAtto on SAv molecules. Note that such low density could not be measured by ellipsometry, so that no comparison can be made.

Discussion

We have presented a method, named pbFFS, which aims at estimating the number density of entities of non uniform brightness. We have shown its potential for more reliable quantification of surface density in the context of biomimetic layer characterization. Hereafter, we discuss two limiting situations.

In this work, we have measured surface densities spanning two orders of magnitude, from ~ 300 to ~ 30000 molecules per μm^2 . This latter value is probably close to the highest

density that can be measured using ICS. Indeed, at high concentration/density of molecules, the relative intensity fluctuations and thus, the autocorrelation amplitude, are very small and may be hidden behind unwanted variations (non-uniformity of the imaging system or the sample). Therefore, it is quite important to properly flatten images, check stability of solutions, etc. High densities can also induce some detrimental photophysical effects, such as quenching. However, we experimentally showed that this does not prevent correct results, provided the biased data points are taken off from the analysis.

The streptavidin molecules studied here were labelled by 1 to 3 fluorophores, so the degree of fluorescent labelling was rather low. One may wonder whether pbFFS would also be suitable for studying entities with a higher degree of fluorescent labelling (several tens of fluorophores or more). In this case, the photobleaching process starts with entities that are initially very bright and must be carried out till only single fluorescent labels are left, which requires a high dynamic range of detection. Using fluorescent nanospheres we could check that, in principle, our framework also applies in such situations, as shown in SI, Section S3.

Besides number density quantification, some applications may benefit from the ability of pbFFS to provide information on the degree of fluorescent labelling (or number of fluorophores per entity). This would be the case of oligomerization studies. Oligomerization is an ubiquitous phenomenon that plays an important role in numerous biological processes. The size of oligomers is usually estimated using fluorescence fluctuation methods (FCS, ICS) by comparing the measured brightness to the one found on a sample containing only monomers, in the same experimental conditions. Such methods suffer from two drawbacks: first, a reference sample with only monomers may not be easily available; second, if all the oligomers do not have the same size, the result is biased resulting in an overestimation of the oligomer size. More advanced techniques have been proposed, such as SpIDA,²² FIF²³ or eN&B²⁴ but still rely on the monomer brightness. The pbFFS method does not require a separate measurement on monomers, since the monomer brightness (ϵ) is provided by the fit: it is *self-calibrated*, which is a significant advantage. Moreover, some information on

the distribution of oligomer size can be obtained, although, as shown in this work, the exact distribution can only be resolved if the number of degrees of freedom is reduced by additional assumptions (*e.g.* only few possible oligomers). This strategy would work not only on fixed samples, but also in living cells. Photobleaching has been proposed in live cell, outside of the oligomerization context, to retrieve molecular brightness and to turn confocal images into concentration maps.²⁵ However this method cannot be used in cases when the studied protein forms homo-oligomers, contrarily to the present work.

Finally, we point out that, while our method contrasts with standard semi-quantitative fluorescence approaches that cannot deal with a distribution of brightness, it can be compared with some single molecules techniques based on stepwise photobleaching.^{6,26} For instance, Madl et al. performed a combination of photobleaching and brightness analysis to measure the subunit composition of membrane proteins.²⁷ In a recent work, Stein et al. have combined FCS with single-molecule localization microscopy to provide the number of docking strands in spatially well-separated origami nanostructures.²⁸ However, single molecules techniques obviously require extremely low surface density of immobilized molecules, while pbFFS works in much higher density regimes, which are more relevant for most biomimetic and biological samples.

Conclusion

In this paper we presented a method, combining fluctuations analysis and photobleaching, that aims at characterizing molecules or particles fluorescently labelled with an unknown distribution of fluorophores. pbFFS can be used both on surfaces or in volume, with immobilized or moving molecules (either in flow or freely diffusing), observed in confocal or TIRF microscopy performed in photon counting mode. It provides the single fluorescent label brightness, as well as a parameter depending on the mean and variance of the distribution of fluorescent labels. If additional assumptions can be used to restrict the number of degrees

of freedom of this distribution, the degree of fluorescent labelling and an unbiased value of the concentration or density can be deduced.

The pbFFS method has been demonstrated on a SA_v base layer of biomimetic samples to estimate the surface density of SA_v, and its propensity to bind a top layer of bAtto molecules. For the base layer density, the density estimated with pbFFS is in agreement with ellipsometry measurements. However, compared to this latter technique or QCM-D, pbFFS has the advantage of allowing *in situ* characterization, since it does not require dedicated substrates, and allows the quantification of low mass of adsorbed molecules (as in the case of bAtto), out of reach of the other techniques, thanks to the intrinsic sensitivity of fluorescence measurements.

We believe pbFFS can provide a powerful framework to attain more reliable fluorescence fluctuations analysis: indeed, standard FFS techniques are completely unable to assess whether their results are biased by a dispersion of brightness values (or number of fluorescent labels), whereas, using pbFFS, the linear decay of the brightness during photobleaching is a simple checkpoint, which contributes to making the measurements more trustworthy.

In addition to number density estimations, the capability of pbFFS to evaluate the number of fluorophores per entity should make it particularly useful for oligomerization studies, as estimating protein oligomerization is essential to understand numerous cellular functions.

Acknowledgement

We acknowledge D. Centanni (LIPhy) for the microwell preparation and the IAB facility for the confocal microscope. We thank M. Balland (LIPhy) and O. Destaing, A. Grichine (IAB) for stimulating discussions. We acknowledge E. Castro Ramirez for her work with PLL-g-PEGb. The project is funded by ANR GlyCON ANR-19-CE13-0031-01.

Supporting Information Available

Section S1 - Theoretical derivation of the brightness decay and exploitation of the measurements; Section S2 - Theoretical derivation of occupancy probabilities and m value ranges; Section S3 - Results and analysis of experiments with 20 nm fluorescent beads; Section S4 - Materials and methods (PDF).

References

- (1) Martino, M. M.; Briquez, P. S.; Maruyama, K.; Hubbell, J. A. Extracellular matrix-inspired growth factor delivery systems for bone regeneration. *Advanced Drug Delivery Reviews* **2015**, *94*, 41–52.
- (2) Migliorini, E.; Guevara-Garcia, A.; Albiges-Rizo, C.; Picart, C. Learning from BMPs and their biophysical extracellular matrix microenvironment for biomaterial design. *Bone* **2020**, *141*, 115540.
- (3) Sefkow-Werner, J.; Machillot, P.; Sales, A.; Castro-Ramirez, E.; Degardin, M.; Borturyn, D.; Cavalcanti-Adam, E. A.; Albiges-Rizo, C.; Picart, C.; Migliorini, E. Heparan sulfate co-immobilized with cRGD ligands and BMP2 on biomimetic platforms promotes BMP2-mediated osteogenic differentiation. *Acta Biomaterialia* **2020**, *114*, 90–103.
- (4) Migliorini, E.; Weidenhaupt, M.; Picart, C. Practical guide to characterize biomolecule adsorption on solid surfaces (Review). *Biointerphases* **2018**, *13*, 06D303.
- (5) Waters, J. C.; Wittmann, T. *Methods in Cell Biology*; Elsevier, 2014; pp 1–18.
- (6) Verdaasdonk, J. S.; Lawrimore, J.; Bloom, K. *Methods in Cell Biology*; Elsevier, 2014; pp 347–365.

- (7) Slaughter, B. D.; Li, R. Toward Quantitative “In Vivo Biochemistry” with Fluorescence Fluctuation Spectroscopy. *Molecular Biology of the Cell* **2010**, *21*, 4306–4311.
- (8) Hennen, J.; Saunders, C. A.; Mueller, J. D.; Luxton, G. W. G. Fluorescence fluctuation spectroscopy reveals differential SUN protein oligomerization in living cells. *Molecular Biology of the Cell* **2018**, *29*, 1003–1011.
- (9) Kolin, D. L.; Wiseman, P. W. Advances in Image Correlation Spectroscopy: Measuring Number Densities, Aggregation States, and Dynamics of Fluorescently labeled Macromolecules in Cells. *Cell Biochemistry and Biophysics* **2007**, *49*, 141–164.
- (10) Kitamura, A.; Kinjo, M. State of the Art Fluorescence Fluctuation Based Spectroscopic Techniques for the Study of Protein Aggregation. *International Journal of Molecular Sciences* **2018**, *19*, 964.
- (11) Müller, J. D. Cumulant Analysis in Fluorescence Fluctuation Spectroscopy. *Biophysical Journal* **2004**, *86*, 3981–3992.
- (12) Delon, A.; Wang, I.; Lambert, E.; Mache, S.; Mache, R.; Derouard, J.; Motto-Ros, V.; Galland, R. Measuring, in Solution, Multiple-Fluorophore Labeling by Combining Fluorescence Correlation Spectroscopy and Photobleaching. *The Journal of Physical Chemistry B* **2010**, *114*, 2988–2996.
- (13) Ciccotosto, G. D.; Kozer, N.; Chow, T. T.; Chon, J. W.; Clayton, A. H. Aggregation Distributions on Cells Determined by Photobleaching Image Correlation Spectroscopy. *Biophysical Journal* **2013**, *104*, 1056–1064.
- (14) Paviolo, C.; Chon, J. W. M.; Clayton, A. H. A. *Advances in Experimental Medicine and Biology*; Springer Singapore, 2018; pp 41–52.
- (15) Mets, R. D.; Wang, I.; Gallagher, J.; Destaing, O.; Balland, M.; Delon, A. Determina-

- tion of protein concentration on substrates using fluorescence fluctuation microscopy. *Single Molecule Spectroscopy and Superresolution Imaging VII*. 2014.
- (16) Dundas, C. M.; Demonte, D.; Park, S. Streptavidin–biotin technology: improvements and innovations in chemical and biological applications. *Applied Microbiology and Biotechnology* **2013**, *97*, 9343–9353.
- (17) Brock, R.; Hink, M. A.; Jovin, T. M. Fluorescence Correlation Microscopy of Cells in the Presence of Autofluorescence. *Biophysical Journal* **1998**, *75*, 2547–2557.
- (18) Bae, W.; Yoon, T.-Y.; Jeong, C. Direct evaluation of self-quenching behavior of fluorophores at high concentrations using an evanescent field. *PLOS ONE* **2021**, *16*, e0247326.
- (19) Hendrickson, W. A.; Pahler, A.; Smith, J. L.; Satow, Y.; Merritt, E. A.; Phizackerley, R. P. Crystal structure of core streptavidin determined from multiwavelength anomalous diffraction of synchrotron radiation. *Proceedings of the National Academy of Sciences* **1989**, *86*, 2190–2194.
- (20) Zanetti-Domingues, L. C.; Tynan, C. J.; Rolfe, D. J.; Clarke, D. T.; Martin-Fernandez, M. Hydrophobic Fluorescent Probes Introduce Artifacts into Single Molecule Tracking Experiments Due to Non-Specific Binding. *PLoS ONE* **2013**, *8*, e74200.
- (21) Elisa Migliorini, Spectroscopic ellipsometry characterisation of Streptavidin Alexa binding to PLL-g-PEGbiotin(50%). 2021; <https://data.mendeley.com/datasets/kmshdrrs6y/1>.
- (22) Godin, A. G.; Rappaz, B.; Potvin-Trottier, L.; Kennedy, T. E.; Koninck, Y. D.; Wiseman, P. W. Spatial Intensity Distribution Analysis Reveals Abnormal Oligomerization of Proteins in Single Cells. *Biophysical Journal* **2015**, *109*, 710–721.

- (23) Stoneman, M. R.; Biener, G.; Ward, R. J.; Padiani, J. D.; Badu, D.; Eis, A.; Popa, I.; Milligan, G.; Raicu, V. A general method to quantify ligand-driven oligomerization from fluorescence-based images. *Nature Methods* **2019**, *16*, 493–496.
- (24) Cutrale, F.; Rodriguez, D.; Hortigüela, V.; Chiu, C.-L.; Otterstrom, J.; Mieruszynski, S.; Seriola, A.; Larrañaga, E.; Raya, A.; Lakadamyali, M.; Fraser, S. E.; Martinez, E.; Ojosnegros, S. Using enhanced number and brightness to measure protein oligomerization dynamics in live cells. *Nature Protocols* **2019**, *14*, 616–638.
- (25) Zhang, L.; Perez-Romero, C.; Dostatni, N.; Fradin, C. Using FCS to accurately measure protein concentration in the presence of noise and photobleaching. *Biophysical Journal* **2021**, *120*, 4230–4241.
- (26) Wang, X.; Li, X.; Deng, X.; Luu, D.-T.; Maurel, C.; Lin, J. Single-molecule fluorescence imaging to quantify membrane protein dynamics and oligomerization in living plant cells. *Nature Protocols* **2015**, *10*, 2054–2063.
- (27) Madl, J.; Weghuber, J.; Fritsch, R.; Derler, I.; Fahrner, M.; Frischauf, I.; Lackner, B.; Romanin, C.; Schütz, G. J. Resting State Orai1 Diffuses as Homotetramer in the Plasma Membrane of Live Mammalian Cells. *Journal of Biological Chemistry* **2010**, *285*, 41135–41142.
- (28) Stein, J.; Stehr, F.; Schueler, P.; Blumhardt, P.; Schueder, F.; Mücksch, J.; Jungmann, R.; Schwille, P. Toward Absolute Molecular Numbers in DNA-PAINT. *Nano Letters* **2019**, *19*, 8182–8190.

III.D Supplementary information

Supporting Information: Combining fluorescence fluctuations and photobleaching to quantify surface density

Julius Sefkow-Werner,^{†,¶} Elisa Migliorini,^{*,†} Catherine Picart,[†] Dwiria Wahyuni,^{‡,§}

Irène Wang,[‡] and Antoine Delon^{*,‡}

[†] *BRM ERL 5000 CEA/CNRS/UGA, France*

[‡] *LIPHY, Université Grenoble Alpes and CNRS, F-38000 Grenoble, France*

[¶] *Univ. Grenoble Alpes, CNRS, Grenoble INP, LMGP, 38000 Grenoble, France*

[§] *Current address: Tanjungpura University, Pontianak, Indonesia*

E-mail: elisa.migliorini@cea.fr; antoine.delon@univ-grenoble-alpes.fr

Summary: Theoretical derivation of the brightness decay and exploitation of the measurements (S1); Theoretical derivation of occupancy probabilities and m value ranges (S2); Results and analysis of experiments with 20 nm fluorescent beads (S3); Materials and methods (S4).

S1. Theoretical derivation of the brightness decay and exploitation of the measurements

Theoretical derivation of the brightness decay

In the following, we derive the rigorous expression of the brightness B_{FFS} as a function of the photobleaching stage (defined as the fraction of remaining fluorescence signal), assuming all fluorophores are independent and have an equal probability to bleach. Although we present the formalism of pbFFS for two-dimensional ICS, the same results apply to mobile molecules and temporal techniques, *e.g.* FCS in solution, Raster ICS,[?] etc.

Let us consider $I(x, y)$ the image intensity at pixel x, y . The fluorescence fluctuations, defined as $\delta I(x, y) = I(x, y) - \langle I(x, y) \rangle$ (where the averaging is performed over the image field), are analyzed using the autocorrelation function:

$$G(\xi, \eta) = \frac{\langle \delta I(x, y) \delta I(x + \xi, y + \eta) \rangle}{\langle I(x, y) \rangle^2} \quad (\text{S1})$$

In spatial ICS, the fluorescent entities of interest are immobile, so that the autocorrelation is only related to the optical resolution of the microscope (described by the PSF) and is very well approximated by a Gaussian:[?]

$$G(\xi, \eta) = \frac{1}{N_{FFS}} \exp\left(-\frac{\xi^2 + \eta^2}{w_r^2}\right) \quad (\text{S2})$$

where N_{FFS} is an apparent mean number of entities in the PSF area of radius w_r . As already pointed out in the Introduction of the primary manuscript (Eq. 1), when the observed species are not equally bright, N_{FFS} is smaller than N , the real number of all the entities. In the case of a mixture of species of different brightness, it can be shown that the FFS techniques leads to:^{??}

$$N_{FFS} = \frac{(\sum \epsilon_i N_i)^2}{\sum \epsilon_i^2 N_i} \quad (\text{S3})$$

where ϵ_i is the brightness of the species i (that is the fluorescence signal of a single entity of the species i) and N_i , the average number of entities of the species i . Note that the true total number of entities is given by $N = \sum N_i$. The key point is that the contributions are weighted by the square of the brightness, leading to an underestimation of the total number of fluorescent entities, when all entities are not equally bright (it's the tree that hides the forest).

Here, we consider that each entity carries several identical fluorescent labels. In the forthcoming derivation we shall assume that fluorescence quenching can be neglected, so that the brightness of a single fluorescent label is constant whatever their number in the entities. In this case, the brightness of an entity carrying n fluorescent labels is $\epsilon_n = n\epsilon$ where ϵ is the brightness of a single fluorescent label, and the fluorescence signal reads (N_n being the number of entities that bear exactly n fluorescent labels):

$$F = \sum n\epsilon N_n \quad (\text{S4})$$

The overall brightness is thus given by:

$$B_{FFS} = \epsilon \frac{\sum n^2 N_n}{\sum n N_n} \quad (\text{S5})$$

To describe the photobleaching effect, we present a derivation based on the same hypothesis as in the work by Ciccotosto *et al.*[?] However, we generalize the formalism in order to provide a simple theoretical expression of the brightness for any initial distribution of fluorescent labels. At a given point during photobleaching, we assume that any fluorophore has the same probability not to be bleached, given by p . This implies that the initial number of fluorescent labels, n , which appears in Eq. S4 and S5 has to be replaced by the mean number of unbleached labels, which is simply given by np . Therefore the remaining fluorescence signal reads:

$$F(p) = \epsilon \sum np N_n = \epsilon pm N \quad (\text{S6})$$

where $m = \frac{1}{N} \sum nN_n$ is the average initial number of fluorescent labels per entity, computed over all fluorescent entities (this can be called *degree of fluorescent labelling*). Note that p is nothing but the fluorescence signal normalized to its initial value, before photobleaching has started, i.e. $p = F(p)/F(1)$. In order to also modify Eq. S5 and make it valid all along photobleaching, we need to replace n^2 by the second order moment of the distribution at the fluorescence stage p . Since any fluorescent label can only be in two states, bleached or unbleached with respective probabilities $(1-p)$ and p , this quantity results from the binomial distribution and equates $np(1-p) + n^2p^2$. As a consequence, Eq. S5 becomes:

$$B_{FFS}(p) = \epsilon \frac{\sum [np(1-p) + n^2p^2]N_n}{pmN} \quad (\text{S7})$$

We see that the numerator of Eq. S7 reveals, in addition to the mean value, m , of the initial number of fluorescent labels per entity, the mean value of its square, $\frac{1}{N} \sum n^2N_n$ that can be written $\sigma^2 + m^2$, where σ is the standard deviation of the initial number of fluorescent labels per entity. Consequently, after a few simplifications, Eq. S7 can be written again:

$$B_{FFS}(p) = \epsilon(1 + S_{\sigma m}p) \quad (\text{S8})$$

where

$$S_{\sigma m} = \sigma^2/m + m - 1 \quad (\text{S9})$$

Hence the measured brightness B_{FFS} is an affine function of the photobleaching stage p : the single fluorescent label brightness ϵ is its intercept at $p = 0$ (note that this is an immediate output of pbFFS, obtained without any assumption) and $S_{\sigma m}$ is its slope normalized by the single fluorescent label brightness. Let us rewrite here the equation stating the initial fluorescence signal:

$$F(1) = \epsilon mN \quad (\text{S10})$$

Eq. S8, S9 and S10 are the core relations around which all our reasoning is based. Note

that studying the variation of the number of entities, instead of the brightness, *versus* the fluorescence signal, would be completely equivalent, as B_{FFS} and N_{FFS} are related through $F = B_{FFS}N_{FFS}$ (we drop out the $_{FFS}$ subscript in F because the fluorescence signal is not biased by fluctuation measurements). We will mostly discuss the brightness because, in absence of background, it always decays as a straight line when plotted as a function of the fluorescence signal (whatever the initial distribution of fluorescent labels), which is quite convenient for visual inspection of the experimental results. At this stage, it is interesting to make a few remarks about the pbFFS approach.

- First, we emphasize the fact that the parameters σ and m appearing in Eq. S9 and S10 characterize the *initial* distribution of brightness. Of course this distribution varies during photobleaching (it can be shown that it always converges towards a Poisson one), but the slope, $S_{\sigma m}$, depends only on the initial distribution.
- Although $B_{FFS}(p)$ is an affine function of p whatever the initial brightness distribution, a very peculiar situation is that of a mixture of entities bearing either no fluorescent label, or exactly one. This leads to $\sigma^2 = m(1 - m)$, hence $S_{\sigma m} = 0$ and the measured brightness, $B_{FFS}(p)$, is constantly equal to ϵ , independently of the photobleaching stage. Indeed, all visible entities can only have the brightness of single labels.
- Another notable case is an ensemble of entities that initially bear the same number of labels, say an integer m (this is a single-valued distribution, with $\sigma = 0$). This would lead to a measured brightness, $B_{FFS}(p)$, that linearly varies from $m\epsilon$ to ϵ .
- In all cases, when the fluorescence signal vanishes ($p \rightarrow 0$), the measured brightness tends towards the one of a single label ($B_{FFS}(0) \rightarrow \epsilon$), since the only entities that remain visible are those bearing one single label. Consequently, one also obtains the total number of fluorophores that is just given by $mN = F(1)/\epsilon$.
- Finally, it is worth to notice that in case of an unknown proportion of dark entities,

there is obviously no way to assess it, and thus, to quantify the true total number of entities.

Exploitation of the measurements

Let us consider now what can be deduced from an experimental photobleaching decay, knowing that the measured normalized slope, $S_{\sigma m} = \sigma^2/m + m - 1$ and the intercept, ϵ , contain all the available information on the initial distribution of fluorescent labels from a pbFFS experiment. Therefore, in the general case, it is impossible to independently determine the mean value and the standard deviation of the number of fluorescent labels per entity. However, the values of these statistical parameters which are compatible with a given measured slope, $S_{\sigma m}$, can be represented by (σ, m) points located on a half circle of center $(0, \frac{1+S_{\sigma m}}{2})$ and radius $\frac{1+S_{\sigma m}}{2}$, as shown in Fig. S1. This half-circle can be seen as the support of the more general (σ, m) solution, independently of any specific kind of distribution.

The case of single-valued distributions (all entities bear the same *integer* number of fluorescent labels) corresponds to discrete points along the $\sigma = 0$ vertical axis. Another particular case is that of a Poisson distribution where the mean and the variance are related by $m = \sigma^2$, as depicted in Fig. S1. In this case, the photobleaching decay provides all necessary information to define the distribution. The measured brightness becomes $B_{FFS}(p) = \epsilon(1 + mp)$, which is the same expression as the one obtained in Ref.,[?] but it is derived here in a more general framework. Note that, for small degrees of fluorescent labelling, the percentage of unlabelled species can be very large since, according to the properties of the Poisson distribution, it is given by e^{-m} .

In the general case where $S_{\sigma m} > 0$, the photobleaching slope can only provide a lower limit of the true number of entities N (and hence the surface density) but no upper bound: since $N = F(1)/m\epsilon$, the condition $m \leq 1 + S_{\sigma m}$ (see Fig. S1) leads to a lower bound, which equals the apparent value, $N_{FFS}(1) = F(1)/B_{FFS}(1)$, corresponding to the case where all entities have the brightness $B_{FFS}(1) = (1 + S_{\sigma m})\epsilon$. The fact that the real N cannot be lower

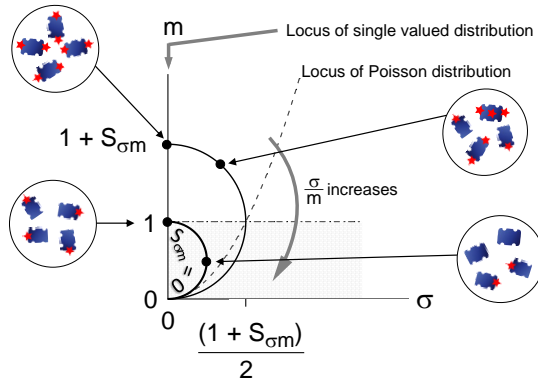


Figure S1: Geometrical representation of the relation between the mean, m , and the standard deviation, σ , of the *initial* number of fluorescent labels per entity. For a given measured slope, $S_{\sigma m}$, the support of the (σ, m) points is a half circle of diameter $1 + S_{\sigma m}$ that always crosses the $(0, 0)$ point; the coefficient of variation of the distribution of the number of fluorescent labels, $\frac{\sigma}{m}$, continuously increases from the top to the base of the half-circle. Single-valued distributions correspond to discrete points located on the vertical axis ($\sigma = 0$), as exemplified for 1 and 2 fluorescent labels. The smallest circle of diameter 1 ($S_{\sigma m} = 0$) corresponds to a mixture of entities bearing either no fluorescent label or exactly one, as depicted at the bottom right. If all molecules bear at least one fluorescent label, for instance a mixture of 1, 2 and 3 fluorescent labels, the (σ, m) solutions are located in the upper half space above the dashed-dotted line $m = 1$. Note that in the case of a Poisson distribution, any given slope $S_{\sigma m}$ corresponds to a unique point (σ, m) located at the intersection of the $m = \sigma^2$ curve (dashed line) and of the half circle of diameter $1 + S_{\sigma m}$ (see text).

than the apparent N_{FFS} is not new, since we argued that a distribution of brightness *always* causes FFS to underestimate the number of entities (see Eq. 1 in the primary manuscript). An upper bound for N can be established if we consider only *fluorescent* entities: in this case, the minimum value of m is larger than 1. Therefore, the true number of *fluorescent* entities is included between $N_{FFS}(1)$ and $F(1)/\epsilon = (1 + S_{\sigma m})N_{FFS}(1)$.

To summarize, the pbFFS method is useful if the initial fluorescent label distribution can be fully described by a limited number of degrees of freedom. When there is only one, the fluorescent label distribution can be estimated from the photobleaching slope, which makes it possible to determine the true number of entities. This is for instance the case for a Poisson law, as already used for DNA or fibrinogen fluorescent labelling.^{??} Another example is that of a sample where all entities are uniformly fluorescently labelled. When the number of

degrees of freedom of the distribution is two, it may nevertheless be possible to infer a range of values for the number of entities, by combining the constraints of the fluorescent label distribution with the relation between σ and m as established by the measured slope. This is the case encountered in the current work with SA_v molecules, which are assumed to bear 1, 2 or 3 fluorescent labels.

S2. Theoretical derivation of occupancy probabilities and m value ranges

When the number of fluorescent labels borne by an entity can only take 3 non-nil values, its distribution depends on 2 independent parameters, because of the normalization. This means that for a measured parameter $S_{\sigma m}$ (that equates $\sigma^2/m + m - 1$), any given possible value of m fully determines the 3 occupancy probabilities. The fact that these probabilities are to be between 0 and 1 implies limited ranges of values for m . We now exploit this simple mathematical framework in the particular case of 1, 2 and 3 fluorescent labels, but it can be easily extended to any distribution with 3 non-nil occupancy probabilities (more generally, when the distribution of the number of fluorescent labels depends on 2 independent parameters, whatever they are, this induces constraints on m that depend on the measured value of $S_{\sigma m}$).

Let us now consider the mean value, m , the standard deviation, σ and the normalisation of the distribution. These are given by:

$$\begin{aligned}
 m &= p_1 + 2p_2 + 3p_3 \\
 \sigma^2 &= (1 - m)^2 p_1 + (2 - m)^2 p_2 + (3 - m)^2 p_3 \\
 p_1 + p_2 + p_3 &= 1
 \end{aligned}
 \tag{S11}$$

where p_1 , p_2 and p_3 are the probabilities to find 1, 2 and 3 fluorescent labels. These

equations can be easily transformed to express p_1 , p_2 and p_3 as functions of m and σ :

$$\begin{aligned}
 p_1 &= 3 + m(S_{\sigma m}/2 - 2) \\
 p_2 &= -3 + m(3 - S_{\sigma m}) \\
 p_3 &= 1 + m(S_{\sigma m}/2 - 1)
 \end{aligned}
 \tag{S12}$$

By writing that each of these probability occupancies is between 0 and 1, one obtains the corresponding constraints on m as a function of $S_{\sigma m}$:

$$\begin{aligned}
 \frac{4}{4 - S_{\sigma m}} &\leq m \leq \frac{6}{4 - S_{\sigma m}} \\
 \frac{3}{3 - S_{\sigma m}} &\leq m \leq \frac{4}{3 - S_{\sigma m}} \\
 0 &\leq m \leq \frac{2}{2 - S_{\sigma m}}
 \end{aligned}
 \tag{S13}$$

We show in Fig. S2 the series of $m(S_{\sigma m})$ curves giving these upper and lower limits. Henceforth, the common region where all the constraints are simultaneously satisfied (hatched area) is defined by:

$$\frac{3}{3 - S_{\sigma m}} \leq m \leq \frac{2}{2 - S_{\sigma m}} \quad \text{for} \quad 0 \leq S_{\sigma m} \leq 1 \tag{S14}$$

$$\frac{3}{3 - S_{\sigma m}} \leq m \leq \frac{6}{4 - S_{\sigma m}} \quad \text{for} \quad 1 \leq S_{\sigma m} \leq 2 \tag{S15}$$

It is possible to add further restrictions regarding the distribution of the number of fluorescent labels. For instance, concerning the SA_v-Alex molecules the specifications of which indicate an average of 2 fluorescent labels per molecule, it is reasonable to discard the cases where $p_3 > p_2$, which leads to $m > \frac{1}{1 - \frac{3}{8}S_{\sigma m}}$.

Finally, it is also interesting to ask what one would expect if one assumed that the entities

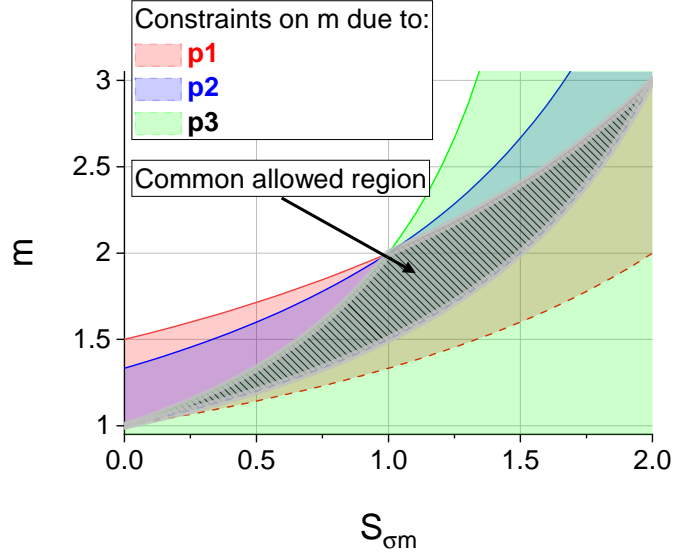


Figure S2: Limits of the possible values of m . For each value of $S_{\sigma m}$, the occupancy probabilities for 1, 2 and 3 fluorescent labels (p_1 (red zone), p_2 (blue) and p_3 (green)) are to be between 0 and 1, which implies corresponding minimum and maximum values of m . The common zone, allowed for any of the occupancy probabilities, is hatched and surrounded in gray.

could carry 2, 3 or 4 fluorescent labels. A derivation analogous to that leading to the above Eq. S11 to S13 gives:

$$\begin{aligned}
 \frac{8}{5 - S_{\sigma m}} &\leq m \leq \frac{9}{5 - S_{\sigma m}} \\
 \frac{10}{6 - S_{\sigma m}} &\leq m \leq \frac{12}{6 - S_{\sigma m}} \\
 \frac{4}{4 - S_{\sigma m}} &\leq m \leq \frac{6}{4 - S_{\sigma m}}
 \end{aligned} \tag{S16}$$

S3. Experiments with 20 nm fluorescent beads

We performed experiments by plating 20 nm red fluorescent polystyrene beads (FluoSpheres™ Carboxylate Modified Microspheres, F8786, Invitrogen) on a glass substrate (Lab-Tek™II Chambered Coverglass, Nunc) that was previously treated with O_2 plasma, covered by poly(l-lysine) and then washed. After a few hours of incubation, the surface was rinsed with miliQ

water to remove unbound beads. 9 different zones of $25.7 \times 25.7 \mu\text{m}^2$ were imaged, using the same acquisition and analysis protocol as the one described in the main part of the manuscript.

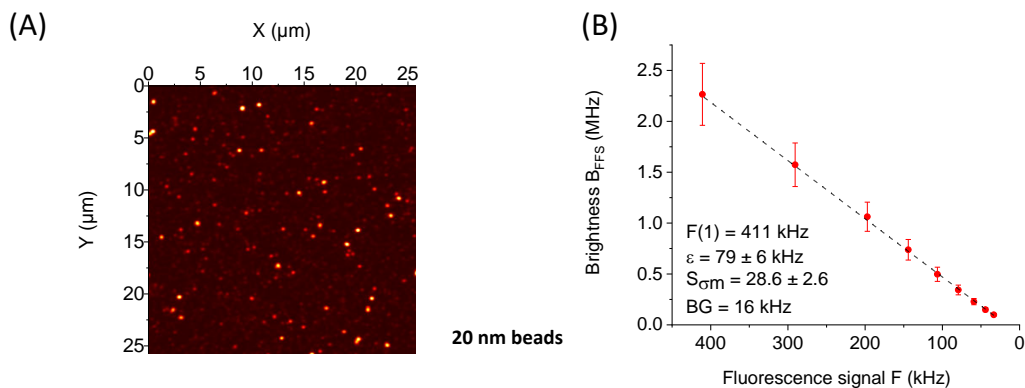


Figure S3: Analysis of 20 nm fluorescent beads deposited on a glass surface. (A) Initial image (before photobleaching) of one of the 9 zones ($25.7 \times 25.7 \mu\text{m}^2$); (B) Corresponding brightness decay, the slope of which, $S_{\sigma m}$, is many tens of times larger than the one measured with SA_v-Alex or bAtto molecules.

We see in Fig. S3A an image of one zone of beads and the corresponding photobleaching decay, the different zones showing the same trend. The striking property is the typical value of the slope, $S_{\sigma m}$, of a few tens (see Fig. S3B), that is much larger than the one obtained with SA_v-Alex or bAtto molecules. Exploratory single particle detection, on images acquired at sufficiently low surface concentration, has confirmed that the bead intensity distribution is very broad, as one can guess according to Fig. S3A. Assuming that the distribution of the number of fluorescent labels follows a Poisson law, we can deduce that the mean number of fluorophores per bead is also of the order of a few tens (since in this case $m = S_{\sigma m}$), in agreement with the rough specifications given by the manufacturer.

We nevertheless stress the fact that the output parameters of the brightness decay fit might be very sensitive to the background. The reason relies in the very small final value of the brightness (that of the last measured point), relatively to the initial (unbleached) brightness. Depending upon the value found or fixed for the background, the estimated single fluorescent label brightness can vary a lot and so can the slope $S_{\sigma m}$.

Finally, these data show that pbFFS can in principle be applied to particles with a high degree of fluorescent labelling, although, to be reliable, measurements should be performed with a high dynamic range and a carefully controlled background.

S4. Materials and methods

Substrate preparation

Microscopy glass coverslips (24×24 mm, Menzel Gläser) were cleaned under sonication with acetone and isopropanol and blow-dried with nitrogen. They were UV/ozone activated (UV/Ozone ProCleaner Plus, Bioforce) for 10 min, attached to a microscopy support and PLL(20)-g[3.5]-PEG(2)/PEGbiotin(3.4)50% (≈ 107 kDa, SuSoS AG) was incubated at 10 $\mu\text{g}/\text{ml}$ in 10 mM Hepes buffer (Fisher, pH=7.2) for 45 min.[?] Streptavidin (≈ 55 kDa, Sigma Aldrich), SAv, and streptavidin Alexa Fluor™555 conjugate (≈ 55 kDa, Molecular probes), SAv-Alex, with a labeling degree of 2 fluorophores (certificate of analysis, Molecular probes) were mixed in a ratio varying from 100:1 to 100:100 at 10 $\mu\text{g}/\text{ml}$ in Hepes buffer and incubated for 30 min. A layer of biotinylated species was prepared by immobilizing Atto-labelled biotin (Atto 565-Biotin, 921 Da, Sigma-Aldrich), bAtto, to a saturated layer of SAv, bAtto occupying the free biotin pockets on SAv. In all cases, the sample was rinsed 5 times with Hepes after incubation.

Confocal imaging and photobleaching of surfaces

Functionalized glass coverslips were imaged using a Leica SP8 confocal microscope with a HC PL APO 63×1.2 water-immersed objective. The focal plane was determined where intensity was at maximum and then stabilized using the Adaptive Focus Control mode. The signal was detected with a hybrid detector working in the photon counting mode. An area of 25×25 μm^2 with 512×512 pixels was imaged 10 times with a pixel dwell time of 5 μs and a reduced laser intensity at 561 nm, so not to saturate and not to bleach the sample during

image acquisitions. Then, this area was photobleached with a sufficient illumination dose (scanning time \times laser power) to loose roughly 30% of the initial signal and 10 images were acquired as before. This procedure was typically repeated 6 to 8 times, in order to finish the acquisition with a remaining signal of at most 10% of the initial one.

Image pre-processing and ICS

Before performing ICS analysis, it is necessary to correct the non-uniformity of the image intensity in the 1 - 10 μm scale range because, as already discussed in,[?] it can have a strong impact on the autocorrelation function. This non-uniformity originates, either from a spatial dependence of the light efficiency of the imaging system, or from an inhomogeneous surface density. It induces long range correlations that add to the autocorrelation of interest with various detrimental effects, such as anomalous base line, width and long range behaviour. Image flattening is especially crucial when the surface density is very high and thus the autocorrelation very weak, because in this case the relative bias can be very pronounced. In order to leave the ratio of the fluctuation amplitude to the mean value unchanged, on which the estimated number of entities depends, the images are flattened by dividing them by their own smoothed version. The latter is obtained by convoluting the original image with a two-dimensional Gaussian function. The width of this Gaussian has to be small enough to damp as much as possible image inhomogeneities, but significantly larger than the radius of the ICS PSF area ($w_r \approx 0.23\mu m$), in order not to bias the number fluctuations. Consistently with our previous study,[?] the $1/e$ half width of the Gaussian function used to smooth and flatten the images was chosen to be 2 μm . In practice, the images are individually flattened and autocorrelated. Then, for each photobleaching stage, the mean autocorrelation is fitted with Eq. S2 (see Supplementary Information), which gives a global estimation of N_{FFS} and the radius w_r . By verifying that the latter varies by much less than 1% during the acquisition process, we check the stability of the focus. The final goal being to analyze the variation of the brightness, B_{FFS} , *versus* the fluorescence signal F (i.e. the intensity), the images

are divided in 8×8 sub-images that are individually analyzed by ICS, while the value of the radius w_r is set at the one estimated from the whole image, thus providing a mean and a standard deviation of the mean of the brightness at each photobleaching stage. The image processing (flattening, autocorrelation and fit) was performed using Matlab (Mathworks).

Sample preparation and photobleaching of solutions

To achieve photobleaching of the fluorescent labels in solution in a reasonable amount of time (a few minutes), with the available laser power (≤ 1 mW), the solutions were confined in poly(dimethylsiloxane) (PDMS) microwells. A regular array containing pillars of $100 \mu\text{m}$ in diameter and $100 \mu\text{m}$ in height with a pitch of $400 \mu\text{m}$ was fabricated on the Si wafer. After peeling off the mold, the 2 mm thick PDMS micropatterned slabs were activated with air plasma (Atto, Diener) for 2 min to achieve a hydrophilic surface.[?] Then a droplet of SAV-Alex or bAtto Hepes solution was placed on the PDMS block to enter the microwells, at initial concentrations around a few 100 nM. Such concentrations, relatively high for FCS, were necessary to saturate the microwell walls and avoid too much adsorption/desorption processes that induce unstable fluorescence signal. For control purposes, we also used solutions of Sulforhodamine B sodium salt, SRB (Sigma-Aldrich, St. Louis, USA), without further purification, diluted in either deionised water or Hepes. The PDMS block was flipped onto a Lab-Tek™ Chambered Coverglass (Nunc) to seal the microwells and thus avoiding fluid exchange with the environment.

FCS acquisition and fit

The signal inside the microwells was acquired using a Nikon confocal microscope (Ti2E - A1R) with a $60 \times$ water-immersed objective and a reduced laser power at 561 nm, to avoid any photobleaching during FCS acquisitions. The latter were performed using a custom made detection system, comprising a 50/50 beam splitter and a pair of avalanche photodiodes (SPCM-AQRH-44-FC, EXCELITAS) to avoid after-pulsing effects, which was connected on

the auxiliary port of the microscope using a multimode optical fiber. The focal plane was set at 20 μm inside the microwells and photons were counted during 5 periods of 20 s to provide an averaged cross-correlation curve (and its corresponding standard error of the mean) using a Correlator.com software (Flex99r-12D). Proper optical adjustments and stability were controlled by fitting the diffusion time[?] and measuring the brightness of a reference dye, namely sulfo-rhodamine B. Each FCS acquisition thus gives an estimation of the number of entities, N_{FFS} and of the corresponding brightness, B_{FFS} , with a given uncertainty; it was followed by a bleaching cycle with a laser intensity adjusted to typically reduce the initial signal by 30% before performing the next acquisition. This was repeated 5 to 8 times until about less than 10% of the initial signal remains, in order to provide the variation of the brightness, B_{FFS} , with error bars, *versus* the fluorescence signal F (or photon count rate).

III.E Transition

In the precedent two chapters, we developed an automated fabrication protocol for biomimetic SA_v platforms and applied for the first time pbICS to quantify molecular surface density *in situ*. With a high-content proof-of-concept, we demonstrated that cells adhered well to the substrate and that these platforms could be used to study iHS-mediated early aBMP2 activity. In the next chapter, we increase the complexity of the system and of the readout and aim at revealing the role of integrins, iHS and BMP2 on cellular adhesion and BMP2 mediated osteogenic differentiation. It is worth to note that the experiments in chapter IV were performed before the studies related to chapter II and III. Gold-based biomimetic platforms were thus the material of choice.

**Chapter IV: Heparan sulfate co-immobilized with
cRGD ligands and BMP2 on biomimetic platforms
promotes BMP2-mediated osteogenic differentiation**

IV.A Article summary (English)

The ECM provides structure and mechanical support to embedded cells and regulates homeostasis and differentiation. Cells adhere to the ECM *via* the specific interaction between binding domains of structural proteins and integrins. These transmembrane receptors are made of α - and β -subunits and in particular, β_3 -integrins have a high affinity for the cRGD adhesion motif (Pfaff *et al.*, 1994). GAGs are elongated polysaccharides and attach to core proteins to form PGs. As components of the ECM, they protect cells due to their high swelling capacity and bind GFs, which makes them regulators of cell differentiation. The GAG HS in particular binds to BMP2, which has a high osteoinductive potential and is clinically applied in large bone fracture repair (Ruppert, Hoffmann and Sebald, 1996; Obradovic Wagner *et al.*, 2010; Sarrazin, Lamanna and Esko, 2011). Previously, it was shown that exogenous HS has a positive effect on BMP2-mediated signaling but its role in osteogenic differentiation if presented in an oriented way is not reported (Migliorini *et al.*, 2017). Further, BMP2 was found to induce the activation of β_3 -integrins-mediated cell adhesion and activated β_3 -integrins in return were required for the phosphorylation of SMAD1/5/9, an early reporter of BMP2 signaling (Fourel *et al.*, 2016). However, the effect of increased integrin recruitment at the cell membrane on BMP2 bioactivity is not studied. In addition, the type of integrins involved in this signaling is context-dependent as shown by Garcia *et al.* who identified β_1 -integrins but not β_3 -integrins as regulators of VEGF activity (García, Clark and García, 2016). Nevertheless, the role of β_1 - and β_3 -integrins in BMP2-mediated osteogenic differentiation is not yet understood and neither the quantitative influence of available integrin ligands.

We address this question with a biomimetic approach aiming at presenting RGD, iHS and BMP2 in a natural way to cells. For that, we engineered platforms based on a SA_v monolayer to which biotinylated molecules as cRGD and iHS or iBMP2 could bind (Migliorini *et al.*, 2014, 2017). aBMP2 adsorbed on iHS was directly compared to iBMP2 after similar surface density was assured. To precisely control the amount of each compound on the surface, we tuned the binding kinetics *via* the molecular concentration in solution and measured the binding to the platform with surface sensitive techniques such as QCM-D and SE. That way, we could co-functionalize the platform by interrupting the binding of a first molecule before saturating the available binding sites and incubate a second and third molecule sequentially. The spacing of the integrin ligand cRGD thus was controlled by different incubation times, or, to decrease significantly the amount of cRGD at the surface, by spacing it out with a biotinylated PEG, a

molecule to which cells don't adhere. To distinguish between different types of integrins, we silenced C2C12 myoblast precursors for β_1 - or β_3 -integrins and plated them on biomimetic surfaces. As a more relevant cell type for medicine applications, we chose hPDSCs. We quantified cell adhesion, early BMP2 signaling *via* pSMAD1/5/9 and osteogenic differentiation through the markers Osterix, Runx2 and ALP.

Increasing areal mass densities of cRGD positively correlated with SMAD1/5/9 phosphorylation in C2C12 cells and at 23 ng/cm² the signal was significantly higher than in cells plated on plastic dishes. On platforms presenting a critical concentration of cRGD regarding cellular adhesion (0.25 ng/cm²), sBMP2 and iBMP2 were able to enhance cellular adhesion. We concluded that the cross-talk between β_3 -integrins and BMP2 was bi-directional and depended on the absolute quantity of the presented adhesion ligand. Indeed, we demonstrated that C2C12 cells adhered specifically *via* β_3 -integrins to cRGD since only silencing β_3 -integrins and not β_1 -integrins decreased cell area down to the level of cells plated on cRAD platforms, a peptide with much lower affinity for integrins. Further, whereas sBMP2 and iBMP2 had a reduced potential to activate SMAD1/5/9 phosphorylation with decreasing surface concentrations of cRGD, aBMP2 adsorbed to iHS with comparable amounts to iBMP2 had a constant bioactivity on C2C12 cells. This positive effect of iHS on SMAD1/5/9 phosphorylation was also observed in hPDSCs. With silencing RNA experiments, we identified both, β_3 - and β_1 -integrins as positive influencers for early BMP2 activity on high adhesive cRGD platforms and only baseline SMAD1/5/9 phosphorylation was measured on low adhesive cRAD platforms. While there was no difference between iBMP2 and aBMP2 on high-adhesive cRGD platforms regarding early BMP2 activity, iHS with aBMP2 up-regulated Osterix, Runx2 and ALP expression with respect to iBMP2. Interestingly, cells differentiated also on cRAD platforms and there as well, iHS had a positive effect compared to sBMP2 and iBMP2, possibly due to the non-SMAD pathway even though we did not measure up-regulated p-p38 signal.

In summary, the cross-talk between integrins and BMP2 was bi-directional and both, β_1 - and β_3 -integrins positively influenced BMP2 signaling and osteogenic differentiation. In addition, oriented iHS together with aBMP2 enhanced osteogenic differentiation, likely by sustaining BMP2 signaling over time and by facilitating proximity between BMP receptors and integrins due to its long molecular structure. Since integrins and iHS positively affected BMP2 signaling, they could be presented together with BMP2 on implants for bone regeneration to reduce BMP2 doses in medicine application.

IV.B Article summary (French)

La ECM fournit une structure et un support mécanique aux cellules incorporées et régule l'homéostasie et la différenciation. Les cellules adhèrent à l'ECM via l'interaction spécifique entre les domaines de liaison des protéines structurales et les intégrines. Ces récepteurs transmembranaires sont constitués de sous-unités α et β et, en particulier, les β_3 -intégrines ont une forte affinité pour le motif d'adhésion cRGD (Pfaff et al., 1994). Les GAGs sont des polysaccharides allongés et s'attachent aux protéines centrales pour former des PGs. En tant que composants de l'ECM, ils protègent les cellules grâce à leur grande capacité de gonflement et lient les GF, ce qui en fait des régulateurs de la différenciation cellulaire. Le GAG HS en particulier se lie à BMP2, qui a un potentiel ostéoinductif élevé et est cliniquement appliqué dans la réparation des gros fractures des os (Ruppert, Hoffmann et Sebald, 1996 ; Obradovic Wagner et al., 2010 ; Sarrazin, Lamanna et Esko, 2011). Auparavant, il a été démontré que le HS exogène a un effet positif sur la signalisation médiée par la BMP2, mais son rôle dans la différenciation ostéogénique s'il est présenté de manière orientée n'est pas rapporté (Migliorini et al., 2017). En outre, il a été constaté que BMP2 induit l'activation de l'adhésion cellulaire médiée par les β_3 -intégrines et que les β_3 -intégrines activées en retour étaient nécessaires à la phosphorylation de SMAD1/5/9, un rapporteur précoce de la signalisation de BMP2 (Fourel et al., 2016). Cependant, l'effet de l'augmentation du recrutement des intégrines à la membrane cellulaire sur la bioactivité de BMP2 n'est pas étudié. De plus, le type d'intégrines impliquées dans cette signalisation est dépendant du contexte comme l'ont montré Garcia et al. qui ont identifié les β_1 -intégrines mais pas les β_3 -intégrines comme régulateurs de l'activité du VEGF (García, Clark et García, 2016). Néanmoins, le rôle des β_1 - et β_3 -intégrines dans la différenciation ostéogénique médiée par BMP2 n'est pas encore compris, ni l'influence quantitative des ligands d'intégrines disponibles.

Nous abordons cette question avec une approche biomimétique visant à représenter RGD, iHS et BMP2 de manière naturelle aux cellules. Pour cela, nous avons conçu des plateformes basées sur une monocouche de SAV à laquelle des molécules biotinylées comme le cRGD et l'iHS ou l'iBMP2 peuvent se lier (Migliorini et al., 2014, 2017). L'aBMP2 adsorbé sur l'iHS a été directement comparé à l'iBMP2 après avoir assuré une densité de surface similaire. Pour contrôler précisément la quantité de chaque composé sur la surface, nous avons réglé la cinétique de liaison *via* la concentration moléculaire en solution et mesuré la liaison à la plateforme avec des techniques sensibles à la surface telles que QCM-D et SE. Ainsi, nous

avons pu co-fonctionnaliser la plateforme en interrompant la liaison d'une première molécule avant de saturer les sites de liaison disponibles et incubé une deuxième et une troisième molécule de manière séquentielle. L'espacement du ligand d'intégrine cRGD a donc été contrôlé par différents temps d'incubation ou, pour diminuer significativement la quantité de cRGD à la surface, en l'espaçant avec un PEG biotinylé, une molécule à laquelle les cellules n'adhèrent pas. Pour distinguer les différents types d'intégrines, nous avons réduit au silence les précurseurs de myoblastes C2C12 pour les β_1 - ou β_3 -intégrines et les avons plaqués sur des surfaces biomimétiques. Nous avons choisi les hPDSC comme type cellulaire plus pertinent pour les applications médicales. Nous avons quantifié l'adhésion cellulaire, la signalisation précoce de BMP2 via pSMAD1/5/9 et la différenciation ostéogénique à travers les marqueurs Osterix, Runx2 et ALP.

Des densités massiques croissantes de cRGD sont positivement corrélées avec la phosphorylation de SMAD1/5/9 dans les cellules C2C12 et à 23 ng/cm² le signal était significativement plus élevé que dans les cellules placées sur des plats en plastique. Sur les plates-formes présentant une concentration critique de cRGD pour l'adhésion cellulaire (0,25 ng/cm²), le sBMP2 et l'iBMP2 ont été capables de renforcer l'adhésion cellulaire. Nous avons conclu que la diaphonie entre les β_3 -intégrines et le BMP2 était bidirectionnelle et dépendait de la quantité absolue du ligand d'adhésion présenté. En effet, nous avons démontré que les cellules C2C12 adhéraient spécifiquement via les β_3 -intégrines au cRGD puisque seule la mise sous silence des β_3 -intégrines et non des β_1 -intégrines a diminué la surface cellulaire jusqu'au niveau des cellules placées sur des plateformes de cRAD, un peptide ayant une affinité beaucoup plus faible pour les intégrines. De plus, alors que le sBMP2 et l'iBMP2 avaient un potentiel réduit d'activation de la phosphorylation de SMAD1/5/9 avec des concentrations de surface décroissantes de cRGD, l'aBMP2 adsorbé sur l'iHS avec des quantités comparables à l'iBMP2 avait une bioactivité constante sur les cellules C2C12. Cet effet positif des iHS sur la phosphorylation de SMAD1/5/9 a également été observé dans les hPDSCs. Grâce à des expériences de silençage de l'RNA, nous avons identifié les β_3 - et β_1 -intégrines comme des influenceurs positifs de l'activité précoce de BMP2 sur les plateformes cRGD hautement adhésives et seule la phosphorylation SMAD1/5/9 de base a été mesurée sur les plateformes cRAD faiblement adhésives. Alors qu'il n'y avait aucune différence entre l'iBMP2 et l'aBMP2 sur les plateformes cRGD hautement adhésives en ce qui concerne l'activité BMP2 précoce, l'iHS avec l'aBMP2 a régulé à la hausse l'expression d'Osterix, Runx2 et ALP par rapport à l'iBMP2. Il est intéressant de noter que les cellules se sont également différenciées sur les

plateformes cRAD et que là aussi, l'iHS a eu un effet positif par rapport à la sBMP2 et à l'iBMP2, peut-être en raison de la voie non-SMAD, même si nous n'avons pas mesuré la régulation du signal p-p38.

En résumé, le dialogue entre les intégrines et BMP2 était bidirectionnel et les β_1 - et β_3 -intégrines ont influencé positivement la signalisation de BMP2 et la différenciation ostéogénique. En outre, l'orientation des iHS en même temps que l'aBMP2 a renforcé la différenciation ostéogénique, probablement en soutenant la signalisation de la BMP2 au fil du temps et en facilitant la proximité entre les récepteurs de la BMP et les intégrines en raison de sa longue structure moléculaire. Puisque les intégrines et les iHS ont un effet positif sur la signalisation du BMP2, ils pourraient être présentés avec le BMP2 sur les implants pour la régénération osseuse afin de réduire les doses de BMP2 dans les applications médicales.

IV.C Article 3 (Published in Acta Biomaterialia)

Heparan sulfate co-immobilized with cRGD ligands and BMP2 on biomimetic platforms promotes BMP2-mediated osteogenic differentiation.

Acta Biomaterialia 114 (2020) 90–103
doi: 10.1016/j.actbio.2020.07.015.

Julius Sefkow-Werner^{1,2}, Paul Machillot^{1,2}, Adria Sales^{1,2}, Elaine Castro-Ramirez^{1,2}, Melissa Degardin³, Didier Boturyn³, Elisabetta Ada Cavalcanti-Adam⁴, Corinne Albiges-Rizo⁵, Catherine Picart^{1,2,6*}, Elisa Migliorini^{1,2*}

¹Grenoble Institute of Technology, Université Grenoble Alpes, LMGP UMR 5628, Grenoble, France

²CEA, CNRS, UGA, BRM ERL 5000, Grenoble, France

³Université Grenoble Alpes, CNRS, DCM, Grenoble, France

⁴University of Heidelberg, Department of Biophysical Chemistry, Heidelberg, Germany

⁵Institut Albert Bonniot, Université Grenoble Alpes, INSERM U1209, CNRS UMR5309, Grenoble, France

⁶CEA, direction of fundamental research, interdisciplinary research institute of Grenoble (IRIG), FRE CNRS

*co-corresponding authors

Elisa Migliorini, 3 parvis L. NEEL 38016 GRENOBLE
Tel: (33)-04 56 52 93 24 Email: elisa.migliorini@grenoble-inp.fr
Catherine Picart, 17 rue des Martyrs, 38016 GRENOBLE
Email: catherine.picart@cea.fr

Abstract

The chemical and physical properties of the extracellular matrix (ECM) are known to be fundamental for regulating growth factor bioactivity. The role of heparan sulfate (HS), a glycosaminoglycan, and of cell adhesion proteins (containing the cyclic RGD (cRGD) ligands) on bone morphogenetic protein 2 (BMP2)-mediated osteogenic differentiation has not been fully explored. In particular, it is not known whether and how their effects can be potentiated when they are presented in controlled close proximity, as in the ECM. Here, we developed SAV platforms to mimic selective aspects of the *in vivo* presentation of cRGD, HS and BMP2, with a nanoscale-control of their surface density and orientation to study cell adhesion and osteogenic differentiation. We showed that whereas a controlled increase in cRGD surface concentration upregulated BMP2 signaling due to β_3 integrin recruitment, silencing both, β_1

and β_3 integrins, negatively affected BMP2-mediated phosphorylation of SMAD1/5/9 and ALP expression. Furthermore, the presence of adsorbed BMP2 promoted cellular adhesion at very low cRGD concentrations. Finally, we proved that HS co-immobilized with cRGD both sustained BMP2 signaling and enhanced osteogenic differentiation compared to BMP2 directly immobilized on SAV, even with a low cRGD surface concentration. Altogether, our results showed that HS facilitated and sustained the synergy between BMP2 and integrin pathways and that the co-immobilization of HS and cRGD peptides optimised BMP2-mediated osteogenic differentiation.

Introduction

The chemical and physical properties of the extracellular matrix (ECM) as the main regulator of processes such as cellular proliferation, migration, adhesion, differentiation and tissue formation have been widely explored [1, 2]. Today, the role of glycosaminoglycans (GAGs) in the preservation, presentation and activation of extracellular components has become an important area for research [3-6]. One of the roles of the extracellular components is to regulate the activity of growth factors (GFs) such as the broadly-studied bone morphogenetic protein 2 (BMP2), known for its osteogenic potential [7] and its clinical use in *de novo* bone formation. BMP2 binds mainly to the BMP2 cell receptor complex formed by the transmembrane BMP receptor type I and BMP receptor type II. This triggers the phosphorylation of SMAD1/5/8 and, together with SMAD 4, it translocates to the nucleus [8] to activate transcription of target genes. BMP2 upregulates transcription factors such as Osterix or Runx2, both of which are markers for osteogenic differentiation. It also activates the SMAD-independent osteogenic signaling cascade, which leads to ALP expression (ALP) [9, 10].

In vivo, BMP2 most likely does not present alone in solution, but rather bound to extracellular matrix (ECM) components, such as the GAG, heparan sulfate (HS) [11-13], and fibronectin [14]. It is generally accepted that this binding protects GFs from degradation and modulates their availability to their receptors in the cell membrane [15-17].

Simplified biomimetic model systems can be used to understand this complex system. They make it possible to assemble individual components of the cell's natural environment to reveal their specific role.

In the osteogenic context, various approaches have been reviewed recently [18, 19], all focusing on presenting GFs *via* ECM molecules such as proteins and GAGs. For example, polyelectrolyte multilayer films can be engineered with tunable stiffness [20] and trap BMP2 with high affinity [21, 22]. To study the isolated or combined effect of single ECM components on cells, versatile surfaces with precise control of molecular orientation and surface density are needed. We previously developed streptavidin (SAv) platforms to study the molecular role of GAGs on GF binding [23, 24] and short-term cellular responses [25, 26]. Gold-sputtered glass surfaces were functionalized with a self-assembled monolayer of biotinylated PEG-thiol on which SAv formed a second monolayer, thus offering free highly specific biotin binding sites. On these platforms, HS was immobilized *via* its reducing end, which mimics its attachment to core proteins on HS proteoglycans [27]. BMP2 binding to iHS was studied at the molecular level [28].

The effect of HS on BMP2 signaling is the subject of scientific debate [13, 29-33]. It was previously shown that HS inhibits BMP2 bioactivity [13, 29-33] as it does for different GFs [36]. But results from our group suggest that exogenous HS in particular has a positive effect on BMP2 bioactivity compared to immobilized BMP2 (iBMP2) [28], partially in line with previous observations on BMP2 bound to soluble HS in cell media [13]. However, insufficient cellular adhesion has prevented additional studies of the effect of immobilized HS on later effectors of the BMP2 signaling cascade and therefore a clear readout on how extracellular HS can influence BMP2 bioactivity through osteogenic differentiation.

To tune the bioactivity of BMP2 by HS and to improve its use for regenerative medicine applications, it is also important to further understand the influence of ECM adhesion proteins [37, 38] on BMP2-mediated osteogenic differentiation. In recent years, the interplay between integrins and GF receptors has been the topic of several studies [38-41], but it remains to be proved and quantified on the same biomaterial whether this crosstalk is bidirectional, in particular regarding integrins and BMP receptors.

Integrins are transmembrane receptors consisting of α and β subunits, which bind to cell adhesion ligands in the ECM [42] and allow cells to spread by developing focal adhesions. It has been shown that surface-presented BMP2 can induce cell spreading on soft films, whereas cells did not spread on soft films devoid of BMP2 [43]. In this particular context, β_3 -integrins are needed for BMP2-induced cell spreading and to control SMAD 1/5/8 phosphorylation and degradation. However, the type of integrins involved in growth factor signaling might be

context dependent. Experiments with VEGF have shown that β_1 -integrins upregulate VEGF-induced vascularization in hydrogels, while β_3 -integrins have no influence [44]. It has further been demonstrated on mesenchymal stem cells that increased lateral spacing of arginine-glycine-aspartic acid (RGD) containing peptide ligands significantly decreases ALP activity and reveals a similar trend on Runx2 expression [45]. *In vivo* studies with *Drosophila* have revealed that integrins are also necessary for a peak p-SMAD1/5/9 signal [40]. Collagen IV mutant embryos presented a reduced p-Mad (the equivalent of p-SMAD) signaling.

How HS is able to contribute to BMP2-mediated signaling and osteogenic differentiation, as well as interfere with the cooperation between BMPRs and integrins, is still an open question.

Here, we studied the influence of integrin activation and the additional role of HS on BMP2-mediated signaling with a well-defined biomimetic SA_v platform. These platforms co-presented cyclic RGD peptides (cRGD) known to bind and activate integrins such as β_1 and β_3 subunits [46] and immobilized and oriented HS (iHS). The cyclic arginine-beta alanine-aspartic acid (cR β AD here named cRAD) peptide was adopted as the negative control as it has a significantly lower affinity for integrins [46]. BMP2 was presented either immobilized or adsorbed to iHS with the same surface density. Cellular responses were assessed by quantifying cell adhesion and cell osteogenic differentiation at early and later stages. To this end, we selected two relevant cell types that are BMP2-responsive: C2C12 murine myoblasts [47] and human periosteum-derived stem cells (hPDSCs) that are currently investigated for their bone regenerative capacities [48]. To gain insight into the role of β_1 and β_3 integrins on early and late BMP2-mediated signaling, we performed knock-down experiments by silencing these receptors.

Experimental procedures

Buffers, heparan sulfate and proteins

10 mM HEPES (Fisher, Illkirch, France) at pH 7.2 was used as the working buffer for surface functionalization, for all quartz-crystal microbalance with dissipation monitoring (QCM-D) and spectroscopic ellipsometry (SE) measurements. Filtered phosphate buffered saline (PBS,

Dublbecco's without MgCl₂ and CaCl₂, Sigma-Aldrich) was applied in all the working steps related to the cells.

HS derived from porcine intestinal mucosa [49] (Celsus Laboratories, Cincinnati, OH, USA) was conjugated with biotin as previously described [24]. Human recombinant BMP2 (26 kDa, homodimer), from a Chinese hamster cell line, was purchased from R&D Systems Inc. (Minneapolis, MN, USA). BMP2 was biotinylated by NHS-ester coupling using EZ-Link® NHS-PEG12-Biotin 5.6 nm long (Thermo Scientific, Rockford, IL, USA) as described in [28]. Lyophilized SAV, (53 kDa) and ATTO 565-Biotin (921 DA, bATTO) were purchased from Sigma-Aldrich. Biotinylated cRGD and cRAD (3.9 and 4.2 kDa, respectively) were obtained by amide-coupling PEG (~ 3.2 kDa), with a biotin at one end and an activated acid group at the other (b-PEG-NHS, Sigma-Aldrich), to a cyclic RGD pentapeptide c(-RGDfK) (GenScript Biotech, Netherlands) or cyclic RAD (RβAD, synthesized in the lab of Dr Didier Boturyn), at the lysine side-chain as written in [26]. Thawed protein solutions were used within a week and further diluted (**Table 1**).

Sensors and surface preparation

Gold-coated QCM-D sensors (QSX301) from Biolin Scientific (Västra Frölunda, Sweden) and gold-sputtered glass cover slips (24 × 24 mm; Menzel Gläser, Braunschweig, Germany) for cellular studies were immersed in 1 mM of PEG disulfide and biotinylated PEG thiol (Polypure, Oslo, Norway) at a molar ratio of thiol equivalents of 95:5 in ethanol to build a monolayer.

For Western blot and qPCR experiments that demand large quantities of the sample, whole surfaces were then placed in a UV-sterilized plastic dish. When samples were prepared for automated imaging with standardized 96-well plates, gold-coated surfaces were attached *via* double-sided adhesive tape (FRAP Sandwich set, Paul Marienfeld GmbH, Lauda-Koenigshofen, Germany) to the bottom side of a UV-sterilized bottom-less 96-well plate (Greiner bio-one, Kremsmünster, Austria), separating 1 surface into 4 wells.

Assembly of biomimetic platforms

The QCM-D sensors were functionalized step-by-step *in situ* tracked by QCM-D or SE as previously reported [28]. Biomimetic platforms were functionalized *ex situ*, incubating molecules at the desired concentration under sterile conditions. To prepare co-functionalized platforms, the following concentrations and incubation times were used:

Table 1: Molecule concentrations and incubation times.

<i>Molecule</i>	<i>Concentration (μM)</i>	<i>Incubation time (min)</i>
Streptavidin (SAv)	0.17	30
Biotinylated cyclic Arginyglycylaspartic acid (cRGD)	0.14	4 (partly saturated) or 10 (saturated)
cRGD-PEG mixture	0.25	3 (partially saturated)
Biotinylated cyclic Arginylalanineaspartic acid (cRAD)	0.24	4 (partly saturated)
Biotinylated Atto 565 (bATTO)	11	20
Biotinylated Heparan sulfate (iHS)	0.83	30
Biotinylated bone morphogenetic protein 2 (iBMP2)	9.6×10^{-2}	60
Adsorbed BMP-2 (aBMP2)	9.6×10^{-2}	90
Soluble BMP-2 (sBMP2)	6×10^{-3}	

The concentrations and time of incubation of cRGD and cRAD were chosen in a way to obtain the desired sub-monolayer surface density which then makes possible the subsequent binding of iHS or iBMP2. Soluble BMP2 (sBMP2) at a concentration of 6 nM was always added into the cell media at the moment when cells were plated on the corresponding condition. The quantity of soluble BMP2 in the media largely corresponds to the amount of either aBMP2 or iBMP2 on the platform surface. The wells of 96-well plates and large round surfaces with surface areas of 35 mm² and 450 mm² respectively therefore had 8.6 ng and 110 ng of iBMP2 or 10.4 ng and 134 ng of aBMP2 on the surface (see **Table 2**). 100 μl of cell media per well and 1 ml of cell media on round surfaces carry 10 ng and 100 ng of sBMP2 respectively. We point out that a direct comparison of sBMP2 and surface-bound BMP2 lags due to the disparity in its dorsal and ventral presentation to the cell.

Quartz crystal microbalance with dissipation monitoring (QCM-D) and spectroscopic ellipsometry (SE)

QCMD and SE were used to characterize molecule binding events on the SA_v monolayer to deduce binding kinetics and areal mass density respectively and was previously described in

detail [25, 50, 51]. All surface functionalization steps were carried out *in situ* using the concentrations and incubation time indicated in **Table 1**.

Cellular culture

Mouse C2C12 myoblasts (CRL-1772, ATCC, USA) and human periosteum-derived stem cells (hPDSCs, kindly provided by Prof. Franck Luyten, Leuven, Belgium) [48, 52, 53], were used for the functional assays. Both cell types were cultured in typical tissue-treated polystyrene cell culture flasks or Petri dishes as sub-confluent monolayers in growth medium consisting of Dulbecco's modified Eagle's medium (DMEM) (Gibco) supplemented with heat-inactivated fetal bovine serum (FBS, 10 %) (FBS, PAA Laboratories, Toronto, Canada) and antibiotic-antimycotic (1 %, Gibco) at 37 °C and 5 % CO₂ until a passage number of less than 12. hPDSCs (< 9 passages) were cultured as previously described [52] in high-glucose Dulbecco's modified medium, supplemented with 10% fetal bovine serum and 1% antibiotic-antimycotic.

Both C2C12 and hPDSCs were always serum-starved 4 hours prior to plating on the biomimetic platforms. Accutase (Sigma Aldrich) was used to detach cells from culture flasks prior to the experiment in DMEM without FBS supplement. Functionalized surfaces with plated cells were always incubated at 37 °C, 5% CO₂ with media (0% FBS) if not specified otherwise.

Knock-down of integrins

To silence integrins on C2C12 cells, we used a protocol optimized in our group [43]. Briefly, C2C12 were transfected twice, 48 h and 24 h before starving and then plating on the surfaces. The transfection mix consisted of lipofectamine RNAiMAX (Invitrogen, Carlsbad, Ca, USA) diluted in Opti-MEM medium (Gibco) which was gently mixed with 100 μM Silencing RNA for β₁-, β₃-integrin (ON-TARGET plus SMART pool SiRNA, Dharmacon, UK) or scrambled silencing RNA (ON-TARGET plus non-targeting siRNA, Dharmacon, UK). This mix was added drop by drop into plastic plates and repeated 24 h later to ensure successful transfection. The moment cells were plated on functionalized surfaces, no more silencing RNA was added to the fresh media.

Cell adhesion and differentiation for microscopy analysis

For live cell imaging used to quantify cell numbers, 30 000 starved cells for each condition were plated on functionalized 96-well plates and incubated for 45 minutes (C2C12 cells) or 1h and 45 minutes (hPDSCs). Nuclei were stained 30 min after plating with 10 ng/mL Hoechst (Invitrogen) in PBS. 15 min later, images were taken on eight defined positions with the Zeiss Axio Observer 7 epifluorescence microscope (Carl Zeiss Sas, Le Pecq, France) with the cell culture environment (37 °C, 5 % CO₂) provided by the heating unit XL S (Zeiss). After rinsing carefully 4 times with 100 µL PBS to remove non-adherent cells, fluorescent images (Colibri 7, 385 nm, 21 % intensity) were taken again with the 20x objective at the same positions to quantify the percentage of adhering cells. 30 minutes after rinsing, the cells were fixed with PFA 4% (Sigma-Aldrich) for 20 min.

To measure C2C12 cell area and p-SMAD1/5/9 translocated to the nucleus [54], 10 000 starved cells per condition were plated on functionalized 96-well plates and fixed after 1.5 hours by rinsing 3 times with 100 µL PBS before adding 100 µL PFA fixation.

To quantify p-SMAD1/5/9 *via* immunofluorescence we adapted existing protocols already published [26, 54, 55]. Fixed cells were first permeabilized with 0.2% Triton X-100 (Sigma-Aldrich) (w/v) in PBS for 3 min and blocked for 1h with 3% BSA (Sigma-Aldrich) at RT. Primary rabbit anti-p-SMAD1/5/9 (Cell Signaling Technology, Danvers, Ma, USA) was diluted 1:400 and for staining, F-actin Phalloidin-Rhodamine (Sigma-Aldrich) was used at a dilution of 1:1000. For β_1 - (rat anti-integrin β_1 , MAB 1997, Millipore, Darmstadt, Germany 1:100) and β_3 -integrins (rat anti-mouse integrin β_3 , Luc-A5, emfret Analytics, Würzburg, Germany 1:100) no Triton treatment was used. All primary antibodies were incubated overnight at 4 °C diluted in PBS with 3% BSA. Secondary antibodies (goat anti-rat/rabbit Alexa Fluor 488, Thermo Fischer Scientific), as well as F-actin and DAPI, were incubated for 90 min at RT in PBS and 3% BSA. As a final step, a solution of 2.5% w/v Dapco (Sigma-Aldrich) in PBS at pH=7.8 preserved the fluorescence activity.

For highly magnified images to visualize β_1 - and β_3 -integrins together with F-actin and the nucleus, a 63x oil-immersed lens (Plan-Apochromat 63x/1,4 Oil DIC, Carl Zeiss Sas, Le Pecq, France) from a Zeiss LSM 700 confocal microscope (Carl Zeiss Sas) was used. Cell area and p-SMAD1/5/9 were simultaneously studied by capturing p-SMAD1/5/9, F-actin and DAPI signals with a 20x objective (Plan-Apochromat 20x/0.8 Ph2, Carl Zeiss Sas) with the Zeiss

Axio Observer 7 microscope. For quantitative analysis, at least 50 cells per condition distributed over the whole surface were imaged.

Image analysis, homogeneity analysis and custom-made macros

All images were analyzed with ImageJ [56]. To quantify the cell number, nuclei were identified in each image *via* this software's Analyze Particles function. The cell number after rinsing was divided by the total cell number before rinsing to obtain a percentage of adherent cells.

Cell area was analyzed by measuring the actin positive area with Analyze Particles (Image J) [56]. The total area of all cells in 1 image was divided by the total number of nuclei, counted as described above, to reduce the influence of overlapping cells [57].

Fluorescently labeled p-SMAD1/5/9 was quantified by measuring its fluorescence intensity inside the nucleus [54, 55]. For this, the nucleus was again identified *via* the DAPI signal using Analyze Particles (ImageJ) which served as a virtual mask. Then, the intensity of the grey levels of the p-SMAD1/5/9 signal which lie under this mask was extracted and the average background signal was subtracted.

β_1 - and β_3 -integrins were only analyzed qualitatively to assess whether or not focal adhesions were formed, and to detect general distribution of integrins in the cell.

The homogeneity of SA_v and cRAD, as an example for the binding of biotinylated molecules to SA_v, was studied *via* the binding of bATTO to the free biotin binding sites of SA_v. After functionalization with bATTO, the surfaces were flipped and put on a microscopy coverslip with an oil-based anti-fade in between. Images were taken with the 63x oil-immersed lens (Plan-Apochromat 63x/1,4 Oil DIC) of a Zeiss LSM 700 confocal microscope (Carl Zeiss Sas) on four different positions per condition and average intensity values were compared to each other.

Protein isolation and western blot analysis

Approximately 200 000 serum-starved cells were lysed in RIPA buffer (Sigma Aldrich) after 1h for p-SMAD1/5/9 or after 1 h, 24 h or 3 days for integrin quantification as previously

reported [28]. Gels were loaded with a protein concentration of 25 µg/ml which was quantified with a micro BCATM assay kit (Thermo Fisher). Blocked membranes were probed with rabbit anti-p-SMAD1/5/9 (1:1000, Cell Signaling Technology), rabbit anti-β₁ (1:2000, produced at the laboratory of Dr Albiges-Rizo, IAB, Grenoble, France) or rat anti-β₃ (1:1000, Luc-A5, Emfret Analytics) together with rabbit anti-GAPDH (1:1000, Cell Signaling Technology) as a reference, all incubated in 1% BSA overnight. Incubation with goat anti-rabbit HRP-conjugated IgG (1:5000 Cell Signaling) and goat anti-rat HRP-conjugated IgG (1:2000 Cell Signaling) was followed by detection with the ChemiDoc Imaging system (Bio-Rad, Hercules, USA) using Clarity or Clarity Maw Western ECL Substrate (Bio-Rad).

RNA extraction and quantitative polymerase chain reaction (qPCR)

Approximately 200 000 cells were cultured for 24 h before lyse with 350 µL lysis buffer (Machery-Nagel, Dueren, Germany). 4 h after plating, the FBS concentration in the cell media was raised from 0% to 2%. RNA was extracted using the NucleoSpin RNA Plus kit (Machery-Nagel) according to the manufacturer's protocol, and quantified with UV-Spectrophotometry (Nanodrop 2000, Thermo Fisher Scientific). cDNA transcription and qPCR were carried out using the CFX96 Real-Time system thermo cycler (Bio-Rad) and the corresponding consumables (Biorad) and primers (Sigma-Aldrich). The C_q values of the target genes were normalized to the reference genes (GUSB, PPIA, Ef1) using the delta-delta-Ct-method [58].

Alkaline phosphatase (ALP) staining

96-well plates with glued functionalized biomimetic platforms were used for ALP staining. 20 000 cells were plated for each well for 3 days in growth media, with 2% FBS, and fixed in 4% PFA. To quantify total cell number, DAPI staining was performed before ALP staining. To stain ALP, we used fast blue RR salt in a 0.01 % (w/v) naphthol AS-MX solution (Sigma Aldrich) according to the manufacturer's instructions. ALP staining was quantified in dry conditions by scanning the 96-well plate with a scanner (V600 photo, EPSON, Seiko-Epson Corporation), and gray-scale images were acquired at a resolution of 1200 dpi [57]. The images (8-bit) were analyzed with Image J. A threshold of gray was fixed for all conditions (between 0 and 160) to measure the percentage of ALP-positive area per well. This number was normalized to the number of cells in each condition.

Statistical analysis

Technical replicates were pulled together by taking the average and standard deviation. To compare independent experiments, the values were normalized to a positive control, the average was calculated and the standard error of the mean was used for the error bars in the figures. Significance between two conditions was tested with the non-parametric Mann-Whitney test and represented in the graphs with * for $p \leq 0.05$ and ** for $p \leq 0.01$.

Results

Increasing cRGD surface concentration enhanced BMP2-mediated SMAD signaling

To investigate the effect of integrin activation on BMP2 signaling we tuned the surface concentration of the integrin-ligand cRGD, bound to biotinylated polyethylene glycol of ~ 3200 Da (b-PEG-RGD here named cRGD), on the SAV platform and stimulated cells with soluble BMP2 (sBMP2) at a constant concentration of 6 nM (**Figure 1a**).

Before performing cellular experiments, we characterized the binding of cRGD to SAV with a combined QCM-D and SE setup (**Figure 1b**). The black curve in **Figure 1b** is a spectroscopic ellipsometry dynamic fitting of the Δ and Ψ ellipsometric angles obtained during the adsorption of cRGD on SAV at a 0.25 μ M soluble concentration. At equilibrium, 22.6 ± 1.2 ng/cm² of cRGD were bound to the SAV monolayer. To reduce the surface amount of cRGD, its adsorption was stopped at 1 and 3 minutes, generating an adsorbed mass of 2.1 ± 0.1 and 10.1 ± 1.0 ng/cm² respectively. Considering a homogenous coating of cRGD molecules on the SAV monolayer (as shown in **Figure S11**) and an average molecular weight of the peptide of 3.9 kDa, we calculated that these values correspond to an intra-molecular distance of ~ 17, 8 and 5 nm for the 1, 3 minutes and saturated cRGD, respectively.

C2C12 cells were plated on these cRGD platforms and after 1 hour of stimulation with sBMP2, the cells were lysed for Western blot analysis. As a positive control, C2C12 cells were plated on plastic Petri dishes (TCPS) and stimulated with the same concentration of sBMP2. **Figures 1c** and **1d** show that SMAD1/5/9 phosphorylation was upregulated in cells plated on higher cRGD surface concentrations (23 ng/cm²) compared to lower cRGD surface

concentrations (2 ng/cm²). These results indicate that SMAD1/5/9 phosphorylation is cRGD dose-dependent. Increasing integrin recruitment at the cell membrane therefore enhances BMP2 bioactivity.

To further prove that this effect is integrin-mediated we replaced cRGD with cRAD peptide (**Figure 1a**). QCM-D measurements (**Figure 1e**) show the binding of three different surface concentrations of cRAD. For that, cRAD adsorption was interrupted before saturation to obtain a sub-monolayer surface density. With a SE and QCM-D combined setup, we quantified the adsorbed amount of cRAD ($\Delta\Gamma$ in ng/cm²) relative to the frequency shift (Δf in Hz) measured with the QCM-D (**Figure 1f**). This curve makes it possible to deduce the optical mass from shifts in frequency and leads to calculated surface concentrations of 19.4 ± 1.1 ng/cm² for the saturated cRAD and 9.3 ± 0.7 and 5.4 ± 0.5 ng/cm² for the partial cRAD coatings. Homogeneous binding of cRAD on SA_v (which was exemplary for biotinylated molecules such as cRGD and bPEG) was measured *via* immunofluorescence using bATTO-565 (**Figure SI1**). As before, C2C12 were plated on cRAD platforms, TCPS and stimulated with sBMP2. On these conditions the increasing surface concentration of cRAD peptide did not improve the cellular p-SMAD1/5/9 response to sBMP2 (**Figure 1g, h**) compared to the cRGD platforms (**Figure 1c**) and TCPS conditions. In **Figure SI2a** we directly compared the effect of cRGD *VS* cRAD peptides with sBMP2 on BMP-SMAD signaling. We demonstrated that p-SMAD1/5/9 levels are significantly lower on cRAD platforms.

However, we observed basal SMAD1/5/9 phosphorylation in conditions without exogenous integrin ligands which was possibly induced by the fibronectin secreted [43]. The ratio of the normalized levels of p-SMAD1/5/9 of cRGD/cRAD at different peptide concentrations (**Figures 1d** and **1h**, respectively) is plotted in **Figure SI2b**, confirming an increase on higher cRGD surface densities.

These results indicate that BMP2 bioactivity was enhanced by cRGD density, probably through increased engagement of integrins at the cell membrane.

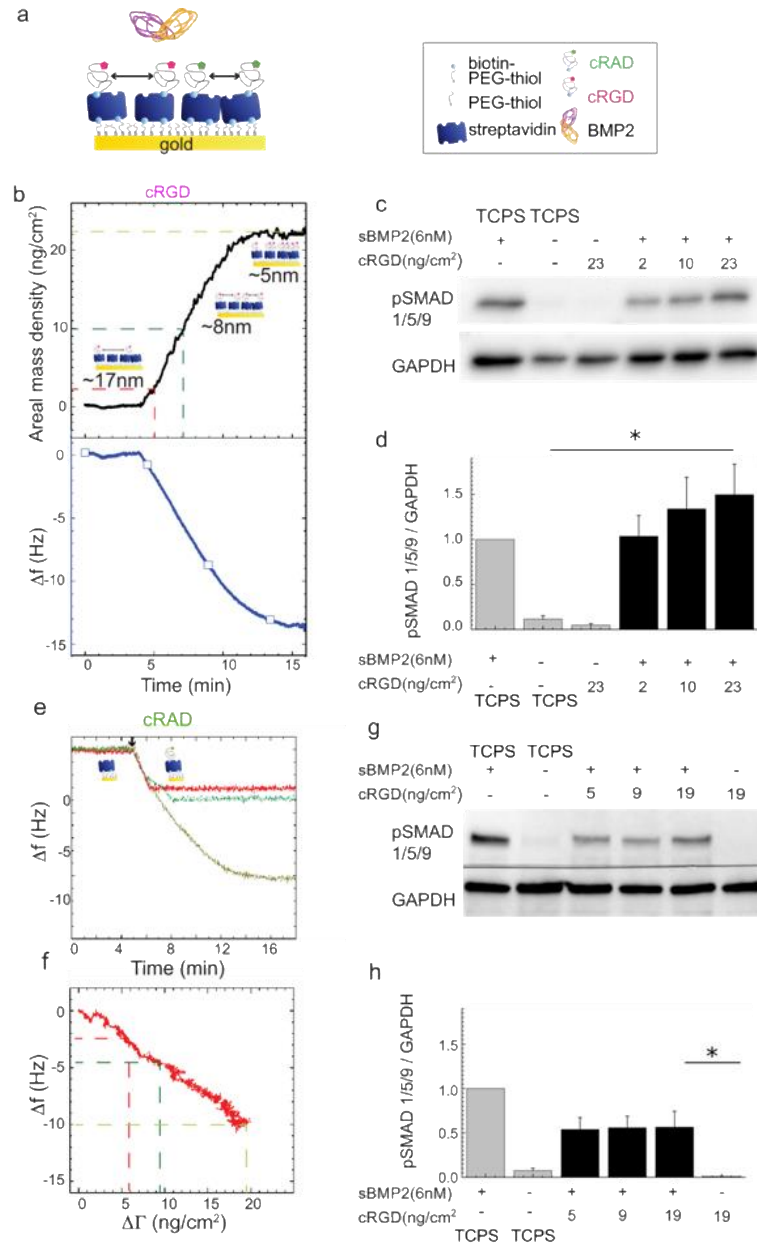


Figure 1: Increasing the surface concentration of cRGD enhances cell response to sBMP2. **a)** Schematic representation of the cRAD and cRAD platforms with variable inter-molecular distances between biotinylated peptides. **b)** Combined QCM-D / SE measurement of cRGD binding to SAV. The black curve corresponds to the SE data and the blue curve to the QCM-D binding of cRGD to SAV. The dashed lines mark the incubation times used to functionalize the platforms and the corresponding adsorbed masses. **c)** Western blot of p-SMAD1/5/9 levels in C2C12 cells plated on surfaces presenting three different cRGD surface concentrations and stimulated with sBMP2 (6 nM). As the internal control, C2C12 cells were plated on TCPS with sBMP2. One hour after plating, the cells were lysed and the level of p-SMAD1/5/9 plotted and normalized to the housekeeping gene GAPDH. **d)** Quantification of the Western blot bands. The TCPS control is shown in light grey. The triplicate experiments are shown in **Ext fig 1 c** and are available online (<http://dx.doi.org/10.17632/p6d4m9gprw.2>) **e)** QCM-D measurement showing the adsorption of cRAD at three different incubation times. **f)** $\Delta\Gamma/\Delta f$ calibration curve obtained thanks to a combined SE-QCM-D setup to quantify the quantity of cRAD ($\Delta\Gamma$ ng/cm²) adsorbed, measured with SE relative to the frequency shift (Δf Hz) measured with the QCM-D. **g)** Western blot of p-SMAD1/5/9 expression on the cRAD platform and its quantification (**h)** as in panel c and d. The triplicate experiments are shown in **Ext fig 1 g** and are available online (<http://dx.doi.org/10.17632/p6d4m9gprw.2>). Bars

correspond to the mean \pm SEM. The non-parametric Mann-Whitney test was used for single comparisons. * $p < 0.05$.

BMP2 improves cell adhesion on low-adhesive platforms

To study the effect of BMP2 on integrin signaling, cell adhesion was considered to be a relevant readout of integrin activation. Previously, BMP2-mediated cell adhesion was demonstrated with soft layer-by-layer biomimetic films presenting matrix-bound BMP2 [43]. Here, we designed low adhesive cRGD platforms with molecular distances of less than 73 nm, previously shown to be the threshold for cellular adhesion of mesenchymal cells [59, 60]. To do so, simply decreasing the incubation time of cRGD for less than a minute (see **Figure 1b**) may cause experimental errors. We therefore diluted the cRGD peptide in the solution with the inert biotinylated polyethylene glycol (iPEG) molecule (~ 3000 Da) (**Figure SI1a**). After synchronizing their binding kinetics, the cRGD molecular distance could be controlled by different mixtures of both molecules (**Figure SI1b**), while maintaining the sub-monolayer surface density constant, indispensable for other biotinylated molecules to bind.

To compare the effect of soluble *vs* immobilized BMP2 (iBMP2), platforms presenting a cRGD/iPEG mixture were co-functionalized with iBMP2 and characterized with combined QCM-D and SE measurements (**Figure 2a** and **b**, respectively). To this end, the adsorption of the mixture cRGD/iPEG was stopped after 3 minutes of incubation, obtaining total adsorption of 10 ± 1 ng/cm² (**Figure 2b** min 38–41). In the case of 10% of cRGD and 90% of iPEG, we expected that 1.0 ± 0.1 ng/cm² of cRGD would be immobilized. Assuming a homogeneous distribution of cRGD and iPEG molecules on the SA_v monolayer, this surface concentration corresponded to an average distance of 25.5 ± 1.3 nm between cRGD peptides. To further increase this inter-molecular distance, 5%, 2.5% and 1% of cRGD was mixed with 95%, 97.5% and 99% of iPEG resulting in lateral distances of about 36, 51 and 81 nm, respectively (see **Table 2**). iBMP2 was sequentially immobilized on to free-biotin pockets left on the SA_v monolayer, generating a frequency shift of -4.3 ± 0.2 Hz, corresponding to a mass of 24.5 ± 0.5 ng/cm² (**Figure 2b** min 46–66 and **Table 2**).

Table 2: Surface concentration for each component of the biomimetic surfaces and root-mean-square anchor distances for each component. The polymeric components such as iHS and cRGD are polydisperse and we therefore assumed that the molecular mass of surface-bound molecules is identical to the average molecular weight of the components in solution [25, 26]. Data were obtained from SE measurements. Mean values and standard errors are presented (n=3)

Compound	Areal mass density (ng cm⁻²)	Distance (nm)
SAv	204.9 ± 9.9	6.9 ± 0.2
+ cRGD	1.0 ± 0.1	25.5 ± 1.3
	0.5 ± 0.1	36.1 ± 1.8
	0.25 ± 0.02	51.1 ± 2.6
	0.10 ± 0.01	80.8 ± 4.1
+ iBMP2 (after rinsing)	24.5 ± 0.5	13.3 ± 0.1
	22.3 ± 0.5	13.9 ± 0.2
+ iHS	14.4 ± 0.5	11.9 ± 0.2
+ aBMP2 (after rinsing)	29.8 ± 1.1	12.1 ± 0.2
	11.8 ± 1.2	19.2 ± 1.0

C2C12 cells were plated on these platforms and after 1 hour they adhered and, after 1.5 h, they formed integrin β_3 clusters, clearly detectable with confocal microscopy, on cRGD 1 ng/cm² but less detectable on lower cRGD surface concentrations, where C2C12 cells became smaller and punctate (**Figure 2c** and **Figure SI4**). ENCODE studies show that β_1 integrins are more expressed on C2C12 cells than β_3 integrins [61]. On cRGD platforms they were distributed over the entire cell membrane and small β_1 clusters were visible at the cell periphery (**Figure SI4**).

The number of cells that remained adherent to the platforms 1 hour after plating followed by manual rinsing decreased with the reduction of cRGD surface concentration (**Figure 2d**). Only ~10% of cells adhered on platforms with cRGD 0.1 ng/cm². Surprisingly, whereas the density of 0.25 ng/cm² cRGD was at the limit for inducing cell adhesion, the presence at this concentration of sBMP2 or iBMP2 significantly increased the number of adherent cells (from 30.1 ± 4.1% on cRGD peptide alone to 55.6 ± 6.7 and 66.1 ± 6.5% on sBMP2 and iBMP2, respectively) (**Figure 2d**). For later differentiation studies, it is important to note that the cell area remained unchanged regardless of the type of BMP2 presentation and cRGD surface density (**Figure 2d**). The effect of the same platforms on the adhesion of human periosteum derived stem cells (hPDSCs) was studied. These cells adhered after only 2 hours on cRGD platforms. hPDSCs adhesion decreased on lower cRGD surface concentrations, as for C2C12 cells. However, cellular adhesion was not improved by the presence of BMP2 (**Figure SI5**),

likely due to hPDSCs cell ability to secrete BMP2 which can mask the effect of surface-presented BMP2 [62]. hPDSCs became round on 0.1 ng/cm², confirming that at an inter-molecular distance of 80 nm, cRGD ligands were too far away to permit cellular spreading.

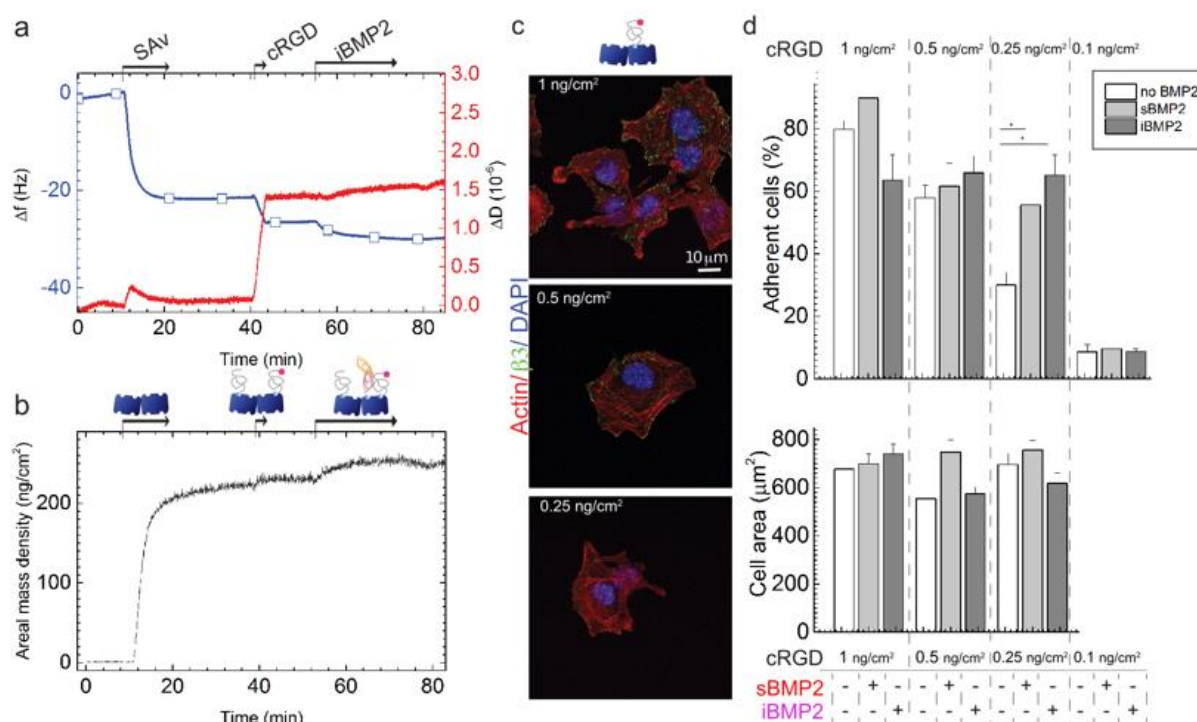


Figure 2: BMP2 improves the number of adherent cells on platforms presenting a 0.25 ng/cm² cRGD surface concentration. **a)** QCM-D measurement shows the co-functionalization of SAw platforms with cRGD and iBMP2. The blue line shows frequency shifts and the red line dissipation shifts. Arrows indicate the start and duration of the injections. In the remaining time, the surfaces were exposed to running buffer. **b)** SE measurement of mass adsorption. **c)** Confocal immunofluorescence images of C2C12 cells plated on biomimetic platforms presenting different cRGD surface concentrations (from 1 to 0.25 ng/cm²) and fixed 1.5 hours after seeding. Immunofluorescence staining was performed to reveal the presence of FAs positive for β_3 integrins (labelled in green). Scale bar = 10 μm **d)** Adherent cells remained on the platforms after rinsing and cell area 1 hour after plating. The analysis of cell area was not carried out on 0.1 ng/cm² as only a residual number of cells remained adherent to the platforms. Bars correspond to the average value \pm standard deviation. A non-parametric Mann-Whitney test was used for single comparisons. * $p < 0.05$.

We found a threshold value for cRGD surface concentrations (0.25 ng/cm²) where C2C12 cell adhesion was improved by the presence of sBMP2 and iBMP2. By means of simple and well-defined surface functionalization we directly proved that integrin activation by cRGD ligands improved BMP2-mediated SMAD signaling and that soluble and immobilized BMP2 enhanced C2C12 adhesion.

C2C12 cell adhesion on cRGD platforms depends on β_3 integrin

We next investigated the involvement of integrins in the synergic signaling observed on cRGD platforms by knocking down either β_1 or β_3 integrins.

First, SAV platforms were engineered to have a comparable amount of cRGD and cRAD, just enough to allow adhesion of a sufficient number of cells to make biomolecular studies possible on both platforms. The concentration in solution of both peptides was adapted to obtain the same binding kinetics measured with QCM-D (**Figure 3a**). After 4 minutes of incubation, the areal mass densities, deduced from the calibration curves shown in **Figures 1b** and **1f**, of cRGD and cRAD were approximately $8.1 \pm 1.2 \text{ ng/cm}^2$ and $7.2 \pm 0.5 \text{ ng/cm}^2$, respectively. In this experiment, a significantly higher cRGD surface concentration was used with respect to **Figure 2**.

We observed that C2C12 cells adhered significantly less on cRAD platforms ($17.9 \pm 7.6\%$) compared to cRGD platforms ($86.5 \pm 4.5\%$) (**Figure 3b**). The presence of sBMP2 and iBMP2 did not significantly improve cellular adhesion at short time points on cRAD platforms ($20.6 \pm 6.8\%$ on sBMP2 and $31.7 \pm 5.8\%$ on iBMP2), in contrast to the cRGD platforms previously presented (**Figure 2d**).

To investigate whether adhesion on the biomimetic platforms was mediated *via* β_3 or β_1 integrins, both ligands for cRGD, we silenced either one or the other as proved in **Figure 3c**. The silencing of β_1 integrin triggered a small compensation of β_3 integrin [63] at 1 hour after plating (**Figure 3c**).

Wild type (WT) C2C12 cells silenced for β_1 or β_3 integrins (si β_1 and si β_3) were plated on the biomimetic platforms presenting cRGD or cRAD ligands with or without sBMP2 (**Figure 3d**). After 1.5 hours on cRGD, WT cells adhered and spread with an area of about $770 \pm 41 \mu\text{m}^2$. β_3 -integrin silencing generated a significant decrease in cell area (to about $328 \pm 9 \mu\text{m}^2$), which means that β_3 -integrins are crucial for cell spreading on cRGD platforms (**Figure 3d**). β_1 -silencing did not affect cell area. The same result was observed in cell adhesion experiments on cRGD platforms (**Figure SI6**). β_3 -silenced cells only adhered very moderately on cRGD platforms ($11 \pm 2\%$) while silencing β_1 integrin did not affect the number of adherent cells. We observed that the area of cells knocked down for β_1 integrins was slightly, but consistently, larger on cRGD platforms with respect to WT cells. This may be explained by the upregulation of β_3 integrins in si β_1 cells observed at 1 h after plating on TCPS (**Figure 3c**). On cRAD platforms, cells were round and their cell area was comparable to that of si β_3 cells. Silencing β_1 or β_3 integrins did not further decrease cell area. All these results indicate that cell adhesion on cRAD platforms was integrin-independent. Furthermore, sBMP2 did not have a significant

effect on the area of integrin silenced cells (**Figure 3d**), which is probably due to the efficient down-regulation of β_3 integrins compared to their reduced engagement *via* low cRGD concentration as seen in **Figure 2d**.

C2C12 adhesion to cRGD platforms was therefore specific and depended on β_3 integrins. In addition, cell adhesion on cRAD peptides is negligible, even in the presence of sBMP2, and integrin-independent, showing that cRAD was an appropriate negative control.

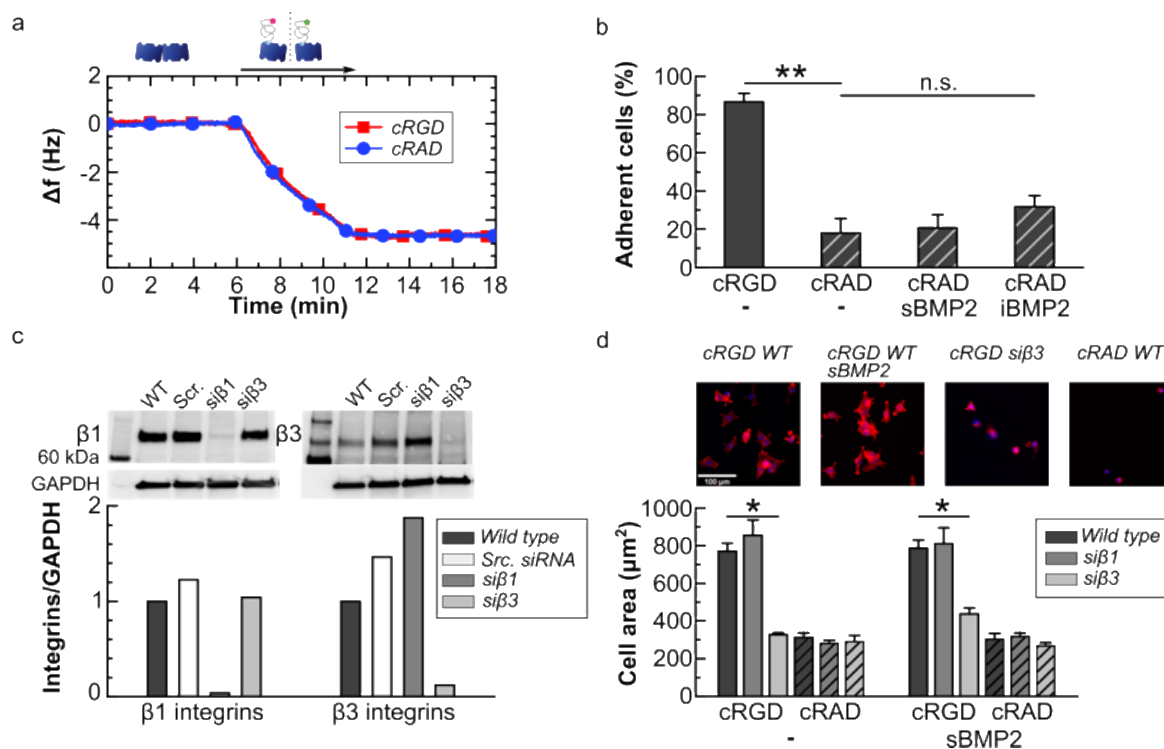


Figure 3: cRGD platforms specifically tune integrin β_3 mediated cell adhesion. **a)** The QCM-D graph shows the cRGD (red curve) and cRAD (blue curve) binding to the SAV monolayer with the same kinetics. **b)** Ratio of adherent wild type C2C12 cells plated on cRGD and cRAD co-functionalized platforms together with sBMP2 and iBMP2. **c)** Western blot and quantification of wild type, scrambled, β_1 and β_3 silenced cells 1 hour after plating. Expression of integrins was normalized to GAPDH **d)** Cell spreading area on cRGD VS cRAD platforms. C2C12 were fixed after 90 min and stained with DAPI (nucleus), phalloidin (F-actin) for fluorescent microscopy. Scale bar = 100 μm . In **b** and **d**, bars represent the mean of three independent experiments \pm SEM. A Mann-Whitney test was used for single comparisons. $*p < 0.05$, $**p < 0.01$, n.s. stands for not statistically significant.

Extracellular HS stabilizes the BMP2-SMAD1/5/9 signaling pathway independently of cRGD surface concentration without influencing cellular adhesion and spreading.

To better understand the role of the ECM on the BMP2 signaling pathway, we added a degree of complexity to these platforms by studying the effect of heparan sulfate on BMP2-mediated cellular adhesion and differentiation.

To study the combined effect of iHS with cRGD ligands on BMP2 bioactivity, we compared BMP2 adsorbed on iHS (aBMP2) to sBMP2 and iBMP2 on different cRGD surface concentrations. Biomimetic platforms presenting iHS were engineered and characterized with QCM-D and SE (**Figure 4a,b**). The surface amount of cRGD was reduced from 1.00 to 0.25 ng/cm², as before in **Figure 2**, by maintaining the same amount of immobilized HS (iHS). iHS was grafted on SAV with a mass density of 14.4 ± 0.5 ng/cm². On iHS, 29.8 ± 1.1 ng/cm² of BMP2 was adsorbed. It is important to note (**Table 2**) that the amount of aBMP2 adsorbed to iHS was comparable to the amount of iBMP2 adsorbed on SAV platforms, as previously characterized (**Figure 2a,b**). After rinsing with Hepes buffer, part of the aBMP2 was removed, confirming the partially reversible binding between HS and BMP2 [28]. The addition of DMEM during the BMP2 rinsing, accelerated the partial (~ 50%) desorption of BMP2, which reached its equilibrium after few minutes (**Figure SI7**).

To study the effect of iHS on aBMP2 bioactivity on different cRGD surface concentrations, we plated C2C12 cells for 1 hour on cRGD platforms with sBMP2, iHS, iHS + aBMP2 and iBMP2 (**Figure 4c**). We analyzed the phosphorylation of SMAD1/5/9 using Western blot. First, we observed that the level of p-SMAD1/5/9 significantly decreased with the decreasing cRGD surface concentrations in the case of both sBMP2 and iBMP2. Platforms functionalized with iHS + aBMP2 maintained constant levels of p-SMAD1/5/9 even at low cRGD surface concentrations (**Figure 4c**).

It is worth noting that SMAD1/5/9 phosphorylation was sustained on iHS + aBMP2 during the first 6 hours after plating, while this signaling decreased with time on both sBMP2 and iBMP2 (**Figure SI8a**).

Cellular adhesion on 0.25 ng/cm² of cRGD, was not improved by iHS alone, but by the presence of iHS + aBMP2 (**Figure SI9b**).

The effect of HS on BMP2 bioactivity was also studied on hPDSCs at a later time point (2 hours), due to the slower cellular adhesion to the platforms compared to C2C12 cells (**Figure SI9c,d**). A cRGD surface concentration of 0.5 ng/cm² was used to obtain a sufficient quantity (75 ± 3%) of cells adhered on the platforms (**Figures SI5a and SI9d**). The levels of p-SMAD1/5/9 were analyzed using Western blot, and the highest levels of p-SMAD1/5/9 were observed on iHS + aBMP2 platforms, condition that significantly upregulated SMAD1/5/9 phosphorylation with respect to the iHS alone (**Figure 4d**).

We proved with two different cell models that iHS had a positive influence on BMP2 bioactivity. For C2C12 cells, it stabilized and sustained the p-SMAD1/5/9 levels over time. For hPDSCs iHS + aBMP2, it enhanced SMAD phosphorylation as compared to sBMP2 and iBMP2.

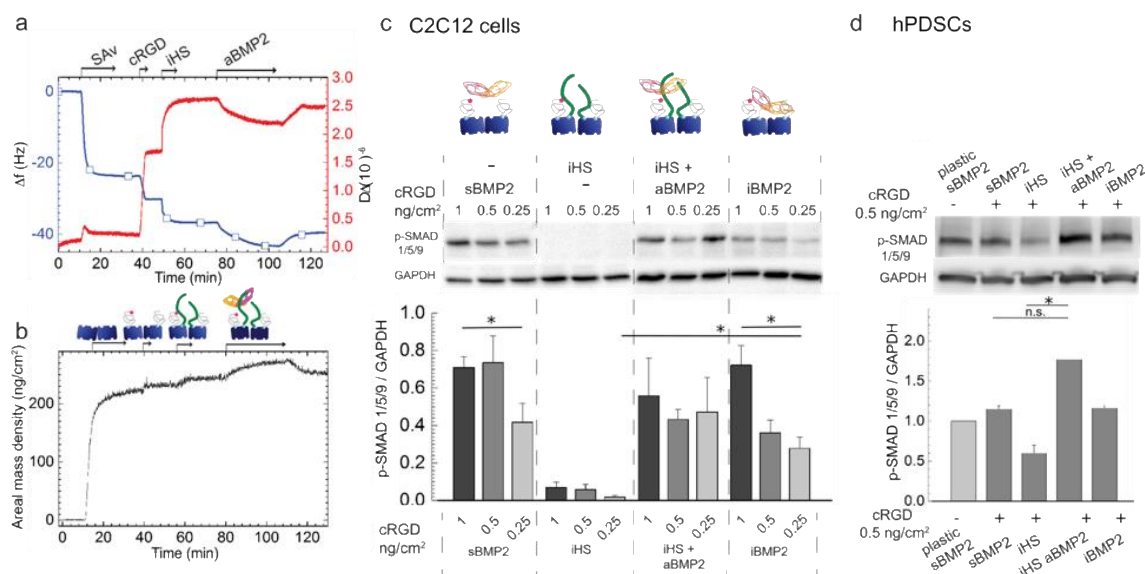


Figure 4: iHS has a positive effect on BMP2-mediated SMAD1/5/9 phosphorylation. a, b) Biomimetic platform characterization using the QCM-D (a) and SE (b) techniques. c) Western blot and quantification of p-SMAD1/5/9 in C2C12 cells plated on platforms functionalized with different cRGD surface concentrations and with sBMP2, iHS, iHS and aBMP2 and iBMP2. Cells were lysed 1 hour after plating and the phosphorylation of SMAD1/5/9 was normalized to GAPDH (n=4). All the Western blots used for quantification are shown in **Ext fig 4 c** and are available online (<http://dx.doi.org/10.17632/y8mscmkcxk.2>) d) Western blot and quantification of p-SMAD1/5/9 after 2h in hPDSCs plated on different platforms presenting sBMP2, iHS, iHS + aBMP2, and iBMP2. Three independent experiments were compared and are shown in **Ext fig 4 d** and are available online (DOI: 10.17632/y8mscmkcxk.2). Bars correspond to the mean \pm SEM. A Mann-Whitney test was used for single comparisons. *p < 0.05, n.s. stands for not statistically significant.

β_3 and β_1 integrins are important for SMAD1/5/9 phosphorylation and ALP expression.

As previous results have shown the cooperation between integrin and BMPRs for driving BMP2 signaling on a BMP2-bound soft matrix [43], we investigated whether integrins play a part in the sustained BMP2 signaling induced by the biomimetic platforms and, if so, which ones. For this purpose, β_1 or β_3 integrins were silenced in the conditions where C2C12 cells were plated on different platforms co-presenting cRGD or cRAD and sBMP2 or iHS or iHS + aBMP2 or iBMP2. BMP2 signaling was analyzed either after 1.5 hours for p-SMAD1/5/9 staining (**Figure 5a**) or after 3 days for ALP staining (**Figure 5c**).

Figure 5b shows quantification of nuclear translocated p-SMAD1/5/9 intensity for each condition and cell type. On cRAD platforms the levels of p-SMAD1/5/9 were significantly lower than on cRGD platforms and not further reduced after silencing either β_3 or β_1 integrins. This result is in agreement with the previous Western blot in **Figures 1g and h** showing that cRGD platforms enhanced the phosphorylation of SMAD compared to cRAD platforms. The phosphorylation of SMAD1/5/9 remained low during the 6 hours after BMP2 stimulation on cRAD platforms (**Figure SI10**).

On cRGD platforms, SMAD1/5/9 phosphorylation was downregulated regardless of whether either β_3 or β_1 integrins were silenced, independently of the type of BMP2 presentation (iHS + aBMP2 *vs* iBMP2), but not down to the levels measured on the cRAD platforms. Both integrins were therefore involved in p-SMAD1/5/9 signaling activation, independently of the presence of iHS.

Silencing β_3 or β_1 integrins also led to downregulated expression of ALP (**Figure 5d**) in particular on cRGD platforms presenting sBMP2 and aBMP2, but this trend was noticeable also on cRAD platforms.

We tested integrin expression 24 h and 3 days after plating, and the levels of silenced integrins remained downregulated (**Figure SI11**), indicating that the silencing was efficient for a long time after transfection.

Surprisingly, after 3 days, C2C12 cells were positive for ALP on both cRGD and cRAD platforms presenting iHS + aBMP2 (**Figures 5c and d**). In particular, iHS + aBMP2 enhanced ALP activity with respect to sBMP2 on cRAD platforms and with respect to iBMP2 on both cRAD and cRGD platforms.

We therefore observed that both integrins, β_3 and β_1 , were important for p-SMAD1/5/9 signaling and, later on, for ALP expression. Moreover, cells were able to differentiate on cRAD platforms presenting iHS + aBMP2, even if p-SMAD1/5/9 levels were low during the first 6 hours after plating, probably due to later cellular expression of matrix proteins [64]. Of note is that the presence of iHS + aBMP2 enhanced ALP staining independently of the adhesion ligands. The downregulation of integrins decreased both p-SMAD and ALP on HS + aBMP2 conditions, revealing that both integrins and iHS were fundamental actors in the promotion of the BMP2-mediated signaling pathway.

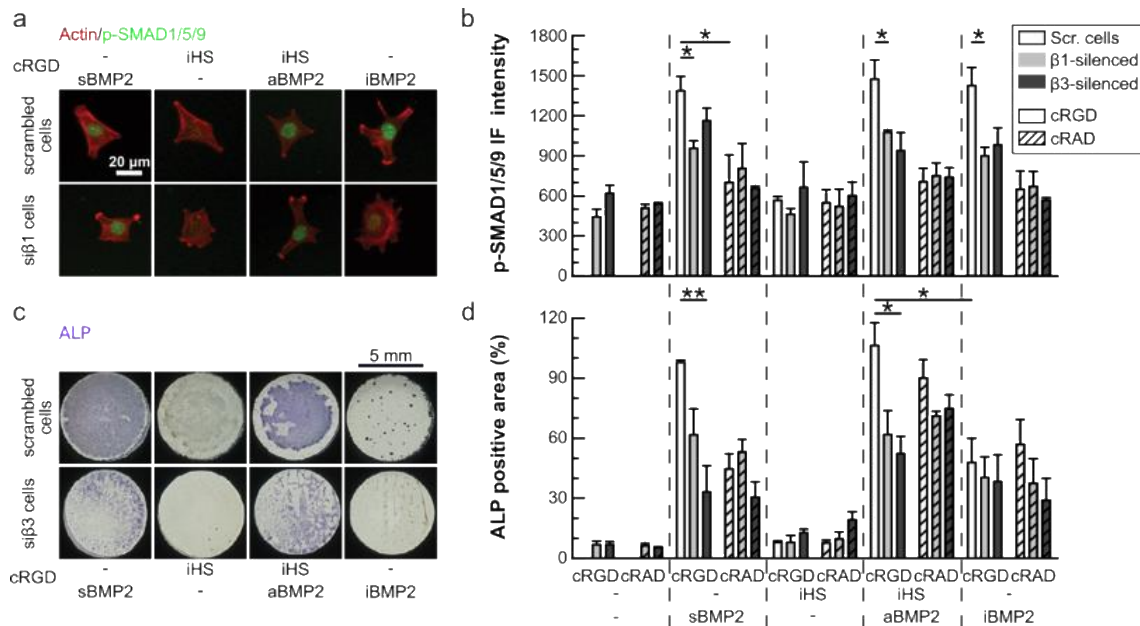


Figure 5: Effect of the ligand (cRAD vs cRGD) and the presence of specific integrins on the regulation of the p-SMAD1/5/9 pathway and ALP expression. Cells were silenced for either β_1 or β_3 integrins and plated on cRGD and cRAD platforms presenting sBMP2, iHS, iHS + aBMP2 and iBMP2, and fixed after 1.5 h for p-SMAD1/5/9 staining (a) or after 3 days for ALP staining (c). a) Representative IF images of scrambled and silenced β_1 (si β_1) cells plated on cRGD platforms and stained for actin (red) and p-SMAD1/5/9 (green). Scale bar = 20 μ m. Representative images of all the conditions are shown in **Ext fig 5 a** and are available online: <http://dx.doi.org/10.17632/ip9m2nmpy.4>. In graphics b and d, scrambled cells are represented with white bars, silenced β_1 cells (si β_1) with grey and silenced β_3 cells (si β_3) with dark grey bars. Cells plated on cRAD platforms are represented with patterned bars. Bars represent the mean of three independent experiments \pm SEM. b) Immunofluorescence intensity of p-SMAD1/5/9 translocated into cell nuclei. Number of quantified cells was >50 for each experiment and condition c) Representative wells after ALP staining for scrambled and silenced β_3 (si β_3) cells plated on cRGD platforms. Representative images of all the conditions are shown in **Ext fig 5 c** and are available online: <http://dx.doi.org/10.17632/ip9m2nmpy.4>. d) ALP positive area normalized by the number of cells in each well (n=3). Scale bar = 5 mm. A Mann-Whitney test was used for single comparisons. *p < 0.05, **p < 0.01.

Immobilized HS enhances BMP2-mediated osteogenic differentiation

To further assess the effect of HS and integrin engagement on BMP2-mediated osteogenic differentiation, expression of osteogenic transcription factors in C2C12 and hPDSCs was analyzed with qPCR. Serum-starved C2C12 cells were plated on biomimetic platforms presenting decreasing cRGD surface concentrations and different types of BMP2 presentations (sBMP2, iHS + aBMP2 and iBMP2). The condition with only iHS was used as the negative control as we had previously proved that iHS alone did not trigger BMP2 activity in either C2C12 or hPDSCs (**Figures 4 c and d** and **Figures 5 b and d**). Expression of the osteogenic markers Osterix and Runx2 was analyzed 24 hours after plating as expression of these markers is detectable after this time period [65]. We observed that neither transcription factor responded to cRGD surface concentrations (**Figures 6a and b**) and they were upregulated on iHS +

aBMP2, in particular with low cRGD surface concentrations (**Figures 6a and b**) with respect to the iBMP2 condition.

Expression of the osteogenic transcription factors Osterix and Dlx5 was upregulated on hPDSCs plated for 3 days on biomimetic platforms presenting iHS + aBMP2, while expression of Runx2 and Sox-9 (a chondrogenic marker) was not influenced by the type of BMP2 presentation (**Figure SI12**). Both results proved that iHS has a positive effect on BMP2-mediated osteogenic differentiation.

We also determined expression of Osterix and Runx2 on cRAD platforms in comparison with cRGD platforms presenting the same peptide surface concentration (**Figure 3a**). On cRAD platforms, expression of Osterix and Runx2 was lower than on cRGD platforms (**Figures 6c and d**) but higher than the negative control. Expression of Runx2 and Osterix was upregulated on cRGD and cRAD platforms presenting HS + aBMP2 with respect to the negative control. However, only on cRGD platforms was the osteogenic differentiation by iHS + aBMP2 significantly higher than on iBMP2 (**Figure 6d**).

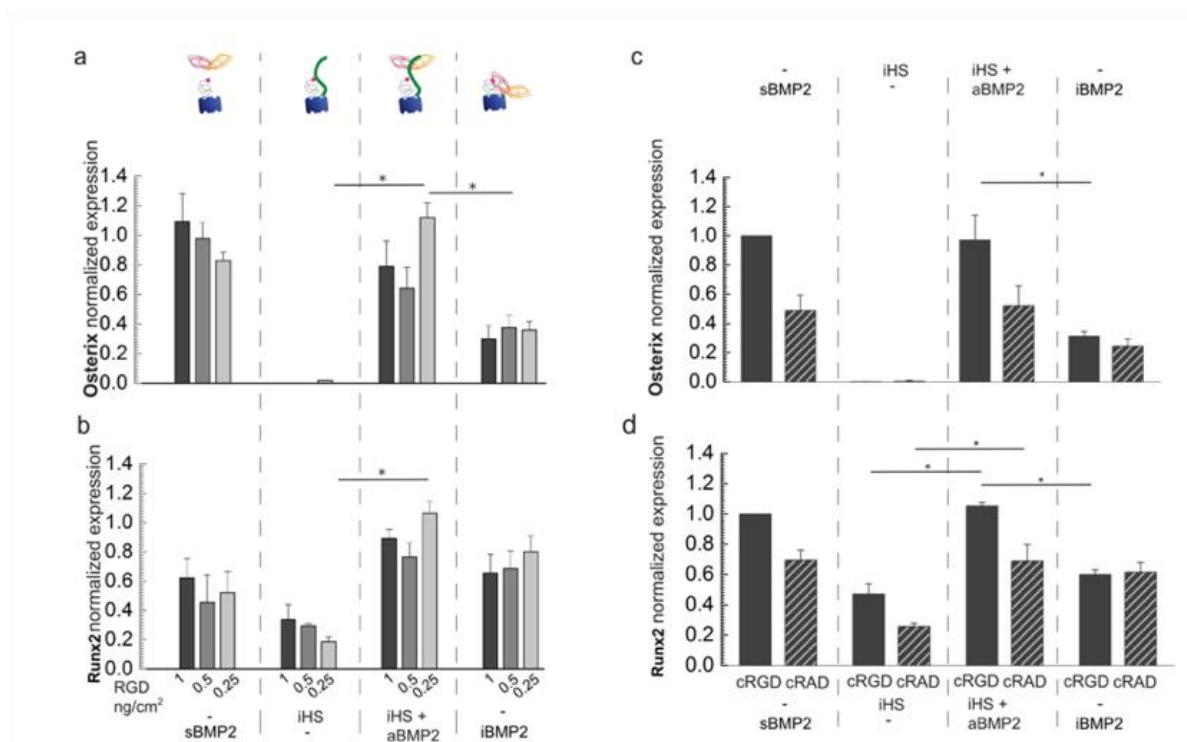


Figure 6: Osteogenic markers are upregulated when aBMP2 is presented by iHS. a) Osterix normalized expression in C2C12 which differentiated 1 day on platforms functionalized with different cRGD surface concentrations, sBMP2, iHS with or without aBMP2 and iBMP2 (n=5). b) Runx2 normalized expression analyzed in parallel to Osterix on the same biomimetic platforms. c) Osterix normalized expression of C2C12 cells plated 1 day on platforms with the same amount of cRGD and cRAD and with BMP2 alone or adsorbed to HS. d) Runx2 normalized expression quantified in parallel on the same conditions as for Osterix. Bars correspond to the average \pm SEM (n=3). A Mann-Whitney test was used for single comparisons. * $p < 0.05$; ** $p < 0.01$.

Discussion

We engineered a multivalent substrate to mimic the extracellular matrix and to control the surface density of the adhesion ligands, iHS and BMP2, to provide previously unknown evidence of the effect of integrin adhesion ligands and HS on BMP2-mediated osteogenic differentiation. We shed light on the role of exogenous, immobilized and oriented HS on BMP2 bioactivity and on its effect on osteogenic differentiation over the course of 72 h.

There are multiple advantages to this biomimetic approach. First, cellular adhesion is specifically controlled by the amount of cRGD peptides immobilized on the platforms. Second, HS and BMP2 are presented homogeneously immobilized and adsorbed on the platforms, resembling their state in the ECM. Finally, each molecule has a controlled and reproducible surface density. This biomimetic approach makes it possible to improve the reproducibility of cellular responses and to diminish the artefacts of *in vitro* cell cultures.

With respect to our previous studies [25, 26, 28], we proposed innovative SAV-based platforms to (i) tune cellular adhesion (ii) better mimic the ECM *via* the co-presentation of multiple ligands at physiological surface concentrations (cRGD, iHS, aBMP2) (iii) couple receptor silencing with specific ligand presentation (iv) answer fundamental biological questions on the role of ECM components on BMP2-mediated cellular adhesion and osteogenic differentiation, and (v) make long-term cellular studies possible.

Regarding the interplay between cellular adhesion and BMP2 signaling, it is now well-accepted that activation of BMPRs can induce integrin-mediated cell adhesion and migration [39, 43]. Other growth factors, such as hepatocyte growth factor, have been shown to modify β_3 integrin conformation to its active form, thus promoting cell migration [66]. Here, we proved and quantified the bidirectionality of this synergistic effect. Increasing integrin recruitment at the cell membrane by a known amount of cRGD peptides enhanced SMAD1/5/9 phosphorylation in response to sBMP2 (**Figures 1c and d**) and iBMP2 (**Figure 4c**). On the other hand, the presence of sBMP2, iBMP2 and aBMP2 enhanced the number of adherent cells after rinsing at a threshold level for cRGD of 0.25 ng/cm^2 where, without BMP2, only 30% of cells adhered (**Figures 2d and SI7a**). Cell area, which is known to regulate BMP2 bioactivity and osteogenesis [67], remained unvaried on platforms presenting different cRGD surface concentrations (**Figures 2d and SI9b**). On cRGD platforms, C2C12 adhered only *via* β_3

integrins (**Figure 3c**), contrary to what has previously been published by blocking β_3 integrins with soluble peptidomimetic ligands [68].

We observed that increased engagement of β_3 integrins by cRGD peptides induced the peak of SMAD1/5/9 phosphorylation, as compared to the low and stable levels of p-SMAD1/5/9 on cRAD platforms (**Figures 1g and SI2b**). On cRAD platforms, the p-SMAD1/5/9 levels remained significantly lower with respect to the cRGD platforms (**Figures 1 cd-gh, and Figure SI2a**).

We observed that BMP2-SMAD signaling and ALP activity were both downregulated on integrin β_1 and in β_3 -silenced cells (**Figure 5b**). Thus, on SA_v platforms, β_1 integrins were not engaged to improve cellular adhesion but had an effect on SMAD1/5/9 phosphorylation and BMP2-mediated osteogenic differentiation. A contradictory *in vitro* study revealed that deleting β_1 integrins did not influence p-SMAD1/5 nuclear translocation in osteoblasts, while *in vivo* p-SMAD1/5 signaling was downregulated in the absence of β_1 integrins [69], proving that this regulation might be cell and context-dependent. Of note is the fact that ALP may be influenced by the total number of cells adherent on the platforms and by cell-cell contact. We took that aspect into consideration by normalizing the ALP positive area to the total number of cells (**Figure 5d**).

On the biomimetic platforms, downstream BMP2-mediated osteogenic differentiation was enhanced by the presentation of BMP2 *via* immobilized HS. Endogenous HS enhanced BMP2-mediated osteogenic differentiation by sustaining and stabilizing BMP2 bioactivity for longer than sBMP2 and iBMP2 (**Figure SI8**). Surprisingly, iHS also enhanced ALP staining even on cRAD platforms, where p-SMAD1/5/9 was otherwise significantly lower. This may be due to activation of the SMAD-independent MAPK pathway [10, 70] or to later secretion of ECM proteins [43, 64] that, after 3 days, may mask the effect of cRAD and cRGD ligands on cell adhesion.

Osteogenic differentiation was lower on immobilized biotinylated BMP2 with respect to aBMP2 (**Figure 5d and Figure 6**). The importance of internalization of the BMP2-BMPRs complex is still under debate and has previously been reviewed [18]. Assuming that iBMP2 is not internalized by the cells, our result is in line with previous observations showing that the inhibition of BMP2 endocytosis attenuates osteogenic differentiation [71]. Furthermore, we have previously shown that Noggin may inhibit iBMP2 but not aBMP2 [28]. The low secretion

of endogenous Noggin by C2C12 cells and hPDSCs [61] might therefore inhibit the bioactivity of iBMP2, but not of aBMP2. The effect of Noggin inhibition may also explain the kinetics of p-SMAD1/5/9 (**Figure SI8**), showing that the levels of p-SMAD1/5/9 decreased after the first hour on iBMP2 but not when aBMP2 was presented *via* iHS (**Figure SI8**).

This positive effect of iHS on BMP2 signaling and osteogenic differentiation seems in contradiction with developmental studies showing that cell-surface HS inhibits BMP2 bioactivity [31, 72]. We hypothesize that extracellular and cell-surface HS play a different role in BMP2 bioactivity. In line with that, a previous study has reported that the type of HS proteoglycan — present on the cell surface or on the ECM — had a different effect on BMP2-mediated chondrogenic differentiation [73]. In particular, it has been shown that exogenous soluble HS improves BMP-2-mediated chondrogenic differentiation as well as heparitinase treatment of cell-surface HS-proteoglycans, while the upregulation of Syndecan-3 (cell-surface HS-proteoglycans) suppresses BMP-2-mediated SMAD phosphorylation [73]. To reinforce this hypothesis, further studies with cells presenting no cell-surface HS will be performed. Another cause of variability in the results may be the source and type of sulfation pattern presented on the HS polysaccharidic chain [29]. It has been shown that removing N-sulfations from heparin oligosaccharides significantly reduced BMP2 binding and bioactivity [74].

An interesting observation was that the positive effect of iHS on BMP2-mediated osteogenic differentiation is cRGD ligand concentration-independent (**Figures 6a and b**). We hypothesize that BMP2 bound to HS chains has a degree of flexibility that makes possible optimal orientation of the GFs to recognize its receptors (unlike in previous computational modelling), in comparison to the biotinylated form and, on the top of that, a lateral freedom of movement that facilitates the proximity between integrins and BMPRs as represented in (**Figure 7**). iHS may therefore facilitate BMPRs-integrin crosstalk by allowing the formation of BMPR-integrin clusters, even on low cRGD surface concentrations. The BMPR-integrins crosstalk may thus be sustained and enhanced by the presence of iHS + aBMP2.

iHS may be able to maintain BMP2 close to the cell surface for longer to enable BMP2-mediated osteogenic differentiation even on cRAD platforms where the BMP2 bioactivity is initially not upregulated (**Figures 1 g and h, Figure SI2 and Figure SI10**). This is confirmed by the upregulation of ALP on iHS + aBMP2 on cRAD platforms (**Figure 5d**).

Regarding the role of iHS alone on integrin-mediated cellular adhesion, we proved that exogenous iHS does not improve cell adhesion even if an interaction between integrins $\alpha_5\beta_1$ and also $\alpha_v\beta_3$ and HS has been previously measured with SPR [75]. The apparent affinity of $2.02 \mu\text{M}$ [75] is probably not enough to induce integrin-mediated cellular adhesion.

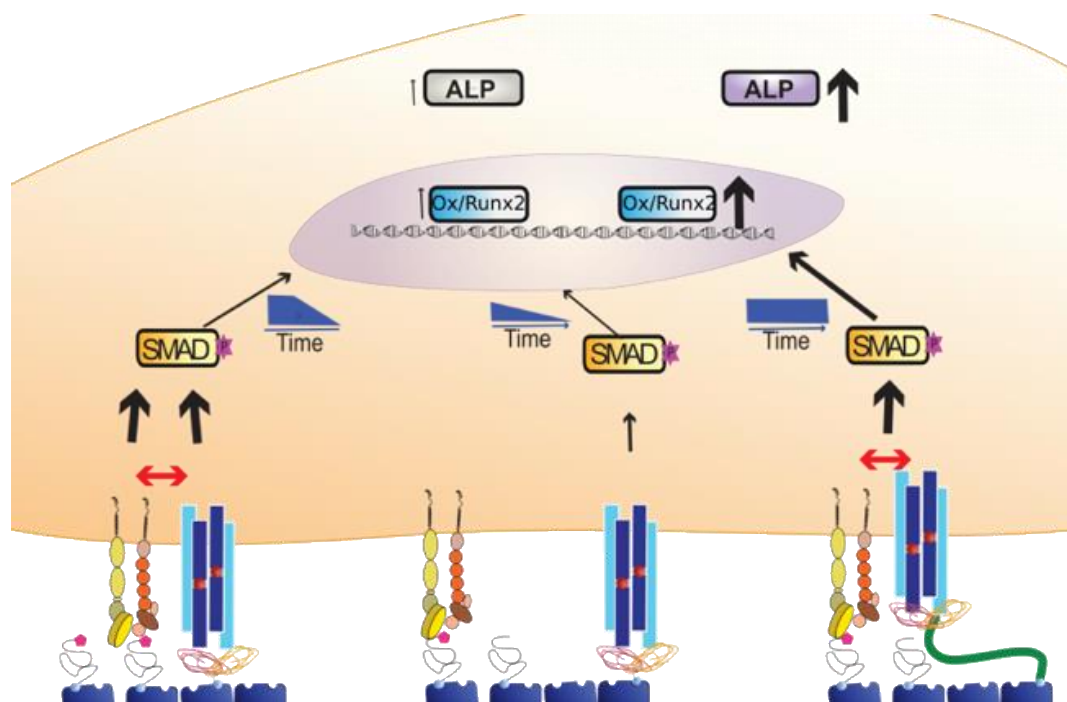


Figure 7: Schematic representation of the effect of integrin-BMPR crosstalk in the presence and absence of HS. The proximity of BMPRs and integrins, promoted by highly concentrated cRGD ligands, enhances SMAD1/5/9 phosphorylation but only in the first few hours after stimulation. This synergistic effect is reduced by decreasing the cRGD surface concentration (central scheme). In the case of iHS + aBMP2 (right side of the image) iHS, being a long molecule, can facilitate the proximity between BMPRs and integrin even in the condition of a low cRGD surface density. Maintaining SMAD phosphorylation for longer, iHS + aBMP2 upregulate the expression of osteogenic markers such as Osterix and Runx2, and promote ALP production.

Conclusion

Thanks to the controlled functionalization of SA_v biomimetic platforms, we revealed the effect of proximity between HS, BMP2 and adhesion ligands on cellular adhesion, BMP2 activity and osteogenic differentiation. While the presentation of exogenous and immobilized HS sustained BMP2-mediated signaling also on platforms which presented low cellular adhesion, its co-immobilization with cRGD peptides optimized BMP2 signaling towards osteogenic differentiation. We also found that both β_1 and β_3 integrins were involved in the upregulation of BMP2-mediated signaling even though cells adhered to the platform only *via* β_3 integrins. The presence of iHS, however, had no effect on cell adhesion. Moreover, the co-

immobilization of cRGD ligands and iHS + aBMP2 upregulated late BMP2-mediated osteogenic differentiation. The adaptable design of the platform makes it a promising candidate for future studies in osteogenic regeneration. Furthermore, positive results on late osteogenic differentiation suggest that biomimetic approaches should be considered for bone repair applications.

Acknowledgments

We would like to acknowledge Prof. Franck Luyten for the donation of hPDSCs, Dr Christian Hiepen, Dr Laure Fourel, Dr Liliane Guerente and Prof. Ralf Richter for the fruitful scientific discussions which inspired some experiments described in this paper. We would like to thank Prof. Joachim Spatz from the Max Planck Institute for Intelligent Systems in Stuttgart (Germany) for his collaboration on the SE measurements. This project received funding from: Fondation Recherche Médicale (No. DEQ20170336746), ANR CODECIDE (No. ANR-17-CE13-022), the European Union's Framework Program for Research and Innovation Horizon 2020 (2014-2020) under the Marie Skłodowska-Curie Grant Agreement No. 658334 and the Initiative de Recherche Stratégique, University Grenoble Alps (IDEX-IRS 2018-2021).

Bibliographic references

- [1] A.J. Engler, S. Sen, H.L. Sweeney, D.E. Discher, Matrix elasticity directs stem cell lineage specification, *Cell* 126(4) (2006) 677-89.
- [2] D.E. Discher, D.J. Mooney, P.W. Zandstra, Growth factors, matrices, and forces combine and control stem cells, *Science (New York, N.Y.)* 324(5935) (2009) 1673-7.
- [3] I. Matsuo, C. Kimura-Yoshida, Extracellular distribution of diffusible growth factors controlled by heparan sulfate proteoglycans during mammalian embryogenesis, *Philosophical transactions of the Royal Society of London. Series B, Biological sciences* 369(1657) (2014).
- [4] R.V. Iozzo, L. Schaefer, Proteoglycan form and function: A comprehensive nomenclature of proteoglycans, *Matrix biology : journal of the International Society for Matrix Biology* 42 (2015) 11-55.
- [5] J.R. Bishop, M. Schuksz, J.D. Esko, Heparan sulphate proteoglycans fine-tune mammalian physiology, *Nature* 446 (2007) 1030.
- [6] K. Jochmann, V. Bachvarova, A. Vortkamp, Reprint of: Heparan sulfate as a regulator of endochondral ossification and osteochondroma development, *Matrix biology : journal of the International Society for Matrix Biology* 35 (2014) 239-47.
- [7] M.R. Urist, B.S. Strates, Bone morphogenetic protein, *Journal of dental research* 50(6) (1971) 1392-406.

- [8] F. Liu, A. Hata, J.C. Baker, J. Doody, J. Carcamo, R.M. Harland, J. Massague, A human Mad protein acting as a BMP-regulated transcriptional activator, *Nature* 381(6583) (1996) 620-3.
- [9] G. Rawadi, B. Vayssiere, F. Dunn, R. Baron, S. Roman-Roman, BMP-2 controls alkaline phosphatase expression and osteoblast mineralization by a Wnt autocrine loop, *Journal of bone and mineral research : the official journal of the American Society for Bone and Mineral Research* 18(10) (2003) 1842-53.
- [10] A. Nohe, S. Hassel, M. Ehrlich, F. Neubauer, W. Sebald, Y.I. Henis, P. Knaus, The mode of bone morphogenetic protein (BMP) receptor oligomerization determines different BMP-2 signaling pathways, *The Journal of biological chemistry* 277(7) (2002) 5330-8.
- [11] R. Ruppert, E. Hoffmann, W. Sebald, Human bone morphogenetic protein 2 contains a heparin-binding site which modifies its biological activity, *European journal of biochemistry / FEBS* 237(1) (1996) 295-302.
- [12] J.T. Gallagher, Heparan sulfate: growth control with a restricted sequence menu, *J Clin Invest* 108(3) (2001) 357-61.
- [13] D.S. Bramono, S. Murali, B. Rai, L. Ling, W.T. Poh, Z.X. Lim, G.S. Stein, V. Nurcombe, A.J. van Wijnen, S.M. Cool, Bone marrow-derived heparan sulfate potentiates the osteogenic activity of bone morphogenetic protein-2 (BMP-2), *Bone* 50(4) (2012) 954-64.
- [14] M.M. Martino, J.A. Hubbell, The 12th-14th type III repeats of fibronectin function as a highly promiscuous growth factor-binding domain, *FASEB journal : official publication of the Federation of American Societies for Experimental Biology* 24(12) (2010) 4711-21.
- [15] S.E. Sakiyama-Elbert, Incorporation of heparin into biomaterials, *Acta biomaterialia* 10(4) (2014) 1581-7.
- [16] M.M. Martino, P.S. Briquez, K. Maruyama, J.A. Hubbell, Extracellular matrix-inspired growth factor delivery systems for bone regeneration, *Advanced drug delivery reviews* 94 (2015) 41-52.
- [17] J. Nickel, P. Ten Dijke, T.D. Mueller, TGF-beta family co-receptor function and signaling, *Acta biochimica et biophysica Sinica* 50(1) (2018) 12-36.
- [18] E. Migliorini, A. Valat, C. Picart, E.A. Cavalcanti-Adam, Tuning cellular responses to BMP-2 with material surfaces, *Cytokine & growth factor reviews* 27 (2016) 43-54.
- [19] A.S. Curry, N.W. Pensa, A.M. Barlow, S.L. Bellis, Taking cues from the extracellular matrix to design bone-mimetic regenerative scaffolds, *Matrix biology : journal of the International Society for Matrix Biology* 52-54 (2016) 397-412.
- [20] T. Crouzier, L. Fourel, T. Boudou, C. Albiges-Rizo, C. Picart, Presentation of BMP-2 from a soft biopolymeric film unveils its activity on cell adhesion and migration, *Advanced materials (Deerfield Beach, Fla.)* 23(12) (2011) H111-8.
- [21] T. Crouzier, K. Ren, C. Nicolas, C. Roy, C. Picart, Layer-by-layer films as a biomimetic reservoir for rhBMP-2 delivery: controlled differentiation of myoblasts to osteoblasts, *Small (Weinheim an der Bergstrasse, Germany)* 5(5) (2009) 598-608.
- [22] R. Anouz, A. Repanas, E. Schwarz, T. Groth, Novel Surface Coatings Using Oxidized Glycosaminoglycans as Delivery Systems of Bone Morphogenetic Protein 2 (BMP-2) for Bone Regeneration, *Macromolecular bioscience* 18(11) (2018) 1800283.
- [23] E. Migliorini, D. Thakar, J. Kuhnle, R. Sadir, D.P. Dyer, Y. Li, C. Sun, B.F. Volkman, T.M. Handel, L. Coche-Guerente, D.G. Fernig, H. Lortat-Jacob, R.P. Richter, Cytokines and growth factors cross-link heparan sulfate, *Open biology* 5(8) (2015).
- [24] D. Thakar, E. Migliorini, L. Coche-Guerente, R. Sadir, H. Lortat-Jacob, D. Boturyn, O. Renaudet, P. Labbe, R.P. Richter, A quartz crystal microbalance method to study the terminal functionalization of glycosaminoglycans, *Chemical communications (Cambridge, England)* 50(96) (2014) 15148-51.

- [25] E. Migliorini, D. Thakar, R. Sadir, T. Pleiner, F. Baleux, H. Lortat-Jacob, L. Coche-Guerente, R.P. Richter, Well-defined biomimetic surfaces to characterize glycosaminoglycan-mediated interactions on the molecular, supramolecular and cellular levels, *Biomaterials* 35(32) (2014) 8903-15.
- [26] D. Thakar, F. Dalonneau, E. Migliorini, H. Lortat-Jacob, D. Boturyn, C. Albiges-Rizo, L. Coche-Guerente, C. Picart, R.P. Richter, Binding of the chemokine CXCL12alpha to its natural extracellular matrix ligand heparan sulfate enables myoblast adhesion and facilitates cell motility, *Biomaterials* 123 (2017) 24-38.
- [27] S. Sarrazin, W.C. Lamanna, J.D. Esko, Heparan Sulfate Proteoglycans, *Cold Spring Harbor Perspectives in Biology* 3(7) (2011).
- [28] E. Migliorini, P. Horn, T. Haraszti, S. Wegner, C. Hiepen, P. Knaus, P. Richter, E. Cavalcanti-Adam, Enhanced biological activity of BMP-2 bound to surface-grafted heparan sulfate, *Advanced Biosystems* 1(4) (2017) 1600041.
- [29] S. Murali, B. Rai, C. Dombrowski, J.L. Lee, Z.X. Lim, D.S. Bramono, L. Ling, T. Bell, S. Hinkley, S.S. Nathan, J.H. Hui, H.K. Wong, V. Nurcombe, S.M. Cool, Affinity-selected heparan sulfate for bone repair, *Biomaterials* 34(22) (2013) 5594-605.
- [30] R.A.A. Smith, R.J.E. Chua, S.M. Carnachan, C.L.L. Tan, I.M. Sims, S.F.R. Hinkley, V. Nurcombe, S.M. Cool, Retention of the structure and function of heparan sulfate biomaterials after gamma irradiation, *Tissue engineering. Part A* (2017).
- [31] J. Huegel, M. Enomoto-Iwamoto, F. Sgariglia, E. Koyama, M. Pacifici, Heparanase stimulates chondrogenesis and is up-regulated in human ectopic cartilage: a mechanism possibly involved in hereditary multiple exostoses, *The American journal of pathology* 185(6) (2015) 1676-85.
- [32] J. Huegel, F. Sgariglia, M. Enomoto-Iwamoto, E. Koyama, J.P. Dormans, M. Pacifici, Heparan sulfate in skeletal development, growth, and pathology: the case of hereditary multiple exostoses, *Developmental dynamics : an official publication of the American Association of Anatomists* 242(9) (2013) 1021-32.
- [33] M. Pacifici, The pathogenic roles of heparan sulfate deficiency in hereditary multiple exostoses, *Matrix biology : journal of the International Society for Matrix Biology* (2017).
- [34] P.C. Billings, M. Pacifici, Interactions of signaling proteins, growth factors and other proteins with heparan sulfate: mechanisms and mysteries, *Connect Tissue Res* 56(4) (2015) 272-80.
- [35] J. Huegel, C. Mundy, F. Sgariglia, P. Nygren, P.C. Billings, Y. Yamaguchi, E. Koyama, M. Pacifici, Perichondrium phenotype and border function are regulated by Ext1 and heparan sulfate in developing long bones: a mechanism likely deranged in Hereditary Multiple Exostoses, *Developmental biology* 377(1) (2013) 100-12.
- [36] L. Koziel, M. Kunath, O.G. Kelly, A. Vortkamp, Ext1-dependent heparan sulfate regulates the range of Ihh signaling during endochondral ossification, *Developmental cell* 6(6) (2004) 801-13.
- [37] E.J. Carragee, E.L. Hurwitz, B.K. Weiner, A critical review of recombinant human bone morphogenetic protein-2 trials in spinal surgery: emerging safety concerns and lessons learned, *The spine journal : official journal of the North American Spine Society* 11(6) (2011) 471-91.
- [38] J. Ivaska, J. Heino, Cooperation between integrins and growth factor receptors in signaling and endocytosis, *Annual review of cell and developmental biology* 27 (2011) 291-320.
- [39] A.I. Monteiro, T. Kollmetz, J. Malmstrom, Engineered systems to study the synergistic signaling between integrin-mediated mechanotransduction and growth factors (Review), *Biointerphases* 13(6) (2018) 06d302.
- [40] A. Sawala, M. Scarcia, C. Sutcliffe, S.G. Wilcockson, H.L. Ashe, Peak BMP responses in

- the drosophila embryo are dependent on the activation of integrin signaling, *Cell reports* 12(10) (2015) 1584-93.
- [41] A. Shekaran, J.R. Garcia, A.Y. Clark, T.E. Kavanaugh, A.S. Lin, R.E. Guldborg, A.J. Garcia, Bone regeneration using an alpha 2 beta 1 integrin-specific hydrogel as a BMP-2 delivery vehicle, *Biomaterials* 35(21) (2014) 5453-61.
- [42] M. Barczyk, S. Carracedo, D. Gullberg, Integrins, *Cell and tissue research* 339(1) (2009) 269-280.
- [43] L. Fourel, A. Valat, E. Faurobert, R. Guillot, I. Bourrin-Reynard, K. Ren, L. Lafanechere, E. Planus, C. Picart, C. Albiges-Rizo, beta3 integrin-mediated spreading induced by matrix-bound BMP-2 controls Smad signaling in a stiffness-independent manner, *The Journal of cell biology* 212(6) (2016) 693-706.
- [44] J.R. Garcia, A.Y. Clark, A.J. Garcia, Integrin-specific hydrogels functionalized with VEGF for vascularization and bone regeneration of critical-size bone defects, *Journal of biomedical materials research. Part A* 104(4) (2016) 889-900.
- [45] J.E. Frith, R.J. Mills, J.J. Cooper-White, Lateral spacing of adhesion peptides influences human mesenchymal stem cell behaviour, *Journal of cell science* 125(Pt 2) (2012) 317-27.
- [46] M. Pfaff, K. Tangemann, B. Muller, M. Gurrath, G. Muller, H. Kessler, R. Timpl, J. Engel, Selective recognition of cyclic RGD peptides of NMR defined conformation by alpha IIb beta 3, alpha V beta 3, and alpha 5 beta 1 integrins, *The Journal of biological chemistry* 269(32) (1994) 20233-8.
- [47] T. Katagiri, A. Yamaguchi, M. Komaki, E. Abe, N. Takahashi, T. Ikeda, V. Rosen, J.M. Wozney, A. Fujisawa-Sehara, T. Suda, Bone morphogenetic protein-2 converts the differentiation pathway of C2C12 myoblasts into the osteoblast lineage, *The Journal of cell biology* 127(6 Pt 1) (1994) 1755-66.
- [48] J. Bolander, W. Ji, J. Leijten, L.M. Teixeira, V. Bloemen, D. Lambrechts, M. Chaklader, F.P. Luyten, Healing of a large long-bone defect through serum-free In vitro priming of human periosteum-derived cells, *Stem cell reports* 8(3) (2017) 758-772.
- [49] B. Mulloy, C. Gee, S.F. Wheeler, R. Wait, E. Gray, T.W. Barrowcliffe, Molecular weight measurements of low molecular weight heparins by gel permeation chromatography, *Thrombosis and haemostasis* 77(4) (1997) 668-74.
- [50] G.V. Dubacheva, T. Curk, B.M. Moggetti, R. Auzely-Velty, D. Frenkel, R.P. Richter, Superselective targeting using multivalent polymers, *J Am Chem Soc* 136(5) (2014) 1722-5.
- [51] R.P. Richter, K.B. Rodenhausen, E.N. B.;, M. Schubert, Coupling spectroscopic ellipsometry and quartz crystal microbalance to study organic films at the solid-liquid interface, Springer, Heidelberg, 2014.
- [52] J. Bolander, W. Ji, L. Geris, V. Bloemen, Y.C. Chai, J. Schrooten, F.P. Luyten, The combined mechanism of bone morphogenetic protein- and calcium phosphate-induced skeletal tissue formation by human periosteum derived cells, *European cells & materials* 31 (2016) 11-25.
- [53] W. Ji, G. Kerckhofs, C. Geeroms, M. Marechal, L. Geris, F.P. Luyten, Deciphering the combined effect of bone morphogenetic protein 6 and calcium phosphate on bone formation capacity of periosteum derived cells-based tissue engineering constructs, *Acta biomaterialia* 80 (2018) 97-107.
- [54] V. Fitzpatrick, L. Fourel, O. Destaing, F. Gilde, C. Albiges-Rizo, C. Picart, T. Boudou, Signal mingle: Micropatterns of BMP-2 and fibronectin on soft biopolymeric films regulate myoblast shape and SMAD signaling, *Scientific reports* 7 (2017) 41479.
- [55] F. Gilde, L. Fourel, R. Guillot, I. Pignot-Paintrand, T. Okada, V. Fitzpatrick, T. Boudou, C. Albiges-Rizo, C. Picart, Stiffness-dependent cellular internalization of matrix-bound

- BMP-2 and its relation to Smad and non-Smad signaling, *Acta biomaterialia* 46 (2016) 55-67.
- [56] J. Schindelin, I. Arganda-Carreras, E. Frise, V. Kaynig, M. Longair, T. Pietzsch, S. Preibisch, C. Rueden, S. Saalfeld, B. Schmid, J.Y. Tinevez, D.J. White, V. Hartenstein, K. Eliceiri, P. Tomancak, A. Cardona, Fiji: an open-source platform for biological-image analysis, *Nature methods* 9(7) (2012) 676-82.
- [57] P. Machillot, C. Quintal, F. Dalonneau, L. Hermant, P. Monnot, K. Matthews, V. Fitzpatrick, J. Liu, I. Pignot-Paintrand, C. Picart, Automated buildup of biomimetic films in cell culture microplates for high-throughput screening of cellular behaviors, *Advanced materials (Deerfield Beach, Fla.)* 30(27) (2018) e1801097.
- [58] J. Hellems, G. Mortier, A. De Paepe, F. Speleman, J. Vandessompele, qBase relative quantification framework and software for management and automated analysis of real-time quantitative PCR data, *Genome biology* 8(2) (2007) R19.
- [59] M. Arnold, E.A. Cavalcanti-Adam, R. Glass, J. Blummel, W. Eck, M. Kantelehner, H. Kessler, J.P. Spatz, Activation of integrin function by nanopatterned adhesive interfaces, *Chemphyschem : a European journal of chemical physics and physical chemistry* 5(3) (2004) 383-8.
- [60] E.A. Cavalcanti-Adam, D. Aydin, V.C. Hirschfeld-Warneken, J.P. Spatz, Cell adhesion and response to synthetic nanopatterned environments by steering receptor clustering and spatial location, *HFSP journal* 2(5) (2008) 276-85.
- [61] E.P. Consortium, An integrated encyclopedia of DNA elements in the human genome, *Nature* 489(7414) (2012) 57-74.
- [62] Q. Wang, C. Huang, M. Xue, X. Zhang, Expression of endogenous BMP-2 in periosteal progenitor cells is essential for bone healing, *Bone* 48(3) (2011) 524-32.
- [63] A. van der Flier, K. Badu-Nkansah, C.A. Whittaker, D. Crowley, R.T. Bronson, A. Lacy-Hulbert, R.O. Hynes, Endothelial alpha5 and alphav integrins cooperate in remodeling of the vasculature during development, *Development (Cambridge, England)* 137(14) (2010) 2439-49.
- [64] V.A. Perez, Z. Ali, T.P. Alastalo, F. Ikeno, H. Sawada, Y.J. Lai, T. Kleisli, E. Spiekerkoetter, X. Qu, L.H. Rubinos, E. Ashley, M. Amieva, S. Dedhar, M. Rabinovitch, BMP promotes motility and represses growth of smooth muscle cells by activation of tandem Wnt pathways, *The Journal of cell biology* 192(1) (2011) 171-88.
- [65] M.H. Lee, T.G. Kwon, H.S. Park, J.M. Wozney, H.M. Ryoo, BMP-2-induced Osterix expression is mediated by *Dlx5* but is independent of *Runx2*, *Biochemical and biophysical research communications* 309(3) (2003) 689 - 694.
- [66] R. Faccio, M. Grano, S. Colucci, A. Villa, G. Giannelli, V. Quaranta, A. Zallone, Localization and possible role of two different alpha v beta 3 integrin conformations in resting and resorbing osteoclasts, *Journal of cell science* 115(Pt 14) (2002) 2919-29.
- [67] Y.K. Wang, X. Yu, D.M. Cohen, M.A. Wozniak, M.T. Yang, L. Gao, J. Eyckmans, C.S. Chen, Bone morphogenetic protein-2-induced signaling and osteogenesis is regulated by cell shape, RhoA/ROCK, and cytoskeletal tension, *Stem cells and development* 21(7) (2012) 1176-86.
- [68] V. Schaufler, H. Czichos-Medda, V. Hirschfeld-Warnecken, S. Neubauer, F. Rechenmacher, R. Medda, H. Kessler, B. Geiger, J.P. Spatz, E.A. Cavalcanti-Adam, Selective binding and lateral clustering of alpha5beta1 and alphavbeta3 integrins: Unraveling the spatial requirements for cell spreading and focal adhesion assembly, *Cell adhesion & migration* 10(5) (2016) 505-515.
- [69] M. Brunner, N. Mandier, T. Gautier, G. Chevalier, A.S. Ribba, P. Guardiola, M.R. Block, D. Bouvard, beta1 integrins mediate the BMP2 dependent transcriptional control of

- osteoblast differentiation and osteogenesis, *PloS one* 13(4) (2018) e0196021.
- [70] A. Ulsamer, M.J. Ortuno, S. Ruiz, A.R. Susperregui, N. Osses, J.L. Rosa, F. Ventura, BMP-2 induces Osterix expression through up-regulation of Dlx5 and its phosphorylation by p38, *The Journal of biological chemistry* 283(7) (2008) 3816-26.
- [71] E. Heining, R. Bhushan, P. Paarmann, Y.I. Henis, P. Knaus, Spatial segregation of BMP/Smad signaling affects osteoblast differentiation in C2C12 cells, *PloS one* 6(10) (2011) e25163.
- [72] C. Mundy, E. Yang, H. Takano, P.C. Billings, M. Pacifici, Heparan sulfate antagonism alters bone morphogenetic protein signaling and receptor dynamics, suggesting a mechanism in hereditary multiple exostoses, *The Journal of biological chemistry* 293(20) (2018) 7703-7716.
- [73] M.C. Fisher, Y. Li, M.R. Seghatoleslami, C.N. Dealy, R.A. Kosher, Heparan sulfate proteoglycans including syndecan-3 modulate BMP activity during limb cartilage differentiation, *Matrix biology : journal of the International Society for Matrix Biology* 25(1) (2006) 27-39.
- [74] R.A.A. Smith, S. Murali, B. Rai, X. Lu, Z.X.H. Lim, J.J.L. Lee, V. Nurcombe, S.M. Cool, Minimum structural requirements for BMP-2-binding of heparin oligosaccharides, *Biomaterials* 184 (2018) 41-55.
- [75] C. Faye, C. Moreau, E. Chautard, R. Jetne, N. Fukai, F. Ruggiero, M.J. Humphries, B.R. Olsen, S. Ricard-Blum, Molecular interplay between endostatin, integrins, and heparan sulfate, *The Journal of biological chemistry* 284(33) (2009) 22029-40.

IV.D Supplementary information

Supplementary figure 1:

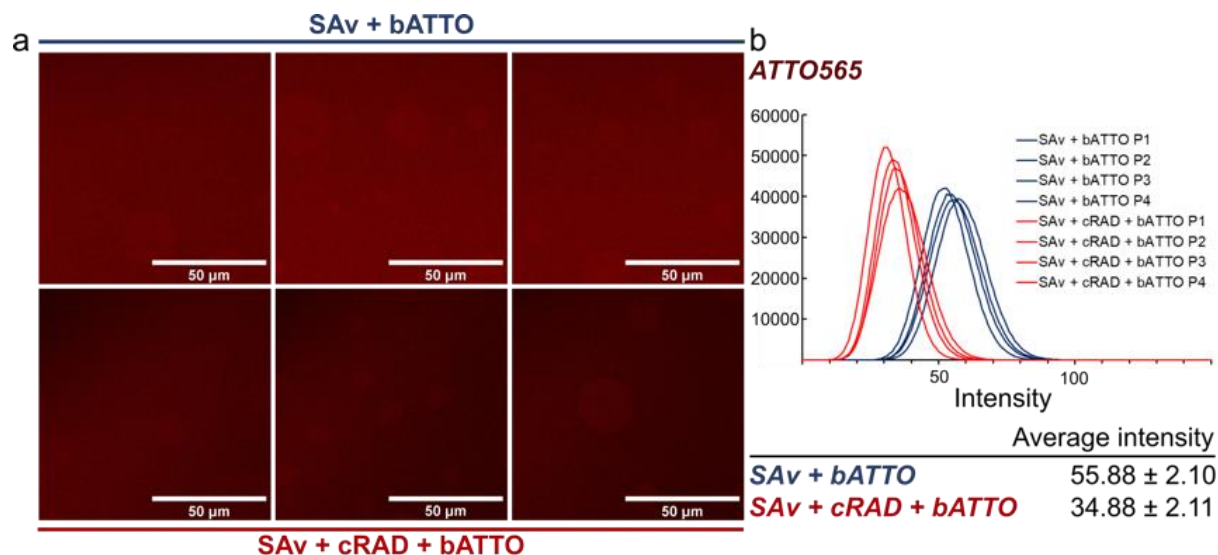


Fig SI1: Homogeneity analysis of SAv monolayer and of biotinylated molecules on SAv (biotinylated cRAD peptide) a) Representative confocal images (63x, 8 bit) of SAv saturated with bATTO (top) and SAv functionalized with cRAD and then bATTO (bottom) on different positions (P1-P4). Images appear to be homogeneous and comparable to each other for both conditions. Intensity of cRAD platforms is lower because less biotin sites are available for bATTO after cRAD was incubated for 4 min to achieve a sub-monolayer. All images were post-treated by adjusting the contrast in an equal manner. b) Histogram of the 8 confocal images and average intensity values with standard deviation of the 4 curves. The curves in between one condition are comparable and the average intensity values only scatter slightly.

Supplementary figure 2:

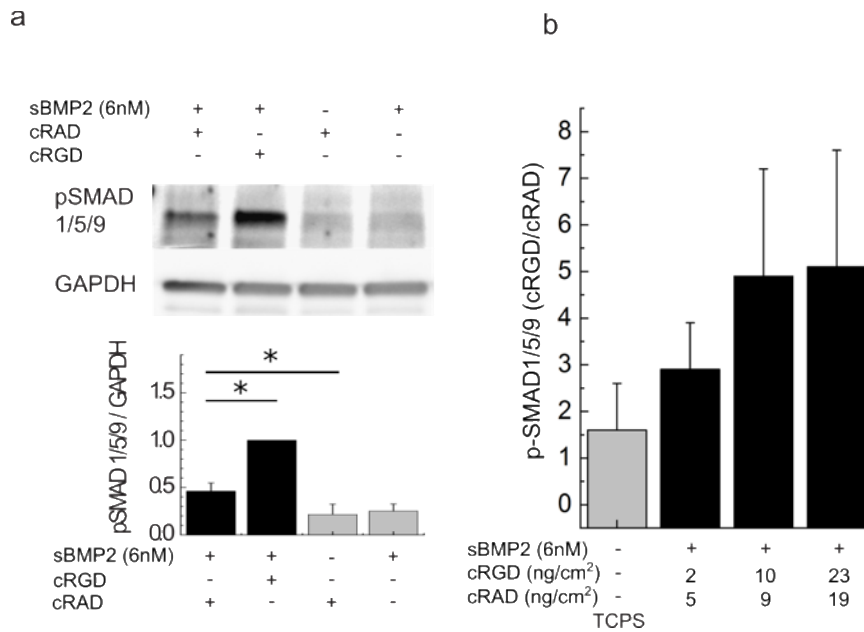


Fig SI2: BMP-SMAD signalling is enhanced on cRGD platforms in comparison to cRAD platforms. a) Western blot of p-SMAD1/5/9 levels in C2C12 cells plated on surfaces presenting cRAD and cRGD peptides, stimulated (or not) with sBMP2 (6 nM). 1 hour after plating cells were lysed and the level of p-SMAD1/5/9 plotted and normalized to the housekeeping gene GAPDH. The differences in SMAD1/5/9 phosphorylation are significant between cRGD and cRAD platforms. b) the ratio of p-SMAD1/5/9/GAPDH of cRGD/cRAD at different and comparable peptide concentrations (from Figure 1d and 1h, respectively). Non-parametric Mann-Whitney test has been used for single comparisons. $*p < 0.05$.

Supplementary figure 3:

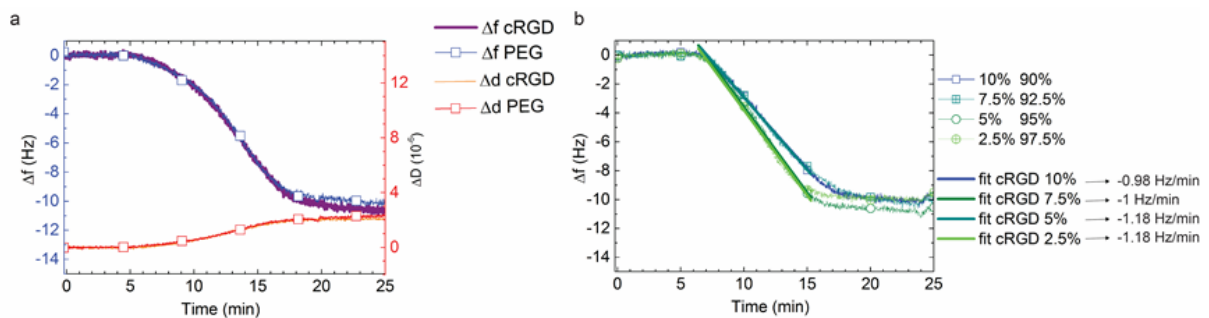


Fig SI3: cRGD surface concentration is diluted with biotinylated PEG (here called PEG) to increase the average inter-molecular distance. a) QCM-D characterization of cRGD and PEG binding to SAV. Their concentrations have been adjusted to obtain the same binding kinetics (see violet and blue line) b) QCM-D study to compare different cRGD and PEG mixtures of different ratios. Here we obtained comparable binding kinetics on all the four different ratios of cRGD and PEG.

Supplementary figure 4:

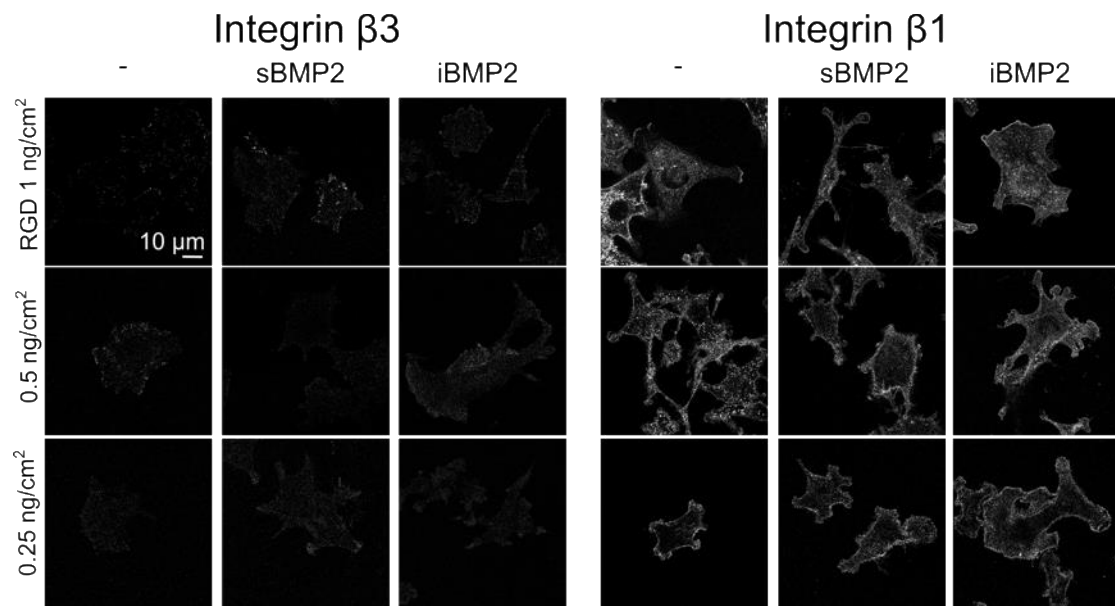


Fig SI4: β_3 integrins are mainly localized at the focal adhesions but they are less visible on lower cRGD surface concentration while β_1 integrins are mainly expressed at the cell membrane for all the cRGD surface concentrations. Immunofluorescent staining of β_3 and β_1 integrins on C2C12 cells plated on biomimetic platforms, presenting different cRGD surface concentrations (from 1 to 0.25 ng/cm²), were fixed 1.5 hour after seeding. Non-adherent cells have been washed away by gently pipetting (see methods) and fixed with 4% paraformaldehyde. Scale bar = 10 μm .

Supplementary figure 5:

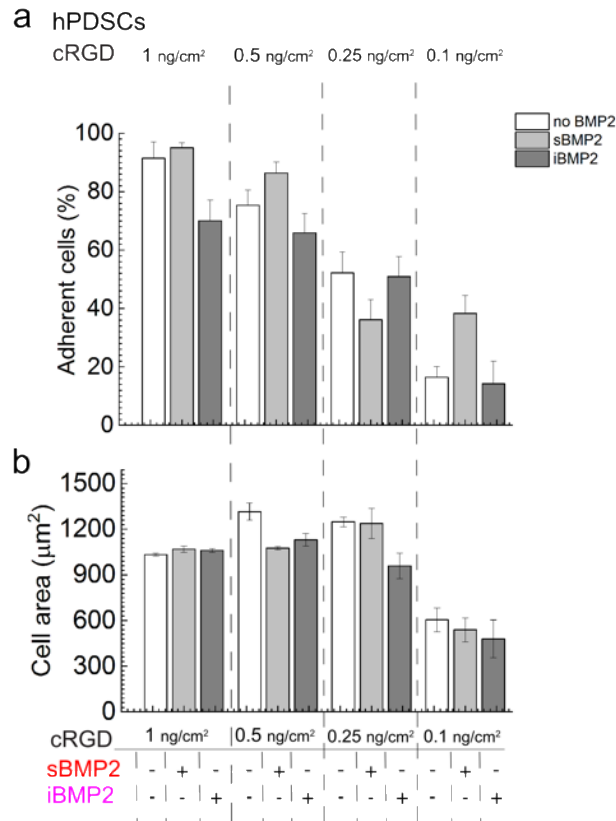


Fig SI5: the adhesion of hPDSCs to biomimetic platforms is not enhanced by the presence of sBMP2 or iBMP2. Cell area is drastically decreased at 0.1 ng/cm². a) hPDSCs adhesion quantification on decreasing cRGD surface concentration and in presence of sBMP2 or iBMP2. b) cell area quantification after fixation on the same platforms. Cell area is comparable for all the surface functionalization, except cRGD 0.1 ng/cm², where it strongly decreases.

Supplementary figure 6

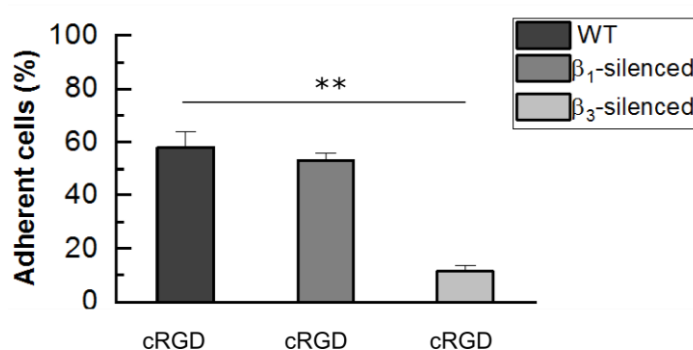


Fig SI6: Knocked-down cells for β₃ integrin do not adhere to cRGD platforms. Adherent wild type and β₁ and β₃ silenced cells on cRGD platforms one hour after plating. Student's *t*-test has been used for single comparisons. ***p* < 0.01

Supplementary figure 7

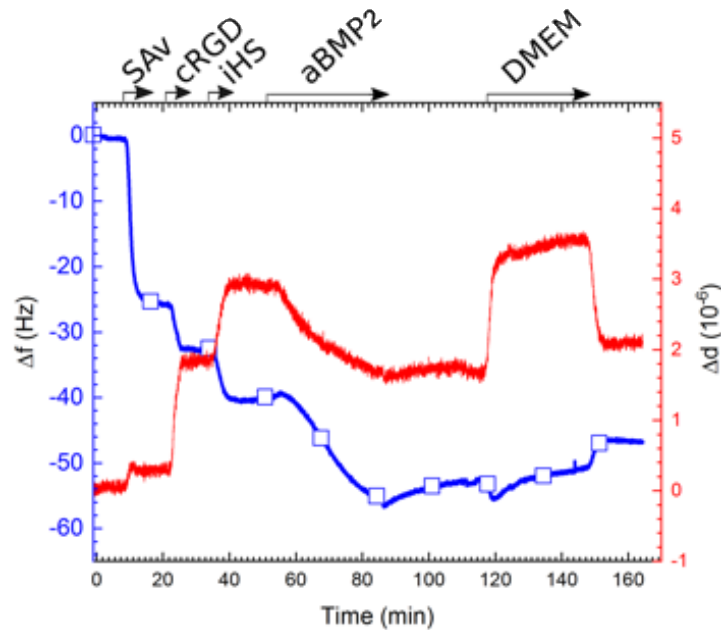


Fig SI7: DMEM media increases the release of BMP2 but it rapidly stabilizes it to 50% of the initial amount. QCM-D characterization of the co-functionalized platform presenting cRGD, iHS and aBMP2. DMEM is added at 116 min to verify the stability of BMP2 binding to HS. The blue line shows frequency shifts and the red line represents dissipation shifts. Arrows indicate the start and the duration of the injections. In the remaining time the surfaces were exposed to running buffer

Supplementary figure 8

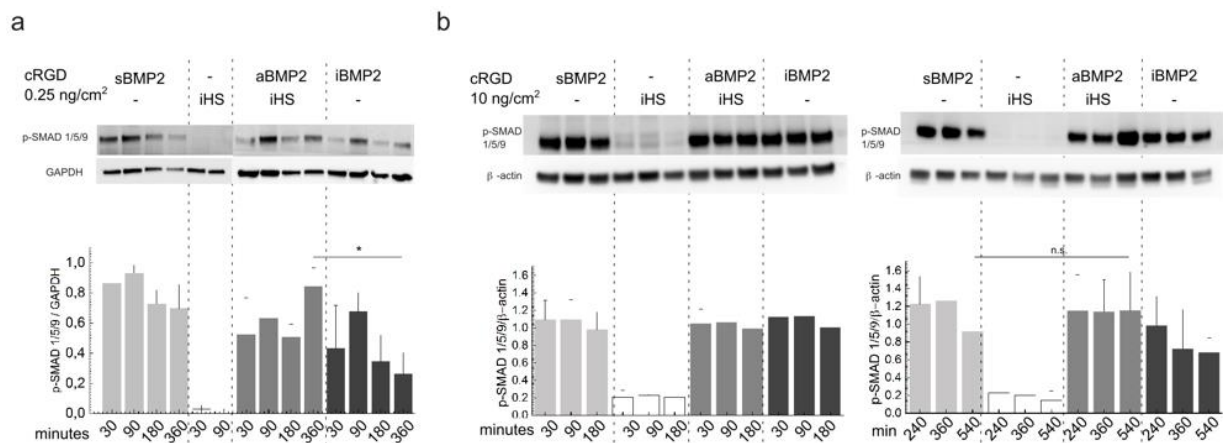


Fig SI8: kinetics of p-SMAD 1/5/9 on biomimetic platforms: the signal is sustained on iHS + aBMP2. **a)** Western blot to quantify the levels of SMAD 1/5/9 phosphorylation over the first six hours after serum-starved C2C12 cells plating on biomimetic platforms presenting a surface concentration of cRGD of 0.25 ng/cm². The presence of HS sustains SMAD 1/5/9 phosphorylation while on sBMP2 and iBMP2 the p-SMAD 1/5/9 levels decrease during this time period. **b)** Western blot quantification of p-SMAD 1/5/9 over longer time points, on high cRGD surface concentration (10 ng/cm²). On these platforms the p-SMAD signalling is sustained on all conditions and only after nine hours it decreases on iBMP2 and sBMP2 but not on iHS + aBMP2 (right graph). Bar plots correspond to the average of three independent experiments \pm SEM. Non-parametric Mann-Whitney test has been used for single comparisons. * $p < 0.05$, n.s. stands for non-significant.

Supplementary figure 9:

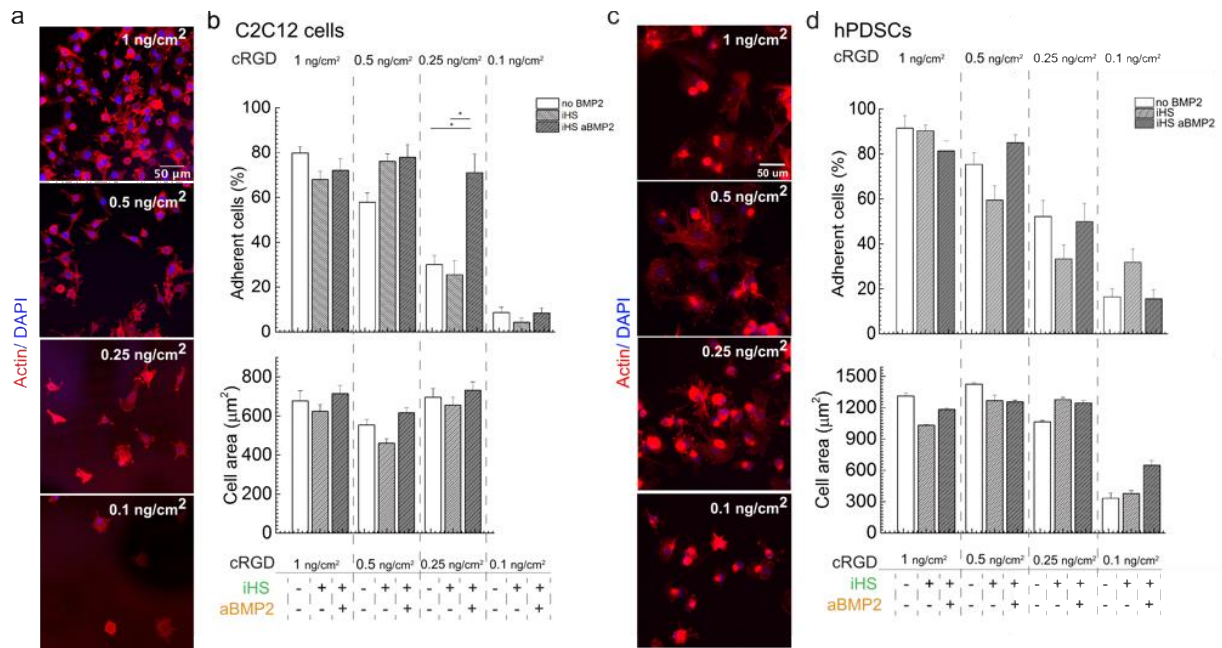


Fig SI9: HS alone, without BMP2, does not promote C2C12 cells and hPDSCs adhesion. a) Representative immunofluorescence images of C2C12 cells plated for one hour on biomimetic platforms presenting decreasing cRGD surface concentration. Actin is stained in red and nuclei in blue. Scale bar = 50 μm . b) Number of adherent C2C12 cells that remain on platforms functionalized with different amount of cRGD and washed with a gentle rinsing. We observed that at 0.25 ng/cm² of cRGD surface concentration, the presentation of aBMP2 by iHS enhanced cellular adhesion in comparison to iHS alone. C2C12 cell area on 1, 0.5 and 0.25 ng/cm² cRGD surface concentrations. The cell area remained constant on the different platforms. c) Immunofluorescence staining of hPDSCs fixed two hours after plating on biomimetic platforms, presenting decreasing concentrations of cRGD. Actin (red) and nuclei (blue) were stained to quantify cell number and cell area. d) Quantification of the number of adherent hPDSCs that have been plated on the same biomimetic platforms as C2C12 cells and left two hours before adhesion experiment. Quantification of hPDSCs area on different cRGD surface concentration, hPDSCs adhesion decreased with the cRGD surface concentration reaching the ~20% of adherent cells on 0.1 ng/cm². Bar plots correspond to the mean \pm SEM of three independent experiments. Non-parametric Mann Withney test has been used for single comparisons. * $p < 0.05$

Supplementary figure 10:

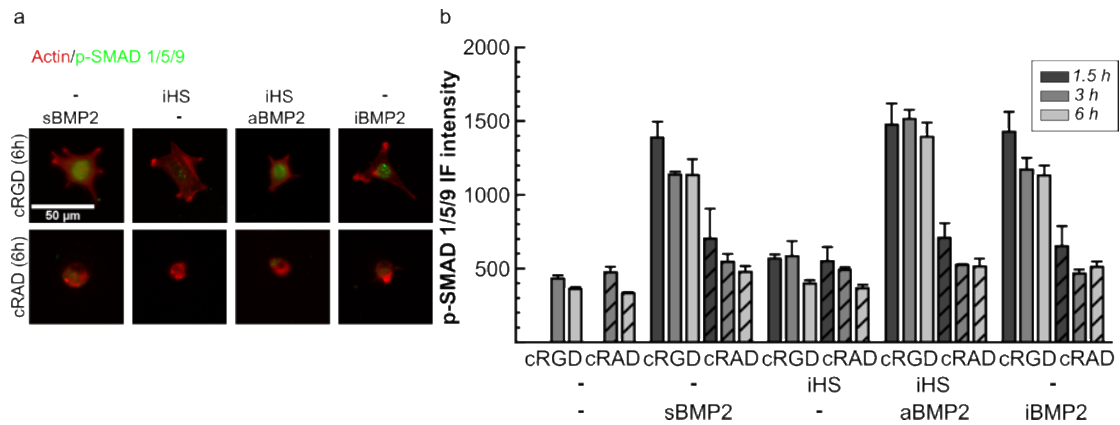


Fig SI10: On cRAD platforms, SMAD 1/5/9 phosphorylation is significantly lower than on cRGD platforms during the first six hours after plating. C2C12 have been plated on cRAD and cRAD platforms presenting sBMP2, iHS, iHS + aBMP2 and iBMP. a) Representative images of cells fixed after six hours on cRGD and cRAD platforms. p-SMAD 1/5/9 is labelled in green and actin in red. b) Average SMAD 1/5/9 nuclear intensity \pm SEM measured at different time points 1.5, three and six hours. n=4. Scale bar = 50 μ m

Supplementary figure 11:

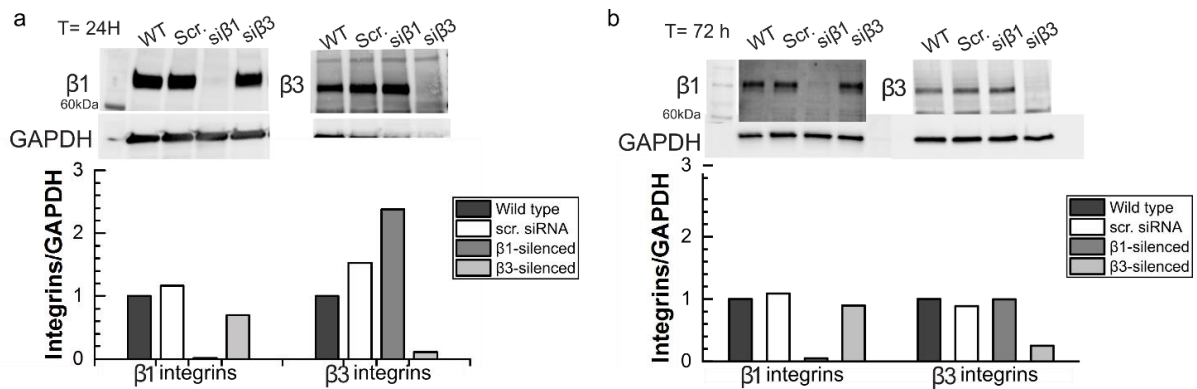


Fig SI11: The silencing of integrins is effective 24 h and three days after cell plating. a) WB to measure β 1 and β 3 integrin expression 24 h after cell plating. b) WB to measure β 1 and β 3 integrin expression 3 days after cell plating. While the effect of integrin compensation is maintained for 24 h it is less evident after 72 hours compared to expression at 1 h (Figure 3). But silenced integrins remain down-regulated.

Supplementary figure 12

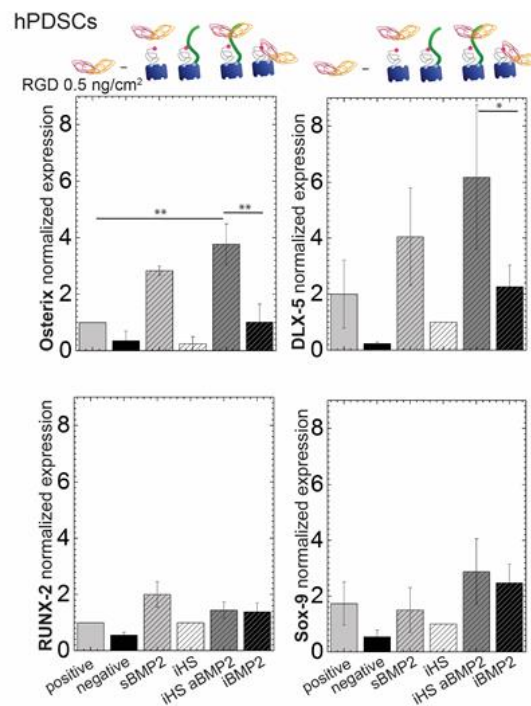
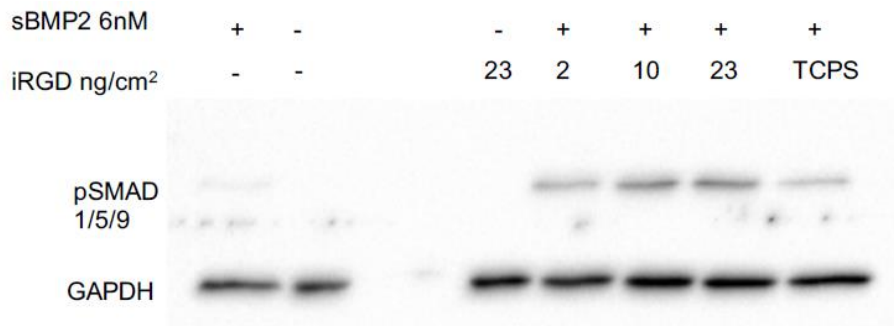


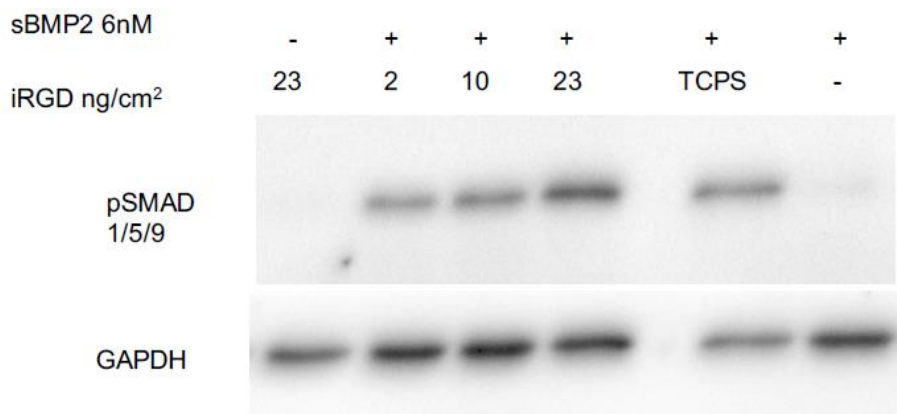
Fig SI12: Osteogenic transcription factors of hPDSCs are up-regulated on HS + aBMP2 platforms. Gene expression quantification of hPDSCs plated 3 days on biomimetic platforms. Osteogenic transcription factors as Osterix and DLX-5 are significantly up-regulated when BMP2 is presented with iHS. The osteogenic transcription factor Runx2 and the chondrogenic transcription factor Sox-9 are stably expressed on all the conditions. Bars correspond to three independent experiments \pm SEM. Mann-Whitney test has been used for single comparisons. * $p < 0.05$, ** $p < 0.01$

IV.E Additional online resources

Extended figure 1 c

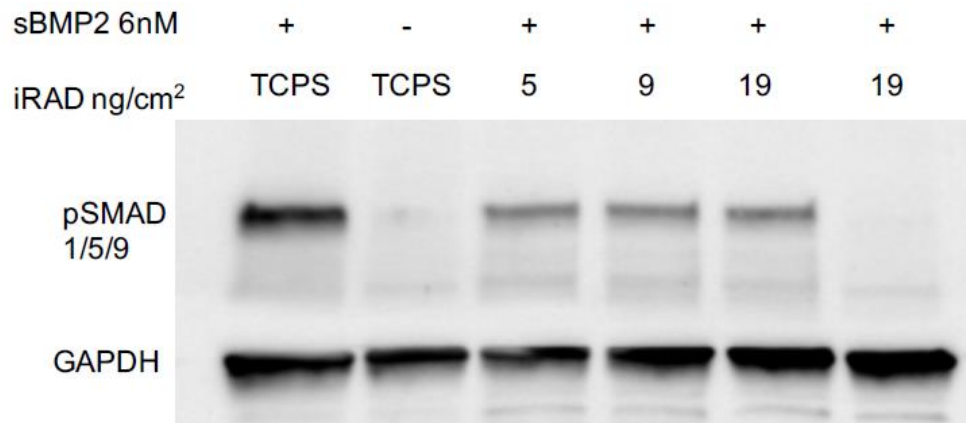


Ext fig 1 c 1: 2nd replicate. Western blot of p-SMAD1/5/9 levels in C2C12 cells plated on surfaces presenting three different cRGD surface concentrations and stimulated with sBMP2 (6 nM). As the internal control, C2C12 cells were plated on TCPS with sBMP2. One hour after plating, the cells were lysed and the level of p-SMAD1/5/9 plotted and normalized to the housekeeping gene GAPDH.

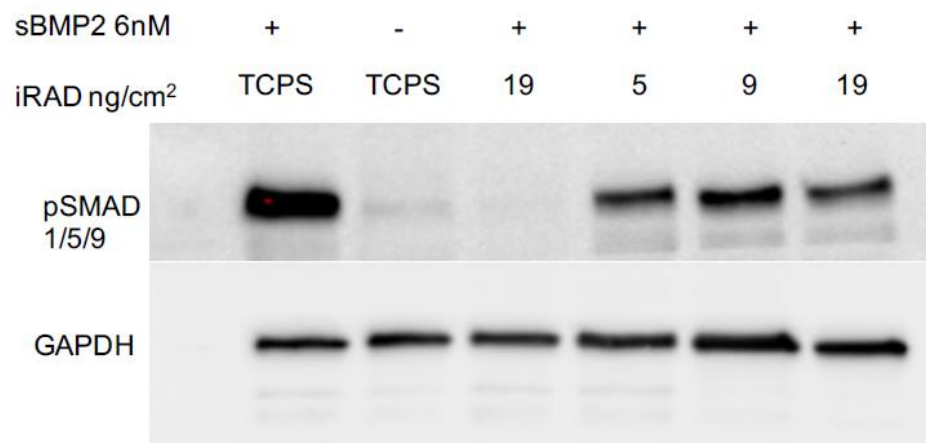


Ext fig 1 c 2: 3rd replicate. Western blot of p-SMAD1/5/9 levels in C2C12 cells plated on surfaces presenting three different cRGD surface concentrations and stimulated with sBMP2 (6 nM). As the internal control, C2C12 cells were plated on TCPS with sBMP2. One hour after plating, the cells were lysed and the level of p-SMAD1/5/9 plotted and normalized to the housekeeping gene GAPDH.

Extended figure 1 g

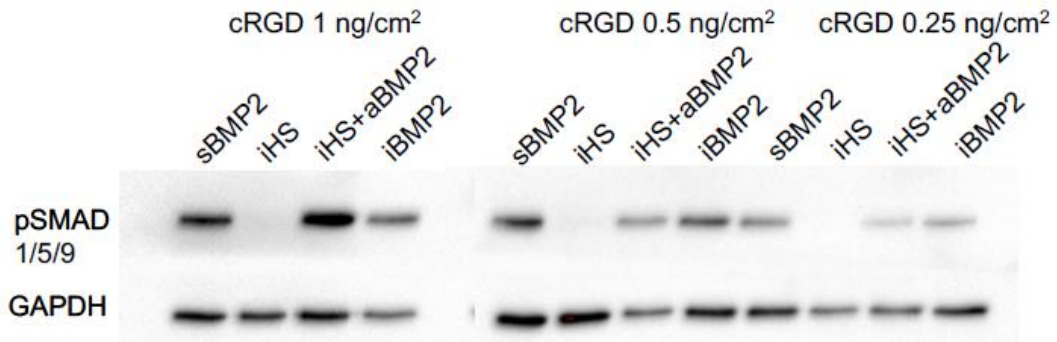


Ext fig 1 g 1: 2nd replicate. Western blot of p-SMAD1/5/9 levels in C2C12 cells plated on surfaces presenting three different cRAD surface concentrations and stimulated with sBMP2 (6 nM). As the internal control, C2C12 cells were plated on TCPS with sBMP2. One hour after plating, the cells were lysed and the level of p-SMAD1/5/9 plotted and normalized to the housekeeping gene GAPDH.

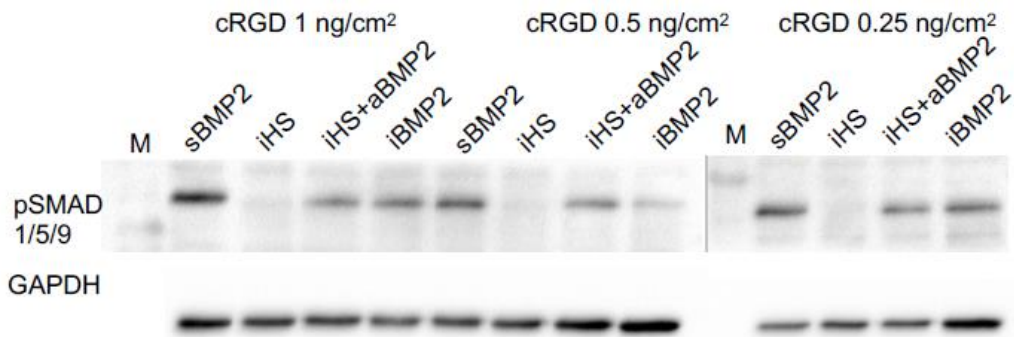


Ext fig 1 g 2: 3rd replicate. Western blot of p-SMAD1/5/9 levels in C2C12 cells plated on surfaces presenting three different cRAD surface concentrations and stimulated with sBMP2 (6 nM). As the internal control, C2C12 cells were plated on TCPS with sBMP2. One hour after plating, the cells were lysed and the level of p-SMAD1/5/9 plotted and normalized to the housekeeping gene GAPDH.

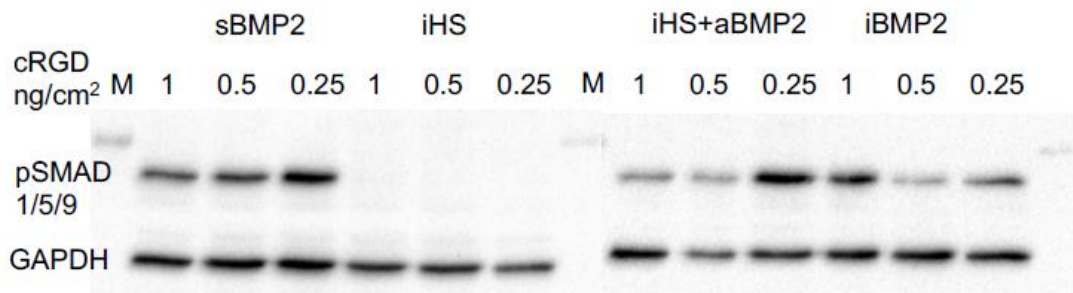
Extended figure 4 c



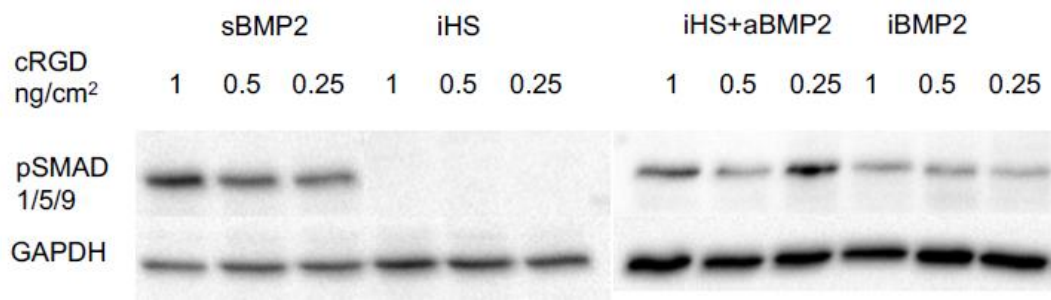
Ext fig 4 c 1: 1st replicate. Western blot of p-SMAD1/5/9 in C2C12 cells plated on platforms functionalized with different cRGD surface concentrations and with sBMP2, iHS, iHS and aBMP2 and iBMP2. Cells were lysed 1 hour after plating.



Ext fig 4 c 2: 2nd replicate. Western blot of p-SMAD1/5/9 in C2C12 cells plated on platforms functionalized with different cRGD surface concentrations and with sBMP2, iHS, iHS and aBMP2 and iBMP2. Cells were lysed 1 hour after plating.

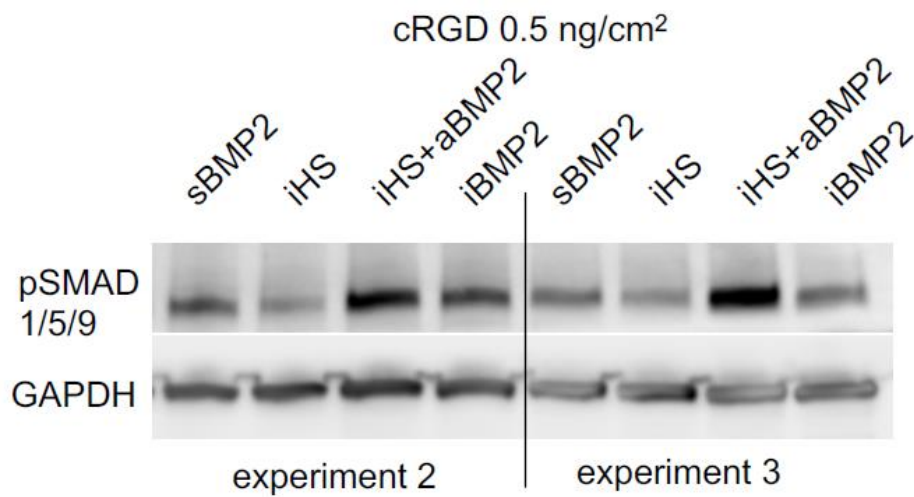


Ext fig 4 c 3: 3rd replicate. Western blot of p-SMAD1/5/9 in C2C12 cells plated on platforms functionalized with different cRGD surface concentrations and with sBMP2, iHS, iHS and aBMP2 and iBMP2. Cells were lysed 1 hour after plating.



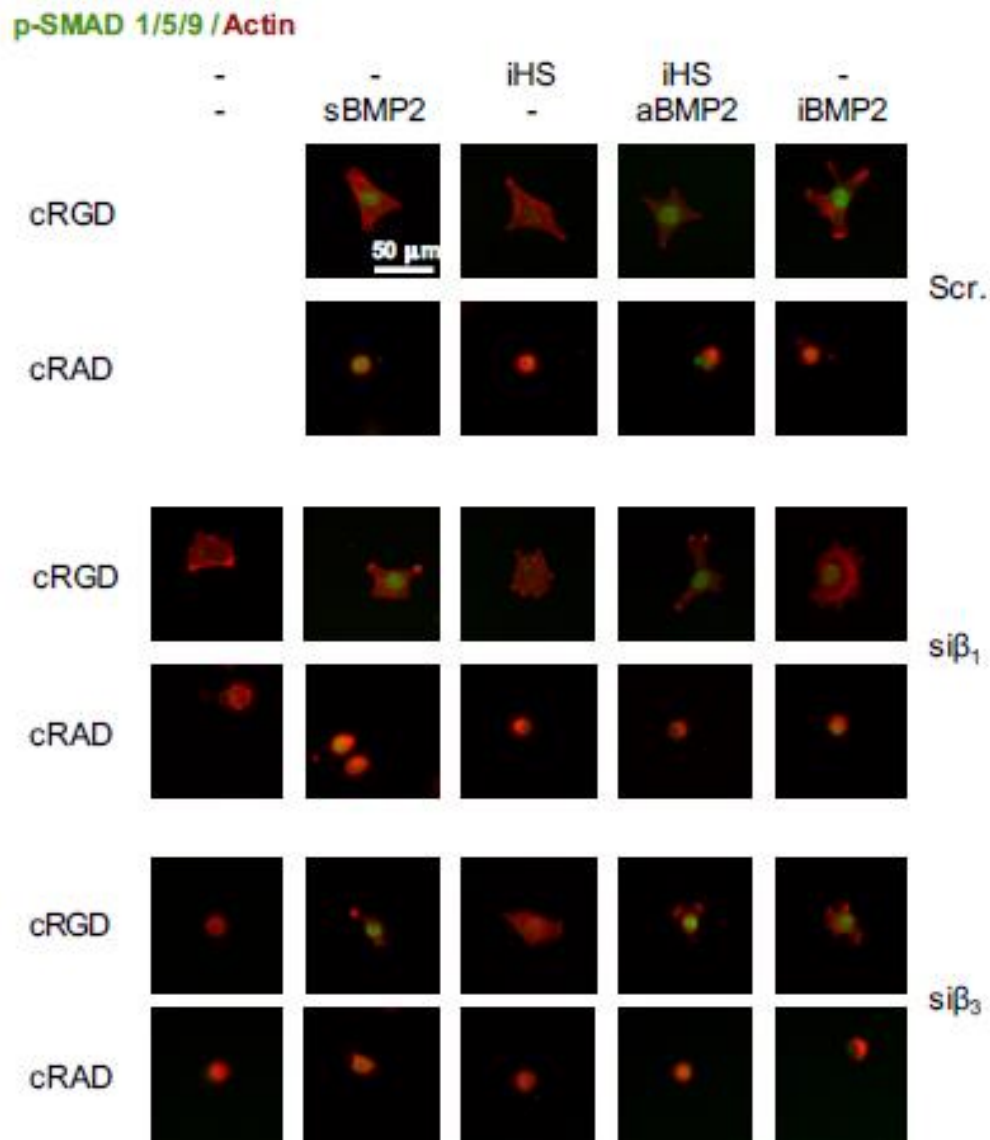
Ext fig 4 c 4: 4th replicate. Western blot of p-SMAD1/5/9 in C2C12 cells plated on platforms functionalized with different cRGD surface concentrations and with sBMP2, iHS, iHS and aBMP2 and iBMP2. Cells were lysed 1 hour after plating.

Extended figure 4 d



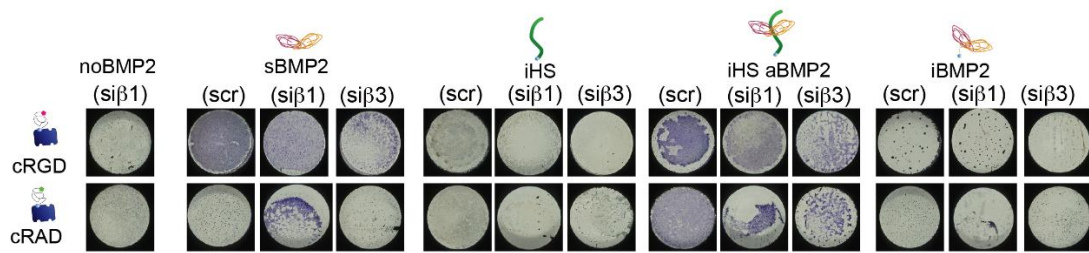
Ext fig 4 d: 2nd and 3rd replicate. Western blot and quantification of p-SMAD1/5/9 after 2h in hPDSCs plated on different platforms presenting sBMP2, iHS, iHS + aBMP2, and iBMP2.

Extended figure 5 a



Ext fig 5 a: Representative images of all conditions. Cells were silenced for either β_1 or β_3 integrins and plated on cRGD and cRAD platforms presenting sBMP2, iHS, iHS + aBMP2 and iBMP2, and fixed after 1.5 h for p-SMAD1/5/9 staining. Representative IF images cells plated on platforms and stained for actin (red) and p-SMAD1/5/9 (green) are shown. Scale bar = 20 μm .

Extended figure 5 c



Ext fig 5 c: Representative wells of all conditions. Cells were silenced for either $\beta 1$ or $\beta 3$ integrins and plated on cRGD and cRAD platforms presenting sBMP2, iHS, iHS + aBMP2 and iBMP2, and fixed after 3 days for ALP staining. Representative wells after ALP staining of all the conditions are shown.

IV.F Transition

We have studied the effect of exogenous iHS and integrin-mediated cell adhesion on osteogenic differentiation with biomimetic SAV platforms. However, the contribution of the csHS was not considered, even though it probably influences the iHS and aBMP2-mediated cellular response. Indeed, csHS is known to regulate cell adhesion *via* its affinity for the HepII binding domain of the ECM molecule fibronectin. It further plays a role in BMP2 signaling and it was shown that cells deficient for csHS up-regulate BMP2 activity, which is an opposite effect compared to exogenous iHS. In the next chapter, we aim at investigating the interaction between csHS and exogenous iHS with a first set of experiments. By plating CHO cells and those deficient for csHS on biomimetic platforms presenting cRGD, iHS and aBMP2 we intend to study cellular adhesion and early BMP2 signaling.

Chapter V: The role of cell surface heparan sulfate and exogenous heparan sulfate on BMP2 signaling and cellular adhesion

V.A Article summary (English)

HSPGs are either bound to structural proteins in the ECM or expressed at the cell surface (Sarrazin, Lamanna and Esko, 2011). They regulate BMP2 activity due to their affinity to bind GFs (Ruppert, Hoffmann and Sebald, 1996) and also mediate cellular morphology by binding to fibronectin (Longley *et al.*, 1999) but this depends on their location. While exogenous iHS enhanced pSMAD1/5/9 signaling and osteogenic differentiation (Migliorini *et al.*, 2017; Sefkow-Werner *et al.*, 2020), experiments with cells and mice deficient for csHS revealed up-regulated BMP2 signaling (Huegel *et al.*, 2013; Pacifici, 2018). Opposite roles also occur for cellular adhesion where exogenous HS was responsible for reduced adhesion (Lundmark *et al.*, 2001) but only cells with csHS were able to adhere to surfaces containing only the heparin binding site (LeBaron *et al.*, 1988). The interaction between csHS and exogenous HS however is rarely studied and few is known about exogenous iHS presented to cells in an oriented way.

We address this subject by plating CHO WT and CHO KO, deficient for csHS, on biomimetic SA_v platforms presenting oriented, exogenous iHS. iHS is co-functionalized with cRGD so that these platforms only present integrin ligands and none for csHS to study the role of iHS and csHS on integrin-mediated cellular adhesion. In a second step, we adsorb critical doses of BMP2 on iHS and compare these conditions with soluble BMP2 at critical concentrations to distinguish BMP2 activity between iHS and csHS. We further treat cells and exogenous iHS with the HS antagonist Surfen to differentiate between function and presence of HS (Schuksz *et al.*, 2008).

CHO WT cells adhered with an elongated morphology on cRGD platform whereas CHO KO cells were round but larger, which means that csHS had a positive influence on cell polarization. When plated on platforms with cRGD and iHS, CHO WT cells became rounder whereas CHO KO cells did not change their phenotype. Exogenous iHS thus had a negative influence on adhesion only in presence of csHS, which indicated an interaction between both. Surfen treatment of both cell types marginally improved cell adhesion on cRGD platforms but significantly up-regulated cellular area and adhesion on cRGD + iHS platforms. This was probably due to crosslinking of csHS or cell surface CS (csCS) with iHS. Indeed, csCS is up-regulated in CHO KO cells (Lidholt *et al.*, 1992).

CHO WT and CHO KO cells plated on cRGD responded similar to sBMP2 at high concentrations (4 nM) but CHO KO cells were less responsive to low BMP2 doses (0.04 nM),

indicating a positive role of csHS on BMP2 signaling. Surfen treatment of both cells was further reducing BMP2 response, which means, that not just the presence but also the function of csHS were positive BMP2 mediators. On cRGD + iHS platforms with adsorbed BMP2 the same trend was observed. In addition, it was shown that aBMP2 was only as bioactive as sBMP2 if csHS was present and functional.

We provided first insights on the interdependence between csHS and iHS regarding cellular adhesion and BMP2 signaling. While the results regarding cellular adhesion were in line with literature, BMP2 signaling at low concentration was contrary to other studies with chondrocytes. Further studies with CHO cells deficient for csHS and csCS as well as with a more relevant cell types from the osteogenic lineage are needed to conclude on the role of other cell surface GAGs as well as to investigate if the effect of csHS is cell type dependent. In addition, the interaction of Surfen with the platform and with the cells needs to be further investigated and additional quantification of cell migration and protrusions is necessary to better understand these first results.

V.B Article summary (French)

Les HSPG sont soit liées à des protéines structurales dans l'ECM, soit exprimées à la surface des cellules (Sarrazin, Lamanna et Esko, 2011). Elles régulent l'activité de la BMP2 en raison de leur affinité à lier les GFs (Ruppert, Hoffmann et Sebald, 1996) et médient également la morphologie cellulaire en se liant à la fibronectine (Longley et al., 1999) mais cela dépend de leur localisation. Alors que les iHS exogènes améliorent la signalisation pSMAD1/5/9 et la différenciation ostéogénique (Migliorini et al., 2017 ; Sefkow-Werner et al., 2020), des expériences avec des cellules et des souris déficientes en csHS ont révélé une signalisation BMP2 régulée à la hausse (Huegel et al., 2013 ; Pacifici, 2018). Des rôles opposés se produisent également pour l'adhésion cellulaire, où l'HS exogène était responsable d'une réduction de l'adhésion (Lundmark et al., 2001), mais seules les cellules avec csHS étaient capables d'adhérer à des surfaces contenant uniquement le site de liaison de l'héparine (LeBaron et al., 1988). L'interaction entre les csHS et les HS exogènes est cependant rarement étudiée et peu de choses sont connues sur les iHS exogènes présentés aux cellules de manière orientée.

Nous abordons ce sujet en plaçant des cellules CHO WT et CHO KO, déficientes pour les csHS, sur des plateformes SAV biomimétiques présentant des iHS exogènes orientés. Les iHS sont co-fonctionnalisés avec les cRGD de sorte que ces plateformes ne présentent que des ligands d'intégrine et aucun csHS afin d'étudier le rôle des iHS et des csHS sur l'adhésion cellulaire médiée par les intégrines. Dans un deuxième temps, nous adsorbons des doses critiques de BMP2 sur l'iHS et comparons ces conditions avec le BMP2 soluble à des concentrations critiques pour distinguer l'activité du BMP2 entre l'iHS et le csHS. Nous traitons ensuite les cellules et les iHS exogènes avec l'antagoniste HS Surfen pour différencier la fonction et la présence de HS (Schuksz et al., 2008).

Les cellules CHO WT ont adhéré avec une morphologie allongée sur la plateforme cRGD alors que les cellules CHO KO étaient rondes mais plus grandes, ce qui signifie que le csHS a eu une influence positive sur la polarisation cellulaire. Lorsqu'elles ont été placées sur des plateformes avec cRGD et iHS, les cellules CHO WT sont devenues plus rondes alors que les cellules CHO KO n'ont pas changé de phénotype. L'iHS exogène a donc eu une influence négative sur l'adhésion uniquement en présence de csHS, ce qui indique une interaction entre les deux. Le traitement au Surfen des deux types de cellules a amélioré de façon marginale l'adhésion cellulaire sur les plateformes cRGD mais a augmenté de façon significative la surface

cellulaire et l'adhésion sur les plateformes cRGD + iHS. Cela était probablement dû à la réticulation du csHS ou du CS de surface cellulaire (csCS) avec l'iHS. En effet, le csCS est régulé à la hausse dans les cellules CHO KO (Lidholt et al., 1992).

Les cellules CHO WT et CHO KO placées sur du cRGD ont répondu de manière similaire au sBMP2 à des concentrations élevées (4 nM), mais les cellules CHO KO ont été moins réactives aux faibles doses de BMP2 (0,04 nM), ce qui indique un rôle positif du csHS sur la signalisation du BMP2. Le traitement au Surfen des deux cellules a encore réduit la réponse au BMP2, ce qui signifie que non seulement la présence mais aussi la fonction des csHS sont des médiateurs positifs du BMP2. La même tendance a été observée sur les plateformes cRGD + iHS avec BMP2 adsorbé. En outre, il a été démontré que l'aBMP2 n'était aussi bioactive que la sBMP2 que si la csHS était présente et fonctionnelle.

Nous avons fourni un premier aperçu de l'interdépendance entre csHS et iHS en ce qui concerne l'adhésion cellulaire et la signalisation de la BMP2. Alors que les résultats concernant l'adhésion cellulaire étaient conformes à la littérature, la signalisation de la BMP2 à faible concentration était contraire à d'autres études sur les chondrocytes. D'autres études avec des cellules CHO déficientes en csHS et csCS ainsi qu'avec des types cellulaires plus pertinents de la lignée ostéogénique sont nécessaires pour conclure sur le rôle d'autres GAG de surface cellulaire ainsi que pour étudier si l'effet du csHS est dépendant du type cellulaire. En outre, l'interaction du Surfen avec la plateforme et avec les cellules doit être étudiée plus en détail et une quantification supplémentaire de la migration et des protrusions cellulaires est nécessaire pour mieux comprendre ces premiers résultats.

V.C Article 4 (in preparation)

The role of cell surface heparan sulfate and exogenous heparan sulfate on BMP2 signaling and cellular adhesion

Julius Sefkow-Werner^{1,2}, Jean Le Pennec², Ann-Christin Severmann³, Fatima Asar³, Velina Bachvarova³, Romain Yves⁴, Catherine Picart^{2,5}, Andrea Vortkamp³, Elisa Migliorini^{2*}

¹Univ. Grenoble Alpes, CNRS, Grenoble INP, LMGP, 38000 Grenoble, France

²Univ. Grenoble Alpes, CEA, CNRS, INSERM, IRIG, ERL 5000, Grenoble, France

³Department of Developmental Biology, Center for Medical Biotechnology, Faculty Biology, University Duisburg-Essen, Germany

⁴Univ. Grenoble Alpes, CNRS, CEA Institut de Biologie Structurale, UMR 5075, 38000 Grenoble, France

⁵CEA, direction of fundamental research, interdisciplinary research institute of Grenoble (IRIG), FRE CNRS, Grenoble, France

Abstract

Heparan sulfate proteoglycans are known to be involved in cellular adhesion and growth factor signaling due to their binding domains for bone morphogenetic protein 2 (BMP2) and ECM compounds. Depending on their location either in the extracellular matrix or at the cell surface, they differ in functionality. Exogenous heparan sulfate (HS) had a negative effect on cellular adhesion whereas cell surface HS binding to ECM compounds positively influenced cell adhesion. Further, exogenous HS sustained BMP2 signaling and up-regulated osteogenic differentiation while cell surface HS had a negative effect on BMP2 signaling as investigated in the disease called hereditary multiple exostosis. There, a defect of EXT1 gene coding an enzyme involved in the HS biosynthesis leads to downregulation of cell surface HS and in consequence to upregulated BMP2 signaling.

While most commonly the effects of csHS or exogenous HS are investigated separately, we aim at developing a system to study the interaction between both types of HS in a biomimetic way. We used biomimetic SAV platforms to co-present the adhesion ligand cRGD and oriented exogenous HS with adsorbed BMP2 to study cellular adhesion and BMP2 signaling. By comparing Chinese hamster ovarian wild type cells to those deficient for cell surface HS, we revealed that csHS and exogenous HS negatively influence each with respect to cellular

adhesion and polarization and that csHS at low BMP2 concentrations had a positive effect on BMP2 signaling.

Introduction

Heparan sulfate (HS) is a glycosaminoglycan (GAG) and is usually bound to a core protein forming heparan sulfate proteoglycans (HSPG) [1], [2]. Depending on their core protein, HSPG are either part of the extra cellular matrix (ECM) as for example perlecan and agrin or bound to the cell membrane, with syndecan 1-4 and glypican 1-6 as common examples [2]. They are synthesized in the Golgi apparatus or at the interface with the endoplasmic reticulum by attaching a tetracharsacharide primer to a serine residue of the core protein. From there, the HS chains are elongated with the help of the glycosyltransferases EXT1 and EXT2. Afterwards, they are further sulfated and expressed at the cell membrane or into the ECM [2]. HSPG are known to regulate mechanical properties of the ECM by providing structure and elasticity [3] but also modulate cellular morphology [4] and GF signaling [5]. Indeed, HS binds to the ECM proteins collagen, fibronectin or laminin [6] and to GFs such as bone morphogenetic protein 2 (BMP2) [7]. BMP2 is a GF from the TGF β -superfamily known to induce chondrogenic and osteogenic differentiation [8] and is combined with 3D scaffolds to repair large bone defects in humans [9].

The role of HS on BMP2 signaling was the object of different studies. A mutation of the EXT 1 gene causes a systematic downregulation of cell surface HS (csHS) and led to the formation of cartilaginous tumors, also called osteochondromas [10]–[13]. It was shown that this csHS deficiency up-regulated BMP2 signaling, which induced ectopic chondrogenesis. Gerstner et al. correlated EXT1 deficiency in mice with increased BMP4 and BMP6 activity [14]. BMP2 with blocked HS binding domain was also more active compared to the wild type suggesting that BMP2-csHS interaction interfered with BMP2 activity [7]. The treatment of csHS with its antagonist Surfen, or the cleavage of HS by heparinase resulted in an increased BMP2-induced chondrogenic response [15]. Effectively, Surfen competes with BMP2 for HS binding by interaction with the sulfated groups of the GAG chain and binds to other GAGs as well [16]. Exogenous HS on the other hand had a positive effect on BMP2 signaling: BMP2 bound to HS in solution up-regulated ALP activity of C2C12 cells probably due to prolonged BMP2 half-life and decreased BMP2 interaction with its antagonist Noggin [17]. Also Fisher

et al. observed that exogenous HS enhanced the ability of BMP2 to induce SMAD1/5/9 phosphorylation and chondrogenic differentiation in micro mass cultures [18]. Meanwhile, removing csHS with heparinase had a similar positive effect and overexpression of cell surface HSPG syndecan-3 on the other hand reduced BMP2 activity. Migliorini et al. further mimicked the natural condition of the ECM by immobilizing biotinylated HS (iHS) side-specifically to streptavidin (SAv) and adsorbed BMP2 (aBMP2) to iHS [19]. BMP2 signaling activity and osteogenic differentiation of C2C12 cells was enhanced compared to immobilized biotinylated BMP2 [19], [20].

HS was shown to mediate cellular adhesion. Chinese hamster ovarian wild-type cells (CHO WT) [21] and those deficient for csHS (CHO KO) [22] adhered to fibronectin substrates containing integrin- and heparin binding sites but only wild type cells adhered to substrates presenting exclusively the heparin binding site [23]. Further, HS-deficient cells did not form focal adhesion on fibronectin substrates. This question was addressed by Mhalanigam et al. who identified syndecan-4 with N-sulfations as prerequisite for focal adhesion formation [24], [25] and heparinase or Surfen treatment reduced cellular adhesion [16], [26]. Experiments with layer-by-layer films functionalized with different peptides revealed, that C2C12 cells were more elongated and migrated further on films with syndecan-I ligand compared to those on RGD [27]. They concluded, that β_1 -integrins and syndecan-I ligands interacted with each other to maintain proliferation whereas RGD-activated β_3 -integrins directed cells into differentiation. Regarding exogenous HS, it was found that perlecan reduced cellular adhesion but treatment with heparinase to remove the HS chains from perlecan was re-establishing cellular adhesion [28], [29]. These findings are specific for HS and heparin chains whereas CS or hyaluronan did not have a negative effect on adhesion. But the cellular source of perlecan coming with different type of glycosylation influenced cellular adhesion [30].

CsHS and iHS thus have opposing roles on cell adhesion and BMP2 signaling, however, no study compared their direct contribution or how they influence each other. We aimed at immobilizing iHS and adsorbed aBMP2 on SAv platforms together with the cell-adhesion ligand cRGD to study the response of CHO WT and CHO KO. We quantified cellular adhesion *via* cellular number, area, elongation [27] and compactness and further studied the effect of Surfen adsorbed to iHS and csHS. To be sensitive to subtle effects, we identified low aBMP2 concentrations on iHS just sufficient to induce SMAD1/5/9 phosphorylation, an early reporter for BMP2 activity [20].

We found that CHO WT cells were elongated on cRGD platforms and smaller than CHO KO cells on the same substrate, which were less elongated. While cRGD + iHS had a negative effect on cell polarization in CHO WT cells compared to cRGD platforms, CHO KO cells with only cell surface CS (csCS) did not change morphology on cRGD + iHS platforms. The absence of csHS had a negative effect on SMAD1/5/9 phosphorylation at low BMP2 doses as well as Surfen treatment of csHS, independently of BMP2 presented *via* iHS or in solution. Further, iHS together with csHS enhanced aBMP2 activity compared to aBMP2 presented *via* iHS in cells deficient for csHS or Surfen treated.

Materials and methods

The experimental procedures of this chapter are similar to those presented in chapter II and IV. Here, they are summarized and complemented in detail in case of new procedures.

Buffers and molecules

SA_v, cRGD, bHS and BMP2 were dissolved in 10 mM Hepes buffer and 150 mM NaCl, which was used as working buffer for surface functionalization and QCM-D. PBS served as rinsing buffer for cell culture steps. bis-2-methyl-4-amino-quinolyl-6-carbamide (Surfen hydrate, Sigma-Aldrich, France) was dissolved at 5 mM in dimethyl sulfoxide (DMSO, Sigma) and stored under nitrogen atmosphere at -20 °C. BSA (Sigma) was used to passivate plastic surfaces to avoid non-specific Surfen binding.

Sensors and surface preparation

Gold-coated QCM-D sensors and gold-sputtered glass coverslips were functionalized with PEG disulfide and biotinylated PEG thiol overnight. Gold-sputtered glass surfaces were attached *via* double-sided adhesive tape to UV-sterilized 96-well plates for automated surface functionalization.

Assembly of biomimetic platforms

The functionalization of QCM-D sensors was tracked *in situ* and followed a sequential routine of incubation and rinsing. Molecule concentrations are listed in **Table 1**. After the binding of SAV to biotinylated PEG-thiol, 5% BSA dissolved in Hepes passed through the micro-fluidic tubes for 2 h to passivate the tubes, the QCM-D chamber and the SAV-surface against non-specific Surfen adsorption.

Gold-surfaces attached to bottomless 96-well plates were functionalized with the Tecan Evo100 liquid handling robot, similar to as described before, starting with SAV in all wells. Then, 5% BSA was incubated and rinsed manually since higher volumes per well were required, not compatible with the automated protocol. cRGD was incubated to form a sub-monolayer and other molecules followed corresponding to the desired experimental conditions.

Table 1: Molecule concentrations and incubation times.

<i>Biomolecule</i>	<i>Abbreviation</i>	<i>Presentation</i>	<i>Concentration (nM)</i>	<i>Incubation time for sturation (min)</i>
Streptavidin	SAV	immobilized	180	30
Biotinylated cyclic arginylglycylaspartic acid	cRGD	immobilized	140	4 min (partly saturated)
Biotinylated heparan sulfate	iHS	immobilized	800	30
adsorbed Surfen	aSurfen	adsorbed on iHS	7500	90
soluble Surfen	sSurfen	soluble	7500	until cell fixation
adsorbed BMP2	aBMP2	adsorbed on iHS	190 - 0.4	90
soluble BMP2	sBMP2	soluble	4 - 0.04	until cell fixation

Cellular culture

C2C12 myoblasts were cultured as described before and served only as a control for the quantification of integrins. Wild type Chinese hamster ovarian k1 cells (CHO WT) [21] and CHO pgsD-677 cells with an EXT1 gene knock-out (CHO KO) [22] were kindly donated from Dr. Andrea Vortkamp's laboratory (Essen, Germany). We chose the cells deficient for csHS and not those deficient for csHS and csCS because we aimed at distinguishing the role of csHS and not of GAGs in general. They were cultured in typical tissue-treated polystyrene cell culture flasks or Petri dishes as sub-confluent monolayers in Dulbecco's Modified Eagle Medium: Nutrient Mixture F-12 (growth media, Thermo Fisher, France) supplemented with 10% FBS at 37 °C and 5% CO₂. Cells were passed before reaching confluence and not more than 3 times after thawing. 4 h prior to plating onto biomimetic platforms, cells were serum-starved and then

detached with trypsin for 5 min. Trypsin was deactivated with growth media and 10% FBS and cells were centrifuged and re-suspended in serum-free growth media. Plated cells were incubated at 37 °C and 5% CO₂.

Cellular adhesion and BMP2 signaling for microscopy analysis

sSufen was diluted in growth media to a concentration of 15 µM which leads to 0.3% DMSO in the solution. Growth media without sSurfen was thus supplemented with the same quantity of DMSO as a control. 50 µl of 15 µM sSurfen or DMSO in growth media were pipetted into each well and 50 µl re-suspended CHO WT or CHO KO cells were added, reaching a final sSurfen concentration of 7.5 µM and 0.15% DMSO and 25 000 cells per well. This assured that cells were in contact with sSurfen before interacting with the platforms. sBMP2 was pre-diluted in growth media to reach final concentration of 4 nM or 0.04 nM after pipetting 1 µl into the wells. Cells were incubated for 75 min at 37 °C and 5% CO₂ and then rinsed 3 times with PBS to remove non-adhering cells. Afterwards, they were fixed with 4% PFA for 20 min and rinsed with PBS. To quantify cellular area, elongation, compactness and pSMAD1/5/9 translocated into the nucleus, cells were permeabilized with triton, blocked with 3% BSA and stained for nucleus, F-actin and pSMAD1/5/9. 20 images per well were acquired with automated immunofluorescence microscopy (20x, InCell Analyzer 2500) on three channels in parallel and pSMAD1/5/9 intensity was measured under a mask defined by nucleus staining using automated image analysis (InCarta). Cellular area, shape and cell number were automatically analyzed with the open source software CellProfiler™ based on F-actin and nucleus signal because of improved accuracy compared to InCarta. It returned cellular area, ellipticity (parameter for cell elongation, ratio of the shortest to the longest axis of the cell) and compactness (parameter to quantify morphological irregularities at the cell membrane, mean squared distance of the object's pixels from the centroid divided by the area). Representative images were equally contrast and brightness-adjusted for improved appearance.

Protein isolation and western blot analysis

To quantify integrins, 100 000 C2C12 cells, CHO WT and CHO KO cells were plated inside polystyrene 6-well plates (Corning, USA) and incubated for 72 h at 37 °C and 5% CO₂. After rinsing, cells were lysed with RIPA buffer and prepared for Western blot. Blocked

membranes were probed with rabbit anti- β_1 (1:2000, produced at the laboratory of Dr Albiges-Rizo, IAB, Grenoble, France), rat anti- β_3 (1:1000, Luc-A5, Emfret Analytics), rabbit anti- α_5 (1:5000, Chemicon Millipore, USA) or mouse anti- α_V (1:2000, BD sciences, France) together with rabbit anti-GAPDH (1:1000, Cell Signaling Technology) as a reference. Secondary HRP-conjugated AB against rabbit (1:5000), mouse (1:5000) and rat (1:2000) were incubated and signal was detected with ChemiDocMP (Bio-rad) using Clarity or Clarity Maw Western ECL Substrate (Bio-Rad). Data was normalized to GAPDH and C2C12 cells were used as a positive control for functional antibodies.

Statistical analysis

For cell experiments, each condition was prepared as technical duplicate in two different wells and experiments were repeated at least three times. Means were tested for statistical significance between different conditions with the non-parametric Mann-Whitney test with $p \leq 0.05$ and based on at least three biological replicates.

Results

We aim at studying the influence of csHS and iHS on integrin-mediated cell adhesion and cell morphology as well as the role of csHS on early BMP2 signaling. We compared CHO WT cells and CHO KO cells regarding their interaction with different biomimetic SA_v platforms and measured cell number, cell area, elongation, compactness and BMP2-mediated signaling. Surfen treatment of iHS and cells aimed at modifying HS-function. Platforms were characterized with QCM-D for Surfen interaction with iHS and aBMP2 and the expression of integrins in both cell types was quantified with Western blot.

The influence of iHS and csHS on cell morphology and number

CHO WT cells and CHO KO were plated on platforms functionalized with the cRGD adhesion ligand with a high affinity for β_3 -integrins. (**Figure 1 a top**). Both cell types adhered after 75 min similarly well to the platform seen *via* equal cell number but in both cases we observed visually that many of the initially plated cells were removed by rinsing (**Figure 1 b**).

CHO WT cells adhered in an elongated way while some of them remained round and CHO KO cells with reduced csHS were less elongated and larger. Indeed, quantification of cell area and ellipticity as a parameter to measure cell elongation (**Figure 1 d**) revealed these differences (**Figure 1 c, e**). The compactness measures the mean square distance of all pixels to the centroid with the value 1 representing a perfect circle and higher values irregularities at the perimeter. Here, no difference was observed between CHO WT and CHO KO cells (**Figure 1 f**). In summary, CHO KO cells were systematically larger than CHO WT cells on cRGD platforms and were less able to polarize. Thus, csHS had a positive effect on polarization but reduced cell area.

Biomimetic platforms were co-functionalized with cRGD and oriented iHS to reveal the role of iHS. CHO WT were smaller and had a more circular morphology on cRGD + iHS platforms than on cRGD platforms but CHO KO cell morphology did not change due to iHS (**Figure 1 a bottom**). CHO WT cells adhered only marginally stronger on iHS than on cRGD whereas CHO KO cells adhered much better compared to cRGD (**Figure 1 b**). Quantification of cell area and ellipticity revealed a slightly reduced cellular area of CHO WT cells. A less elongated phenotype (**Figure 1 c, e**) and a decreased compactness indicated a more circular appearance (**Figure 1 f**). While cell area or elongation did not change in CHO KO cells, the increased compactness was due to more irregularities at the cell perimeter. Indeed, while on cRGD both cell types had a comparable compactness, on cRGD + iHS they presented differences with CHO KO cells being more irregular. In the presence of csHS, iHS had a negative effect on cell elongation and area but improved cellular adhesion for cells deficient for csHS.

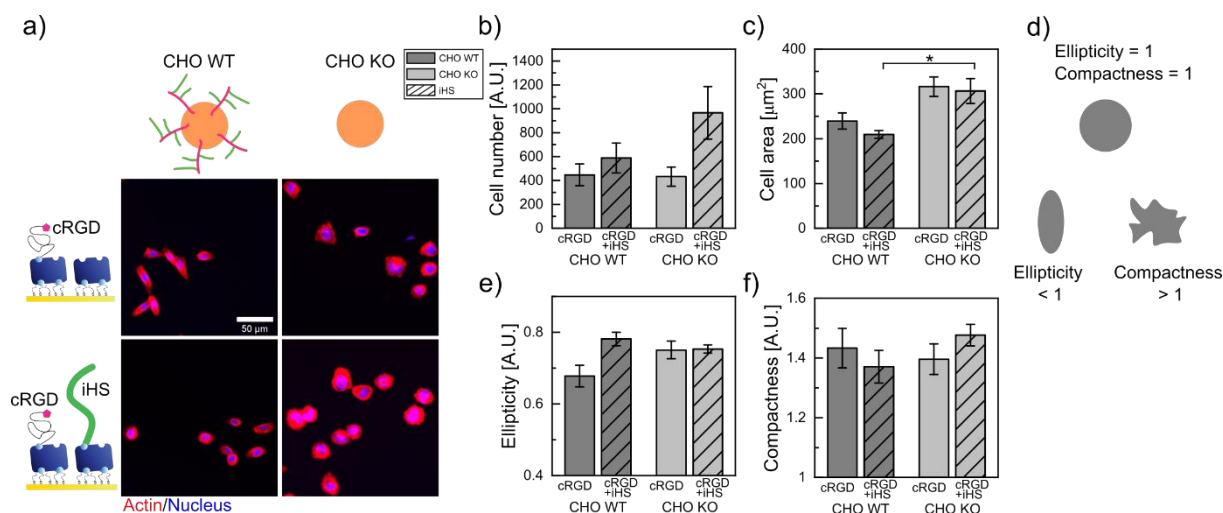


Figure 1: csHS promoted cell elongation on cRGD platforms and iHS negatively influenced cell elongation and area in CHO WT cells. a) Representative images of CHO WT and CHO KO cells plated on cRGD and cRGD + iHS platforms and fixed after 75 min. b) Absolute cell number quantification after rinsing 3 times with PBS and based on 20 20x images with an area of 0.44 cm² per image. c) Cell area quantification d) Schematic of cell morphology parameters: Ellipticity measures the ratio between the short and the long axis of a fitted cell with 1 being a perfectly circular cell and 0 being a line. Compactness measures the mean square distance of all pixels to the centroid with the value 1 representing a perfectly round cell and higher values irregularities at the perimeter. e) Ellipticity quantification f) Compactness quantification. SB = 50 μm, Values in graphs are mean ± SEM of n ≥ 4 experiments with 2 independent replicates per experiment. Significance was tested with non-parametric Mann-Whitney test and p < 0.05 was considered significant (*).

To distinguish the role of csHS and iHS from the role of integrins, we characterized CHO WT and CHO KO cells regarding their integrin protein quantity after 72 h of culture on plastic petri dishes and compared it to C2C12 cells as a control (**Figure 2**). The expression of β₁-integrins precursor was comparable in both cell types but CHO KO cells express much less mature β₁-integrins. β₃-integrins were fairly detectable compared to C2C12 cells. While α_v-integrins were comparable in CHO WT and CHO KO cells, α₅-integrins were less present in CHO KO cells. It can be concluded that the EXT1-mutation also altered integrin expression next to decreased levels of csHS.

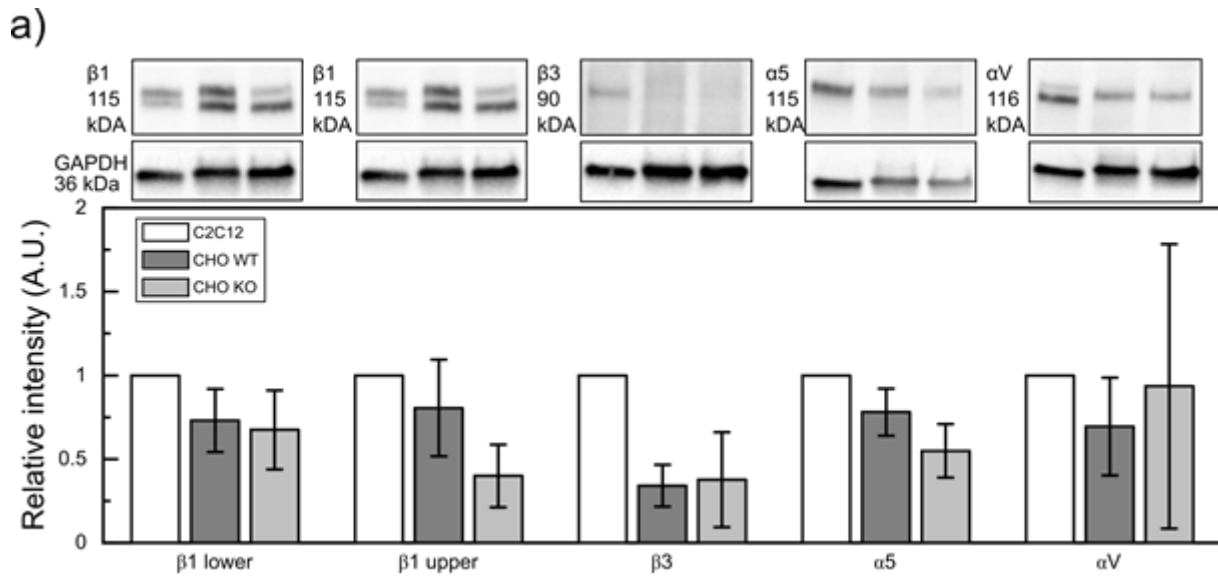


Figure 2: Integrin protein quantity was downregulated in CHO KO cells compared to CHO WT cells.
a) Representative Western blots of C2C12 cells, CHO WT and CHO KO cells cultured for 72 h on plastic Petri dishes until lyse with Ripa buffer. Bands were normalized to GAPDH and results present mean \pm SD for n = 3 experiments.

As a control to downregulation of csHS *via* gene mutation, we treated CHO WT and CHO KO cells with the HS antagonist sSurfen (7.5 μ M) and plated cells on platforms presenting cRGD. CHO WT cells spread with slightly increased cell area and became slightly less polarized. sSurfen did not alter cell morphology in CHO KO cells (**SI Fig 1 a, c, d, e**). On the other hand, sSurfen increased cell adhesion in CHO KO cells while it remained unchanged in CHO WT cells (**SI Fig 1 b**). The differences in morphology between both cells persisted and sSurfen did not have the same effect as the EXT1 gene mutations.

Then, we plated sSurfen-treated cells on cRGD platforms together with iHS. CHO WT cells responded with a significantly increased cell area and spread in a triangular-like shape (**Figure 3 a, c**). CHO KO cells as well became larger but spread in a more circular shape. In addition, some of them developed protrusions visible at the cell perimeter (**Figure 3 a**). While the change in morphology of CHO WT cells did not express itself in changes of the parameters ellipticity or compactness, CHO KO cells became less compact with more irregularities at the cell perimeter (**Figure 3 d, e**). sSurfen further strongly enhanced cellular adhesion of CHO WT cells and even more of CHO KO cells with respect to non-sSurfen treated cells (**Figure 3 b**) but also compared to sSurfen treated cells on cRGD platforms (**SI Fig 1 b**). We conclude that csHS treated with sSurfen enhanced cellular adhesion and cell area on platforms presenting iHS. Surprisingly, CHO KO with down-regulated csHS reacted similarly to sSurfen, probably due to sSurfen binding to remaining csCS.

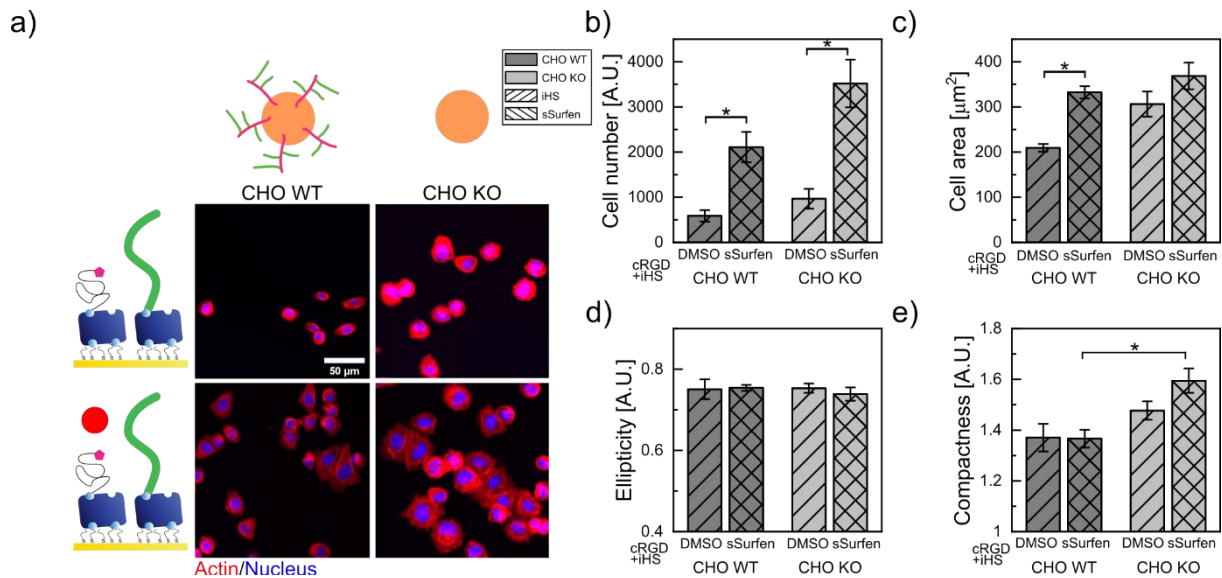


Figure 3: sSurfen enhanced adhesion and cell area on iHS platforms of CHO WT and CHO KO cells
a) Representative images of sSurfen-treated (7.5 μM) CHO WT and CHO KO cells plated on cRGD + iHS platforms and fixed after 75 min. b) Absolute cell number quantification after rinsing 3 times with PBS and based on 20 20x images with an area of 0.44 cm² per image. c) Cell area quantification. d) Ellipticity quantification e) Compactness quantification. SB = 50 μm, Values in graphs are mean ± SEM of n ≥ 4 experiments with 2 independent replicates per experiment. Significance was tested with non-parametric Mann-Whitney test and p < 0.05 was considered significant (*).

To probe if the effect of sSurfen was due to binding to iHS on the platform instead of interacting with the cells, we incubated Surfen (aSurfen, 7.5 μM) for 90 min on cRGD + iHS platforms and rinsed well. The morphology of both cell types on iHS + aSurfen surfaces did not change compared to iHS (SI Fig 2 a, b, c, e). Cell adhesion increased marginally in both cell types (SI Fig 2 b). In summary, the properties of iHS treated with aSurfen did not change besides a small improvement of cellular adhesion.

To conclude, we distinguished the effect of csHS and iHS by plating CHO WT and CHO KO cells on different biomimetic platforms and further treated cells or iHS with the GAG antagonist Surfen. The downregulation of csHS increased cellular area but decreased cell elongation. In contrast, iHS negatively interacted with csHS by decreasing cell elongation and area but enhanced cellular adhesion for csHS deficient cells. sSurfen treatment of csHS did not influence adhesion and morphology remarkably on cRGD platforms but strongly upregulated cell number and cell area on iHS platforms. However, aSurfen neglected the negative influence of iHS regarding cellular adhesion of CHO WT.

The role of iHS and csHS on BMP2 response

To investigate the role of iHS and csHS on BMP2 mediated signaling we built up biomimetic platforms presenting cRGD, iHS and aBMP2 as well as cRGD and sBMP2. aBMP2 and sBMP2 concentration were chosen in a way that CHO WT cell response to BMP2 fell into the dynamic range of SMAD1/5/9 phosphorylation and cells were further treated with sSurfen.

The sequential platform build-up was characterized with QCM-D as previously reported [20]. **Figure 4 a** shows SAV binding to gold *via* bPEGthiol/PEGthiol and cRGD occupying some of the free biotin binding sites. Interruption of cRGD incubation before saturation allowed sequential binding of iHS to the surface until saturation and aBMP2 (200 nM) adsorbed on iHS. For experiments with Surfen, functionalized 96-well plates were passivated after SAV incubation with 5% BSA to avoid Surfen binding to the borders of the wells and non-specifically to the platform. BSA incubation on SAV induced a strong shift in frequency but after rinsing, a neglectable amount of BSA remained on the surface (**Figure 4 b**). Indeed, bHS still bound to biotin binding sites and aBMP2 adsorbed on iHS. Worth to note is that in **Figure 4 a**, BMP2 was incubated under flow whereas in **Figure 4 b**, the incubation was static, influencing the binding kinetics. After rinsing, Surfen was incubated with 7.5 μ M and saturated the surface after 15 min with an increased frequency and a decreased dissipation. Interestingly, rinsing decreased the frequency back to the level before incubation whereas the dissipation remained at the same level. Surfen interacted with iHS and aBMP2 on the surface, notably by rigidification of the platform. Regarding BMP2, it can not be concluded if it was removed from iHS. However, preliminary results on simple iHS platforms without aBMP2 showed a similar response to Surfen and suggested that shifts in frequency and dissipation were due to interaction with iHS and not with aBMP2 (data not shown).

DMSO or sSurfen-treated CHO WT and CHO KO cells were plated on biomimetic surfaces and sBMP2 at 0.04 and 4 nM was added to the cell media. At 4 nM sBMP2 concentration on cRGD platforms, CHO WT and CHO KO cells showed similar levels of pSMAD1/5/9 with CHO KO cells being slightly more responsive (**Figure 4 c**). sSurfen treatment did not alter sBMP2 activity either. On cRGD platforms without sBMP2 stimulation, CHO WT cells had a significantly higher pSMAD1/5/9 baseline signal compared to CHO KO cells but sSurfen treatment had no further influence. sBMP2 with the low concentration of 0.04 nM induced a reduced SMAD1/5/9 phosphorylation compared to the 4 nM condition but higher than the negative control without BMP2 treatment. Interestingly, CHO KO cells responded significantly

less to the low sBMP2 concentration than CHO WT cells and sSurfen treatment further reduced response in both cell types. We conclude that csHS has a positive effect BMP2 activity in CHO cells at low BMP2 concentration. A downregulation of csHS or the blocking of iHS with sSurfen decreased CHO response to BMP2. Interestingly, CHO KO cells had lower baseline pSMAD1/5/9 levels.

To investigate the role of iHS on BMP2 signaling, CHO cells were plated on cRGD + iHS surfaces with and without low concentrations of aBMP2. On iHS surfaces, a pSMAD1/5/9 baseline signal of CHO WT cells was comparable to cRGD surfaces but CHO KO baseline signal was slightly downregulated compared to cRGD platforms (**Figure 4 d**). Surprisingly, sSurfen treatment of both cell types further decreased baseline pSMAD1/5/9 levels, contrarily to cRGD conditions. Thus, iHS had a negative role on baseline pSMAD1/5/9 levels only if csHS was downregulated. sSurfen interacting with the csHS and iHS in parallel further reduced baseline signaling. At 0.4 nM aBMP2 concentration, CHO WT cells were less responsive to aBMP2 compared to the positive control and CHO KO cells had significantly lower levels compared to CHO WT cells. sSurfen treatment further decreased SMAD1/5/9 phosphorylation in both cell types. To quantify the relative influence of iHS on exogenous aBMP2 activity compared to sBMP2 activity, the ratio of aBMP2 at 0.4 nM to sBMP2 at 0.04 nM was calculated, since in WT CHO cells without Surfen treatment, low aBMP2 and low sBMP2 concentration induced the same level of SAMD1/5/9 phosphorylation in the kinetic range. Changes in the ratio between the effect of sBMP2 and aBMP2 would thus indicate a role of iHS (**Figure 3 e**). This revealed, that aBMP2 presented by iHS was less effective for cells with downregulated csHS or csHS treated with sSurfen compared to untreated CHO WT cells. Nevertheless, a direct comparison between sBMP2 and aBMP2 is not possible since the absolute amount of aBMP2 adsorbed on iHS was not quantifiable.

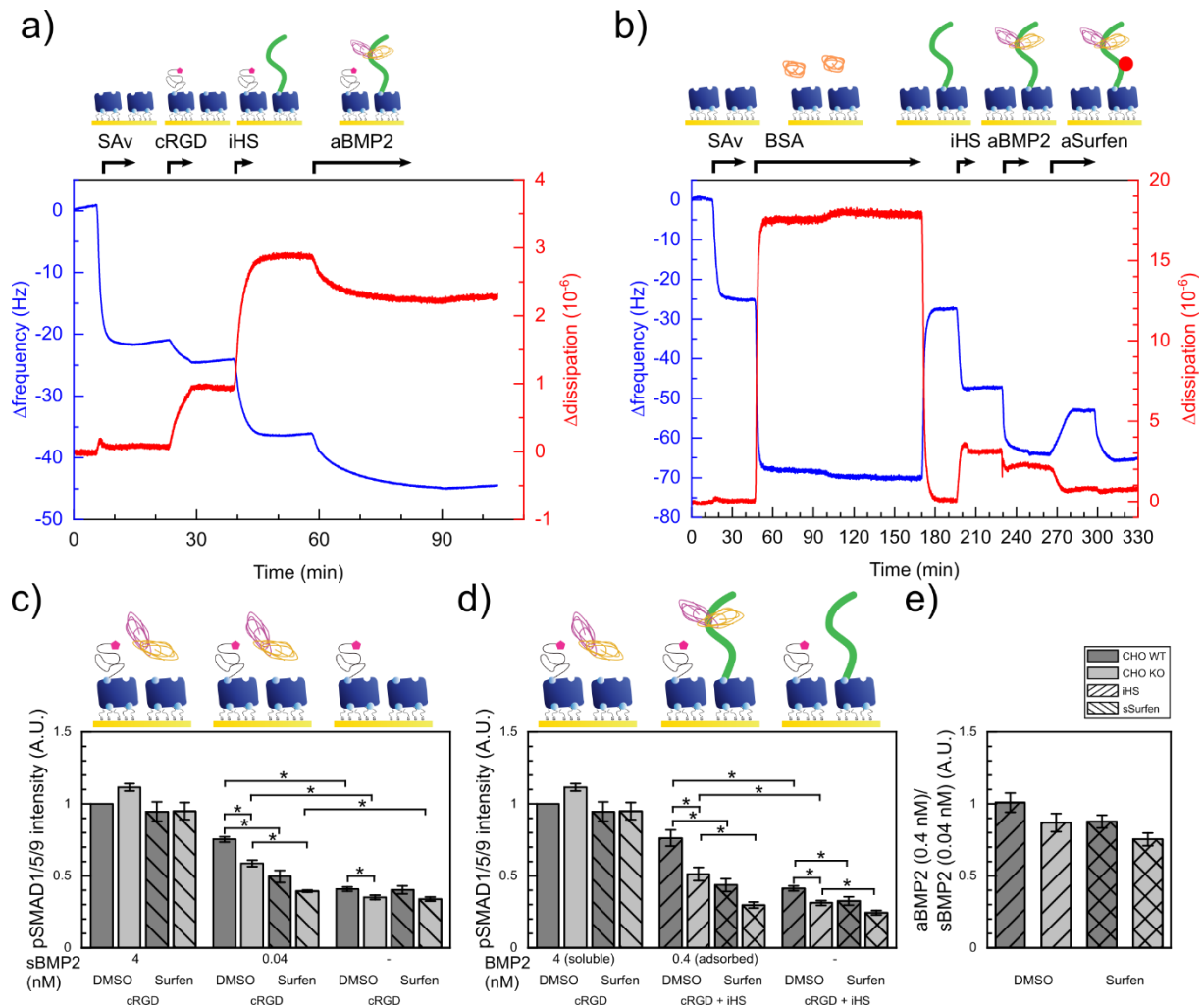


Figure 4: aBMP2 bound next to cRGD to iHS and Surfen interacted with the platform. CHO KO cells responded less to sBMP2 and aBMP2 at critical concentrations. a) Graph showing the change in frequency and dissipation up-on molecular binding measured with QCM-D. cRGD and iHS bound sequentially to SAV and aBMP2 (200 nM) adsorbed to iHS. Black arrows indicate periods of incubation and blanc segments periods of rinsing b) QCM-D graph shows how BSA blocked the surface and iHS bound to SAV. aBMP2 (200 nM) adsorbed to iHS. Surfen at 7.5 μ M was incubated and rinsed. c) Graph showing the normalized pSAMAD1/5/9 signaling in DMSO and sSurfen-treated (7.5 μ M) CHO WT and CHO KO cells to 4 nM and 0.04 nM sBMP2 concentration on cRGD platforms. d) The intermediate sBMP2 concentration and the negative controls were replaced by 0.4 nM aBMP2 incubated for 90 min on iHS and cRGD + iHS surface without BMP2 treatment e) Graph showing the ratio of the pSAMAD1/5/9 signal induced by 0.4 nM aBMP2 to the signal induced by 0.04 nM sBMP2. Values in graphs are mean \pm SEM of $n \geq 4$ experiments with 2 independent replicates per experiment. Significance was tested with non-parametric Mann-Whitney test and $p < 0.05$ was considered significant (*).

Discussion

We compared the role of iHS and csHS on cell morphology, cell number and BMP2 signaling by plating CHO WT cells and csHS-deficient CHO KO cells on biomimetic platforms.

We observed that CHO WT were less elongated when plated on cRGD+iHS surfaces compared to cRGD surfaces, which is in line with Lundmark et al. who also identified exogenous HS as a negative influencer for cell adhesion [28]. Cells treated with sSurfen on iHS surfaces were much larger compared to DMSO-treated cells but this effect was due to Surfen binding to csHS and not due to changes in surface rigidity, since aSurfen on iHS did not have the same effect. Indeed, the possible change of mechanical properties regarding increased rigidity due to Surfen cross-linking iHS could positively influence cellular adhesion [31]. aSurfen on iHS reduced the negative interaction between iHS and csHS, probably by reducing the negative charge on the surface. Schuksz et al. in the contrary evidenced reduced CHO WT cell adhesion mediated by sSurfen at comparable concentrations [16]. On the other hand, their substrates presented only the HepII domain of fibronectin, ligand for csHS, and blocking csHS with Surfen withheld cells from HS-mediated binding. Our cRGD surfaces privilege integrin-dependent cellular adhesion and appear less dependent from csHS. The positive effect of sSurfen on cell area could be due to crosslinking iHS and csHS, which accelerates integrin-mediated adhesion. Another explanation would be the cross-linking of different csHS-chains, the latter possibly leading to better exposure of integrins at the cell membrane. This would explain, why the effect of Surfen is dominant on iHS platform and much less expressed on cRGD platforms.

CHO KO cells on cRGD substrates were larger but had a round and less polarized phenotype compared to CHO WT cells. Kempf et al. published a similar phenotype of the same cell line on Poly-L-Lysine (PLL) substrates but in their study, CHO WT cells were spreading much better than CHO KO cells [32]. Indeed, PLL with its positive charge is known to improve cell adhesion *via* the anionic sites at the cell surfaces [33]. CHO WT cells with negatively charged csHS could favor this substrate compared to cRGD surfaces, targeting primarily β_3 -integrins. Characterization of CHO KO cells demonstrated a fully effective suppression of HS biosynthesis but meanwhile up-regulated chondroitin sulfate (CS) expression to a level 3-4 times higher than in CHO WT [22]. It thus appears that csCS is less potent to induce charge-mediated cellular adhesion but it does not explain, why they adhered similar on cRGD substrate as on PLL substrates [32]. Integrin quantification further showed that in both cell types β_3 -integrins were barely detectable and mature β_1 -integrins partly downregulated in CHO KO cells. This should have led to reduced cellular adhesion on cRGD platforms as demonstrated earlier with C2C12 cells [20] but was not the case in this study. This could be due to the dominant β_1 -integrins expression in CHO cells or the influence of for example β_5 -integrins [34].

Further investigations are needed to better understand CHO cell binding to cRGD substrates and if other integrins were up-regulated for compensation.

Interestingly, CHO KO cells did not respond negatively to iHS compared to CHO WT cells but rather increased cellular adhesion. This means that the negative effect of iHS on CHO WT cells was due to csHS but not due to csCS, probably due to lower degree of sulfation and thus lower negative charge [16]. Studies with exogenous CS confirmed that CS was not negatively influencing cell adhesion [28]. sSurfen did not change morphology of CHO KO cells on cRGD platforms but increased cell adhesion. Since Surfen also binds to CS [16], integrins might be more available at the surface due to cross-linked csCS as explained above. However, it is difficult to explain, why CHO WT cells react rather *via* increased area but CHO KO cells by increased adhesion. Especially on iHS platforms, CHO KO cells spread much better upon sSurfen treatment, probably also due to crosslinking between csCS and csHS, and develop protrusions. Protrusions are closely related to cell migration [35], which opens a door for future studies. We conclude that csHS is involved in integrin-mediated adhesion and spreading and that iHS and csHS negatively interact with each other, which can be reduced by neutralizing the negative charge of iHS with Surfen treatment. However, changing csHS or csCS structure with sSurfen did not have a strong effect on morphology and adhesion. The probable Surfen-induced cross-linking between csHS or csCS with iHS is interesting and could indicate a role of HS-binding GFs on adhesion *via* crosslinking. Future studies would involve experiments with CHO cells deficient for csHS and csCS to investigate the influence and compensation capacity of csCS. Also, co-presenting HS or CS ligands and cRGD ligands on the surface together with iHS could reveal the interplay between adhesion mediating csHS, csCS, integrins and iHS [27].

We further found that CHO KO cells were less responsive to sBMP2 and aBMP2 at low concentrations, indicating a positive role of csHS on BMP2 signaling. High BMP2 concentrations in contrary did not reveal differences between both cell types. In a comparable study, an EXT1 mutation in chondrocytes led to a reduced HS synthesis, which was compensated by CS [36]. Both cell types responded equally to 1 nM sBMP2, which is probably a relatively high concentration compared to our study. Then, removing csCS by chondroitinase led to a downregulation of sBMP2 mediated SMAD1/5/9 phosphorylation in both cells. It appeared that at high BMP2 concentration, the absence of iHS was not sufficient to reveal its negative effect but removing in addition csCS, eventually demonstrated the positive effect of

cell surface GAGs on BMP2 signaling. However, this is in contradiction to other studies with csHS deficient cells, who identified csHS as a negative mediator for BMP2 signaling [10]–[13], [18]. Fisher et al. found that treatment with heparinase of limb mesenchymal micromass cultures and thus removing csHS decreased the dose necessary for BMP2 induced SMAD1/5/9 phosphorylation whereas overexpression of syndecan-3 had an opposite effect. Huegel et al. also observed increased BMP2 signaling in EXT1 mutants *in vivo* [11]. Gerstner et al. found that EXT1 deficient cells up-regulated BMP4 and BMP6 response at low BMP concentrations [14]. Regarding the effect of Surfen, Huegel et al. showed that treating csHS with Surfen led to an increase in SMAD phosphorylation after 4 h and endogenous BMP2 expression after 8 h in contrary to our findings [11]. Overall, the effect of csHS on BMP2 signaling is complex and may depend on the cell type, the BMP type, the BMP concentration, *in vivo* or *in vitro* experiments, the fixation time, the substrate or the influence of other GAGs at the surface. Further, it makes a difference if csHS is modified *via* gene mutation, heparinase treatment, overexpression, Surfen treatment and if endogenous BMP is involved.

Platforms were characterized with QCM-D which revealed, that cRGD and iHS were co-functionalized on SA_v and aBMP2 (200 nM) adsorbed on iHS. The amount of cRGD with 8 ng/cm² was about 16 times higher than the critical surface density required for C2C12 adhesion to cRGD platforms [20] and was thus expected to be sufficient for cellular adhesion and spreading of CHO cells. The amount of aBMP2 adsorbed to iHS corresponds to approximately 12 ng/cm² [20] and in preliminary experiments we observed that this quantity was sufficient to induce a plateau level of pSMAD1/5/9 in CHO WT and CHO KO cells, comparable to the plateau level induced by 4 nM sBMP2. The concentration of 0.4 nM aBMP2 incubated for 90 min was identified as critical concentration for SMAD1/5/9 phosphorylation between the plateau level and the negative control in CHO WT and CHO KO cells after 75 min. However, the amount of aBMP2 at 0.4 nM adsorbed on iHS was not detectable by QCM-D and thus conclusions about the effect of aBMP2 on SMAD1/5/9 phosphorylation can only be made relatively between different cells on the same platform.

Further, we investigated how Surfen interacted with the biomimetic platform. QCM-D measures the hydrated mass of a biofilm, including the bound molecule and the coupled solvent [37]. The binding of iHS induced a high shift in dissipation relative to the shift in frequency, which indicated a highly hydrated layer. BMP2 binding to iHS decreased the dissipation probably by cross-linking iHS chains and thus resulting into a more rigid film. Interestingly,

Surfen increased the frequency but at the same time reduced the dissipation. Surfen probably interacted with iHS by strongly crosslinking the HS chains and thus dehydrating the layer. The decrease in frequency upon rinsing back to slightly below the initial value of aBMP2 with unchanged dissipation is probably caused by only loosely adsorbed Surfen exchanged with solvent whereas chemically bound Surfen remained. In summary, we have no evidence that aBMP2 is removed from iHS upon Surfen interaction. This is of relevance because due to sSurfen in the media and the fast Surfen-HS binding kinetics, Surfen interaction with biomimetic surfaces during cell experiments was inevitable.

We have shown earlier that β_1 and β_3 -integrins have a positive influence on BMP2 signaling in C2C12 cells [20] and reduced β_1 -integrin expression in CHO KO cells might have an influence on reduced BMP2 signaling. It was further interesting to see that the positive role of iHS on BMP2 signaling [18], [20] gets reduced if csHS is downregulated and indicates an interdependence between both, csHS and iHS.

Conclusion

We investigated the effect of csHS and iHS on cell morphology and BMP2 signaling. The use of cRGD platforms specific for integrin ligands but not offering HS binding sites together with iHS allowed us to reveal the interaction between csHS and iHS. We found that csHS had a negative effect on cell elongation on cRGD platforms and on cell area if platforms presented iHS and cRGD. At low BMP2 concentrations, we further showed that csHS had a positive influence on BMP2 signaling in contradiction to other studies. Future experiments with csHS and csCS deficient CHO cells will aim to study the role of csCS as well as with primary chondrocytes as a more relevant cell type. To better understand the role of integrin-mediated, HS-mediated and charge-mediated adhesion, SA_v platforms may be co-functionalized presenting different combinations of the respective ligands.

Bibliographic references

- [1] S. Sarrazin, W. C. Lamanna, and J. D. Esko, "Heparan Sulfate Proteoglycans," *Cold Spring Harb. Perspect. Biol.*, vol. 3, no. 7, pp. a004952–a004952, Jul. 2011, doi: 10.1101/cshperspect.a004952.

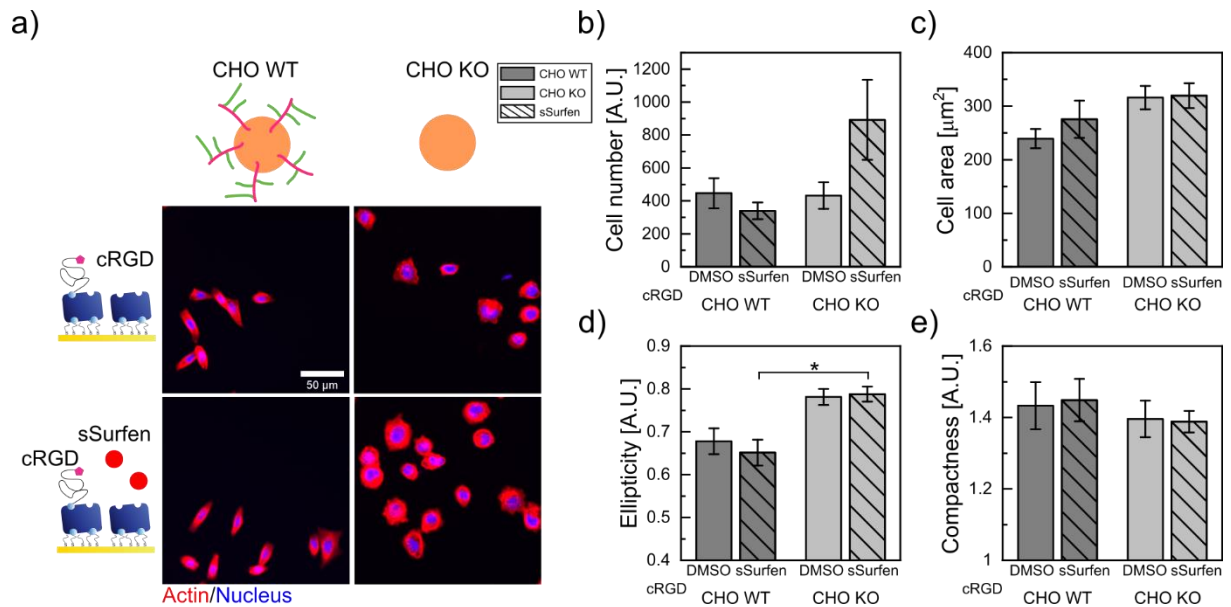
- [2] T. AnnaVal, R. Wild, Y. Créton, R. Sadir, R. R. Vivès, and H. Lortat-Jacob, “Heparan sulfate proteoglycans biosynthesis and post synthesis mechanisms combine few enzymes and few core proteins to generate extensive structural and functional diversity,” *Molecules*, vol. 25, no. 18, 2020, doi: 10.3390/molecules25184215.
- [3] D. Chen et al., “Distinct effects of different matrix proteoglycans on collagen fibrillogenesis and cell-mediated collagen reorganization,” *Sci. Rep.*, vol. 10, no. 1, pp. 1–13, 2020, doi: 10.1038/s41598-020-76107-0.
- [4] R. L. Longley, A. Woods, A. Fleetwood, G. J. Cowling, J. T. Gallagher, and J. R. Couchman, “Control of morphology, cytoskeleton and migration by syndecan-4,” *J. Cell Sci.*, vol. 112, no. 20, pp. 3421–3431, 1999, doi: 10.1242/jcs.112.20.3421.
- [5] J. R. Bishop, M. Schuksz, and J. D. Esko, “Heparan sulphate proteoglycans fine-tune mammalian physiology,” *Nature*, vol. 446, no. 7139, pp. 1030–1037, 2007, doi: 10.1038/nature05817.
- [6] J. L. Dreyfuss, C. V. Regatieri, T. R. Jarrouge, R. P. Cavalheiro, L. O. Sampaio, and H. B. Nader, “Heparan sulfate proteoglycans: Structure, protein interactions and cell signaling,” *An. Acad. Bras. Cienc.*, vol. 81, no. 3, pp. 409–429, 2009, doi: 10.1590/S0001-37652009000300007.
- [7] R. Ruppert, E. Hoffmann, and W. Sebald, “Human bone morphogenetic protein 2 contains a heparin-binding site which modifies its biological activity,” *Eur. J. Biochem.*, vol. 237, no. 1, pp. 295–302, 1996, doi: 10.1111/j.1432-1033.1996.0295n.x.
- [8] D. Obradovic Wagner, C. Sieber, R. Bhushan, J. H. Borgermann, D. Graf, and P. Knaus, “BMPs: From Bone to Body Morphogenetic Proteins,” *Sci. Signal.*, vol. 3, no. 107, pp. mr1–mr1, Feb. 2010, doi: 10.1126/scisignal.3107mr1.
- [9] M. Geiger, R. H. Li, and W. Friess, “Collagen sponges for bone regeneration with rhBMP-2,” *Adv. Drug Deliv. Rev.*, vol. 55, no. 12, pp. 1613–1629, 2003, doi: 10.1016/j.addr.2003.08.010.
- [10] M. Pacifici, “The pathogenic roles of heparan sulfate deficiency in hereditary multiple exostoses,” *Matrix Biol.*, vol. 71–72, pp. 28–39, Oct. 2018, doi: 10.1016/j.matbio.2017.12.011.
- [11] J. Huegel, M. Enomoto-Iwamoto, F. Sgariglia, E. Koyama, and M. Pacifici, “Heparanase stimulates chondrogenesis and is up-regulated in human ectopic cartilage: A mechanism possibly involved in hereditary multiple exostoses,” *Am. J. Pathol.*, vol. 185, no. 6, pp. 1676–1685, 2015, doi: 10.1016/j.ajpath.2015.02.014.
- [12] M. Pacifici, “Hereditary Multiple Exostoses: New Insights into Pathogenesis, Clinical Complications, and Potential Treatments.,” *Curr. Osteoporos. Rep.*, vol. 15, no. 3, pp. 142–152, Jun. 2017, doi: 10.1007/s11914-017-0355-2.
- [13] K. Kawashima et al., “Heparan sulfate deficiency leads to hypertrophic chondrocytes by increasing bone morphogenetic protein signaling,” *Osteoarthr. Cartil.*, vol. 28, no. 11, pp. 1459–1470, Nov. 2020, doi: 10.1016/j.joca.2020.08.003.
- [14] M. Gerstner, A. C. Severmann, S. Chasan, A. Vortkamp, and W. Richter, “Heparan sulfate deficiency in cartilage: Enhanced bmp-sensitivity, proteoglycan production and an anti-apoptotic expression signature after loading,” *Int. J. Mol. Sci.*, vol. 22, no. 7, pp. 1–19, 2021, doi: 10.3390/ijms22073726.
- [15] J. Huegel et al., “Perichondrium phenotype and border function are regulated by Ext1 and heparan sulfate in developing long bones: A mechanism likely deranged in Hereditary Multiple Exostoses,” *Dev. Biol.*, vol. 377, no. 1, pp. 100–112, 2013, doi: 10.1016/j.ydbio.2013.02.008.
- [16] M. Schuksz et al., “Surfen, a small molecule antagonist of heparan sulfate,” *Proc. Natl. Acad. Sci. U. S. A.*, vol. 105, no. 35, pp. 13075–13080, 2008, doi:

- 10.1073/pnas.0805862105.
- [17] D. S. Bramono et al., “Bone marrow-derived heparan sulfate potentiates the osteogenic activity of bone morphogenetic protein-2 (BMP-2),” *Bone*, vol. 50, no. 4, pp. 954–964, 2012, doi: 10.1016/j.bone.2011.12.013.
- [18] M. C. Fisher, Y. Li, M. R. Seghatoleslami, C. N. Dealy, and R. A. Kosher, “Heparan sulfate proteoglycans including syndecan-3 modulate BMP activity during limb cartilage differentiation,” *Matrix Biol.*, vol. 25, no. 1, pp. 27–39, Jan. 2006, doi: 10.1016/j.matbio.2005.07.008.
- [19] E. Migliorini et al., “Enhanced biological activity of BMP-2 bound to surface-grafted heparan sulfate,” *Adv. Biosyst.*, vol. 1, no. 4, p. 1600041, 2017, doi: 10.1002/adbi.201600041.
- [20] J. Sefkow-Werner et al., “Heparan sulfate co-immobilized with cRGD ligands and BMP2 on biomimetic platforms promotes BMP2-mediated osteogenic differentiation,” *Acta Biomater.*, vol. 114, pp. 90–103, Sep. 2020, doi: 10.1016/j.actbio.2020.07.015.
- [21] J. H. Tjio and T. T. Puck, “GENETICS OF SOMATIC MAMMALIAN CELLS,” *J. Exp. Med.*, vol. 108, no. 2, pp. 259–268, Aug. 1958, doi: 10.1084/jem.108.2.259.
- [22] K. Lidholt et al., “A single mutation affects both N-acetylglucosaminyltransferase and glucuronosyltransferase activities in a Chinese hamster ovary cell mutant defective in heparan sulfate biosynthesis,” *Proc. Natl. Acad. Sci. U. S. A.*, vol. 89, no. 6, pp. 2267–2271, 1992, doi: 10.1073/pnas.89.6.2267.
- [23] R. G. LeBaron, J. D. Esko, A. Woods, S. Johansson, and M. Hook, “Adhesion of glycosaminoglycan-deficient Chinese hamster ovary cell mutants to fibronectin substrata,” *J. Cell Biol.*, vol. 106, no. 3, pp. 945–952, 1988, doi: 10.1083/jcb.106.3.945.
- [24] Y. Mahalingam, J. T. Gallagher, and J. R. Couchman, “Cellular Adhesion Responses to the Heparin-binding (HepII) Domain of Fibronectin Require Heparan Sulfate with Specific Properties,” *J. Biol. Chem.*, vol. 282, no. 5, pp. 3221–3230, Feb. 2007, doi: 10.1074/jbc.M604938200.
- [25] R. P. Cavalheiro et al., “Coupling of vinculin to F-actin demands Syndecan-4 proteoglycan,” *Matrix Biol.*, vol. 63, pp. 23–37, 2017, doi: 10.1016/j.matbio.2016.12.006.
- [26] J. J. Moon, M. Matsumoto, S. Patel, L. Lee, J. L. Guan, and S. Li, “Role of cell surface heparan sulfate proteoglycans in endothelial cell migration and mechanotransduction,” *J. Cell. Physiol.*, vol. 203, no. 1, pp. 166–176, 2005, doi: 10.1002/jcp.20220.
- [27] V. Gribova et al., “Control of the Proliferation/Differentiation Balance in Skeletal Myoblasts by Integrin and Syndecan Targeting Peptides,” *ACS Biomater. Sci. Eng.*, vol. 2, no. 3, pp. 415–425, 2016, doi: 10.1021/acsbiomaterials.5b00557.
- [28] K. Lundmark, P. K. Tran, M. G. Kinsella, A. W. Clowes, T. N. Wight, and U. Hedin, “Perlecan inhibits smooth muscle cell adhesion to fibronectin: Role of heparan sulfate,” *J. Cell. Physiol.*, vol. 188, no. 1, pp. 67–74, Jul. 2001, doi: 10.1002/jcp.1094.
- [29] J. M. Whitelock, L. D. Graham, J. Melrose, A. D. Murdoch, R. V. Iozzo, and P. Anne Underwood, “Human perlecan immunopurified from different endothelial cell sources has different adhesive properties for vascular cells,” *Matrix Biol.*, vol. 18, no. 2, pp. 163–178, Apr. 1999, doi: 10.1016/S0945-053X(99)00014-1.
- [30] M. S. Lord, C. Y. Chuang, J. Melrose, M. J. Davies, R. V. Iozzo, and J. M. Whitelock, “The role of vascular-derived perlecan in modulating cell adhesion, proliferation and growth factor signaling,” *Matrix Biol.*, vol. 35, pp. 112–122, 2014, doi: 10.1016/j.matbio.2014.01.016.
- [31] T. Cruzier, L. Fourel, T. Boudou, C. Albigès-Rizo, and C. Picart, “Presentation of BMP-2 from a soft biopolymeric film unveils its activity on cell adhesion and migration,” *Adv. Mater.*, vol. 23, no. 12, pp. 111–118, 2011, doi: 10.1002/adma.201004637.

- [32] A. Kempf et al., “Control of Cell Shape, Neurite Outgrowth, and Migration by a Nogo-A/HSPG Interaction,” *Dev. Cell*, vol. 43, no. 1, pp. 24–34.e5, 2017, doi: 10.1016/j.devcel.2017.08.014.
- [33] D. Mazia, G. Schatten, and W. Sale, “Adhesion of cells to surfaces coated with polylysine. Applications to electron microscopy,” *J. Cell Biol.*, vol. 66, no. 1, pp. 198–200, Jul. 1975, doi: 10.1083/jcb.66.1.198.
- [34] A. Singh, H. F. Kildegaard, and M. R. Andersen, “An Online Compendium of CHO RNA-Seq Data Allows Identification of CHO Cell Line-Specific Transcriptomic Signatures,” *Biotechnol. J.*, vol. 13, no. 10, pp. 1–11, 2018, doi: 10.1002/biot.201800070.
- [35] P. A. Gagliardi et al., “Real-time monitoring of cell protrusion dynamics by impedance responses,” *Sci. Rep.*, vol. 5, pp. 1–12, 2015, doi: 10.1038/srep10206.
- [36] V. Bachvarova, T. Dierker, J. Esko, D. Hoffmann, L. Kjellen, and A. Vortkamp, “Chondrocytes respond to an altered heparan sulfate composition with distinct changes of heparan sulfate structure and increased levels of chondroitin sulfate,” *Matrix Biol.*, vol. 93, pp. 43–59, Nov. 2020, doi: 10.1016/j.matbio.2020.03.006.
- [37] I. Reviakine, D. Johannsmann, and R. P. Richter, “Hearing What You Cannot See and Visualizing What You Hear,” *Anal. Chem.*, vol. 83, pp. 8838–8848, 2011.

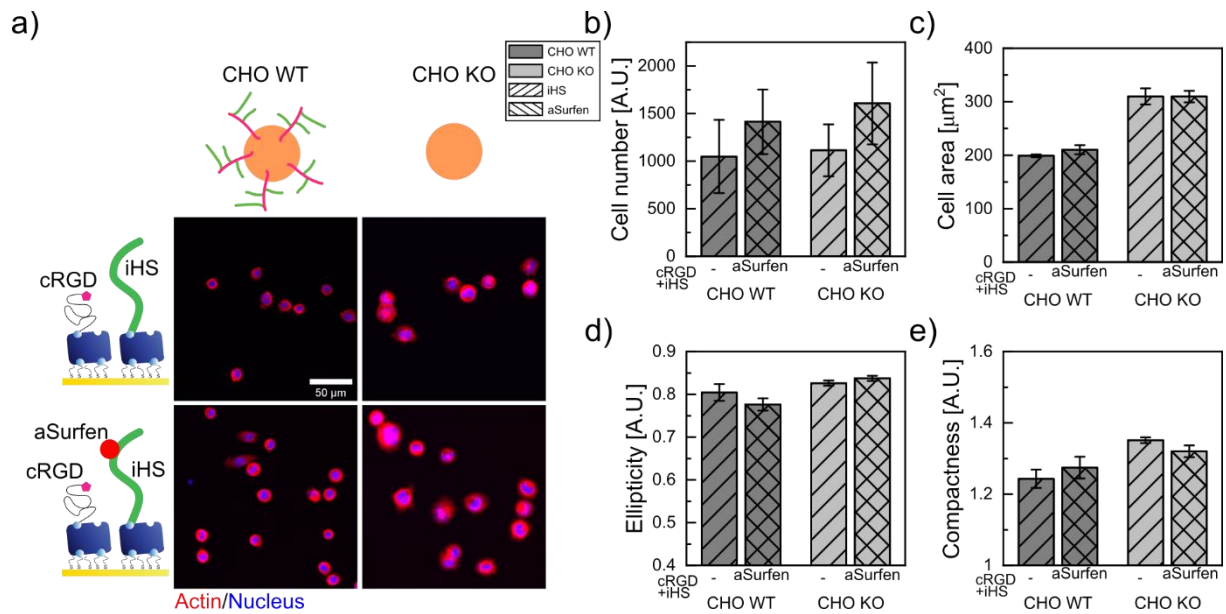
V.D Supplementary information

Supplementary figure 1



SI Fig 1: sSurfen did not have the same effect on cell morphology as the EXT1 gene mutation. a) Representative images of sSurfen-treated (7.5 μM) CHO WT and CHO KO cells plated on cRGD platforms and fixed after 75 min. b) Absolute cell number quantification after rinsing 3 times with PBS and based on 20 20x images with an area of 0.44 cm^2 per image. c) Cell area quantification. d) Ellipticity quantification e) Compactness quantification. SB = 50 μm , Values in graphs are mean \pm SEM of $n \geq 4$ experiments with 2 independent replicates per experiment. Significance was tested with non-parametric Mann-Whitney test and $p < 0.05$ was considered significant (*).

Supplementary figure 2



SI Fig 2: aSurfen did not alter iHS properties besides marginal improvement of cellular adhesion. a) Representative images of CHO WT and CHO KO cells plated on cRGD + iHS platforms and adsorbed Surfen (aSurfen incubated for 90 min at 7.5 μ M). Cells were not treated with DMSO and were fixed after 75 min. b) Absolute cell number quantification after rinsing 3 times with PBS and based on 20 20x images with an area of 0.44 cm² per image. c) Cell area quantification. d) Ellipticity quantification e) Compactness quantification. SB = 50 μ m, Value in graphs are mean \pm SEM of n = 3 experiments with 2 independent replicates per experiment. Significance was tested with non-parametric Mann-Whitney test and p < 0.05 was considered significant (*).

Chapter VI: Conclusion and outlook

The presented work comprises results divided into three global projects: The automated fabrication of biomimetic SA_v platforms, the *in situ* characterization of the number of molecules on surfaces and in volumes as well as cellular studies on the role of exogenous iHS, csHS and integrins on BMP2 signaling and adhesion. In summary, we provided an automated and well-characterized system to reveal cell mechanisms related to HS and BMP2 in a biomimetic way. This high content approach can serve in the future to reveal the role of different GAGs and peptides on GF signaling in a precisely controlled way.

VI.A Automated fabrication of biomimetic streptavidin platforms

We developed an automated protocol to fabricate biomimetic SA_v platforms inside 96-well plates upon user demand using a liquid handling robot.

For that, we adopted and calibrated PLL-g-PEGbiotin50% as a linker between SA_v and glass, the most common substrate for cellular studies. This eliminated the expensive and time-consuming preparation of gold-sputtered surfaces and came along with enhanced imaging properties. However, by attaching gold-sputtered surfaces onto bottom-less 96-well plates, these well-studied substrates were adapted to fit the automated fabrication protocol. The homogeneously functionalized platforms provided a high degree in parallelization since up to three 96-well plates could be fabricated in parallel and user involvement decreased dramatically. In addition, each well of the plate could present a unique condition based on user input and 24 different dissolved molecules. The flexibility of this approach as well as its high-content potential combined with automated image acquisition and analysis make it a great candidate to study systematically the effect of GAGs and peptides on GF signaling in different cell types.

Nevertheless, this technique offers potential for further development. The number of different solutions could easily be increased and is only limited by the physical space available in the workstation as well as the capacity of the user to prepare them. Currently, biomimetic platforms are fabricated and immediately used for cellular studies. It is of interest to decouple those two steps with the objective to increase the number of simultaneously fabricated plates and to store them afterwards. This would further reduce the involvement of the user but in return demands for testing the stability of the platforms upon storage. Further, platform fabrication inside 384-well or 6-well plates for a higher degree of miniaturization and parallelization or for

larger surface area, respectively, is an interesting objective. This would come along with technical adaptations in the liquid handling routine but more importantly with characterization of the fabrication homogeneity due to altered fluid dynamics. In addition, bottomless 96-well plates open doors for various more sophisticated platform designs while maintaining the advantages of automated fabrication. Micro-patterned gold substrates could present specific topographies of interest so that biomimetic platforms are only presented *via* those features (Oberhansl *et al.*, 2014; Schaufler *et al.*, 2016; Fitzpatrick *et al.*, 2017). Indeed, the possible combinations of different topographies with different conditions of the biomimetic platforms and different cell types are infinite. Even the combination of curvatures, adhesion ligands and GAGs could add to this study (Pieuchot *et al.*, 2018). To further streamline the entire experimental workflow, the liquid handling routine could be modified to enable the automated seeding of cells under sterile condition as well as executing the classical immunostaining protocol. Both processes are based on either a variety of different solutions to handle or repetitive incubation and rinsing steps very similar to the fabrication routine of biomimetic SAV platforms. Further downstream following after the image analysis, automated data processing and representation with developed scripts could complete the automated experimental pipeline, in line with the predictions of Vasilevich *et al.* (Vasilevich and de Boer, 2018). In a more broader perspective, the automated fabrication of other biomimetic surfaces with a similar incubation and rinsing routine of a variety of different compounds could profit from this development (Colak, Di Cio and Gautrot, 2018; Pang *et al.*, 2021).

VI.B *In situ* characterization of the number of molecules volumes

For the first time, we applied pbICS to characterize 2D biomimetic surfaces for molecular surface density *in situ via* the example of SAVAlexa monolayers. Meanwhile, we increased the accuracy of this method.

With this technique, we solved three major problems. First, *in situ* characterization of 2D biomimetic surfaces inside 96-well plates was either not quantitative or not adapted for biomimetic SAV platforms. In addition, geometrical and physical constraints of 96-well plates restrict compatibility with SE, SPR or OWLS. Quantitative pbICS, however, relies on confocal images acquired inside 96-well plates and thus overcame these limitations. Secondly, classic ICS and FCS were biased in the case of heterogeneously labelled molecules since they

contribute to fluorescence fluctuations and in consequence, the calculated number of molecules was underestimating the real number of molecules. Applying a photobleaching routine, we deduced mean and standard deviation of the distribution of fluorophores to eliminate this bias and rendering ICS fully self-calibrated. Lastly, we demonstrated that *ex situ* measurements with SE and QCM-D on auxiliary substrates were comparable with *in situ* pbICS measurements. This validates the *ex situ* techniques used for efficient platform design and precise dynamic characterization. Nonetheless, only with pbICS we were able to quantify the adsorption of bAtto with less than 1 ng/cm², not detectable with our experiments with SE or QCM-D.

This set of methods thus permits the quantification of labelled molecules on surfaces and in solutions with commonly available laboratory equipment and expertise in image analysis. However, molecules need to be labelled, which might alter binding kinetics or affinity to other molecules and non-labelled molecules do not contribute to the measurement. We observed further that the technique was not applicable on gold-sputtered surfaces due to optical interference and in addition demanded for homogenous samples without optical artefacts, aggregates or defects. Whereas the image acquisition combined with the photobleaching routine can be adapted by other research facilities, the analysis tools to calculate distribution of fluorophores and then the number of molecules is not available to the scientific community.

pbICS and pbFCS can be further developed and transferred to different applications. Simplification of the analysis software to facilitate a user-friendly toolbox would help to propagate these methods to research facilities not specialized on FFS methods. This involves the development of an at least semi-automated way to set the assumptions needed for identifying the mean and the standard deviation of the fluorophore distribution. Regarding biomimetic SA_v platforms, a quantification of labelled PLL-g-PEGbiotin50% would allow to compare this base layer formation between *in situ* and *ex situ* surfaces as well as to values found in literature (Morgenthaler *et al.*, 2006). Consequently, quantifying labelled aBMP2 adsorbed to iHS is of great interest since the low surface concentrations identified as critical for aBMP2 mediated SMAD1/5/9 phosphorylation in CHO were not possible to detect with SE or QCM-D. This information however is key to allow absolute conclusions on the influence of aBMP2 dose. The technique could further be of interest for other groups working with 2D biomimetic surfaces and aim at absolute surface characterization (Migliorini *et al.*, 2016; Monteiro A., Kollmetz and Malmström, 2018). There is also an interest in absolute protein quantification in cells. A recent study quantified molecular brightness using FCS and photobleaching in cells to

then deduce in a second step the molecular number in confocal images (Zhang *et al.*, 2021). Our more simple and self-calibrated approach could be applied in this context and in addition respond to proteins forming homo-oligomers.

VI.C The role of iHS and csHS on BMP2 signaling and adhesion

With biomimetic SAV platforms, we co-presented cRGD in different surface concentrations with iHS and aBMP2 or with iBMP2 to study the cross-talk between integrins, HS and BMP2 with respect to C2C12 adhesion and BMP2 signaling. Afterwards, we started to distinguish the role of csHS and iHS *via* CHO WT cells and those deficient for csHS.

We found that β_3 -integrins with increasing surface concentrations up-regulated SMAD1/5/9 phosphorylation and that iBMP2 enhanced cRGD-mediated cellular adhesion at critical cRGD surface concentrations. We conclude that the cross-talk is bi-directional and depends on the absolute adhesion ligand availability. Whereas, sBMP2 and iBMP2 mediated-SMAD1/5/9 phosphorylation decreased with decreasing cRGD surface concentrations, aBMP2 adsorbed on iHS maintained the same level of pSMAD1/5/9 independently of cRGD surface concentration. This suggests that long iHS chains provided sufficient flexibility to facilitate proximity of BMP receptors and scarce integrins. With siRNA experiments, we further showed that both, β_1 - and β_3 -integrins, were involved in BMP2 signaling and osteogenic differentiation even though only β_3 -integrins mediated cellular adhesion. Lastly, while aBMP2 and iBMP2 had a similar influence on early BMP2 signaling, iHS enhanced osteogenic differentiation compared to iBMP2. This we explained with sustained BMP2 signaling by aBMP2 adsorbed on iHS as quantified with time-resolved SMAD1/5/9 signaling. Overall, iHS and β_1 - and β_3 -integrins were positive mediators of BMP2 signaling and osteogenic differentiation.

In first experiments, we found that csHS had a negative effect on CHO cell elongation on cRGD platforms but iHS only reduced elongation of cells with csHS, indicating that iHS and csHS negatively influence each other regarding cellular elongation. Interestingly, upregulated csCS in csHS deficient cells did not have this negative interaction, making this an HS-specific property. Surfen treatment interacted with csHS, csCS and iHS and eventually led to increased cellular area and adhesion in both cell types probably due to crosslinking cells to the platform *via* HS. This suggests that GFs binding to HS might enhance adhesion and spreading due to crosslinking similar to Surfen. Whereas sBMP2 and aBMP2 at high concentrations induced

comparable SMAD1/5/9 phosphorylation, at low doses, CHO WT cell were more responsive compared to CHO KO cells or cells treated with sSurfen. The same effect was observed for aBMP2 at low concentrations. Functional csHS had thus a positive influence on BMP2 signaling at low concentrations, which is contradictory to literature. The effect of csHS appeared to be dose dependent and probably cell type dependent. Surprisingly, aBMP2 was only able to induce SMAD1/5/9 phosphorylation as strong as sBMP2 if csHS was present and functional. The previously concluded positive role of iHS hence depends to a certain degree on csHS. In summary, csHS and iHS interacted with each other with respect to cell polarization, adhesion and BMP2 signaling.

HS has demonstrated to be an important mediator of cell fate, which in consequence opens new questions to better understand the underlying mechanisms. It is known that the sulfation pattern of HS is species- and cell type-dependent and influences HS function (Annaval *et al.*, 2020). Identifying the influence of specific sulfations on aBMP2 activity aims at revealing the biochemical function of HS. Indeed, current research at our group addresses this topic by systematically testing a library of HS fractions immobilized on automatically fabricated SAV platforms. Meanwhile, distinguishing the role of immobilized CS from iHS is a complementary approach, motivated by studies suggesting that these exogenous GAGs have a different influence on cell adhesion (Whitelock *et al.*, 1999; Lundmark *et al.*, 2001). On the other hand, it would be interesting to find out how a chemically completely different polymer chain with similar length as HS regulated BMP2 signaling. This would give isolated hints on the influence of lateral mobility of polymer chains. For that, a way needs to be identified how to bind BMP2 to this polymer without altering its functionality. Following-up on the cross-talk between integrins and BMP2 signaling, the interaction between HS-mediated adhesion and integrin-mediated adhesion can be subject to future studies. Biomimetic SAV platforms presenting iHS, cRGD and the HepII domain in parallel and in combination with CHO WT and CHO KO cells are an interesting experimental set-up and can be extended to also include other GAGs and GFs (LeBaron *et al.*, 1988). With respect to the results in CHO cells, a variant deficient for csHS and csCS as well as one only missing a specific HS fraction could help to further conclude on the role of csHS. Nevertheless, CHO cells are endothelial cells whereas the EXT1 mutation *in vivo* is responsible for upregulated BMP2 signaling and ectopic bone formation occurs in chondrocytes (Huegel *et al.*, 2013; Pacifici, 2018). In consequence, we plan with the group of Prof. Andrea Vortkamp to conduct future experiments with primary chondrocytes deficient for csHS, which in preliminary experiments showed to adhere on cRGD platforms. Lastly, we

consider profiting from the positive effect of endogenous iHS on BMP2 signaling with application in bone repair. Indeed, the advantage of dose reduction of BMP2 due to the effect of iHS make this system a great candidate for surface coatings of scaffolds. Nevertheless, the strength of the biomimetic SA_v platform lies in its flexibility, control and high-content ability and thus is an ideal candidate to for studying cellular mechanisms.

Overall, future studies will most likely always be a combination of automated liquid handling, *in situ* and *ex situ* characterization and sophisticated biomimetic platform design to study cell response to elements from the ECM.

VI.D Conclusion (French summary)

Le travail présenté comprend des résultats divisés en trois projets globaux : La fabrication automatisée de plateformes SAV biomimétiques, la caractérisation *in situ* du nombre de molécules sur les surfaces et dans les volumes ainsi que des études cellulaires sur le rôle des iHS, csHS et intégrines exogènes sur la signalisation et l'adhésion au BMP2. En résumé, nous avons fourni un système automatisé et bien caractérisé pour révéler les mécanismes cellulaires liés au HS et au BMP2 d'une manière biomimétique. Cette approche à haut contenu peut servir à l'avenir à révéler le rôle de différents GAGs et peptides sur la signalisation du GF d'une manière contrôlée avec précision.

Nous avons développé un protocole automatisé pour fabriquer des plateformes SAV biomimétiques à l'intérieur de plaques de 96 puits à la demande de l'utilisateur en utilisant un robot de manipulation de liquides. Les plates-formes fonctionnalisées de manière homogène ont permis un haut degré de parallélisation puisque jusqu'à trois plaques de 96 puits ont pu être fabriquées en parallèle et que l'implication de l'utilisateur a considérablement diminué. En outre, chaque puits de la plaque pouvait présenter une condition unique basée sur l'entrée de l'utilisateur et 24 molécules dissoutes différentes. La flexibilité de cette approche ainsi que son potentiel de contenu élevé combiné à l'acquisition et à l'analyse automatisées des images en font un excellent candidat pour étudier systématiquement l'effet des GAG et des peptides sur la signalisation du GF dans différents types de cellules.

Pour la première fois, nous avons appliqué pbICS pour caractériser les surfaces biomimétiques 2D pour la densité de surface moléculaire *in situ via* l'exemple des monocouches SAVAlexa. Parallèlement, nous avons amélioré la précision de cette méthode. Grâce à cette technique, nous avons résolu trois problèmes majeurs. Tout d'abord, la caractérisation *in situ* des surfaces biomimétiques 2D à l'intérieur de plaques à 96 puits n'était pas quantitative ou n'était pas adaptée aux plateformes SAV biomimétiques. De plus, les contraintes géométriques et physiques des plaques 96 puits limitent la compatibilité avec les techniques SE, SPR ou OWLS. La pbICS quantitative, en revanche, repose sur des images confocales acquises à l'intérieur de plaques 96 puits et a donc permis de surmonter ces limitations. Deuxièmement, les ICS et FCS classiques étaient biaisés dans le cas de molécules marquées de manière hétérogène car elles contribuent aux fluctuations de fluorescence et, par conséquent, le nombre de molécules calculé sous-estimait le nombre réel de molécules. En appliquant une routine de

photoblanchiment, nous avons déduit la moyenne et l'écart-type de la distribution des fluorophores pour éliminer ce biais et rendre le ICS entièrement auto-calibré. Enfin, nous avons démontré que les mesures *ex situ* avec SE et QCM-D sur des substrats auxiliaires étaient comparables aux mesures pbICS *in situ*. Ceci valide les techniques *ex situ* utilisées pour une conception efficace de la plateforme et une caractérisation dynamique précise. Néanmoins, seulement avec pbICS nous avons pu quantifier l'adsorption de bAtto avec moins de 1 ng/cm², non détectable avec nos expériences avec SE ou QCM-D.

Avec les plateformes SAV biomimétiques, nous avons coprésenté le cRGD à différentes concentrations de surface avec l'iHS et l'aBMP2 ou avec l'iBMP2 pour étudier la diaphonie entre les intégrines, l'HS et le BMP2 en ce qui concerne l'adhésion des C2C12 et la signalisation du BMP2. Ensuite, nous avons commencé à distinguer le rôle des csHS et iHS via les cellules CHO WT et celles déficientes en csHS.

Nous avons constaté que les β_3 -intégrines avec des concentrations de surface croissantes régulent la phosphorylation de SMAD1/5/9 et que l'iBMP2 augmente l'adhésion cellulaire médiée par le cRGD à des concentrations de surface critiques du cRGD. Nous concluons que la diaphonie est bidirectionnelle et dépend de la disponibilité absolue du ligand d'adhésion. Alors que la phosphorylation de sBMP2 et iBMP2 médiée par SMAD1/5/9 diminue avec des concentrations de surface de cRGD décroissantes, aBMP2 adsorbé sur iHS a maintenu le même niveau de pSMAD1/5/9 indépendamment de la concentration de surface de cRGD. Ceci suggère que les longues chaînes iHS ont fourni une flexibilité suffisante pour faciliter la proximité des récepteurs BMP et des intégrines rares. Grâce à des expériences de siRNA, nous avons également montré que les β_1 - et β_3 -intégrines étaient toutes deux impliquées dans la signalisation de BMP2 et la différenciation ostéogénique, même si seules les β_3 -intégrines assurent la médiation de l'adhésion cellulaire. Enfin, alors que l'aBMP2 et l'iBMP2 avaient une influence similaire sur la signalisation précoce de la BMP2, l'iHS a augmenté la différenciation ostéogénique par rapport à l'iBMP2. Ceci s'explique par la signalisation BMP2 soutenue par l'aBMP2 adsorbée sur l'iHS, quantifiée par la signalisation SMAD1/5/9 résolue dans le temps. Globalement, l'iHS et les β_1 - et β_3 -intégrines sont des médiateurs positifs de la signalisation de BMP2 et de la différenciation ostéogénique.

Dans les premières expériences, nous avons constaté que le csHS avait un effet négatif sur l'élongation des cellules CHO sur les plateformes cRGD, mais que le iHS ne réduisait que l'élongation des cellules avec le csHS, ce qui indique que le iHS et le csHS s'influencent

négalement l'un l'autre concernant l'élongation cellulaire. Il est intéressant de noter que le csCS régulé à la hausse dans les cellules déficientes en csHS ne présentait pas cette interaction négative, ce qui en fait une propriété spécifique au csHS. Le traitement par Surfen a interagi avec la csHS, la csCS et l'iHS et a finalement conduit à une augmentation de la surface cellulaire et de l'adhésion dans les deux types de cellules, probablement en raison de la réticulation des cellules à la plate-forme via la HS. Cela suggère que la liaison des GFs à la HS pourrait améliorer l'adhésion et la propagation en raison d'une réticulation similaire à celle du Surfen. Alors que le sBMP2 et l'aBMP2 à des concentrations élevées ont induit une phosphorylation SMAD1/5/9 comparable, à faibles doses, les cellules CHO WT étaient plus réactives que les cellules CHO KO ou les cellules traitées avec le sSurfen. Le même effet a été observé pour l'aBMP2 à de faibles concentrations. La csHS fonctionnelle a donc eu une influence positive sur la signalisation de la BMP2 à de faibles concentrations, ce qui est en contradiction avec la littérature. L'effet de la csHS semble dépendre de la dose et probablement du type de cellule. De manière surprenante, l'aBMP2 n'était capable d'induire une phosphorylation de SMAD1/5/9 aussi forte que la sBMP2 que si la csHS était présente et fonctionnelle. Le rôle positif précédemment conclu de l'iHS dépend donc dans une certaine mesure du csHS. En résumé, csHS et iHS interagissent l'un avec l'autre en ce qui concerne la polarisation cellulaire, l'adhésion et la signalisation de BMP2.

Bibliographic references

- Almodóvar, J. *et al.* (2014) ‘Spatial patterning of BMP-2 and BMP-7 on biopolymeric films and the guidance of muscle cell fate’, *Biomaterials*, 35(13), pp. 3975–3985. doi: 10.1016/j.biomaterials.2014.01.012.
- Alom Ruiz, S. and Chen, C. S. (2007) ‘Microcontact printing: A tool to pattern’, *Soft Matter*, 3(2), pp. 168–177. doi: 10.1039/B613349E.
- Anjum, F. *et al.* (2016) ‘Enzyme responsive GAG-based natural-synthetic hybrid hydrogel for tunable growth factor delivery and stem cell differentiation’, *Biomaterials*, 87, pp. 104–117. doi: 10.1016/j.biomaterials.2016.01.050.
- Annaval, T. *et al.* (2020) ‘Heparan sulfate proteoglycans biosynthesis and post synthesis mechanisms combine few enzymes and few core proteins to generate extensive structural and functional diversity’, *Molecules*, 25(18). doi: 10.3390/molecules25184215.
- Anouz, R. *et al.* (2018) ‘Novel Surface Coatings Using Oxidized Glycosaminoglycans as Delivery Systems of Bone Morphogenetic Protein 2 (BMP-2) for Bone Regeneration’, *Macromolecular Bioscience*, 18(11), pp. 1–10. doi: 10.1002/mabi.201800283.
- Arnold, M. *et al.* (2004) ‘Activation of integrin function by nanopatterned adhesive interfaces’, *ChemPhysChem*, 5(3), pp. 383–388. doi: 10.1002/cphc.200301014.
- Ashikari-Hada, S. *et al.* (2004) ‘Characterization of Growth Factor-binding Structures in Heparin/Heparan Sulfate Using an Octasaccharide Library’, *Journal of Biological Chemistry*. © 2004 ASBMB. Currently published by Elsevier Inc; originally published by American Society for Biochemistry and Molecular Biology., 279(13), pp. 12346–12354. doi: 10.1074/jbc.M313523200.
- Azria, D. *et al.* (2018) ‘Elaboration of materials with functionality gradients by assembly of chitosan-collagen microspheres produced by microfluidics’, *Journal of Renewable Materials*, 6(3), pp. 314–324. doi: 10.7569/JRM.2017.634186.
- Bachvarova, V. *et al.* (2020) ‘Chondrocytes respond to an altered heparan sulfate composition with distinct changes of heparan sulfate structure and increased levels of chondroitin sulfate’, *Matrix Biology*. Elsevier B.V., 93, pp. 43–59. doi: 10.1016/j.matbio.2020.03.006.
- Bain, C. D. *et al.* (1989) ‘Formation of Monolayer Films by the Spontaneous Assembly of Organic Thiols from Solution onto Gold’, *Journal of the American Chemical Society*, 111(1), pp. 321–335. doi: 10.1021/ja00183a049.
- Ballester-Beltrán, J. *et al.* (2012) ‘Dorsal and Ventral Stimuli in Cell–Material Interactions: Effect on Cell Morphology’, *Biointerphases*, 7(1), p. 39. doi: 10.1007/s13758-012-0039-5.
- Balzarotti, F. *et al.* (2017) ‘Nanometer resolution imaging and tracking of fluorescent molecules with minimal photon fluxes’, *Science*, 355(6325), pp. 606–612. doi: 10.1126/science.aak9913.
- Barczyk, M., Carracedo, S. and Gullberg, D. (2010) ‘Integrins’, *Cell and Tissue Research*. Germany, 339(1), pp. 269–280. doi: 10.1007/s00441-009-0834-6.
- Barth, A. and Zscherp, C. (2002) ‘What vibrations tell us about proteins’, *Quarterly Reviews of Biophysics*, 35(4), pp. 369–430. doi: 10.1017/S0033583502003815.
- Billings, P. C. *et al.* (2018) ‘Domains with highest heparan sulfate-binding affinity reside at opposite ends in BMP2/4 versus BMP5/6/7: Implications for function’, *JOURNAL OF BIOLOGICAL CHEMISTRY*. 9650 ROCKVILLE PIKE, BETHESDA, MD 20814-3996 USA: AMER SOC BIOCHEMISTRY MOLECULAR BIOLOGY INC, 293(37), pp. 14371–14383. doi: 10.1074/jbc.RA118.003191.
- Bishop, J. R., Schuksz, M. and Esko, J. D. (2007) ‘Heparan sulphate proteoglycans fine-tune

- mammalian physiology', *Nature*, 446(7139), pp. 1030–1037. doi: 10.1038/nature05817.
- Bolander, J. *et al.* (2017) 'Healing of a Large Long-Bone Defect through Serum-Free In Vitro Priming of Human Periosteum-Derived Cells', *Stem Cell Reports*. Elsevier Company., 8(3), pp. 758–772. doi: 10.1016/j.stemcr.2017.01.005.
- Boudou, T. *et al.* (2010) 'Multiple Functionalities of Polyelectrolyte Multilayer Films: New Biomedical Applications', *Advanced Materials*, 22(4), pp. 441–467. doi: 10.1002/adma.200901327.
- Bouyer, M. *et al.* (2020) '3D printed scaffold combined to 2D osteoinductive coatings to repair a critical-size mandibular bone defect', *bioRxiv*, p. 2020.12.08.415778. doi: 10.1101/2020.12.08.415778.
- Bramono, D. S. *et al.* (2012) 'Bone marrow-derived heparan sulfate potentiates the osteogenic activity of bone morphogenetic protein-2 (BMP-2)', *Bone*. Elsevier Inc., 50(4), pp. 954–964. doi: 10.1016/j.bone.2011.12.013.
- Bürgi, T. (2015) 'Properties of the gold–sulphur interface: from self-assembled monolayers to clusters', *Nanoscale*. Royal Society of Chemistry, 7(38), pp. 15553–15567. doi: 10.1039/C5NR03497C.
- Cardin, A. D. and Weintraub, H. J. (1989) 'Molecular modeling of protein-glycosaminoglycan interactions.', *Arteriosclerosis: An Official Journal of the American Heart Association, Inc.*, 9(1), pp. 21–32. doi: 10.1161/01.ATV.9.1.21.
- Carragee, E. J., Hurwitz, E. L. and Weiner, B. K. (2011) 'A critical review of recombinant human bone morphogenetic protein-2 trials in spinal surgery: Emerging safety concerns and lessons learned', *Spine Journal*. Elsevier Inc, 11(6), pp. 471–491. doi: 10.1016/j.spinee.2011.04.023.
- Cauchy, A. L. (1836) *Mémoire sur la dispersion de la lumière*. Prague: chez J. G. Calve. doi: 10.3931/e-rara-26157.
- Cavalheiro, R. P. *et al.* (2017) 'Coupling of vinculin to F-actin demands Syndecan-4 proteoglycan', *Matrix Biology*, 63, pp. 23–37. doi: 10.1016/j.matbio.2016.12.006.
- Chaiet, L. and Wolf, F. J. (1964) 'The properties of streptavidin, a biotin-binding protein produced by Streptomycetes', *Archives of Biochemistry and Biophysics*, 106, pp. 1–5. doi: 10.1016/0003-9861(64)90150-X.
- Chen, D. *et al.* (2020) 'Distinct effects of different matrix proteoglycans on collagen fibrillogenesis and cell-mediated collagen reorganization', *Scientific Reports*. Nature Publishing Group UK, 10(1), pp. 1–13. doi: 10.1038/s41598-020-76107-0.
- Chen, D., Zhao, M. and Mundy, G. R. (2004) 'Bone Morphogenetic Proteins', *Growth Factors*. Taylor & Francis, 22(4), pp. 233–241. doi: 10.1080/08977190412331279890.
- Chen, R. *et al.* (2018) 'Tuning the bioactivity of bone morphogenetic protein-2 with surface immobilization strategies', *Acta Biomaterialia*. Acta Materialia Inc., 80, pp. 108–120. doi: 10.1016/j.actbio.2018.09.011.
- Choi, J. *et al.* (2015) 'Biomimetics: forecasting the future of science, engineering, and medicine', *International Journal of Nanomedicine*, p. 5701. doi: 10.2147/IJN.S83642.
- Choi, Y. J. *et al.* (2010) 'The identification of a heparin binding domain peptide from bone morphogenetic protein-4 and its role on osteogenesis', *Biomaterials*. Elsevier Ltd, 31(28), pp. 7226–7238. doi: 10.1016/j.biomaterials.2010.05.022.
- Chopra, P. *et al.* (2021) 'The 3-O-sulfation of heparan sulfate modulates protein binding and lyase degradation', *Proceedings of the National Academy of Sciences of the United States of America*, 118(3), pp. 1–12. doi: 10.1073/PNAS.2012935118.
- Coffman, V. C. and Wu, J.-Q. (2012) 'Counting protein molecules using quantitative fluorescence microscopy', *Trends in Biochemical Sciences*. Elsevier Ltd, 37(11), pp. 499–506. doi: 10.1016/j.tibs.2012.08.002.

- Colak, B., Di Cio, S. and Gautrot, J. E. (2018) 'Biofunctionalized Patterned Polymer Brushes via Thiol-Ene Coupling for the Control of Cell Adhesion and the Formation of Cell Arrays', *Biomacromolecules*, 19(5), pp. 1445–1455. doi: 10.1021/acs.biomac.7b01436.
- Colnot, C. (2009) 'Skeletal Cell Fate Decisions Within Periosteum and Bone Marrow During Bone Regeneration', *Journal of Bone and Mineral Research*, 24(2), pp. 274–282. doi: 10.1359/jbmr.081003.
- Crouzier, T. *et al.* (2009) 'Layer-by-layer films as a biomimetic reservoir for rhBMP-2 delivery: Controlled differentiation of myoblasts to osteoblasts', *Small*, 5(5), pp. 598–608. doi: 10.1002/smll.200800804.
- Crouzier, T. *et al.* (2011) 'Presentation of BMP-2 from a soft biopolymeric film unveils its activity on cell adhesion and migration', *Advanced Materials*, 23(12), pp. 111–118. doi: 10.1002/adma.201004637.
- Czekanska, E. M. *et al.* (2012) 'In search of an osteoblast cell model for in vitro research', *European Cells and Materials*, 24, pp. 1–17. doi: 10.22203/eCM.v024a01.
- Czekanska, E. M. *et al.* (2014) 'A phenotypic comparison of osteoblast cell lines versus human primary osteoblasts for biomaterials testing', *Journal of Biomedical Materials Research Part A*, 102(8), pp. 2636–2643. doi: 10.1002/jbm.a.34937.
- Delon, A. *et al.* (2010) 'Measuring, in solution, multiple-fluorophore labeling by combining fluorescence correlation spectroscopy and photobleaching', *Journal of Physical Chemistry B*, 114(8), pp. 2988–2996. doi: 10.1021/jp910082h.
- Dhavalikar, P. *et al.* (2020) 'Review of Integrin-Targeting Biomaterials in Tissue Engineering', *Advanced Healthcare Materials*, 9(23), pp. 1–26. doi: 10.1002/adhm.202000795.
- Dreyfuss, J. L. *et al.* (2009) 'Heparan sulfate proteoglycans: Structure, protein interactions and cell signaling', *Anais da Academia Brasileira de Ciencias*, 81(3), pp. 409–429. doi: 10.1590/S0001-37652009000300007.
- Dubacheva, G. V. *et al.* (2017) 'Controlling multivalent binding through surface chemistry: Model study on streptavidin', *Journal of the American Chemical Society*, 139(11), pp. 4157–4167. doi: 10.1021/jacs.7b00540.
- Dubiel, E. A., Martin, Y. and Vermette, P. (2011) 'Bridging the Gap Between Physicochemistry and Interpretation Prevalent in Cell–Surface Interactions', *Chemical Reviews*, 111(4), pp. 2900–2936. doi: 10.1021/cr9002598.
- Dundas, C. M., Demonte, D. and Park, S. (2013) 'Streptavidin-biotin technology: improvements and innovations in chemical and biological applications.', *Applied microbiology and biotechnology*. Germany, 97(21), pp. 9343–9353. doi: 10.1007/s00253-013-5232-z.
- Duval, K. *et al.* (2017) 'Modeling Physiological Events in 2D vs. 3D Cell Culture', *Physiology*, 32(4), pp. 266–277. doi: 10.1152/physiol.00036.2016.
- Edlund, U., Dänmark, S. and Albertsson, A. C. (2008) 'A strategy for the covalent functionalization of resorbable polymers with heparin and osteoinductive growth factor', *Biomacromolecules*, 9(3), pp. 901–905. doi: 10.1021/bm701267u.
- Eggert, S. *et al.* (2021) 'An open-source technology platform to increase reproducibility and enable high-throughput production of tailorable gelatin methacryloyl (GelMA) - based hydrogels', *Materials and Design*. The Author, 204, p. 109619. doi: 10.1016/j.matdes.2021.109619.
- Fairhead, M. and Howarth, M. (2015) 'Site-Specific Biotinylation of Purified Proteins Using BirA', in, pp. 171–184. doi: 10.1007/978-1-4939-2272-7_12.
- De Feijter, J. A., Benjamins, J. and Veer, F. A. (1978) 'Ellipsometry as a tool to study the adsorption behavior of synthetic and biopolymers at the air–water interface', *Biopolymers*, 17(7), pp. 1759–1772. doi: 10.1002/bip.1978.360170711.

- Fisher, M. C. *et al.* (2006) 'Heparan sulfate proteoglycans including syndecan-3 modulate BMP activity during limb cartilage differentiation', *Matrix Biology*, 25(1), pp. 27–39. doi: 10.1016/j.matbio.2005.07.008.
- Fitzpatrick, V. *et al.* (2017) 'Signal mingle: Micropatterns of BMP-2 and fibronectin on soft biopolymeric films regulate myoblast shape and SMAD signaling', *Scientific Reports*, 7(1), p. 41479. doi: 10.1038/srep41479.
- Flaim, C. J., Chien, S. and Bhatia, S. N. (2005) 'An extracellular matrix microarray for probing cellular differentiation', *Nature Methods*, 2(2), pp. 119–125. doi: 10.1038/nmeth736.
- Fleischmann, M., Hendra, P. J. and McQuillan, A. J. (1974) 'Raman spectra of pyridine adsorbed at a silver electrode', *Chemical Physics Letters*, 26(2), pp. 163–166. doi: 10.1016/0009-2614(74)85388-1.
- Van der Flier, A. and Sonnenberg, A. (2001) 'Function and interactions of integrins', *Cell and Tissue Research*, 305(3), pp. 285–298. doi: 10.1007/s004410100417.
- Fourrel, L. *et al.* (2016) 'β3 integrin-mediated spreading induced by matrix-bound BMP-2 controls Smad signaling in a stiffness-independent manner', *Journal of Cell Biology*, 212(6), pp. 693–706. doi: 10.1083/jcb.201508018.
- Frantz, C., Stewart, K. M. and Weaver, V. M. (2010) 'The extracellular matrix at a glance', *Journal of Cell Science*, 123(24), pp. 4195–4200. doi: 10.1242/jcs.023820.
- Frith, J. E., Mills, R. J. and Cooper-White, J. J. (2012) 'Lateral spacing of adhesion peptides influences human mesenchymal stem cell behaviour', *Journal of Cell Science*, 125(2), pp. 317–327. doi: 10.1242/jcs.087916.
- García, J. R., Clark, A. Y. and García, A. J. (2016) 'Integrin-specific hydrogels functionalized with VEGF for vascularization and bone regeneration of critical-size bone defects', *Journal of Biomedical Materials Research Part A*, 104(4), pp. 889–900. doi: 10.1002/jbm.a.35626.
- Geiger, M., Li, R. H. and Friess, W. (2003) 'Collagen sponges for bone regeneration with rhBMP-2', *Advanced Drug Delivery Reviews*, 55(12), pp. 1613–1629. doi: 10.1016/j.addr.2003.08.010.
- Gerstner, M. *et al.* (2021) 'Heparan sulfate deficiency in cartilage: Enhanced bmp-sensitivity, proteoglycan production and an anti-apoptotic expression signature after loading', *International Journal of Molecular Sciences*, 22(7), pp. 1–19. doi: 10.3390/ijms22073726.
- Gilde, F. *et al.* (2016) 'Stiffness-dependent cellular internalization of matrix-bound BMP-2 and its relation to Smad and non-Smad signaling', *Acta Biomaterialia*, 46, pp. 55–67. doi: 10.1016/j.actbio.2016.09.014.
- Gribova, V., Auzely-Velty, R. and Picart, C. (2012) 'Polyelectrolyte Multilayer Assemblies on Materials Surfaces: From Cell Adhesion to Tissue Engineering', *Chemistry of Materials*, 24(5), pp. 854–869. doi: 10.1021/cm2032459.
- Groeneveldt, L. C. *et al.* (2020) 'The Bone-Forming Properties of Periosteum-Derived Cells Differ Between Harvest Sites', *Frontiers in Cell and Developmental Biology*, 8(November), pp. 1–17. doi: 10.3389/fcell.2020.554984.
- Grubb, M. L. and Caliri, S. R. (2021) 'Fabrication approaches for high-throughput and biomimetic disease modeling', *Acta Biomaterialia*. Elsevier Ltd, 132(xxxx), pp. 52–82. doi: 10.1016/j.actbio.2021.03.006.
- Hauff, K. *et al.* (2015) 'Matrix-immobilized BMP-2 on microcontact printed fibronectin as an in vitro tool to study BMP-mediated signaling and cell migration', *Frontiers in Bioengineering and Biotechnology*, 3(MAY), pp. 1–13. doi: 10.3389/fbioe.2015.00062.
- Heremans, A. *et al.* (1990) 'The core protein of the matrix-associated heparan sulfate proteoglycan binds to fibronectin', *Journal of Biological Chemistry*, 265(15), pp. 8716–8724. doi: 10.1016/s0021-9258(19)38948-3.

- Hettiaratchi, M. H. *et al.* (2014) ‘Heparin microparticle effects on presentation and bioactivity of bone morphogenetic protein-2’, *Biomaterials*. Elsevier Ltd, 35(25), pp. 7228–7238. doi: 10.1016/j.biomaterials.2014.05.011.
- Hinrichs, K. and Eichhorn, K.-J. (2014) *Ellipsometry of Functional Organic Surfaces and Films*. Edited by K. Hinrichs and K.-J. Eichhorn. Berlin, Heidelberg: Springer Berlin Heidelberg (Springer Series in Surface Sciences). doi: 10.1007/978-3-642-40128-2.
- Hoyos-Nogués, M. *et al.* (2017) ‘Regenerating Bone via Multifunctional Coatings: The Blending of Cell Integration and Bacterial Inhibition Properties on the Surface of Biomaterials’, *ACS Applied Materials & Interfaces*, 9(26), pp. 21618–21630. doi: 10.1021/acsami.7b03127.
- Huang, B., Yuan, Y. and Liu, C. (2020) ‘Biomaterial-guided immobilization and osteoactivity of bone morphogenetic protein-2’, *Applied Materials Today*. Elsevier Ltd, 19, p. 100599. doi: 10.1016/j.apmt.2020.100599.
- Huang, N.-P. *et al.* (2002) ‘Biotin-Derivatized Poly(ε-lysine)-g-poly(ethylene glycol): A Novel Polymeric Interface for Bioaffinity Sensing’, *Langmuir*, 18(1), pp. 220–230. doi: 10.1021/la010913m.
- Huegel, J. *et al.* (2013) ‘Perichondrium phenotype and border function are regulated by Ext1 and heparan sulfate in developing long bones: A mechanism likely deranged in Hereditary Multiple Exostoses’, *Developmental Biology*. Elsevier, 377(1), pp. 100–112. doi: 10.1016/j.ydbio.2013.02.008.
- Huegel, J. *et al.* (2015) ‘Heparanase stimulates chondrogenesis and is up-regulated in human ectopic cartilage: A mechanism possibly involved in hereditary multiple exostoses’, *American Journal of Pathology*, 185(6), pp. 1676–1685. doi: 10.1016/j.ajpath.2015.02.014.
- Humphries, J. D. *et al.* (2019) ‘Signal transduction via integrin adhesion complexes’, *Current Opinion in Cell Biology*. Elsevier Ltd, 56, pp. 14–21. doi: 10.1016/j.ceb.2018.08.004.
- Humphries, J. D., Byron, A. and Humphries, M. J. (2006) ‘Integrin ligands at a glance’, *Journal of Cell Science*, 119(19), pp. 3901–3903. doi: 10.1242/jcs.03098.
- Iozzo, R. V. and Schaefer, L. (2015) ‘Proteoglycan form and function: A comprehensive nomenclature of proteoglycans’, *Matrix Biology*. Elsevier B.V., 42, pp. 11–55. doi: 10.1016/j.matbio.2015.02.003.
- Ivaska, J. and Heino, J. (2011) ‘Cooperation Between Integrins and Growth Factor Receptors in Signaling and Endocytosis’. doi: 10.1146/annurev-cellbio-092910-154017.
- James, A. W. *et al.* (2016) ‘A Review of the Clinical Side Effects of Bone Morphogenetic Protein-2’, *Tissue Engineering Part B: Reviews*, 22(4), pp. 284–297. doi: 10.1089/ten.teb.2015.0357.
- Jérôme, V. *et al.* (2017) ‘Comparison of cell-based versus cell-free mammalian systems for the production of a recombinant human bone morphogenetic growth factor’, *Engineering in Life Sciences*, 17(10), pp. 1097–1107. doi: 10.1002/elsc.201700005.
- Jiao, X. *et al.* (2007) ‘Heparan Sulfate Proteoglycans (HSPGs) Modulate BMP2 Osteogenic Bioactivity in C2C12 Cells’, *Journal of Biological Chemistry*. © 2007 ASBMB. Currently published by Elsevier Inc; originally published by American Society for Biochemistry and Molecular Biology., 282(2), pp. 1080–1086. doi: 10.1074/jbc.M513414200.
- Johnson, W. E. B. *et al.* (2005) ‘Human intervertebral disc aggrecan inhibits endothelial cell adhesion and cell migration in vitro’, *Spine*, 30(10), pp. 1139–1147. doi: 10.1097/01.brs.0000162624.95262.73.
- Karimi, F. *et al.* (2018) ‘Beyond RGD; nanoclusters of syndecan- and integrin-binding ligands synergistically enhance cell/material interactions’, *Biomaterials*. Elsevier,

- 187(September), pp. 81–92. doi: 10.1016/j.biomaterials.2018.10.002.
- Karimi, F. *et al.* (2021) ‘Biomaterials functionalized with nanoclusters of integrin- and syndecan-binding ligands improve cell adhesion and mechanosensing under shear flow conditions’, *Journal of Biomedical Materials Research Part A*, 109(3), pp. 313–325. doi: 10.1002/jbm.a.37024.
- Kartsogiannis, V. and Ng, K. W. (2004) ‘Cell lines and primary cell cultures in the study of bone cell biology’, *Molecular and Cellular Endocrinology*, 228(1–2), pp. 79–102. doi: 10.1016/j.mce.2003.06.002.
- Katagiri, T. *et al.* (1994) ‘Bone morphogenetic protein-2 converts the differentiation pathway of C2C12 myoblasts into the osteoblast lineage’, *Journal of Cell Biology*, 127(6 I), pp. 1755–1766. doi: 10.1083/jcb.127.6.1755.
- Katagiri, T. (1994) ‘Bone morphogenetic protein-2 converts the differentiation pathway of C2C12 myoblasts into the osteoblast lineage [published erratum appears in J Cell Biol 1995 Feb;128(4):following 713]’, *The Journal of Cell Biology*, 127(6), pp. 1755–1766. doi: 10.1083/jcb.127.6.1755.
- Katagiri, T. and Watabe, T. (2016) ‘Bone morphogenetic proteins’, *Cold Spring Harbor Perspectives in Biology*, 8(6). doi: 10.1101/cshperspect.a021899.
- Kawashima, K. *et al.* (2020) ‘Heparan sulfate deficiency leads to hypertrophic chondrocytes by increasing bone morphogenetic protein signaling’, *Osteoarthritis and Cartilage*. Elsevier Ltd, 28(11), pp. 1459–1470. doi: 10.1016/j.joca.2020.08.003.
- Kechagia, J. Z., Ivaska, J. and Roca-Cusachs, P. (2019) ‘Integrins as biomechanical sensors of the microenvironment’, *Nature Reviews Molecular Cell Biology*, 20(8), pp. 457–473. doi: 10.1038/s41580-019-0134-2.
- Kim, M. G. *et al.* (2021) ‘Selective endocytosis of recombinant human BMPs through cell surface heparan sulfate proteoglycans in CHO cells: BMP-2 and BMP-7’, *Scientific Reports*. Nature Publishing Group UK, 11(1), pp. 1–15. doi: 10.1038/s41598-021-82955-1.
- Kim, Sung Eun *et al.* (2014) ‘Improving osteoblast functions and bone formation upon BMP-2 immobilization on titanium modified with heparin’, *Carbohydrate Polymers*, 114, pp. 123–132. doi: 10.1016/j.carbpol.2014.08.005.
- Kisiel, M., Klar, A. S., *et al.* (2013) ‘Complexation and Sequestration of BMP-2 from an ECM Mimetic Hyaluronan Gel for Improved Bone Formation’, *PLoS ONE*, 8(10), pp. 1–13. doi: 10.1371/journal.pone.0078551.
- Kisiel, M., Martino, M. M., *et al.* (2013) ‘Improving the osteogenic potential of BMP-2 with hyaluronic acid hydrogel modified with integrin-specific fibronectin fragment’, *Biomaterials*. Elsevier Ltd, 34(3), pp. 704–712. doi: 10.1016/j.biomaterials.2012.10.015.
- Kjellén, L. and Lindahl, U. (1991) ‘PROTEOGLYCANS: STRUCTURES AND INTERACTIONS’, *Annual Review of Biochemistry*. Annual Reviews, 60(1), pp. 443–475. doi: 10.1146/annurev.bi.60.070191.002303.
- Kobata, A. (2004) ‘Glycoproteins’, in Martini, L. B. T.-E. of E. D. (ed.). New York: Elsevier, pp. 279–285. doi: <https://doi.org/10.1016/B0-12-475570-4/00542-4>.
- Kolin, D. L. and Wiseman, P. W. (2007) ‘Advances in image correlation spectroscopy: Measuring number densities, aggregation states, and dynamics of fluorescently labeled macromolecules in cells’, *Cell Biochemistry and Biophysics*, 49(3), pp. 141–164. doi: 10.1007/s12013-007-9000-5.
- Kong, F. *et al.* (2012) ‘Automatic liquid handling for life science: A critical review of the current state of the art’, *Journal of Laboratory Automation*, 17(3), pp. 169–185. doi: 10.1177/2211068211435302.
- Kourouklis, A. P., Kaylan, K. B. and Underhill, G. H. (2016) ‘Substrate stiffness and matrix

- composition coordinately control the differentiation of liver progenitor cells', *Biomaterials*. Elsevier Ltd, 99, pp. 82–94. doi: 10.1016/j.biomaterials.2016.05.016.
- Kozma, P. *et al.* (2014) 'Integrated planar optical waveguide interferometer biosensors: A comparative review', *Biosensors and Bioelectronics*. Elsevier, 58, pp. 287–307. doi: 10.1016/j.bios.2014.02.049.
- Kreuger, J. and Kjellén, L. (2012) 'Heparan Sulfate Biosynthesis: Regulation and Variability', *Journal of Histochemistry and Cytochemistry*, 60(12), pp. 898–907. doi: 10.1369/0022155412464972.
- Kuo, W.-J., Digman, M. A. and Lander, A. D. (2010) 'Heparan Sulfate Acts as a Bone Morphogenetic Protein Coreceptor by Facilitating Ligand-induced Receptor Hetero-oligomerization', *Molecular Biology of the Cell*. American Society for Cell Biology (mboc), 21(22), pp. 4028–4041. doi: 10.1091/mbc.e10-04-0348.
- Laitinen, O. H. *et al.* (2006) 'Genetically engineered avidins and streptavidins', *Cellular and Molecular Life Sciences*, 63(24), pp. 2992–3017. doi: 10.1007/s00018-006-6288-z.
- Lapin, N. A. and Chabal, Y. J. (2009) 'Infrared characterization of biotinylated silicon oxide surfaces, surface stability, and specific attachment of streptavidin', *Journal of Physical Chemistry B*, 113(25), pp. 8776–8783. doi: 10.1021/jp809096m.
- LeBaron, R. G. *et al.* (1988) 'Adhesion of glycosaminoglycan-deficient Chinese hamster ovary cell mutants to fibronectin substrata', *Journal of Cell Biology*, 106(3), pp. 945–952. doi: 10.1083/jcb.106.3.945.
- Lee, G. H. *et al.* (2018) 'Construction of neurospheroids via surface modified concave microwells', *Journal of Industrial and Engineering Chemistry*. The Korean Society of Industrial and Engineering Chemistry, 62, pp. 341–351. doi: 10.1016/j.jiec.2018.01.014.
- Levy-Adam, F. *et al.* (2008) 'Heparanase Facilitates Cell Adhesion and Spreading by Clustering of Cell Surface Heparan Sulfate Proteoglycans', *PLoS ONE*. Edited by J. P. R. O. Orgel, 3(6), p. e2319. doi: 10.1371/journal.pone.0002319.
- Lewis, N. E. *et al.* (2013) 'Genomic landscapes of Chinese hamster ovary cell lines as revealed by the *Cricetulus griseus* draft genome', *Nature Biotechnology*, 31(8), pp. 759–765. doi: 10.1038/nbt.2624.
- Lidholt, K. *et al.* (1992) 'A single mutation affects both N-acetylglucosaminyltransferase and glucuronosyltransferase activities in a Chinese hamster ovary cell mutant defective in heparan sulfate biosynthesis', *Proceedings of the National Academy of Sciences of the United States of America*, 89(6), pp. 2267–2271. doi: 10.1073/pnas.89.6.2267.
- Lima, M., Rudd, T. and Yates, E. (2017) 'New applications of heparin and other glycosaminoglycans', *Molecules*, 22(5), pp. 1–11. doi: 10.3390/molecules22050749.
- Lin, X. *et al.* (2020) 'The Bone Extracellular Matrix in Bone Formation and Regeneration', *Frontiers in Pharmacology*, 11(May), pp. 1–15. doi: 10.3389/fphar.2020.00757.
- Llopis-Hernández, V. *et al.* (2016) 'Material-driven fibronectin assembly for high-efficiency presentation of growth factors', *Science Advances*, 2(8), pp. 1–10. doi: 10.1126/sciadv.1600188.
- Lohmander, S. (1988) 'Proteoglycans of joint cartilage. Structure, function, turnover and role as markers of joint disease', *Bailliere's Clinical Rheumatology*, 2(1), pp. 37–62. doi: 10.1016/S0950-3579(88)80004-9.
- Long, F. (2012) 'Building strong bones: molecular regulation of the osteoblast lineage', *Nature Reviews Molecular Cell Biology*, 13(1), pp. 27–38. doi: 10.1038/nrm3254.
- Longley, R. L. *et al.* (1999) 'Control of morphology, cytoskeleton and migration by syndecan-4', *Journal of Cell Science*, 112(20), pp. 3421–3431. doi: 10.1242/jcs.112.20.3421.
- Lord, M. S. *et al.* (2014) 'The role of vascular-derived perlecan in modulating cell adhesion, proliferation and growth factor signaling', *Matrix Biology*. International Society of Matrix

- Biology, 35, pp. 112–122. doi: 10.1016/j.matbio.2014.01.016.
- Lundmark, K. *et al.* (2001) ‘Perlecan inhibits smooth muscle cell adhesion to fibronectin: Role of heparan sulfate’, *Journal of Cellular Physiology*, 188(1), pp. 67–74. doi: 10.1002/jcp.1094.
- Ma, X. *et al.* (2018) ‘3D bioprinting of functional tissue models for personalized drug screening and in vitro disease modeling’, *Advanced Drug Delivery Reviews*, 132, pp. 235–251. doi: 10.1016/j.addr.2018.06.011.
- Macháň, R. and Wohland, T. (2014) ‘Recent applications of fluorescence correlation spectroscopy in live systems’, *FEBS Letters*, 588(19), pp. 3571–3584. doi: 10.1016/j.febslet.2014.03.056.
- Machillot, P. *et al.* (2018) ‘Automated Buildup of Biomimetic Films in Cell Culture Microplates for High-Throughput Screening of Cellular Behaviors’, *Advanced Materials*, 30(27), pp. 1–8. doi: 10.1002/adma.201801097.
- Macri, L., Silverstein, D. and Clark, R. A. F. (2007) ‘Growth factor binding to the pericellular matrix and its importance in tissue engineering’, *Advanced Drug Delivery Reviews*, 59(13), pp. 1366–1381. doi: 10.1016/j.addr.2007.08.015.
- Mahalingam, Y., Gallagher, J. T. and Couchman, J. R. (2007) ‘Cellular Adhesion Responses to the Heparin-binding (HepII) Domain of Fibronectin Require Heparan Sulfate with Specific Properties’, *Journal of Biological Chemistry*. © 2007 ASBMB. Currently published by Elsevier Inc; originally published by American Society for Biochemistry and Molecular Biology., 282(5), pp. 3221–3230. doi: 10.1074/jbc.M604938200.
- Mantha, S. *et al.* (2019) ‘Smart Hydrogels in Tissue Engineering and Regenerative Medicine’, *Materials*, 12(20), p. 3323. doi: 10.3390/ma12203323.
- Martino, M. M. and Hubbell, J. A. (2010) ‘The 12th–14th type III repeats of fibronectin function as a highly promiscuous growth factor-binding domain’, *The FASEB Journal*. United States, 24(12), pp. 4711–4721. doi: 10.1096/fj.09-151282.
- Mauriz, E., García-Fernández, M. C. and Lechuga, L. M. (2016) ‘Towards the design of universal immunosurfaces for SPR-based assays: A review’, *TrAC - Trends in Analytical Chemistry*. Elsevier B.V., 79, pp. 191–198. doi: 10.1016/j.trac.2016.02.006.
- Meneghetti, M. C. Z. *et al.* (2015) ‘Heparan sulfate and heparin interactions with proteins’, *Journal of The Royal Society Interface*, 12(110), p. 20150589. doi: 10.1098/rsif.2015.0589.
- Mets, R. De *et al.* (2014) ‘Determination of protein concentration on substrates using fluorescence fluctuation microscopy’, in *Proc.SPIE*. doi: 10.1117/12.2040355.
- Michael Green, N. (1990) ‘[5] Avidin and streptavidin’, in, pp. 51–67. doi: 10.1016/0076-6879(90)84259-J.
- Migliorini, E. *et al.* (2014) ‘Well-defined biomimetic surfaces to characterize glycosaminoglycan-mediated interactions on the molecular, supramolecular and cellular levels’, *Biomaterials*. Elsevier Ltd, 35(32), pp. 8903–8915. doi: 10.1016/j.biomaterials.2014.07.017.
- Migliorini, E. *et al.* (2016) ‘Tuning cellular responses to BMP-2 with material surfaces’, *Cytokine and Growth Factor Reviews*. Elsevier Ltd, 27, pp. 43–54. doi: 10.1016/j.cytogfr.2015.11.008.
- Migliorini, E. *et al.* (2017) ‘Enhanced biological activity of BMP-2 bound to surface-grafted heparan sulfate’, *Advanced Biosystems*, 1(4), p. 1600041. doi: 10.1002/adbi.201600041.
- Migliorini, E. *et al.* (2020) ‘Learning from BMPs and their biophysical extracellular matrix microenvironment for biomaterial design’, *Bone*. Elsevier, 141(July), p. 115540. doi: 10.1016/j.bone.2020.115540.
- Migliorini, E., Weidenhaupt, M. and Picart, C. (2018) ‘Practical guide to characterize biomolecule adsorption on solid surfaces (Review)’, *Biointerphases*, 13(6), p. 06D303.

- doi: 10.1116/1.5045122.
- Mikami, T. and Kitagawa, H. (2013) 'Biosynthesis and function of chondroitin sulfate', *Biochimica et Biophysica Acta - General Subjects*. Elsevier B.V., 1830(10), pp. 4719–4733. doi: 10.1016/j.bbagen.2013.06.006.
- Miller, E. *et al.* (2009) 'Inkjet Printing of Growth Factor Concentration Gradients and Combinatorial Arrays Immobilized on Biologically-Relevant Substrates', *Combinatorial Chemistry & High Throughput Screening*, 12(6), pp. 604–618. doi: 10.2174/138620709788681907.
- Monge, C. *et al.* (2015) 'Spatio-Temporal Control of LbL Films for Biomedical Applications: From 2D to 3D', *Advanced Healthcare Materials*, 4(6), pp. 811–830. doi: 10.1002/adhm.201400715.
- Monteiro A., I., Kollmetz, T. and Malmström, J. (2018) 'Engineered systems to study the synergistic signaling between integrin-mediated mechanotransduction and growth factors (Review)', *Biointerphases*, 13(6), p. 06D302. doi: 10.1116/1.5045231.
- Moon, J. J. *et al.* (2005) 'Role of cell surface heparan sulfate proteoglycans in endothelial cell migration and mechanotransduction', *Journal of Cellular Physiology*, 203(1), pp. 166–176. doi: 10.1002/jcp.20220.
- Morgenthaler, S. *et al.* (2006) 'Poly(1-lysine)-grafted-poly(ethylene glycol)-based surface-chemical gradients. Preparation, characterization, and first applications', *Biointerphases*, 1(4), pp. 156–165. doi: 10.1116/1.2431704.
- Mosier-Boss, P. A. (2017) 'Review of SERS substrates for chemical sensing', *Nanomaterials*, 7(6). doi: 10.3390/nano7060142.
- Müller, J. D. (2004) 'Cumulant analysis in fluorescence fluctuation spectroscopy', *Biophysical Journal*, 86(6), pp. 3981–3992. doi: 10.1529/biophysj.103.037887.
- Murali, S. *et al.* (2013) 'Affinity-selected heparan sulfate for bone repair', *Biomaterials*. Elsevier Ltd, 34(22), pp. 5594–5605. doi: 10.1016/j.biomaterials.2013.04.017.
- Nugent, M. A., Zaia, J. and Spencer, J. L. (2013) 'Heparan sulfate-protein binding specificity', *Biochemistry (Moscow)*, 78(7), pp. 726–735. doi: 10.1134/S0006297913070055.
- Oberhansl, S. *et al.* (2014) 'Mesopattern of immobilised bone morphogenetic protein-2 created by microcontact printing and dip-pen nanolithography influence C2C12 cell fate', *RSC Advances*, 4(100), pp. 56809–56815. doi: 10.1039/c4ra10311d.
- Obradovic Wagner, D. *et al.* (2010) 'BMPs: From Bone to Body Morphogenetic Proteins', *Science Signaling*, 3(107), pp. mr1–mr1. doi: 10.1126/scisignal.3107mr1.
- Oliver-Cervelló, L. *et al.* (2021a) 'An Engineered Biomimetic Peptide Regulates Cell Behavior by Synergistic Integrin and Growth Factor Signaling', *Advanced Healthcare Materials*, 10(7). doi: 10.1002/adhm.202001757.
- Oliver-Cervelló, L. *et al.* (2021b) 'An Engineered Biomimetic Peptide Regulates Cell Behavior by Synergistic Integrin and Growth Factor Signaling', *Advanced Healthcare Materials*, 10(7), pp. 1–10. doi: 10.1002/adhm.202001757.
- Pacifici, M. (2017) 'Hereditary Multiple Exostoses: New Insights into Pathogenesis, Clinical Complications, and Potential Treatments.', *Current osteoporosis reports*. United States, 15(3), pp. 142–152. doi: 10.1007/s11914-017-0355-2.
- Pacifici, M. (2018) 'The pathogenic roles of heparan sulfate deficiency in hereditary multiple exostoses', *Matrix Biology*. Elsevier B.V., 71–72, pp. 28–39. doi: 10.1016/j.matbio.2017.12.011.
- Pang, X. *et al.* (2021) 'Hyaluronan (HA) Immobilized on Surfaces via Self-Assembled Monolayers of HA-Binding Peptide Modulates Endothelial Cell Spreading and Migration through Focal Adhesion', *ACS Applied Materials and Interfaces*, 13(22), pp. 25792–25804. doi: 10.1021/acsami.1c05574.

- Pearce, A. *et al.* (2007) ‘Animal models for implant biomaterial research in bone: A review’, *European Cells and Materials*, 13(0), pp. 1–10. doi: 10.22203/eCM.v013a01.
- Petersen, N. O. *et al.* (1993) ‘Quantitation of membrane receptor distributions by image correlation spectroscopy: concept and application’, *Biophysical Journal*, 65(3), pp. 1135–1146. doi: 10.1016/S0006-3495(93)81173-1.
- Pfaff, M. *et al.* (1994) ‘Selective recognition of cyclic RGD peptides of NMR defined conformation by alpha IIb beta 3, alpha V beta 3, and alpha 5 beta 1 integrins.’, *The Journal of biological chemistry*. United States, 269(32), pp. 20233–20238.
- Pieuchot, L. *et al.* (2018) ‘Curvotaxis directs cell migration through cell-scale curvature landscapes’, *Nature Communications*, 9(1), p. 3995. doi: 10.1038/s41467-018-06494-6.
- Plow, E. F. *et al.* (2000) ‘Ligand binding to integrins’, *Journal of Biological Chemistry*. © 2000 ASBMB. Currently published by Elsevier Inc; originally published by American Society for Biochemistry and Molecular Biology., 275(29), pp. 21785–21788. doi: 10.1074/jbc.R000003200.
- Posa, F. *et al.* (2021) ‘Surface Co-presentation of BMP-2 and integrin selective ligands at the nanoscale favors $\alpha 5\beta 1$ integrin-mediated adhesion’, *Biomaterials*. Elsevier Ltd, 267(October 2020), p. 120484. doi: 10.1016/j.biomaterials.2020.120484.
- Qin, D., Xia, Y. and Whitesides, G. M. (2010) ‘Soft lithography for micro- and nanoscale patterning’, *Nature Protocols*, 5(3), pp. 491–502. doi: 10.1038/nprot.2009.234.
- Ramel, M.-C. and Hill, C. S. (2013) ‘The ventral to dorsal BMP activity gradient in the early zebrafish embryo is determined by graded expression of BMP ligands’, *Developmental Biology*, 378(2), pp. 170–182. doi: 10.1016/j.ydbio.2013.03.003.
- Ramesh, N., Moratti, S. C. and Dias, G. J. (2018) ‘Hydroxyapatite–polymer biocomposites for bone regeneration: A review of current trends’, *Journal of Biomedical Materials Research - Part B Applied Biomaterials*, 106(5), pp. 2046–2057. doi: 10.1002/jbm.b.33950.
- Ranga, A. *et al.* (2014) ‘3D niche microarrays for systems-level analyses of cell fate’, *Nature Communications*. Nature Publishing Group, 5, pp. 1–10. doi: 10.1038/ncomms5324.
- Reviakine, I., Johannsmann, D. and Richter, R. P. (2011) ‘Hearing what you cannot see and visualizing what you hear’, *Analytical chemistry*, 83, pp. 8838–8848.
- Richter, R. P. *et al.* (2007) ‘Membrane-Grafted Hyaluronan Films: A Well-Defined Model System of Glycoconjugate Cell Coats’, *Journal of the American Chemical Society*, 129(17), pp. 5306–5307. doi: 10.1021/ja068768s.
- Rigler, R. and Elson, E. S. (2001) *Fluorescence Correlation Spectroscopy*. Berlin, Heidelberg: Springer Berlin Heidelberg (Springer Series in Chemical Physics). doi: 10.1007/978-3-642-59542-4.
- Roddy, E. *et al.* (2018) ‘Treatment of critical-sized bone defects: clinical and tissue engineering perspectives’, *European Journal of Orthopaedic Surgery and Traumatology*. Springer Paris, 28(3), pp. 351–362. doi: 10.1007/s00590-017-2063-0.
- Rossow, M. J. *et al.* (2010) ‘Raster image correlation spectroscopy in live cells’, *Nature Protocols*, 5(11), pp. 1761–1774. doi: 10.1038/nprot.2010.122.
- Roth, E. A. *et al.* (2004) ‘Inkjet printing for high-throughput cell patterning’, *Biomaterials*, 25(17), pp. 3707–3715. doi: 10.1016/j.biomaterials.2003.10.052.
- Rudd, T. R. *et al.* (2017) ‘The nature of the conserved basic amino acid sequences found among 437 heparin binding proteins determined by network analysis.’, *Molecular bioSystems*. England: Royal Society of Chemistry, 13(5), pp. 852–865. doi: 10.1039/c6mb00857g.
- Ruppert, R., Hoffmann, E. and Sebald, W. (1996) ‘Human bone morphogenetic protein 2 contains a heparin-binding site which modifies its biological activity’, *European Journal of Biochemistry*, 237(1), pp. 295–302. doi: 10.1111/j.1432-1033.1996.0295n.x.
- Saftics, A. *et al.* (2021) ‘Data evaluation for surface-sensitive label-free methods to obtain real-

- time kinetic and structural information of thin films: A practical review with related software packages', *Advances in Colloid and Interface Science*, 294. doi: 10.1016/j.cis.2021.102431.
- Salazar, V. S., Gamer, L. W. and Rosen, V. (2016) 'BMP signalling in skeletal development, disease and repair', *Nature Reviews Endocrinology*. Nature Publishing Group, 12(4), pp. 203–221. doi: 10.1038/nrendo.2016.12.
- Sanderson, M. J. *et al.* (2014) 'Fluorescence Microscopy', *Cold Spring Harbor Protocols*, 2014(10), p. pdb.top071795-pdb.top071795. doi: 10.1101/pdb.top071795.
- Sarkar, A. and Desai, U. R. (2015) 'A Simple Method for Discovering Druggable, Specific Glycosaminoglycan-Protein Systems. Elucidation of Key Principles from Heparin/Heparan Sulfate-Binding Proteins', *PLOS ONE*. Public Library of Science, 10(10), pp. 1–18. doi: 10.1371/journal.pone.0141127.
- Sarrazin, S., Lamanna, W. C. and Esko, J. D. (2011) 'Heparan Sulfate Proteoglycans', *Cold Spring Harbor Perspectives in Biology*, 3(7), pp. a004952–a004952. doi: 10.1101/cshperspect.a004952.
- Sasisekharan, R. and Venkataraman, G. (2000) 'Heparin and heparan sulfate: Biosynthesis, structure and function', *Current Opinion in Chemical Biology*, 4(6), pp. 626–631. doi: 10.1016/S1367-5931(00)00145-9.
- Sauerbrey, G. (1959) 'Verwendung von Schwingquarzen zur Wägung dünner Schichten und zur Mikrowägung', *Zeitschrift für Physik*, 155(2), pp. 206–222. doi: 10.1007/BF01337937.
- Saunders, R. E. and Derby, B. (2014) 'Inkjet printing biomaterials for tissue engineering: bioprinting', *International Materials Reviews*, 59(8), pp. 430–448. doi: 10.1179/1743280414Y.0000000040.
- Sawala, A. *et al.* (2015) 'Peak BMP Responses in the Drosophila Embryo Are Dependent on the Activation of Integrin Signaling Report Peak BMP Responses in the Drosophila Embryo Are Dependent on the Activation of Integrin Signaling', *CellReports*. The Authors, 12(10), pp. 1584–1593. doi: 10.1016/j.celrep.2015.08.012.
- Schaufler, V. *et al.* (2016) 'Selective binding and lateral clustering of $\alpha 5 \beta 1$ and $\alpha v \beta 3$ integrins: Unraveling the spatial requirements for cell spreading and focal adhesion assembly', *Cell Adhesion & Migration*. Taylor & Francis, 10(5), pp. 505–515. doi: 10.1080/19336918.2016.1163453.
- Scheufler, C., Sebald, W. and Hülsmeier, M. (1999) 'Crystal structure of human bone morphogenetic protein-2 at 2.7 Å resolution' Edited by R. Huber', *Journal of Molecular Biology*, 287(1), pp. 103–115. doi: https://doi.org/10.1006/jmbi.1999.2590.
- Schuksz, M. *et al.* (2008) 'Surfen, a small molecule antagonist of heparan sulfate', *Proceedings of the National Academy of Sciences of the United States of America*, 105(35), pp. 13075–13080. doi: 10.1073/pnas.0805862105.
- Schwab, E. H. *et al.* (2015) 'Nanoscale control of surface immobilized BMP-2: Toward a quantitative assessment of BMP-mediated signaling events', *Nano Letters*, 15(3), pp. 1526–1534. doi: 10.1021/acs.nanolett.5b00315.
- Sedlmeier, G. and Sleeman, J. P. (2017) 'Extracellular regulation of BMP signaling: welcome to the matrix', *Biochemical Society Transactions*, 45(1), pp. 173–181. doi: 10.1042/BST20160263.
- Seetharaman, S. and Etienne-Manneville, S. (2018) 'Integrin diversity brings specificity in mechanotransduction', *Biology of the Cell*, 110(3), pp. 49–64. doi: 10.1111/boc.201700060.
- Sefkow-Werner, J. *et al.* (2020) 'Heparan sulfate co-immobilized with cRGD ligands and BMP2 on biomimetic platforms promotes BMP2-mediated osteogenic differentiation.', *Acta biomaterialia*. Elsevier Ltd, 114, pp. 90–103. doi: 10.1016/j.actbio.2020.07.015.

- Sefkow-Werner, J. *et al.* (2021) ‘Combining fluorescence fluctuations and photobleaching to quantify surface density’. doi: arXiv:2110.14319.
- Shin, H. *et al.* (2020) ‘Protein quantification and imaging by surface-enhanced raman spectroscopy and similarity analysis’, *Advanced Science*, 7(11), pp. 1–9. doi: 10.1002/advs.201903638.
- Slaughter, B. D. and Li, R. (2010) ‘Toward Quantitative “In Vivo Biochemistry” with Fluorescence Fluctuation Spectroscopy’, *Molecular Biology of the Cell*. Edited by D. Kellogg, 21(24), pp. 4306–4311. doi: 10.1091/mbc.e10-05-0451.
- Smith, P. K. *et al.* (1985) ‘Measurement of protein using bicinchoninic acid’, *Analytical Biochemistry*, 150(1), pp. 76–85. doi: 10.1016/0003-2697(85)90442-7.
- Smith, R. A. A. *et al.* (2017) ‘Retention of the Structure and Function of Heparan Sulfate Biomaterials After Gamma Irradiation’, *Tissue Engineering Part A*. Mary Ann Liebert, Inc., publishers, 24(9–10), pp. 729–739. doi: 10.1089/ten.tea.2017.0263.
- Smith, R. A. A. *et al.* (2018) ‘Minimum structural requirements for BMP-2-binding of heparin oligosaccharides’, *Biomaterials*. Elsevier, 184(June), pp. 41–55. doi: 10.1016/j.biomaterials.2018.08.056.
- Stangegaard, M. *et al.* (2009) ‘Automated extraction of DNA and PCR setup using a Tecan Freedom EVO® liquid handler’, *Forensic Science International: Genetics Supplement Series*, 2(1), pp. 74–76. doi: 10.1016/j.fsigss.2009.07.002.
- Stevens, M. M. (2008) ‘Biomaterials for bone tissue engineering’, *Materials Today*. Elsevier Ltd, 11(5), pp. 18–25. doi: 10.1016/S1369-7021(08)70086-5.
- Sun, L. *et al.* (2020) ‘The effects of syndecan on osteoblastic cell adhesion onto nano-zirconia surface’, *International Journal of Nanomedicine*, 15, pp. 5061–5072. doi: 10.2147/IJN.S263053.
- Tellier, L. E. *et al.* (2015) ‘Hydrolysis and sulfation pattern effects on release of bioactive bone morphogenetic protein-2 from heparin-based microparticles’, *Journal of Materials Chemistry B*. Royal Society of Chemistry, 3(40), pp. 8001–8009. doi: 10.1039/c5tb00933b.
- Thakar, D. *et al.* (2017) ‘Binding of the chemokine CXCL12 α to its natural extracellular matrix ligand heparan sulfate enables myoblast adhesion and facilitates cell motility’, *Biomaterials*. Elsevier Ltd, 123, pp. 24–38. doi: 10.1016/j.biomaterials.2017.01.022.
- Tjio, J. H. and Puck, T. T. (1958) ‘GENETICS OF SOMATIC MAMMALIAN CELLS’, *Journal of Experimental Medicine*, 108(2), pp. 259–268. doi: 10.1084/jem.108.2.259.
- Urist, M. R. (1965) ‘Bone: Formation by Autoinduction’, *Science*, 150(3698), pp. 893–899. doi: 10.1126/science.150.3698.893.
- Vallet, S. D., Clerc, O. and Ricard-Blum, S. (2021) ‘Glycosaminoglycan–Protein Interactions: The First Draft of the Glycosaminoglycan Interactome’, *Journal of Histochemistry & Cytochemistry*, 69(2), pp. 93–104. doi: 10.1369/0022155420946403.
- Vasilevich, A. and de Boer, J. (2018) ‘Robot-scientists will lead tomorrow’s biomaterials discovery’, *Current Opinion in Biomedical Engineering*. Elsevier Ltd, 6, pp. 74–80. doi: 10.1016/j.cobme.2018.03.005.
- Velleman, S. G. and Song, Y. (2017) ‘Development and Growth of the Avian Pectoralis Major (Breast) Muscle: Function of Syndecan-4 and Glypican-1 in Adult Myoblast Proliferation and Differentiation’, *Frontiers in Physiology*, 8(AUG), pp. 1–11. doi: 10.3389/fphys.2017.00577.
- Verdaasdonk, J. S., Lawrimore, J. and Bloom, K. (2014) ‘Chapter 19 - Determining absolute protein numbers by quantitative fluorescence microscopy’, in Waters, J. C. and Wittman, T. B. T.-M. in C. B. (eds) *Quantitative Imaging in Cell Biology*. Academic Press, pp. 347–365. doi: <https://doi.org/10.1016/B978-0-12-420138-5.00019-7>.
- Verhulsel, M. *et al.* (2014) ‘A review of microfabrication and hydrogel engineering for micro-

- organs on chips', *Biomaterials*. Elsevier Ltd, 35(6), pp. 1816–1832. doi: 10.1016/j.biomaterials.2013.11.021.
- Villar, M. J., Hassell, J. R. and Brandan, E. (1999) 'Interaction of skeletal muscle cells with collagen type IV is mediated by perlecan associated with the cell surface', *Journal of Cellular Biochemistry*, 75(4), pp. 665–674. doi: 10.1002/(SICI)1097-4644(19991215)75:4<665::AID-JCB12>3.0.CO;2-S.
- Vörös, J. *et al.* (2002) 'Optical grating coupler biosensors', *Biomaterials*, 23(17), pp. 3699–3710. doi: 10.1016/S0142-9612(02)00103-5.
- Wang, W. Y. *et al.* (2018) 'Extracellular matrix alignment dictates the organization of focal adhesions and directs uniaxial cell migration', *APL Bioengineering*, 2(4), p. 046107. doi: 10.1063/1.5052239.
- Whitelock, J. M. *et al.* (1999) 'Human perlecan immunopurified from different endothelial cell sources has different adhesive properties for vascular cells', *Matrix Biology*, 18(2), pp. 163–178. doi: 10.1016/S0945-053X(99)00014-1.
- Woods, A. and Couchman, J. R. (1994) 'Syndecan 4 heparan sulfate proteoglycan is a selectively enriched and widespread focal adhesion component', *Molecular Biology of the Cell*, 5(2), pp. 183–192. doi: 10.1091/mbc.5.2.183.
- Wozney, J. *et al.* (1988) 'Novel regulators of bone formation: molecular clones and activities', *Science*, 242(4885), pp. 1528–1534. doi: 10.1126/science.3201241.
- Wu, M., Chen, G. and Li, Y. P. (2016) 'TGF- β and BMP signaling in osteoblast, skeletal development, and bone formation, homeostasis and disease', *Bone Research*, 4(December 2015). doi: 10.1038/boneres.2016.9.
- Würzler, K. K. *et al.* (2004) 'Evaluation of the osteoinductive potential of genetically modified BMP-2 variants', *Mund-, Kiefer- und Gesichtschirurgie: MKG*, 8(2), pp. 83–92. doi: 10.1007/s10006-004-0528-x.
- Xu, D. and Esko, J. D. (2014) 'Demystifying Heparan Sulfate–Protein Interactions', *Annual Review of Biochemistry*, 83(1), pp. 129–157. doi: 10.1146/annurev-biochem-060713-035314.
- Xu, J. and Mosher, D. (2011) 'Fibronectin and Other Adhesive Glycoproteins', in *The Extracellular Matrix: an Overview*. Berlin, Heidelberg: Springer Berlin Heidelberg, pp. 41–75. doi: 10.1007/978-3-642-16555-9_2.
- YAFFE, D. and SAXEL, O. (1977) 'Serial passaging and differentiation of myogenic cells isolated from dystrophic mouse muscle', *Nature*, 270(5639), pp. 725–727. doi: 10.1038/270725a0.
- Yamada, M. and Sekiguchi, K. (2015) 'Chapter Six - Molecular Basis of Laminin–Integrin Interactions', in Miner, J. H. B. T.-C. T. in M. (ed.) *Basement Membranes*. Academic Press, pp. 197–229. doi: <https://doi.org/10.1016/bs.ctm.2015.07.002>.
- Yue, B. (2014) 'Biology of the extracellular matrix: An overview', *Journal of Glaucoma*, 23(8), pp. S20–S23. doi: 10.1097/IJG.000000000000108.
- Yue, S. *et al.* (2020) 'Hydrogel as a biomaterial for bone tissue engineering: A review', *Nanomaterials*, 10(8), pp. 1–25. doi: 10.3390/nano10081511.
- Zalipsky, S. and Harris, J. M. (1997) 'Introduction to Chemistry and Biological Applications of Poly(ethylene glycol)', in, pp. 1–13. doi: 10.1021/bk-1997-0680.ch001.
- Zeng, W. *et al.* (2020) 'High-throughput screening technology in industrial biotechnology', *Trends in Biotechnology*. Elsevier Ltd, 38(8), pp. 1–19. doi: 10.1016/j.tibtech.2020.01.001.
- Zhang, D., Lee, J. and Kilian, K. A. (2017) 'Synthetic Biomaterials to Rival Nature's Complexity—a Path Forward with Combinatorics, High-Throughput Discovery, and High-Content Analysis', *Advanced Healthcare Materials*, 6(19), p. 1700535. doi: 10.1002/adhm.201700535.

- Zhang, F., Zhang, Z. and Linhardt, R. J. (2010) 'Chapter 3 - Glycosaminoglycans', in Cummings, R. D. and Pierce, J. M. B. T.-H. of G. (eds). San Diego: Academic Press, pp. 59–80. doi: <https://doi.org/10.1016/B978-0-12-373600-0.00003-2>.
- Zhang, L. *et al.* (2021) 'Using FCS to accurately measure protein concentration in the presence of noise and photobleaching', *Biophysical Journal*, 120(19), pp. 4230–4241. doi: [10.1016/j.bpj.2021.06.035](https://doi.org/10.1016/j.bpj.2021.06.035).
- Zhen, G. *et al.* (2004) 'Immobilization of the Enzyme β -Lactamase on Biotin-Derivatized Poly(α -lysine)-*g*-poly(ethylene glycol)-Coated Sensor Chips: A Study on Oriented Attachment and Surface Activity by Enzyme Kinetics and *in situ* Optical Sensing', *Langmuir*, 20(24), pp. 10464–10473. doi: [10.1021/la0482812](https://doi.org/10.1021/la0482812).
- Zhu, W. *et al.* (2006) 'Noggin regulation of bone morphogenetic protein (BMP) 2/7 heterodimer activity *in vitro*', *Bone*, 39(1), pp. 61–71. doi: [10.1016/j.bone.2005.12.018](https://doi.org/10.1016/j.bone.2005.12.018).
- Zoch, M. L., Clemens, T. L. and Riddle, R. C. (2016) 'New insights into the biology of osteocalcin', *Bone*. Elsevier Inc., 82, pp. 42–49. doi: [10.1016/j.bone.2015.05.046](https://doi.org/10.1016/j.bone.2015.05.046).

Annex

Estimation of contribution

This thesis is written in the style of articles, which implies the contribution of various people in the presented work. Here, I estimate my share in the four result chapters regarding the categories experimental results and writing. The main introduction (Chapter I), the summaries and transitions before and after the articles as well as the conclusion and outlook (Chapter VI) were my work only.

Chapter II

Experimental results: I was performing about 90% of the experiments. The data related to the last figure was the work of the Master student Bertin Ndayishimiye. Jean Le Pennec was modifying the graphical user interface between the user and the robot to be compatible with the routine used for the fabrication of biomimetic platforms.

Writing: I was writing the entire manuscript and prepared all figures.

Chapter III

Experimental results: I was preparing 80% of the samples and imaged them together with Antoine Delon. While Antoine Delon was analyzing the images, I was helping by writing an ImageJ macro to easily compute and organize image stacks.

Writing: I was writing a part of the introduction and a part of the methods. I was further making comments on the manuscript. It is worth to note that the theory around pbICS was developed by Antoine Delon and his group at LiPhy.

Chapter IV

Experimental results: I performed about 50% of the experiments. Elisa Migliorini did most of the other experiments.

Writing: I wrote the introduction and the methods and prepared some of the figures. I was further making comments on the other chapters.

Chapter V

Experimental results: I was performing 90% of the experiments. Fatima Asar was analyzing images of fixed and stained cells for area, ellipticity and compactness.

Writing. I wrote the entire manuscript and prepared all figures.

Julius Sefkow-Werner

31 rue Marx Dormoy, 38000 Grenoble, France
julius.sefkow-werner@cea.fr | +33 7 72 77 96 12

Curriculum Vitae

Personal Data

Date of birth: 14 May 1992 in Hamburg (GER)
Nationality: German

Education

Sep 2018 – Dec 2021 (exp.) LMGP and CEA IRIG Département Santé, Grenoble
PhD project “Engineered biomimetic platforms to analyze the molecular and cellular role of heparan sulfate on BMP2 bioactivity”
Techniques: Western blot, RT-qPCR, automated fluorescence microscopy, cell culture, clean room, surface sensitive techniques, automated liquid handling, image correlation spectroscopy
Teaching and supervision: Supervision of two M2 interns and one M1 group project.

Sep 2015 – Sep 2018 Technical University Berlin (GER)
Msc in Industrial Engineering and Management
Focus on biomedical engineering and biomaterials, (GPA 1,4)

Oct 2011 – Aug 2015 Karlsruhe Institute of Technology (KIT), Karlsruhe (GER)
BSc in Industrial Engineering and Management, (GPA 2,1)

Scientific Communications

January 2021 CEA IRIG Département Santé BMPs thematic meeting, virtual
15 min oral presentation

Dec 2020 World Biomaterials Congress 2020, virtual
15 min oral presentation

November 2020 BIOMIM webinar, virtual
15 min oral presentation

October 2020 GDR 2088 BIOMIM 1st annual meeting “Biomimicry and Bioinspiration”, Nice
15 min oral presentation

September 2020 CEA IRIG Département Santé webinar, virtual
15 min oral presentation

July 2020 1st author scientific publication, Acta Biomaterialia,
“Heparan sulfate co-immobilized with cRGD ligands and BMP2 biomimetic platforms promotes BMP2-mediated osteogenic differentiation”

June 2020 Biomat jeunes chercheurs webinar, virtual
15 min oral presentation

June 2019 Congrès Biomat Matériaux pour la Santé, La grande motte
15 min oral presentation

April 2019 LMGP PhD day, Grenoble
10 min oral presentation

Julius Sefkow-Werner

31 rue Marx Dormoy, 38000 Grenoble, France
julius.sefkow-werner@cea.fr | +33 7 72 77 96 12

December 2018 Journée 2018 du WP3 Interface cellules-l'environnement, Lyon
3 min oral presentation

International Experience

Sep 2017 – Feb 2018 Grenoble INP – Phelma (France)
MSc in “Biomedical Engineering”
Semester abroad with focus on medical imaging and biomaterials

Feb 2014 – Jul 2014 Instituto Tecnológico Buenos Aires (ITBA), Buenos Aires (AR)
Semester abroad with focus on materials and marketing

Aug 2008 – Jul 2009 Cumberland High School, Wisconsin (USA)
High School Year

Sep 2012 (2 weeks) Leadership and entrepreneurship summer academy, Sofia (BG)
Directed by Prof. Jim Platts (Cambridge University)

Work Experience

Oct 2015 – Jan 2016 Falabella S.A., Santiago de Chile (CL)
Internship in product management in e-commerce

May 2015 – Sep 2015 Karlsruhe Institute of Technology (KIT), Karlsruhe (Germany)
Research assistant at an institute for ceramic materials

Sep 2012 – Jan 2013 Fotografen Online Service GmbH, Berlin (Germany)
Internship in business development and marketing

Other

Languages German (native), English (fluent), Spanish (fluent), French (fluent)

IT skills EvoWare (advanced), ImageJ (advanced), Excel (advanced), InkScape (advanced), Python (basic)

Social Vice president of corporate relations, VWI-ESTIEM Karlsruhe (2012-13)

Interests Hiking, climbing, playing the saxophone, ski-touring, alpinism, road biking



Julius Sefkow-Werner